TECHNISCHE UNIVERSITÄT DRESDEN

Schriftenreihe aus dem
Institut für Strömungsmechanik

Band 29

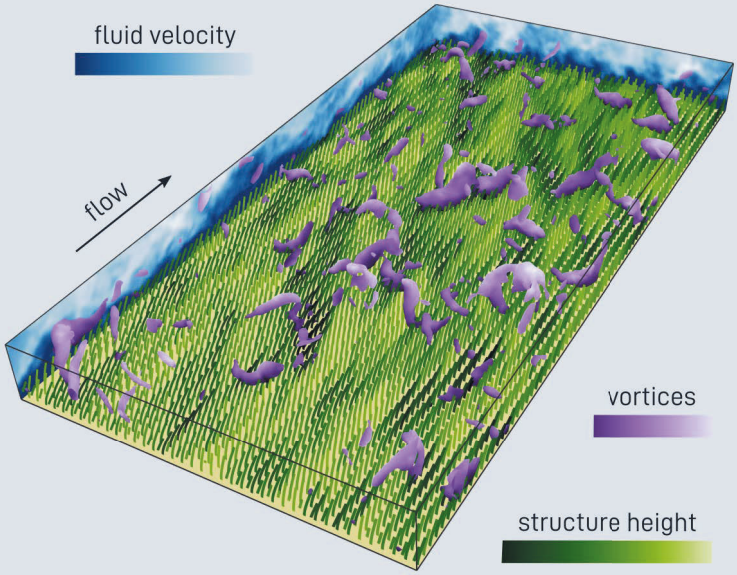

Silvio Tschisgale

A numerical method for fluid-structure interactions of slender rods in turbulent flow

TUDpress

ISM

Schriftenreihe aus dem Institut für Strömungsmechanik

Herausgeber
J. Fröhlich, R. Mailach

Institut für Strömungsmechanik
Technische Universität Dresden
D-01062 Dresden

Band 29

Silvio Tschisgale

A numerical method for fluid-structure interactions of slender rods in turbulent flow

TUD*press*
2020

Die vorliegende Arbeit wurde am 4. May 2018 an der Fakultät Maschinenwesen der Technischen Universität Dresden als Dissertation eingereicht und am 19. März 2019 erfolgreich verteidigt.

This work was submitted as a PhD thesis to the Faculty of Mechanical Science and Engineering of TU Dresden on 4 May 2018 and successfully defended on 19 March 2019.

Gutachter | Reviewers
1. Prof. Dr.-Ing. habil. J. Fröhlich
2. Prof. Dr.-Ing. habil. V. Ulbricht

Bibliografische Information der Deutschen Nationalbibliothek
Die Deutsche Nationalbibliothek verzeichnet diese Publikation in der Deutschen Nationalbibliografie; detaillierte bibliografische Daten sind im Internet über http://dnb.d-nb.de abrufbar.

Bibliographic information published by the Deutsche Nationalbibliothek
The Deutsche Nationalbibliothek lists this publication in the Deutsche Nationalbibliografie; detailed bibliographic data are available in the Internet at http://dnb.d-nb.de.

ISBN 978-3-95908-195-5

bei Thelem Universitätsverlag
und Buchhandlung GmbH & Co. KG
Dresden
http://www.tudpress.de

Gesetzt vom Autor. | Typeset by the author.
Printed in Germany.

Technische Universität Dresden
Institute of Fluid Mechanics
2019

A numerical method for fluid-structure interactions of slender rods in turbulent flow

A thesis accepted by the Faculty of Mechanical Engineering of the Technische Universität Dresden in partial fulfillment of the requirements for the degree of Doctor of Engineering Sciences (Dr.-Ing.)

by

Silvio Tschisgale

born in Schlema, Germany

Referees: Prof. Dr.-Ing. habil. Jochen Fröhlich
Technische Universität Dresden

Prof. Dr.-Ing. habil. Volker Ulbricht
Technische Universität Dresden

Date of submission: May 4, 2018
Date of defence: March 19, 2019

Danksagung

Die vorliegende Dissertation entstand im Zeitraum von 2012 bis 2018 im Rahmen meiner Tätigkeit als wissenschaftlicher Mitarbeiter an der Professur für Strömungsmechanik der Technischen Universität Dresden.

Mein ganz besonderer Dank gilt dem Inhaber der Professur, Herrn Prof. Dr.-Ing. habil. Jochen Fröhlich. Ihre langjährige Unterstützung und Betreuung als Doktorvater haben ganz wesentlich zum Gelingen dieser Doktorarbeit beigetragen. Vielen Dank für Ihr stetiges Interesse an neuen Ideen und kniffligen Problemstellungen, für die zahlreichen fachlichen Diskussionen und nicht zuletzt für die vertrauensvolle Zusammenarbeit. Weiterhin möchte ich Ihnen danken, dass Sie während meiner Tätigkeit stets auf ein breites Ausbildungsspektrum Wert gelegt haben. Sei es die Ausübung von Lehrtätigkeiten, die Betreuung von Studierenden, die Unterstützung bei Forschungsanträgen, die Veröffentlichung von wissenschaftlichen Inhalten oder deren Präsentation auf internationalen Konferenzen. Es war eine äußerst lehrreiche und spannende Zeit.

Ich möchte mich ebenfalls bei allen Mitgliedern der Promotionskommission für deren Unterstützung bedanken: Ganz besonderer Dank gilt hierbei Herrn Prof. Dr.-Ing. habil. Volker Ulbricht. Ihre Grundlagenvorlesungen weckten frühzeitig meine Begeisterung für die Mechanik. Es war mir daher eine große Freude, dass Sie der Begutachtung meiner Arbeit zugestimmt haben. Gedankt sei weiterhin Herrn Prof. Dr.-Ing. habil. Ronald Mailach für die Leitung der Kommission, Herrn Prof. Dr.-Ing. habil. Markus Kästner für die Abnahme der Fachprüfung sowie dem Beisitzenden Herrn Dr.-Ing. habil. Jörg Stiller.

Die Finanzierung meiner Tätigkeit als wissenschaftlicher Mitarbeiter erfolgte durch die Deutsche Forschungsgemeinschaft (DFG) sowie durch Haushaltsmittel der Technischen Universität Dresden. Diesen Institutionen gilt mein Dank. Für die Organisation und Verwaltung der Finanzmittel möchte ich einen besonderen Dank an Herrn Dr.-Ing. Frank Rüdiger aussprechen. Die für mich durchweg kontinuierliche und sorgenfreie Finanzsituation ermöglichte stets ein freies und kreatives wissenschaftliches Arbeiten und trug wesentlich zur Qualität der Arbeit bei. Des Weiteren gilt mein Dank der Gesellschaft von Freunden und Förderern der TU Dresden e.V. für die finanzielle Unterstützung zur Teilnahme an internationalen Konferenzen.

Der Erfolg von Arbeiten im Bereich der numerischen Strömungsmechanik hängt stark von den vorhandenen Rechenressourcen ab. Für deren unkomplizierte Bereitstellung sowie für die Administration und Wartung der genutzten Rechencluster möchte ich mich bei allen Mitarbeitern des Zentrums für Informationsdienste und Hochleistungsrechnen (ZIH) bedanken.

Bei meinen Kollegen der Professur bedanke ich mich herzlichst für die gute Zusammenarbeit, deren uneingeschränkte Hilfsbereitschaft sowie für das äußerst angenehme Arbeitsklima. Besonderer Dank gilt dabei Herrn Dipl.-Ing. Benjamin Krull, Dr.-Ing. Denis Koschichow, Dipl.-Ing. Bastian Löhrer und Prof. Dr.-Ing. Tobias Kempe für die zahlreichen intensiven Diskussionen und deren konstruktive Kritik. All dies hat deutlich zur Qualität der Arbeit beigetragen. Als kompetenter Ratgeber in Belangen jeglicher Art möchte ich mich bei Herrn Dr.-Ing. Frank Rüdiger bedanken, welcher stets ein offenes Ohr für Probleme des wissenschaftlichen Alltags hatte. Gleichermaßen gilt mein Dank den Kolleginnen aus dem Sekretariat, Frau Claudia Wiegand und Frau Annette Roewer, für die Unterstützung bei bürokratischen Angelegenheiten.

Für die erfolgreiche Zusammenarbeit möchte ich mich ebenfalls bei allen Diplomanden, Belegstudenten und studentischen Hilfskräften bedanken. Es hat mir stets viel Freude bereitet mit euch gemeinsam an wissenschaftlichen Problemstellungen zu wachsen.

Der wohl größte Dank gilt meiner Familie und Freunden, die mich in jeder nur erdenklichen Hinsicht unterstützt haben. Besonders danke ich euch für euer Zutrauen, die vielen motivierenden Gespräche, aber vor allem für eure mentale Unterstützung in schwierigen Phasen. Die größten Entbehrungen in den letzten Jahren musstest wohl du hinnehmen, liebe Franziska. Du hast mir stets den nötigen privaten Rückhalt gegeben und mich unterstützt, wo du nur konntest. Dafür danke ich dir aus tiefstem Herzen.

Silvio Tschisgale.

Kurzfassung

Die vorliegende Arbeit beschäftigt sich mit der Entwicklung einer numerischen Methode zur Simulation von Problemstellungen der Fluid-Struktur-Interaktion (FSI) auf Hochleistungsrechnern. Die Methode ist zugeschnitten auf die Interaktion von inkompressiblen Newtonschen Fluiden mit einer großen Anzahl schlanker viskoelastischer Strukturen, wobei letztere als Cosserat-Balken modelliert werden. Aufgrund der hohen Flexibilität und der vergleichsweise geringen Masse der betrachteten Balkenstrukturen reagieren diese mit großen Verformungen auf äußere Fluidlasten. Gleichzeitig beeinflusst die Strukturbewegung das umgebende Fluid, welches wiederum auf die Struktur einwirkt. Diese aus numerischer Sicht starke Kopplung von Fluid und Struktur erfordert spezielle Techniken, um die Stabilität der Methode zu gewährleisten. Im Falle einer partitionierten Kopplung von Fluid und Struktur wird dies üblicherweise mittels iterativer Kopplungsverfahren erreicht, was einen erhöhten Rechenaufwand zur Folge hat. Die vorliegende Arbeit präsentiert einen alternativen Kopplungsansatz auf Basis einer Immersed-Boundary-Methode (IBM). Das Kopplungsschema ist numerisch stabil und vermeidet eine globale Iteration zwischen beiden Teilproblemen gänzlich. Neben der Bewertung der Genauigkeit und des Konvergenzverhaltens der vorgeschlagenen IBM erfolgt eine gründliche Validierung mittels verschiedener Testkonfigurationen. Zusätzlich zur numerischen Realisierung der Fluid-Struktur-Interaktion bietet die entwickelte Methode ein Kollisionsmodell zur Berücksichtigung etwaiger Struktur-Struktur-Interaktionen. Dadurch ist der FSI-Löser in der Lage, eine sehr allgemeine Klasse von kollisionsbehafteten Fluid-Struktur-Interaktionen zu simulieren. Im Rahmen dieser Arbeit wurde die Strömung über eine dichte Vegetationsschicht simuliert, welche sich durch eine wellenartige Bewegung der Vegetationselemente sowie durch ausgeprägte turbulente Strukturen auszeichnet. Das hierfür verwendete abstrahierte Modell der Vegetationsschicht besteht aus 800 regelmäßig angeordneten flexiblen Streifenstrukturen, was derzeit die größte skalenauflösende Simulation einer turbulenten Vegetationsschichtüberströmung darstellt. Die daraus gewonnenen Datensätze wurden mittels verschiedener Analysemethoden ausgewertet, um ein tieferes Verständnis der physikalischen Vorgänge in Vegetationsschichten zu erhalten, z.B. hinsichtlich der Existenz und Form kohärenter Strukturen. Hierbei offenbarte sich eine einzigartige Klasse von Wirbelstrukturen, welche im Übergangsbereich der Vegetationsschicht zur darüber liegenden freien Strömung entstehen.

Abstract

This thesis presents a numerical method for the simulation of fluid-structure interaction (FSI) problems on high-performance computers. The proposed method is specifically tailored to interactions between Newtonian fluids and a large number of slender viscoelastic structures, the latter being modeled as Cosserat rods. Because of their high flexibility and low weight, the rods considered here respond by large deflections under the influence of external fluid loads. This motion in turn modifies the flow, so that the fluid and the structures are strongly coupled to each other. From a numerical point of view, such a strong coupling requires special techniques to reach numerical stability. When using a partitioned fluid-structure coupling approach this is usually achieved by an iterative procedure, which drastically increases the computational effort. In the present work, an alternative coupling approach is developed based on an immersed boundary method (IBM). It is unconditionally stable and exempt from any global iteration between the fluid part and the structure part, outperforming previous approaches. The contribution presents the underlying methodology and its algorithmic realization, including an assessment of accuracy and convergence by systematic studies. Various validation cases illustrate performance and versatility of the proposed IBM. In addition to the numerical realization of fluid-structure interactions, the present method provides a collision model able to capture possible structure-structure interactions. Consequently, this enables the FSI-solver to simulate a very general class of fluid-structure interaction problems prone to collisions. In the context of this work, the solver is employed to simulate the flow over a dense layer of vegetation elements, usually designated as canopy flow. This flow is characterized by an organized wave-like motion of the vegetation, caused by pronounced turbulent structures on top of the canopy. The abstracted canopy model used in the simulation consists of 800 regularly arranged strip-shaped blades, which is the largest canopy-resolving simulation of this type done so far. The simulation data obtained are analyzed to get a deeper understanding of the physics of aquatic canopy flows, e.g., concerning the existence and shape of coherent structures. The analysis revealed a unique class of vortical structures, developing in the transition zone from the vegetation layer to the free-flow region above.

Contents

1 Introduction

1.1 Motivation and research aims

When a solid structure is influenced by a flow field in such a manner that it in turn modifies the flow this is termed *fluid-structure interaction* (FSI). It is of crucial importance in various areas, e.g. in the technical field to optimize the design of parachutes [39], in the medical sector to support design processes of artificial heart valves [53], or in the biological field where FSI is used by animals to aid locomotion [130]. In classical FSI problems, the structures involved deform under the influence of external fluid loads. Depending on the specific shape of the structures, their response can vary considerably, ranging from a flow-induced vibration of massive solid bodies, up to the chaotic motion of thin flags subjected to wind.
This work focuses on a particular class of FSI problems which involve a large number of long and slender elastic structures, commonly referred to as *beams* or *rods*. With sufficiently slender rods, even low fluid loads may cause large displacements and a complex dynamic behavior of the coupled system. The latter becomes even more complicated when the rods interact with each other in a dense arrangement and thus influence the system behavior through collisions. Examples of such kind of FSI problems prone to collisions are fiber flows as a part of the production process of textiles [75] or natural vegetation flows with flexible plants in an aquatic environment [169, 174]. In order to optimize technical processes or to clarify physical processes in biological systems, the required information is usually gathered using complementary experimental and numerical efforts. However, experimental observations are particularly difficult when slender rods are highly flexible and close to each other. In such cases, an accurate measure of fluid and structure related quantities is often not feasible due to various instrumental limitations [173]. The motivation of this work is to close this gap by means of scale-resolving simulations with a minimum level of abstraction. With this approach, a wealth of high-resolution data can be obtained to investigate the physical processes involved, usually not accessible via experimental approaches. In order to provide such data sets for the FSI problems considered here, enormous computational requirements are placed on the numerical method employed. This defines the main research aim of the present work:

> **Development of an efficient numerical method suited for scale-resolving simulations of a large number of slender flexible rods in a turbulent flow regime.**

In this context, particular emphasis must be placed on the efficiency of the method, since an analysis of turbulent flows usually requires long-term simulations over a substantial time interval to accumulate statistics. In order to keep the overall computational time within reasonable bounds, this is achieved by employing high-performance computers with thousands of processors in combination with an own innovative, non-iterative coupling algorithm specially developed for this purpose.

To demonstrate the ability of the proposed numerical approach, it is applied to the turbulent flow over and trough a layer of densely arranged aquatic plants, usually denoted as canopy flow. Figure 1.1a shows a seagrass canopy, frequently occurring in nature. Such aquatic ecosystems constitute a topic of high relevance due to their abundance and their various roles on different scales, ranging from the quality of drinking water taken from the local river to the large-scale impact on climate change [46]. The interaction between the flow and the flexible plants in an aquatic canopy plays a central role in hydraulics as well as transport of sediment, nutrients and pollutants [109, 169]. Such vegetation flows are extremely difficult to measure experimentally, especially within and on top of the canopy [173]. This is exactly where numerical simulations can exploit their advantages and supplement missing information. The numerical study of canopy flows is a rather young research field and there is a need for scale-resolving flow data, since little is known about the three-dimensional nature of turbulent structures in canopy flows. This lack of knowledge is addressed in this work by conducting highly resolved simulations of a model canopy flow, shown in Fig. 1.1b. The data obtained from the simulations are used to achieve the second research aim envisaged here:

Gaining a deeper understanding of the physics of flow-biota interaction in aquatic canopy flows, with emphasis on the formation and importance of three-dimensional coherent structures.

It will become apparent that unique vortical structures are generated at the top of the canopy, exciting the plants to an organized wavelike motion. This interesting dynamic behavior has often been observed in nature and is usually designated as *monami* (Japanese: *mo* = aquatic plant, *nami* = wave [3, 179]). This may remind the reader of waving crop fields on a windy day, known as *honami* (*ho* = cereal) in the context of terrestrial canopies.

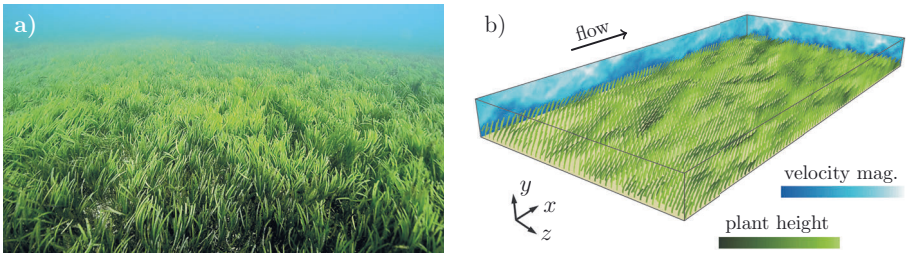

Figure 1.1: *Seagrass meadow as an example of dense submerged canopies. a) Real configuration to be found in nature [276]. b) Simplified model canopy employed for scale-resolving simulations. The model vegetation is made out of flexible blades of equal properties, arranged uniformly in the fluid domain (same spacing in x- and z-direction).*

1.2 Structure of the thesis

In order to achieve both research aims highlighted above, they have been divided into the following consecutive methodical objectives. This separation is reflected by the overall structure of this thesis, so that each methodical objective is addressed in a separate chapter.

Chap. 1 – **Physical model of the FSI problem:** The first chapter presents the physical model tailored to the present kind of FSI with slender flexible rods in a turbulent environment. In this context, appropriate model assumptions and simplifications are introduced to provide the basis for an efficient numerical method.

Chap. 2 – **Numerical models of fluid and structure:** Based on the continuous model derived in the previous chapter, the governing equations of the fluid and the structure motion are discretized in space and time. At this point, the coupling between fluid and structure is not yet accounted for, allowing to use existing and optimized solvers for the partitioned problems.

Chap. 3 – **Numerical coupling of partitioned solvers*:** The solvers implemented for the fluid and the structure need to be coupled by an appropriate algorithm to describe the motion of the entire FSI system. This chapter presents the underlying methodology and the algorithmic realization of the coupling scheme, including an assessment of accuracy and convergence. In addition, the FSI-solver is validated for selected benchmark cases taking into account the FSI of single elastic rods subjected to flow.

Chap. 4 – **Collision model for Cosserat rods*:** One research aim of this thesis is to provide a FSI-solver for large numbers of densely arranged rods prone to collide with each other. Consequently, the basic FSI-solver addressed in Chapter 3 has to be extended by an appropriate collision model for Cosserat rods. Chapter 4 presents a detailed derivation of the model, including contact detection and the numerical treatment of multiple simultaneous collisions between numerous rods. The efficiency and robustness of the approach is illustrated with a number of simple basic tests as well as more realistic configurations.

Chap. 5 – **Application of FSI-solver to canopy flows*:** In the final chapter, the FSI-solver is employed to simulate the flow through an aquatic model canopy. The high-resolution data obtained from the simulations are used to achieve the second research aim, i.e. to gain fundamental information on the physics of aquatic canopy flows. In particular, the hydrodynamic coupling between the flow and the slender flexible blades shall be elucidated here. Questions to be answered include: How is the fluid flow over and through a canopy affected by the flexible blades? What is the relation between characteristics of blade motion and characteristics of fluid motion? Which kind of three-dimensional coherent structures are observed and what is their impact?

∗ Selected contents of the chapter have already been published by the present author in scientific journals or presented at international conferences. The list of published contributions can be found on page 167.

2 Physical model and governing equations

2.1 Problem definition and assumptions

The physical configuration addressed here consists of a viscous fluid interacting with a large number of slender flexible structures, e.g. a fiber suspension flow or a canopy flow illustrated in Fig. 2.1. Moreover, the configurations are characterized by a pronounced emergent dynamic behavior resulting from a highly unsteady response of both the fluid and the structure part. During their interaction, isothermal conditions are assumed, and thus a decoupling of thermal and mechanical effects. The viscous fluid considered is incompressible and exhibits constant material properties. All structures are completely immersed in the fluid and are geometrically characterized by a long and slender shape with cross sections much smaller than their longitudinal expansion. When the structures are subjected to fluid loads, local deformations and associated internal strains are assumed to be small but may agglomerate to large overall displacements in space. As a result, geometrically nonlinear effects are of crucial importance and must be taken into account. During motion, the structures may lose energy due to internal friction, but do not exhibit any plastic deformation. Consequently, a viscoelastic material behavior is expected here. The corresponding material properties are assumed to be isotropic and constant in time and space.
The domain of the entire physical configuration $\Omega \in \mathbb{R}^3$ consists of the closed subset $\Omega^{\mathrm{f}} \subset \Omega$, defining the fluid domain, and a certain number of structures N_{s}, which combine to form the closed subset $\Omega^{\mathrm{s}} \subset \Omega$, the structure domain. Therefore, the union of the fluid domain and the set of all structures gives the entire domain $\Omega = \Omega^{\mathrm{f}} \cup \Omega^{\mathrm{s}}$ assumed to be time-independent here. Despite this restriction, the fluid domain Ω^{f} and the structure domain Ω^{s} may change their shape while interacting and thus are time-dependent. The associated boundaries of both subdomains are $\partial^{\mathrm{f}}\Omega \subset \Omega^{\mathrm{f}}$ and $\partial\Omega^{\mathrm{s}} \subset \Omega^{\mathrm{s}}$, respectively, so that their intersection defines a time-dependent fluid-structure interface $\Gamma = \partial\Omega^{\mathrm{f}} \cap \partial\Omega^{\mathrm{s}}$. The boundary of the entire domain is given by $\partial\Omega = (\partial\Omega^{\mathrm{f}} \cup \partial\Omega^{\mathrm{s}}) \setminus \Gamma$.

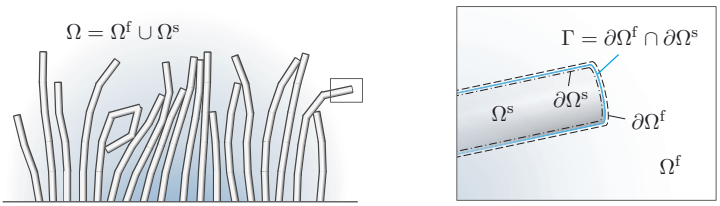

Figure 2.1: *Type of fluid-structure interaction considered in the present work, namely the interaction between viscous fluids and a larger number of slender flexible structures. The fluid domain and structure domain are designated as* Ω^{f} *and* Ω^{s}*, respectively, with the corresponding boundaries* $\partial\Omega^{\mathrm{f}}$ *and* $\partial\Omega^{\mathrm{s}}$*. The fluid-structure interface is referred to as* Γ*.*

2.2 Fluid mechanics

2.2.1 Navier-Stokes equations

The governing equations for the fluid motion are the unsteady three-dimensional Navier-Stokes equations (NSE) for a Newtonian fluid of constant density [245, 39]

$$\frac{\partial \mathbf{u}}{\partial t} + \nabla \cdot (\mathbf{u} \otimes \mathbf{u}) = \frac{1}{\rho_\mathrm{f}} \nabla \cdot \boldsymbol{\sigma} + \mathbf{f} \tag{2.1a}$$

$$\nabla \cdot \mathbf{u} = 0 \tag{2.1b}$$

in the fluid domain Ω^f, where $\mathbf{u} = (u, v, w)^\top$ designates the velocity vector in Cartesian components along the Cartesian coordinates x, y, z, while t represents the time, p the pressure field, and ρ_f the fluid density. The constitutive relations for the hydrodynamic stress tensor $\boldsymbol{\sigma}$ are given by

$$\boldsymbol{\sigma} = -p\,\mathbb{I} + \mu_\mathrm{f}\,(\,\nabla\mathbf{u} + \nabla\mathbf{u}^\top)\,, \tag{2.2}$$

with $\mu_\mathrm{f} = \rho_\mathrm{f}\,\nu_\mathrm{f}$ the dynamic viscosity and ν_f the kinematic viscosity, $\mathbb{I}$ the identity matrix, and $\mathbf{f} = (f_x, f_y, f_z)^\top$ a mass-specific force. The latter consists of two parts, $\mathbf{f} = \mathbf{f}_V + \mathbf{f}_\Gamma$, where $\mathbf{f}_V$ is a mass-specific volume force like gravitational acceleration, e.g., and $\mathbf{f}_\Gamma$ a coupling force used to impose the no-slip condition on the fluid-structure interface Γ, as described in Chapter 4 below. Depending on the physical scenario to be modeled, different boundary conditions can be applied at $\partial\Omega^\mathrm{f}$, e.g. Dirichlet conditions to realize velocity inlets or no-slip walls, Neumann conditions to impose free-slip rigid lids or conditions of periodicity. Details on their numerical realization are provided in [118].

2.2.2 Large eddy simulation and subgrid-scale model

The aim of this work is to provide time-dependent high-resolution data to study the dynamic behavior of the coupled system and the role of coherent structures, also for higher turbulence intensities of the fluid. Under the latter conditions, the direct numerical simulation (DNS) of the Navier-Stokes equations (2.1), i.e. resolving all turbulent scales, is technically not feasible with the present discretization technique (Section 3.1). In such cases, the large eddy simulation (LES) approach is employed here [77, 70], which captures large scales of the flow while small scale turbulence is modeled by an appropriate model. This approach is motivated by the self-similarity hypothesis of Kolmorogov which states that large scales exhibit an energy-carrying and anisotropic character while small scales reveal a universal and isotropic nature. When performing an LES, the velocity vector $\mathbf{u}$ in the Navier-Stokes equations (2.1) represents the resolved part of the velocity field while the influence of the unresolved scales is captured by a subgrid-scale stress tensor $\boldsymbol{\tau}_\mathrm{sgs}$. It is introduced into the momentum balance of the fluid replacing $\boldsymbol{\sigma}$ in Eq. (2.1) by $\boldsymbol{\sigma}_\mathrm{LES} = \boldsymbol{\sigma} - \boldsymbol{\tau}_\mathrm{sgs}$. In the present work, the Smagorinsky model [221] is employed which models the subgrid-scale stress as

$$\boldsymbol{\tau}_\mathrm{sgs} = -\mu_\mathrm{sgs}\,2\,\mathbf{S} + \frac{1}{3}\,\mathrm{tr}(\boldsymbol{\tau}_\mathrm{sgs})\,\mathbb{I}\,, \qquad \mu_\mathrm{sgs} = \rho_\mathrm{f}(C_\mathrm{s}\,h)^2\,\|\mathbf{S}\| \tag{2.3}$$

with the strain rate tensor $\mathbf{S} = (\,\nabla\mathbf{u} + \nabla\mathbf{u}^\top)/2$ and its norm $\|\mathbf{S}\| = \sqrt{2\,\mathbf{S}:\mathbf{S}}$. The isotropic part of the stress tensor in Eq. (2.3) is added to the pressure p of the hydrodynamic stress

tensor (2.2) so that, in case of an LES, the resulting modified pressure $p_{\text{LES}} = p - \text{tr}(\boldsymbol{\tau}_{\text{sgs}})/3$ is computed instead of the filtered pressure p. The filter size is chosen to be $h = \sqrt[3]{\Delta x\,\Delta y\,\Delta z}$ based on the step sizes of the Cartesian grid in the $x-$, $y-$ and z-direction. The Smagorinsky constant C_{s} is assumed to be spatially and temporally constant, but tailored to the specific physical problem (see Section 3.3.1 and Chapter 6).
In the present work it is assumed, that the grid spacing of the Eulerian grid is fine enough to capture both the flow near the walls and at the fluid-structure interface Γ, so that no additional modeling is required, e.g. by a wall function. However, it is well known that the standard Smagorinsky model causes non-physical values of the eddy viscosity μ_{sgs} in the region close to walls since the mean velocity gradient contributes to the eddy viscosity supposed to model turbulent fluctuations. For this reason, μ_{sgs} is reduced near walls by a Van Driest damping function [60]. A similar strategy is pursued here for movable fluid-structure interfaces. As described in Section 4.3.1 below, the interface is represented by a finite set of discrete surface marker points. At these points, a damping function D is introduced which smoothly switches off μ_{sgs} in the range of a few steps of the Eulerian fluid grid in the vicinity of the interface. The damping function is given by $D = 1 - \left(\frac{3}{2}\,h\right)^3 \delta_h$, where δ_h is a regularized delta function (4.19) defined in Section 4.3.2 below.

2.3 Structural mechanics

2.3.1 Continuum mechanical description

The governing equation for the structure motion is the balance of linear momentum. From a Lagrangian point of view it is stated as [245, 39]

$$\frac{\mathrm{d}\mathbf{v}}{\mathrm{d}t} = \frac{1}{\rho_s}\,\nabla\cdot\mathbf{P} + \mathbf{f}\,, \tag{2.4}$$

with the velocity vector $\mathbf{v} = \mathrm{d}\mathbf{x}/\mathrm{d}t = \dot{\mathbf{x}}$ of a material point $\mathbf{x} \in \Omega^{\text{s}}$ in the current configuration of the structure Ω^{s}. The structural motion is influenced by an external mass-specific force $\mathbf{f}$ and internal stresses. These are measured via the 1st Piola-Kirchhoff stress tensor $\mathbf{P}$ between the current configuration $\Omega^{\text{s}}(t)$ and the reference configuration $\Omega^{\text{s}}_0 = \Omega^{\text{s}}(t=0)$ of the undeformed structure at time $t=0$. The latter has a spatially constant density ρ_{s}. Each material point $\mathbf{x} \in \Omega^{\text{s}}$ of the current state is related to a point $\mathbf{X} \in \Omega^{\text{s}}_0$ of the reference configuration by a smooth mapping $\mathbf{x} = \boldsymbol{\chi}(\mathbf{X}, t)$, where $\boldsymbol{\chi} : \Omega^{\text{s}}_0 \times [0,T] \to \mathbb{R}^3$. The associated deformation gradient tensor

$$\mathbf{F} = \frac{\partial\,\boldsymbol{\chi}(\mathbf{X},t)}{\partial\mathbf{X}} \tag{2.5}$$

quantifies the overall rotation of the structure and its change in shape during motion, and is employed to measure internal strains via the Green-Lagrange strain tensor

$$\mathbf{E} = \frac{1}{2}\left(\mathbf{F}^{\top}\cdot\mathbf{F} - \mathbb{I}\right)\,. \tag{2.6}$$

Using a linear elastic constitutive relation between the strain tensor $\mathbf{E}$ and the internal stresses, the 1st and 2nd Piola-Kirchhoff stress tensor are given by

$$\mathbf{P} = \mathbf{S}\cdot\mathbf{F}^{\top}\,, \qquad \mathbf{S} = \lambda_{\text{s}}\,\text{tr}(\mathbf{E})\,\mathbb{I} + 2G_{\text{s}}\,\mathbf{E}\,, \tag{2.7}$$

respectively, with the first Lamé constant $\lambda_\mathrm{s} > 0$ and the shear modulus $G_\mathrm{s} > 0$. Both material parameters are related to the Young's modulus E_s and the Poisson's ratio ν_s via

$$\lambda_\mathrm{s} = \frac{E_\mathrm{s}\nu_\mathrm{s}}{(1+\nu_\mathrm{s})(1-2\nu_\mathrm{s})}\,, \qquad G_\mathrm{s} = \frac{E_\mathrm{s}}{2(1+\nu_\mathrm{s})}\,. \tag{2.8}$$

Analogous to the Navier-Stokes equations (2.1), the mass-specific force $\mathbf{f} = \mathbf{f}_V - \mathbf{f}_\Gamma$ in the momentum balance (2.4) consists of a volume force $\mathbf{f}_V$ and a coupling force $\mathbf{f}_\Gamma$, whereby the latter force captures the influence of fluid loads in case of a fluid-structure interaction. Note that $\mathbf{f}_\Gamma$ occurs with opposite sign in the momentum balance of fluid (2.1a) as required by the dynamic coupling condition (principle of "actio et reactio"), described in Section 2.4.1 below.

2.3.2 Rod models for slender structures

The structures addressed here are characterized by a long and slender shape with cross sections much smaller than their longitudinal expansion. Usually such kind of structure is referred to as a *beam*, *cantilever* or *rod*, the latter term being used in the present work. In principle, such geometrical constraints on shape can be used to employ model reduction techniques which reduce the degrees of freedom required to describe the structure motion. These techniques are of crucial importance when simulating large numbers of individual resolved rod structures due to the enormous reduction of computational effort. Especially for the slender rods considered here, the general three-dimensional equations of motion (2.4) are well approximated by one-dimensional rod models without loss of physical correctness. The history on rod theories reaches far back into the 13th century and caught the attention of many brilliant mathematicians, e.g. Galileo, the Bernoullis, Euler, Coulomb, Saint-Venant, Poisson, to name just a few [139, 196]. Very comprehensive historic overviews of early developments in this field are given by Love [147] and Timoshenko [241]. It was discovered that different loads acting on the rod cause four principal *deformation modes* designated as *axial extension* (or *compression*), *bending*, *shear* and *torsion*. In the general case, these deformation modes may couple with each other due to nonlinear kinematic or constitutive relations. As a result, various models for rod structures have been created with different complexity. Even if no fully consistent nomenclature of different rod models can be found in the literature, a classification is provided in the comprehensive work of Meier [157]. Rod models which capture axial tension, torsion and bending, are denoted as *Euler-Bernoulli beams* [241] when initially straight rods with isotropic cross sections are considered. The *Kirchhoff-Love beam* theory [147] provides an extension to arbitrary initial shapes and anisotropic cross-sections. So-called inextensible Euler-Bernoulli beams and Kirchhoff-Love beams inhibit a longitudinal elongation of the rod by additional constraints. All four modes, including shear, are captured by the *Simo-Reissner theory* [215, 199] which is often denoted as *Cosserat rod theory* [45]. Shear-deformability in the geometrically linear regime is captured by so-called *Timoshenko beam* models [240].

Here, the linear regime implies infinitesimally small displacements of the rod, so that the kinematic relations can be linearized. This usually yields a decoupling of the principal modes of deformation, i.e. extension, shear, bending and torsion. For finite displacements, however, this is not the case and the deformation modes are geometrically coupled. In this regime, the associated rod models are commonly specified as nonlinear, geometrically nonlinear or *geo-*

metrically exact rod models. Geometrical (or kinematic) nonlinearities are not to be confused with nonlinear constitutive relations that describe the relation between strains and resulting internal stresses. Geometrical nonlinearities, on the other hand, refer to the relation between displacements and strains.

2.3.3 Geometrically exact Cosserat rod model

One of the most complex rod models is the so-called *geometrically exact Cosserat rod* which covers both the rigid body motion and the common deformation modes of a rod [215, 7, 9, 131]. This model is used in the present work, since it captures large structural displacements to be considered here, and offers a broad range of applications. A discussion on less complex rod models derived from the Cosserat rod model is provided in Appendix B. The basic idea of the Cosserat rod theory is quite simple. From a kinematic point of view, each cross section of the rod is assumed to remain rigid during deformation while internal strains are measured by the relative position and orientation between adjacent cross sections. On the basis of this kinematic constraint of rigid cross-sections, the three-dimensional linear momentum balance (2.4) (and the angular momentum balance) can be converted into the equations of motion of the Cosserat rod.

Derivation of the Cosserat rod equations. Starting point of the derivation are the kinematic relations between a material point of the rod $\mathbf{x} \in \Omega^s$ in the current configuration at time t and a material point $\mathbf{X} = (X, Y, Z)^\top \in \Omega_0^s$ in the reference configuration at $t = 0$. As described in Section 2.3.1, these points are related to each other by a smooth mapping $\boldsymbol{\chi} : \Omega_0^s \times [0, T] \to \mathbb{R}^3$ with $\mathbf{x} = \boldsymbol{\chi}(\mathbf{X}, t)$. In the Cosserat rod theory, a special parametrization is used for χ given by

$$\mathbf{x}(\mathbf{X}, t) = \mathbf{c}(Z, t) + X\,\mathbf{r}_X(Z, t) + Y\,\mathbf{r}_Y(Z, t)\,, \tag{2.9}$$

where $\mathbf{c}$ denotes the position vector to a point on the center line $\zeta \subset \Omega^s$ along the longitudinal coordinate Z, and $\mathbf{r}_X$, $\mathbf{r}_Y$ are two direction vectors of unit length, which span the cross sections of the rod in the lateral X- and Y-direction, respectively (see Fig. 2.2). By

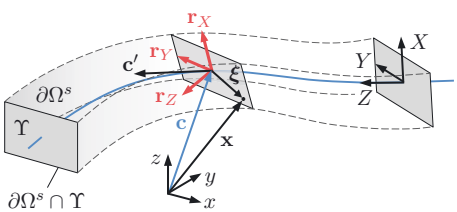

Figure 2.2: *Instantaneous configuration of a deformed Cosserat rod Ω^s at time $t > 0$. Each of the cross sections $\Upsilon(Z) \subset \Omega^s$ along the arc length Z remains rigid and plane, while its orientation is described by three orthonormal direction vectors. The latter can be combined to the rotation matrix $\mathbf{R} = [\mathbf{r}_X\, \mathbf{r}_Y\, \mathbf{r}_Z]$. The location of a material point $\mathbf{x} \in \Omega^s$ can be decomposed into a longitudinal part along $\mathbf{c}$ and a lateral part $\boldsymbol{\xi} = \mathbf{R} \cdot \boldsymbol{\xi}_0$ within the associated cross-section Υ, so that $\mathbf{x} = \mathbf{c} + \mathbf{R} \cdot \boldsymbol{\xi}_0$. In cases where shear is generated in the rod, the direction vector $\mathbf{r}_Z$ and the Z-direction are not aligned, i.e. $\mathbf{c}' \cdot \mathbf{r}_Z \leq \|\mathbf{c}'\|$.*

introducing an additional direction vector $\mathbf{r}_Z$, the mapping (2.9) can be expressed in the equivalent form

$$\mathbf{x}(\mathbf{X},t) = \mathbf{c}(Z,t) + \mathbf{R}(Z,t)\cdot\boldsymbol{\xi}_0(X,Y)\,, \tag{2.10}$$

with the matrix $\mathbf{R}(Z,t) = [\mathbf{r}_X\,\mathbf{r}_Y\,\mathbf{r}_Z]$ and the cross section vector $\boldsymbol{\xi}_0 = (X,Y,0)^\top$ in the Lagrangian reference frame. Here, a specific cross-section $\Upsilon \subset \Omega^\mathrm{s}$ is defined by

$$\Upsilon : \tilde{Z} \mapsto \left\{\mathbf{x}\in\Omega^\mathrm{s} : \mathbf{x} = \boldsymbol{\chi}\left((X,Y,\tilde{Z})^\top, t\right)\right\} \tag{2.11}$$

and is thus uniquely assigned to a selected arc length $Z = \tilde{Z}$. In case of long slender rods the cross sections exhibit only small distortions and the *Euler–Bernoulli hypothesis* [21] states that these remain plane during deformation. Consequently, the motion of the cross sections is well approximated by a pure rigid body motion. The associated kinematic constraint is incorporated into the mapping (2.10) by a special choice of the tensor $\mathbf{R}$, which has to feature the properties of a common rotation matrix $\mathbf{R}\in SO(3)$, as an element of the rotation group $SO(3) = \{\mathbf{R}\in\mathbb{R}^{3\times3} : \mathbf{R}\cdot\mathbf{R}^\top = \mathbf{R}^\top\cdot\mathbf{R} = \mathbb{I},\ \det(\mathbf{R})=1\}$. The corresponding equations of motion of the rod can be derived by replacing $\mathbf{x}$ in the common linear and angular momentum balance

$$\int_{\Omega_0^\mathrm{s}} \frac{\mathrm{d}\dot{\mathbf{x}}}{\mathrm{d}t}\,\mathrm{d}V_0 = -\frac{1}{\rho_\mathrm{s}}\int_{\partial\Omega_0^\mathrm{s}} \mathbf{P}^\top\cdot\mathbf{n}_0\,\mathrm{d}S_0 + \int_{\Omega_0^\mathrm{s}} \mathbf{f}\,\mathrm{d}V_0 \tag{2.12a}$$

$$\int_{\Omega_0^\mathrm{s}} \frac{\mathrm{d}}{\mathrm{d}t}(\mathbf{x}\times\dot{\mathbf{x}})\,\mathrm{d}V_0 = -\frac{1}{\rho_\mathrm{s}}\int_{\partial\Omega_0^\mathrm{s}} \mathbf{x}\times(\mathbf{P}^\top\cdot\mathbf{n}_0)\,\mathrm{d}S_0 + \int_{\Omega_0^\mathrm{s}} \mathbf{x}\times\mathbf{f}\,\mathrm{d}V_0\,, \tag{2.12b}$$

with the constrained mapping $\mathbf{x} = \mathbf{c} + \mathbf{R}\cdot\boldsymbol{\xi}_0$ and the inward pointing unit normal vector $\mathbf{n}_0$. Both equations are then transferred into a linear and angular equation of motion for $\mathbf{c}$ and $\mathbf{R}$, respectively, both usually denoted as (geometrically exact) Cosserat rod equations (2.13). Their derivation from Eq. (2.12) is very extensive and not provided here. For details, refer to the comprehensive works of Auricchio [9] and Clerici [44]. It is important to note that in addition to the kinematic constraint (2.10), further assumptions and simplifications are required to entirely derive the standard Cosserat rod equations (2.13). These can be summarized as followed:

- The cross-sections feature a spatially constant density ρ_s, while their mass centroids coincide with the positions $\mathbf{c}(Z,t)$ of the center line ζ. Furthermore, the direction vectors $\mathbf{r}_X(Z,t)$ and $\mathbf{r}_Y(Z,t)$ are principal axes of the associated cross section $\Upsilon(Z)$.

- The constitutive relations are assumed to be linear elastic with two independent material parameters, e.g. the Young's modulus E_s and the Poisson's ratio ν_s (see Eq. (2.8)). In case of rigid cross sections the constitutive relations are satisfied only with a Poisson's ratio of $\nu_\mathrm{s} = 0$, i.e. without a lateral contraction of the cross sections. However, in the common Cosserat rod equations, ν_s usually remains adjustable and is used to influence the dynamic behavior of the rod.

- It is well known that the cross sections of shorter rods warp under shear and torsional loads. This warping effect can not be captured directly by the Cosserat rod, but is often modeled by a shear corrected cross sectional area $k_\mathrm{s}A$ and a torsion corrected polar moment of

inertia $k_t J$. Selected shear correction factors k_s and torsion correction factors k_t of different cross-sectional shapes are provided in [76].

- The reference rod Ω_0^s at time $t = 0$ is assumed to be straight. As shown in Li [140], an initially curved reference configuration massively increases the complexity of the derivation of the Cosserat equations. However, the error remains small for slightly curved reference configurations with local curvatures of a rod $\kappa \ll 1/W$, with cross sections of width W.

The Cosserat rod equations. The derivation from the three-dimensional structural equations (2.12) results in two spatially one-dimensional differential equations for the rod motion. One equation describes the temporal evolution of $\mathbf{c}(Z,t) \in \zeta$, i.e. the positions of the center line $\zeta \subset \Omega^s$. The second equation describes the rotation of the cross sections $\Upsilon(Z) \subset \Omega^s$ along the Lagrangian arc length coordinate Z, captured by the rotation matrix $\mathbf{R}(Z,t) \in SO(3)$. Both equations are referred to as (geometrically exact) Cosserat rod equations which are given by [215, 7, 131]

$$\rho_s A\, \ddot{\mathbf{c}} = \overset{\triangle}{\mathbf{f}}{}' + \overset{\triangledown}{\mathbf{f}} \tag{2.13a}$$

$$\rho_s \mathbf{I}{\cdot}\dot{\boldsymbol{\omega}} \,+\, \boldsymbol{\omega} \times \rho_s \mathbf{I}{\cdot}\boldsymbol{\omega} = \overset{\triangle}{\mathbf{m}}{}' + \mathbf{c}' \times \overset{\triangle}{\mathbf{f}} + \overset{\triangledown}{\mathbf{m}}\,, \tag{2.13b}$$

where the first and second time derivative are abbreviated with $\dot{\mathbf{v}} = \mathrm{d}\mathbf{v}/\mathrm{d}t$ and $\ddot{\mathbf{v}} = \mathrm{d}^2\mathbf{v}/\mathrm{d}t^2$, respectively, for an arbitrary vector $\mathbf{v} \in \mathbb{R}^3$. Furthermore, the spatial derivative along Z is denoted as $\mathbf{v}' = \partial\mathbf{v}/\partial Z$. The angular equation of motion (2.13b) is not formulated directly for the rotation matrix $\mathbf{R}(Z,t)$, but for the angular velocity $\boldsymbol{\omega}(Z,t)$ of the cross sections. Both quantities are related via

$$[\boldsymbol{\omega}]_\times = \dot{\mathbf{R}}{\cdot}\mathbf{R}^\top, \tag{2.14}$$

where $[\boldsymbol{\omega}]_\times$ is the skew matrix of $\boldsymbol{\omega}$, so that $[\boldsymbol{\omega}]_\times{\cdot}\mathbf{v} = \boldsymbol{\omega} \times \mathbf{v}$. The rods considered here have spatially constant geometrical properties, i.e. a constant cross sectional area A and tensor of inertia $\mathbf{I}_0 = \mathbf{R}^\top \mathbf{I}\, \mathbf{R}$, as well as constant material properties, e.g. a constant density ρ_s. Their motion governed by Eqs. (2.13) depends on the internal forces $\overset{\triangle}{\mathbf{f}}$ and moments $\overset{\triangle}{\mathbf{m}}$, as well as on the external forces $\overset{\triangledown}{\mathbf{f}}$ and moments $\overset{\triangledown}{\mathbf{m}}$. The latter contain gravitational forces $\overset{\triangledown}{\mathbf{f}}_g = (\rho_s{-}\rho_f)\, A\, \mathbf{g}$, and external fluid loads acting on the fluid-structure interface Γ, denoted as $\overset{\triangledown}{\mathbf{f}}_\Gamma$ and $\overset{\triangledown}{\mathbf{m}}_\Gamma$. In case of a collision between rods these are additionally subjected to the collision loads $\overset{\triangledown}{\mathbf{f}}_c$ and $\overset{\triangledown}{\mathbf{m}}_c$. The internal forces $\overset{\triangle}{\mathbf{f}}_\Gamma$ and moments $\overset{\triangle}{\mathbf{m}}_\Gamma$ in Eqs. (2.13) are formulated for a linear viscoelastic material of Kelvin-Voigt type [158, 131], i.e.

$$\overset{\triangle}{\mathbf{f}} = \mathbf{C}_\varepsilon{\cdot}(\boldsymbol{\varepsilon} \,-\, \boldsymbol{\varepsilon}|_{t=0}) \,+\, \mathbf{C}_{\dot{\varepsilon}}{\cdot}\dot{\boldsymbol{\varepsilon}} \tag{2.15a}$$

$$\overset{\triangle}{\mathbf{m}} = \mathbf{C}_\kappa{\cdot}(\boldsymbol{\kappa} - \boldsymbol{\kappa}|_{t=0}) \,+\, \mathbf{C}_{\dot{\kappa}}{\cdot}\dot{\boldsymbol{\kappa}}\,. \tag{2.15b}$$

Here, the first term on the right-hand side of Eq. (2.15a) and (2.15b) constitutes the linear elastic part of $\overset{\triangle}{\mathbf{f}}$ and $\overset{\triangle}{\mathbf{m}}$. Internal strains generated during deformation are measured by the strain vector $\boldsymbol{\varepsilon}$ and the curvature vector $\boldsymbol{\kappa}$. Both vectors are defined by [131]

$$\boldsymbol{\varepsilon} = \mathbf{c}' \qquad \text{and} \qquad [\boldsymbol{\kappa}]_\times = \mathbf{R}'\,, \tag{2.16}$$

respectively, which can be interpreted as the relative change of position and orientation of adjoining cross sections. Their linear relation to the internal loads $\overset{\triangle}{\mathbf{f}}$ and $\overset{\triangle}{\mathbf{m}}$ are represented

by the two constitutive matrices $\mathbf{C}_\varepsilon = \mathbf{R}\cdot\mathbf{C}_{\varepsilon_0}\cdot\mathbf{R}^\top$ with $\mathbf{C}_{\varepsilon_0} = \mathrm{diag}(k_{s_1}G_s,\, k_{s_2}G_s,\, E_s)\, A$, and $\mathbf{C}_\kappa = \mathbf{R}\cdot\mathbf{C}_{\kappa_0}\cdot\mathbf{R}^\top$ with $\mathbf{C}_{\kappa_0} = \mathrm{diag}(E_s,\, E_s,\, k_t G_s)\,\mathbf{I}_0$. Here, the geometric tensor of inertia $\mathbf{I}_0 = \mathrm{diag}(I_X, I_Y, J)$ contains the 2nd moments of area I_X, I_Y and $J = I_Z$ around the $\mathbf{r}_X$-, $\mathbf{r}_Y$- and $\mathbf{r}_Z$-axis of the cross section. The shear and torsion correction factors k_{s_1}, k_{s_2} and k_t are used to model the influence of warping effects in case of shear and torsional loads.
The second term on the right-hand side of Eq. (2.15) takes into account the dissipative part of the internal loads $\hat{\mathbf{f}}$ and $\hat{\mathbf{m}}$ due to internal friction. For the Kelvin-Voigt material used here, these depend linearly on the strain rate $\dot{\boldsymbol{\varepsilon}}$ and the curvature rate $\dot{\boldsymbol{\kappa}}$, respectively, while the corresponding constitutive matrices are given by $\mathbf{C}_{\dot\varepsilon} = \mathbf{R}\cdot\mathbf{C}_{\dot\varepsilon_0}\cdot\mathbf{R}^\top$ with $\mathbf{C}_{\dot\varepsilon_0} = \mathrm{diag}(c_{s1}, c_{s2}, c_e)$, and $\mathbf{C}_{\dot\kappa} = \mathbf{R}\cdot\mathbf{C}_{\dot\kappa_0}\cdot\mathbf{R}^\top$ with $\mathbf{C}_{\dot\kappa_0} = \mathrm{diag}(c_{b1}, c_{b2}, c_t)$. The subscript of each damping parameter c denotes the associated deformation mode, i.e. shear, extension, bending and torsion.
A useful feature of the kinematic constraint (2.10) is that each vector quantity described in the global Eulerian frame can be transformed very easily into the Lagrangian frame of the reference configuration Ω_0^s at $t = 0$. At a specific arc length Z, it is realized by a linear transformation via the rotation matrix $\mathbf{R}(Z,t)$, e.g. to obtain

$$\boldsymbol{\omega}_0 = \mathbf{R}^\top\cdot\boldsymbol{\omega}\,, \qquad \mathbf{I}_0 = \mathbf{R}^\top\cdot\mathbf{I}\cdot\mathbf{R}, \qquad \hat{\mathbf{f}}_0 = \mathbf{R}^\top\cdot\hat{\mathbf{f}}\,, \qquad \hat{\mathbf{m}}_0 = \mathbf{R}^\top\cdot\hat{\mathbf{m}}\,, \qquad \ldots\,, \tag{2.17}$$

in the co-rotated Lagrangian frame $[\mathbf{r}_X\, \mathbf{r}_Y\, \mathbf{r}_Z]$ of an individual cross section, labeled with a subscript zero.

2.4 Fluid-structure coupling

2.4.1 Coupling conditions

The coupling between the Navier-Stokes equations (2.1) and the structure equations (2.4) is realized by the kinematic and the dynamic coupling condition. Both take place at the common fluid-structure interface Γ. The dynamic condition addresses the balance of forces between the fluid and the structure on Γ. This implies the equality of their stress vectors, i.e.

$$\boldsymbol{\sigma}\cdot\mathbf{n} = \boldsymbol{\sigma}_s\cdot\mathbf{n} \qquad \forall\mathbf{x}\in\Gamma\,, \tag{2.18}$$

with the hydrodynamic stress tensor $\boldsymbol{\sigma}$, the structural Cauchy stress tensor $\boldsymbol{\sigma}_s = \det(\mathbf{F})^{-1}\mathbf{F}\cdot\mathbf{P}$, and the unit normal vector $\mathbf{n}$ pointing from the fluid domain Ω^f into the solid domain Ω^s. From a different point of view, the stress vector can be interpreted as a surface-specific coupling force $\mathbf{f}_S = \boldsymbol{\sigma}\cdot\mathbf{n}$ connecting both parts of the coupled system at the interface Γ. In order to impose the dynamic coupling condition (2.18), $\mathbf{f}_S$ has to be introduced in the momentum balances of the fluid and the structure with opposite sign, according to the principle of *actio et reactio*. In particular for the one-dimensional Cosserat rod considered here, the coupling force is transformed into an appropriate one-dimensional variant, consisting of a coupling force $\check{\mathbf{f}}_\Gamma(Z,t)$ and a coupling moment $\check{\mathbf{m}}_\Gamma(Z,t)$. These are given by

$$\check{\mathbf{f}}_\Gamma = -\int_{\Gamma\cap\Upsilon}\mathbf{f}_S\,\mathrm{d}C\,, \qquad \check{\mathbf{m}}_\Gamma = -\int_{\Gamma\cap\Upsilon}\mathbf{x}\times\mathbf{f}_S\,\mathrm{d}C \tag{2.19}$$

and are obtained by integrating the hydrodynamic stress vector $\mathbf{f}_S = \boldsymbol{\sigma}\cdot\mathbf{n}$ along the fluid-solid contour $\Gamma\cap\Upsilon(Z)$ of an individual cross section $\Upsilon(Z)$ (see Fig. 2.2).
In general, the viscous fluids considered here stick at the surface of the rod structure without

any mass transfer across the fluid-structure interface Γ. Consequently, the kinematic coupling is realized by the *no-slip* boundary condition

$$\mathbf{u} = \mathbf{v} \quad \forall \mathbf{x} \in \Gamma \,, \tag{2.20}$$

which imposes the equality of the fluid velocity $\mathbf{u}$ and the structure velocity $\mathbf{v} = \mathrm{d}\mathbf{x}/\mathrm{d}t$ at their common moving interface Γ. Concerning the kinematic constraint (2.10) of the Cosserat rod, i.e. $\mathbf{x} = \mathbf{c} + \mathbf{R}\cdot\boldsymbol{\xi}_0$, the no-slip condition (2.20) can be transferred into

$$\mathbf{u} = \dot{\mathbf{c}} + \boldsymbol{\omega} \times \boldsymbol{\xi} \quad \forall \mathbf{X} \in \Gamma_0 \,, \tag{2.21}$$

with the linear velocity $\dot{\mathbf{c}}$ of an individual cross section $\Upsilon(Z)$, its angular velocity $\boldsymbol{\omega}$ and the cross section vector $\boldsymbol{\xi} = \mathbf{R}\cdot\boldsymbol{\xi}_0 \in \Upsilon(Z)$ (see Fig. 2.2).

2.4.2 Zero-thickness assumption and jump conditions

The long slender rods considered in this work have cross sections much smaller than their longitudinal expansion. Especially when focusing on FSI problems with a large number of slender rods in an appropriately large fluid domain, the exact geometrical shape of the cross sections is usually of less importance for the global dynamic behavior of the fluid. Consequently, the rods are sufficiently well represented in the fluid as simple one-dimensional curves, e.g. to model fibers, or as two-dimensional geometries in case of strip-shaped rods (Fig. 2.3). Since at least one lateral expansion of the structure is neglected, this strategy is often referred to as *zero-thickness assumption (approximation)* which is widely used in the literature to model rods or membranes, e.g. [39, 56, 102, 135, 273, 239, 53]. This strategy is pursued here as well. The present FSI model is tailored to rectangular cross sections of width W and thickness T, with an aspect ratio of $T \ll W$. While the Cosserat-rod equations (2.13) are solved for the three-dimensional volumetric rod with $T > 0$, it is represented in the fluid as a two-dimensional version with $T = 0$, illustrated in Fig. 2.3. When applying

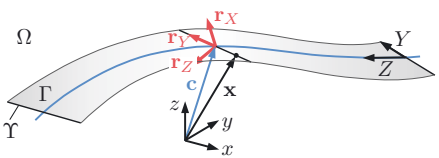

Figure 2.3: *Representation of a strip-shaped rod in the fluid domain $\Omega^{\mathrm{f}} = \Omega$ as an infinitely thin Cosserat rod $\Omega^{\mathrm{s}} = \Gamma$. In contrast to the three-dimensional volumetric rod shown in Fig.2 2, the cross sections $\Upsilon(Z)$ are one-dimensional and a subset of the fluid-structure interface Γ.*

the zero-thickness assumption in the fluid domain, the structure domain Ω^{s} completely coincides with the fluid-structure interface Γ, so that $\Omega^{\mathrm{s}} = \Gamma$. Moreover, the fluid domain now represents the entire domain of the coupled problem, i.e. $\Omega = \Omega^{\mathrm{f}} \cup \Omega^{\mathrm{s}} = \Omega^{\mathrm{f}}$, and contains the structure as an embedded fluid-structure interface Γ. To discuss this issue the limiting case of a so-called *interface problem* is considered, where the entire fluid domain Ω is separated by the interface Γ into two disjoint regions. If differential equations are used to model such an interface problem, quantities in the governing equations are discontinuous across the

interface [142], as demonstrated in the following. For this purpose, consider a small finite volume $\omega \subset \Omega$ which is entirely cut by the interface $\gamma \subset \Gamma$ into two subdomains $\omega^+ \subset \omega$ and $\omega^- \subset \omega$, as illustrated in Fig. 2.4. The fluid inside ω is described by the Navier-Stokes

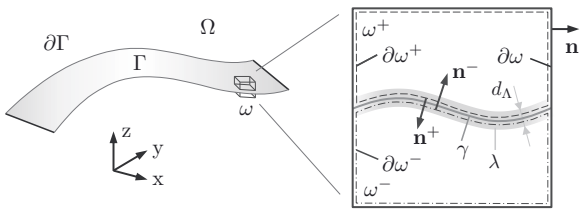

$$\omega = \omega^+ \cup \omega^- \tag{2.22a}$$

$$\gamma = \partial\omega^+ \cap \partial\omega^- \tag{2.22b}$$

$$\partial\omega = (\partial\omega^+ \cup \partial\omega^-) \setminus \gamma \tag{2.22c}$$

Figure 2.4: *Illustration of an interface problem in which the fluid domain Ω is cut by the interface Γ. On a smaller scale, the finite volume $\omega \subset \Omega$ is separated into two subdomains ω^+ and ω^-. The intersection of their boundaries $\partial\omega^+$and $\partial\omega^-$ defines the common interface $\gamma \subset \Gamma$. The vectors $\mathbf{n}$, $\mathbf{n}^+$ and $\mathbf{n}^-$ are out-pointing unit normal vectors at the boundaries $\partial\omega$, $\partial\omega^+$and $\partial\omega^-$. The gray shaded area around γ represents a compact, volumetric layer λ of infinitesimally small thickness $d_\Lambda \to 0$, as described in Section 2.4.3.*

equations (2.1), where the velocity field $\mathbf{u}^+$ and $\mathbf{u}^-$ belongs to the associated subdomain ω^+ and ω^-, respectively. Concerning Eq. (2.1a), the corresponding integral momentum balances of both subdomains are given by

$$\int_{\omega^+} \left(\rho_\mathrm{f} \frac{\mathrm{d}\mathbf{u}^+}{\mathrm{d}t} - \mathbf{f}_\mathrm{V}^+ \right) \mathrm{d}V = \int_{\partial\omega^+} \boldsymbol{\sigma}^+ \cdot \mathbf{n}^+ \, \mathrm{d}S \tag{2.23a}$$

$$\int_{\omega^-} \left(\rho_\mathrm{f} \frac{\mathrm{d}\mathbf{u}^-}{\mathrm{d}t} - \mathbf{f}_\mathrm{V}^- \right) \mathrm{d}V = \int_{\partial\omega^-} \boldsymbol{\sigma}^- \cdot \mathbf{n}^- \, \mathrm{d}S \,, \tag{2.23b}$$

with the hydrodynamic stress tensors $\boldsymbol{\sigma}^+$ and $\boldsymbol{\sigma}^-$, according to Eq. (2.2), being defined in ω^+ and ω^-, respectively. From the boundary integrals over $\partial\omega^+$ and $\partial\omega^-$, the common part of the interface γ can be isolated formally concerning definition (2.22c). Doing so, Eq. (2.23a) and Eq. (2.23b) can be converted into

$$\int_{\omega^+} \left(\rho_\mathrm{f} \frac{\mathrm{d}\mathbf{u}^+}{\mathrm{d}t} - \mathbf{f}_V^+ \right) \mathrm{d}V = \int_{\partial\omega^+\setminus\gamma} \boldsymbol{\sigma}^+ \cdot \mathbf{n}^+ \, \mathrm{d}S + \int_\gamma \boldsymbol{\sigma}^+ \cdot \mathbf{n}^+ \, \mathrm{d}S \tag{2.24a}$$

$$\int_{\omega^-} \left(\rho_\mathrm{f} \frac{\mathrm{d}\mathbf{u}^-}{\mathrm{d}t} - \mathbf{f}_V^- \right) \mathrm{d}V = \int_{\partial\omega^-\setminus\gamma} \boldsymbol{\sigma}^- \cdot \mathbf{n}^- \, \mathrm{d}S + \int_\gamma \boldsymbol{\sigma}^- \cdot \mathbf{n}^- \, \mathrm{d}S \,. \tag{2.24b}$$

To access the behavior of the entire domain ω cut by γ, both momentum balances, separated so far in ω^+ and ω^-, are added to obtain their union $\omega = \omega^+ \cup \omega^-$, i.e.

$$\underbrace{\int_{\omega^+} \left(\rho_\mathrm{f} \frac{\mathrm{d}\mathbf{u}^+}{\mathrm{d}t} - \mathbf{f}_V^+ \right) \mathrm{d}V + \int_{\omega^-} \left(\rho_\mathrm{f} \frac{\mathrm{d}\mathbf{u}^-}{\mathrm{d}t} - \mathbf{f}_V^- \right) \mathrm{d}V}_{\omega = \omega^+ \cup \omega^-} = \underbrace{\int_{\partial\omega^+\setminus\gamma} \boldsymbol{\sigma}^+ \cdot \mathbf{n}^+ \, \mathrm{d}S + \int_{\partial\omega^-\setminus\gamma} \boldsymbol{\sigma}^- \cdot \mathbf{n}^- \, \mathrm{d}S}_{\partial\omega = (\partial\omega^+ \cup \partial\omega^-)\setminus\gamma} + \ldots$$

$$\ldots + \int_\gamma \left(\boldsymbol{\sigma}^+ \cdot \mathbf{n}^+ + \boldsymbol{\sigma}^- \cdot \mathbf{n}^- \right) \mathrm{d}S \,. \tag{2.25}$$

By renaming the field quantities belonging to ω and setting $\mathbf{n} = \mathbf{n}^+ = -\mathbf{n}^-$, the momentum balance over ω is given by

$$\int_\omega \left(\rho_\mathrm{f} \frac{\mathrm{d}\mathbf{u}}{\mathrm{d}t} - \mathbf{f}_V \right) \mathrm{d}V = \int_{\partial\omega} \boldsymbol{\sigma}\cdot\mathbf{n} \, \mathrm{d}S + \underbrace{\int_\gamma (\boldsymbol{\sigma}^+ - \boldsymbol{\sigma}^-)\cdot\mathbf{n} \, \mathrm{d}S}_{\text{jump term}} . \tag{2.26}$$

Here, the second term on the right-hand side of Eq. (2.26) is referred to as *jump term*. The associated jump in the stress vectors, i.e. $(\boldsymbol{\sigma}^+ - \boldsymbol{\sigma}^-)\cdot\mathbf{n}$, has the unit of a surface-specific force $\mathbf{f}_S$ related to the interface γ [187, 142, 133]. Using this force, the jump term can be expressed as

$$\int_\gamma \mathbf{f}_S \, \mathrm{d}S = \int_\gamma \boldsymbol{\sigma}^+\cdot\mathbf{n} \, \mathrm{d}S - \int_\gamma \boldsymbol{\sigma}^-\cdot\mathbf{n} \, \mathrm{d}S \, , \tag{2.27}$$

which illustrates, that $\mathbf{f}_S$ is the resulting fluid load caused by the hydrodynamic stresses $\boldsymbol{\sigma}^+$ and $\boldsymbol{\sigma}^-$ acting on γ from both sides, i.e. from ω^+ and ω^-, respectively. Only in cases where the stresses across γ are discontinuous, the force $\mathbf{f}_S$ does not vanish. This is obviously the reason for the designation "jump term" in Eq. 2.26.

As described in the previous Section 2.4.1, the force $\mathbf{f}_S$ can also be interpreted as a coupling force introduced into the Navier-Stokes equations (2.1) and the Cosserat rod equations (2.13) to impose the kinematic and dynamic coupling condition. In this context, the coupling force is defined locally at each point on $\mathbf{x} \in \Gamma$, opposed to its integral formulation according to Eq. (2.27). However, if the control volume ω shown in Fig. 2.4 is decreased to an infinitesimally small size, Eq. (2.27) can be transferred to a local relation between the coupling force and the hydrodynamic stresses, so that $\mathbf{f}_S = (\boldsymbol{\sigma}^+ - \boldsymbol{\sigma}^-)\cdot\mathbf{n} \;\; \forall \mathbf{x} \in \Gamma$. At the interface edge $\partial\Gamma$ the local force $\mathbf{f}_S$ vanishes, since $\boldsymbol{\sigma}^+$ and $\boldsymbol{\sigma}^-$ coincide in the free flow region without Γ.

The analysis of the cut volume ω via the momentum balance (2.1a) revealed that the hydrodynamic stresses $\boldsymbol{\sigma}$ are discontinuous at γ. To gain information about the velocity field $\mathbf{u}$ cut by γ, the same procedure is applied to the continuity equation (2.1b). This results in

$$\int_{\partial\omega} \mathbf{u}\cdot\mathbf{n} \, \mathrm{d}S + \int_\gamma (\mathbf{u}^+ - \mathbf{u}^-)\cdot\mathbf{n} \, \mathrm{d}S = 0 \, , \tag{2.28}$$

with the velocities $\mathbf{u}^+$ and $\mathbf{u}^-$ evaluated as the upper and lower limit, respectively, with respect to both sides of γ. Due to continuity at the outer boundary $\partial\omega$, the first integral on the left-hand side vanishes, so that Eq. (2.28) turns into the kinematic relation

$$\int_\gamma (\mathbf{u}^+ - \mathbf{u}^-)\cdot\mathbf{n} \, \mathrm{d}S = 0 \, , \tag{2.29}$$

between the upper and the lower limit of $\mathbf{u}$ on γ. Following the argumentation above, this integral formulation can be transferred into the local condition $\mathbf{u}^+\cdot\mathbf{n} = \mathbf{u}^-\cdot\mathbf{n} \;\; \forall \mathbf{x} \in \Gamma$, which implies the continuity of $\mathbf{u}(\mathbf{x}, t)$ in normal direction of Γ. With the no-slip condition (2.20) assumed in Section 2.4.1, the tangential part of the velocity must coincide as well, so that $\mathbf{u}^+ = \mathbf{u}^- \;\; \forall \mathbf{x} \in \Gamma$. Therefore, the velocity field $\mathbf{u}(\mathbf{x}, t)$ is continuous in the entire fluid domain, in contrast to the hydrodynamic stresses $\boldsymbol{\sigma}\cdot\mathbf{n}$ as described above. However, the discontinuity of the stresses $(\boldsymbol{\sigma}^+ - \boldsymbol{\sigma}^-)\cdot\mathbf{n} \neq \mathbf{0}$ implies that the velocity field does not need to be differentiable at Γ. As a result $\mathbf{u}(\mathbf{x}, t)$ exhibits a continuity of class C^0.

2.4.3 Coupling via distributive sources

In the previous sections, the coupling force $\mathbf{f}_S = (\boldsymbol{\sigma}^+ - \boldsymbol{\sigma}^-)\cdot\mathbf{n}$ was derived as a surface-specific force acting on the fluid-structure interface Γ with the associated coupling term appearing as an additional surface integral in the momentum balance (2.26) of the fluid. The IBM coupling strategy used here is based on the idea of converting this surface integral into a volume integral. For this purpose, the surface-specific coupling force $\mathbf{f}_S$ is transformed into a mass-specific coupling force $\mathbf{f}_\Gamma$. As a result, $\mathbf{f}_\Gamma$ can be introduced directly into the differential momentum balance (2.1a) as a regular volume force, such as gravitational acceleration. This simplifies the numerical treatment of the Navier-Stokes equations (2.1), since a special handling of surface-specific quantities is not necessary.
The transformation of the integral coupling term is realized by using common techniques of distribution theory. In this context, a properly defined delta function δ_V allows replacing the surface-specific force $\mathbf{f}_S$ by its volumetric complement $\mathbf{f}_\Gamma$, in such a way that the same momentum is transferred to the fluid [180, 66], i.e.

$$\int_\gamma \mathbf{f}_S \,\mathrm{d}S = \int_\omega \delta_V \,\mathbf{f}_S \,\mathrm{d}V = \int_\lambda \rho_\mathrm{f}\,\mathbf{f}_\Gamma \,\mathrm{d}V\,, \tag{2.30}$$

where $\lambda \subset \Lambda$ is the compact, volumetric support of the delta function δ_V enveloping the interface $\gamma \subset \Gamma$ in the cut volume $\omega \subset \Omega$ (see Fig. 2.4 above). On a larger scale, this support constitutes a thin "coating" layer Λ enclosing entirely the interface Γ. For the exact continuous problem the thickness of Λ is infinitesimally small, i.e. $d_\Lambda \to 0$. Thus, $\mathbf{f}_\Gamma$ applies a finite amount of "force" to the fluid in an arbitrarily thin layer Λ, which indicates the *distributive nature* of the coupling force. This perspective constitutes the basis for the later discrete formulation of the FSI problem via an immersed boundary method, described in Chapter 4 below.
According to the principle of *actio et reactio*, the distributive force $\mathbf{f}_\Gamma$, introduced into the momentum balance of the fluid, must also appear in the equations of motion of the Cosserat rod, with opposite sign. So far, the forces $\overset{\triangledown}{\mathbf{f}}_\Gamma$ and moments $\overset{\triangledown}{\mathbf{m}}_\Gamma$ acting on the rod are defined via $\mathbf{f}_S$, according to Eq. (2.19). Considering the zero-thickness approximation with $\Gamma\cap\Upsilon = \Upsilon$, both are given by

$$\overset{\triangledown}{\mathbf{f}}_\Gamma(Z) = -\int_\Upsilon \mathbf{f}_S \,\mathrm{d}Y\,, \qquad \overset{\triangledown}{\mathbf{m}}_\Gamma(Z) = -\int_\Upsilon \boldsymbol{\xi}\times\mathbf{f}_S \,\mathrm{d}Y\,, \tag{2.31}$$

with $\mathbf{f}_S = (\boldsymbol{\sigma}^+ - \boldsymbol{\sigma}^-)\cdot\mathbf{n}$. According to transformation (2.30), $\mathbf{f}_\Gamma$ emerges from a surface integration of $\mathbf{f}_S$. Instead, Eq. (2.31) provides a line integral over $\Upsilon(Z)$. Consequently, $\overset{\triangledown}{\mathbf{f}}_\Gamma(Z)$ and $\overset{\triangledown}{\mathbf{m}}_\Gamma(Z)$ must be integrated along the arc length Z to enable an incorporation of $\mathbf{f}_\Gamma$ via

$$\int_\zeta \overset{\triangledown}{\mathbf{f}}_\Gamma \,\mathrm{d}Z = -\int_\Gamma \mathbf{f}_S \,\mathrm{d}S = -\int_\Lambda \rho_\mathrm{f}\,\mathbf{f}_\Gamma \,\mathrm{d}V \tag{2.32a}$$

$$\int_\zeta \overset{\triangledown}{\mathbf{m}}_\Gamma \,\mathrm{d}Z = -\int_\Gamma \boldsymbol{\xi}\times\mathbf{f}_S \,\mathrm{d}S = -\int_\Lambda \boldsymbol{\xi}\times(\rho_\mathrm{f}\,\mathbf{f}_\Gamma) \,\mathrm{d}V\,, \tag{2.32b}$$

taking advantage of the fact that the interface Γ equals the union of the cross-sections $\Upsilon(Z)$ (Fig. 2.3), i.e. $\Gamma = \bigcup_{Z\in\zeta}\Upsilon(Z)$. At a later stage, this relation is of crucial importance for the spatial discretization of the Cosserat rod by a finite set of structural elements e. In this context, the average hydrodynamic loads acting on the element interface Γ_e are given by $\overset{\triangledown}{\mathbf{f}}_{\Gamma_e} = \int_{\zeta_e} \overset{\triangledown}{\mathbf{f}}_\Gamma \,\mathrm{d}Z/\Delta Z$ and $\overset{\triangledown}{\mathbf{m}}_{\Gamma_e} = \int_{\zeta_e} \overset{\triangledown}{\mathbf{m}}_\Gamma \,\mathrm{d}Z/\Delta Z$, with $\zeta_e \subset \zeta$ and $\Delta Z = \int_{\zeta_e} \mathrm{d}Z$.

3 Numerical models of partitioned problems

3.1 Navier Stokes equations

3.1.1 Temporal discretization

The basic fluid solver was adopted from the in-house code PRIME (Phase-Resolving sIMulation Environment), primarily implemented by Kempe in 2011 [118, 119]. Due to its high efficiency and capability for IBMs, it is frequently employed in simulations of coupled problems [251, 119, 35, 246]. This section shortly summarizes relevant information in terms of the temporal and spatial discretization. Remaining technical details are provided in [118, 119]. The time integration of the Navier-Stokes equations (2.1) is accomplished by a special variant of the pressure projection method [43, 123, 194, 37], used to impose the incompressibility constraint (2.1b). In PRIME the variant of Uhlmann [251] is used which combines an explicit three-step third-order low-storage Runge-Kutta scheme for the convective term and a second-order implicit Crank-Nicolson scheme for the viscous term in each Runge-Kutta sub-step. Furthermore, in this variant the pressure is considered in the predictor step of the projection method which conserves an overall second order accuracy in time for both, the pressure as well as the velocity [37]. Numerical stability of the Runge-Kutta scheme is achieved for Courant numbers $CFL < \sqrt{3}$ [194] which extends to the entire time advancement scheme. In each Runge-Kutta sub-step $r = 1, 2, 3$ the following equations need to be solved:

$$\frac{\tilde{\mathbf{u}} - \mathbf{u}^{r-1}}{\Delta t} = 2\alpha_r \, \nu_\mathrm{f} \, \nabla^2 \mathbf{u}^{\,r-1} - 2\alpha_r \, \nabla\left(\frac{p^{\,r-1}}{\rho_\mathrm{f}}\right) - \gamma_r \, \nabla\cdot(\mathbf{u}\otimes\mathbf{u})^{\,r-1} - \zeta_r \, \nabla\cdot(\mathbf{u}\otimes\mathbf{u})^{\,r-2} + \mathbf{f}_V \tag{3.1a}$$

$$\nabla^2 \mathbf{u}^* - \frac{\mathbf{u}^*}{\alpha_r \, \nu_\mathrm{f} \, \Delta t} = \nabla^2 \mathbf{u}^{r-1} - \frac{\tilde{\mathbf{u}} + 2\alpha_r \, \Delta t \, \overline{\mathbf{f}}_\Gamma}{\alpha_r \, \nu_\mathrm{f} \, \Delta t} \tag{3.1b}$$

$$\nabla^2 \phi^r = \nabla \cdot \mathbf{u}^* \tag{3.1c}$$

$$\mathbf{u}^r = \mathbf{u}^* - \nabla \phi^r \tag{3.1d}$$

$$\frac{p^{\,r}}{\rho_\mathrm{f}} = \frac{p^{\,r-1}}{\rho_\mathrm{f}} + \frac{\phi^r}{2\,\alpha_r \, \Delta t} - \frac{\nu_\mathrm{f}}{2} \, \nabla^2 \phi^r \,, \tag{3.1e}$$

where the coefficients α_r, γ_r and ζ_r of the present Runge-Kutta scheme can be found in [194, 251]. At level $r = 1$, the velocity field $\mathbf{u}^0$ and the pressure field p^0 provide the initial conditions of the current time step and are identical to field variables of the previous time level t^n, i.e. $\mathbf{u}^0 = \mathbf{u}^n$ and $p^0 = p^n$. For the three-step scheme employed here, the velocity field $\mathbf{u}^3 = \mathbf{u}^{n+1}$ and the pressure field $p^3 = p^{n+1}$ constitute field variables at the new time $t^{n+1} = t^n + \Delta t$, with the current time step size $\Delta t = t^{n+1} - t^n$.

Initially, in each Runge-Kutta step r, a preliminary velocity field $\tilde{\mathbf{u}}$ is determined by a fully explicit Runge-Kutta sub-step. Afterwards, the viscous term is treated implicitly by the Helmholtz equation (3.1b) yielding a non-divergence free velocity field $\mathbf{u}^*$. The force $\bar{\mathbf{f}}_\Gamma$ in Eq. (3.1b) is used at a later stage for the fluid-structure coupling, described in Chapter 4 below. In the next step, the scalar pressure correction field ϕ is determined by the Poisson equation (3.1c). Subsequently, it is used to correct $\mathbf{u}^*$ to a divergence free field $\mathbf{u}^r$ by means of the projection (3.1d). Finally, the pressure field p^r at the new time level is obtained explicitly from the pressure correction field ϕ via Eq. (3.1e).
In this scheme the main computational effort is consumed by the Helmholtz equation (3.1b) and the Poisson equation (3.1c). Hence, the performance and efficiency of the fluid solver depends essentially on the computational approaches applied to solve these systems. As described in Section 4.6, this issue is outsourced by using parallel solvers of the modern libraries PETSc [13] and Hypre [132].

3.1.2 Spatial discretization

The spatial discretization of the system (3.1) is performed by a second-order finite-volume scheme of Ham [94] on a staggered Eulerian grid. Here, the pressures p_{ijk} are stored in the cell centers of the control volumes, while the velocity components are shifted by a half cell width in the corresponding direction and thus are located at the cell faces, so that $\mathbf{u}_{ijk} = (u_{i,j-\frac{1}{2},k}, v_{i,j-\frac{1}{2},k}, w_{i,j,k-\frac{1}{2}})^\top$. The discretization scheme fully conserves mass, momentum and energy even on non-uniform grids and avoids checkerboard oscillations of the pressure [118]. In the present work the computational domain $\Omega = [0; L_x] \times [0; L_y] \times [0; L_z]$ has a rectangular shape, where L_x, L_y and L_z denote the extend of the domain in x-, y- and z-direction, respectively. Different boundary conditions were implemented for the velocity field: a Dirichlet boundary condition to realize velocity inlets or no-slip walls, a Neumann condition to impose free-slip rigid lids and periodicity conditions, connecting two opposite boundaries in one direction. Furthermore, a convective outlet condition [191, 118] is provided, enabling flow structures to leave the domain almost without affecting the interior flow field. In terms of the pressure correction field ϕ a zero gradient condition [88] is used for all types of boundary conditions except for periodic boundaries.

3.2 Cosserat rod equations

3.2.1 Parametrization of finite rotations

The Cosserat rod equations (2.13b) are constituted by a linear and an angular equation of motion. The former equation describes the motion of the center line position $\mathbf{c}$ which is a vector quantity $\mathbf{c} \in \mathbb{R}^3$. The angular equation of motion is formulated in terms of the rotation matrix $\mathbf{R} \in SO(3)$ additionally subjected to the properties of the rotation group $SO(3)$, i.e. the orthogonality constraint $\mathbf{R} \cdot \mathbf{R}^\top = \mathbf{R}^\top \cdot \mathbf{R} = \mathbb{I}$. Consequently, this constraint needs to be taken into account when parameterizing $\mathbf{R}$. Several approaches were developed and applied to rod models in the recent past, all accompanied by advantages and disadvantages [104, 262, 140, 148]. Common variants are the formulation via Euler angles, by means of the Rodriques formula or hybrid forms [29, 236]. In principle, only three degrees of freedom are required to describe uniquely a finite rotation in space due to the orthogonality of $\mathbf{R}$. State of the art is to describe rotations via quaternions. Among other advantages, these avoid the

gimbal lock effect or singularities [129]. A quaternion $\mathbf{q}$ exhibits four degrees of freedom, i.e. $\mathbf{q} = (q_\mathrm{r}; \hat{q}) \in \mathbb{S}^3$, where $\mathbb{S}^3 = \{\mathbf{q} \in \mathbb{H} : \|\mathbf{q}\| = 1\} \subset \mathbb{H}$ is the set of unit quaternions, a subgroup of the multiplicative quaternionic group $\mathbb{H}$ [129]. The real part of the quaternion is given by $\Re(\mathbf{q}) = q_\mathrm{r} \in \mathbb{R}$. Furthermore, the imaginary part is $\Im(\mathbf{q}) = \hat{q} \in \mathbb{R}^3$, while $\overline{\mathbf{q}} = (q_\mathrm{r}; -\hat{q})$ denotes the conjugate of a quaternion $\mathbf{q}$, such that $\mathbf{q}{*}\overline{\mathbf{q}} = (\|\mathbf{q}\|^2; 0)$. The multiplication of two quaternions $\mathbf{p}, \mathbf{q} \in \mathbb{H}$ is defined as

$$\mathbf{p}{*}\mathbf{q} = p_\mathrm{r} q_\mathrm{r} - \hat{p}{\cdot}\hat{q} + p_\mathrm{r}\hat{q} + q_\mathrm{r}\hat{p} + \hat{p} \times \hat{q} \qquad \text{for} \quad \mathbf{p}, \mathbf{q} \in \mathbb{H} \tag{3.2}$$

and thus is non-commutative. The multiplication between a matrix $\mathbf{M} \in \mathbb{R}^{4\times4}$ and a quaternion $\mathbf{q} \in \mathbb{S}^3$ is treated as a common matrix vector multiplication $\mathbf{M}\cdot\mathbf{q}$, while a scalar multiplication $s\mathbf{q}$, with $s \in \mathbb{R}$, is executed componentwise. The dot-product is defined as $\mathbf{p}{\cdot}\mathbf{q} = p_\mathrm{r} q_\mathrm{r} + \hat{p}{\cdot}\hat{q}$ and the cross-product is given by $\mathbf{p} \times \mathbf{q} = (\mathbf{p}{*}\mathbf{q} - \mathbf{q}{*}\mathbf{p})/2$. Using these definitions, a rotation of any vector quantity $\mathbf{v} \in \mathbb{R}^3$ between a local and the global coordinate frame can be formulated as follows:

$$\mathbf{v} = \mathbf{R}{\cdot}\mathbf{v}_0 = \mathbf{q}{*}\mathbf{v}_0{*}\overline{\mathbf{q}} \qquad \textit{(forward rotation)} \tag{3.3a}$$

$$\mathbf{v}_0 = \mathbf{R}^\top{\cdot}\mathbf{v} = \overline{\mathbf{q}}{*}\mathbf{v}{*}\mathbf{q} \qquad \textit{(backward rotation)} \tag{3.3b}$$

Recall that vectors indicated with index zero, e.g. $\mathbf{v}_0 \in \mathbb{R}^3$, are given in the local co-rotated Lagrangian frame of a cross section and conventional letters, $\mathbf{v} \in \mathbb{R}^3$, in the global Eulerian frame. Furthermore, $\Im(\mathbb{H}) = \mathbb{R}^3$ stating that each vector $\mathbf{v} \in \mathbb{R}^3$ is treated as a pure imaginary quaternion $\mathbf{v} = \hat{v}$. For a quaternion $\mathbf{q}$ the corresponding rotation $\mathbf{R} = [\mathbf{r}_X\, \mathbf{r}_Y\, \mathbf{r}_Z]$ of a cross section is given by the Euler map [131]

$$\mathbf{R}(\mathbf{q}) = \left(2q_\mathrm{r}^2 - \|\mathbf{q}\|^2\right)\mathbb{I} \,+\, 2\hat{q}\otimes\hat{q} \,+\, 2q_\mathrm{r}\,[\hat{q}]_\times \qquad \text{for} \quad \mathbf{q} \in \mathbb{H}\,. \tag{3.4}$$

In the present context, Lang *et al.* [131] showed that the Cosserat rod equations (2.13) can be reformulated by standard index reduction techniques as an equivalent system

$$\ddot{\mathbf{c}} = \frac{1}{\rho_\mathrm{s} A}\left\{\left(\mathbf{q}{*}\hat{\mathbf{f}}_0{*}\overline{\mathbf{q}}\right)' + \bar{\mathbf{f}}\right\} \tag{3.5a}$$

$$\ddot{\mathbf{q}} = \frac{2}{\rho_\mathrm{s}}\boldsymbol{\mathcal{M}}{\cdot}\left\{4\rho_\mathrm{s}\,\dot{\mathbf{q}}{*}\boldsymbol{\mathcal{I}}_0{\cdot}\left(\dot{\overline{\mathbf{q}}}{*}\mathbf{q}\right) + \mathbf{c}'{*}\mathbf{q}{*}\hat{\mathbf{f}}_0 + \left(\mathbf{q}{*}\hat{\mathbf{m}}_0\right)' + \mathbf{q}'{*}\hat{\mathbf{m}}_0 + \bar{\mathbf{m}}{*}\mathbf{q}\right\} - \|\dot{\mathbf{q}}\|^2\mathbf{q}\,, \tag{3.5b}$$

with the quaternion matrix of inertia $\boldsymbol{\mathcal{I}}_0 = 0 \oplus \mathbf{I}_0$ and the "inverse" quaternion matrix of inertia $\boldsymbol{\mathcal{M}} = \frac{1}{4}\boldsymbol{\mathcal{Q}}{\cdot}\boldsymbol{\mathcal{I}}_0^{-1}{\cdot}\boldsymbol{\mathcal{Q}}^\top$. Here, the matrix $\boldsymbol{\mathcal{Q}}$ allows to express a multiplication of $\mathbf{p}, \mathbf{q} \in \mathbb{S}^3$ as a matrix-vector product, i.e. $\mathbf{p}{*}\mathbf{q} = \boldsymbol{\mathcal{Q}}(\mathbf{p}){\cdot}\mathbf{q}$ [131]. According to Eq. (2.15), internal forces $\hat{\mathbf{f}}_0$ and internal moments $\hat{\mathbf{m}}_0$ are formulated in terms of the strain vector $\boldsymbol{\varepsilon}_0$ and the curvature vector $\boldsymbol{\kappa}_0$, respectively. Their quaternionic expressions are given by

$$\boldsymbol{\varepsilon}_0 = \overline{\mathbf{q}}{*}\mathbf{c}'{*}\mathbf{q} \qquad \text{and} \qquad \boldsymbol{\kappa}_0 = 2\,\overline{\mathbf{q}}{*}\mathbf{q}'\,. \tag{3.6}$$

In contrast to the conventional formulation of the Cosserat rod equations (2.13), the quaternionic form (3.5) can be transformed into a system of first-order ordinary differential equations (3.8), which is advantageous from a numerical point of view.

3.2.2 Temporal and spatial discretization

In the literature, the Cosserat rod equations (2.13) are usually discretized by finite element methods (FEM), e.g. in [20, 217, 105, 107, 202, 99, 275] to name just a few. In rare cases finite difference methods (FDM) are used [57, 25, 131, 110]. Usually, FE methods are preferred as they provide a simple way to assemble numerous rod structures to complex supporting structures. Due to technical issues which may arise for low-order schemes, e.g. the "shear locking" effect [128, 6], high expertise is required when employing FEM for this purpose. In contrast to that, a discretization via FDM is more straightforward, which reduces the implementation effort. In addition, rod models discretized with finite differences are often employed in real-time applications [131] as they keep the computational effort as small as possible. This is especially important when simulating a large number of rods simultaneously. For these reasons, the FDM approach is favored in the present work as well. Following recommendations of Lang *et al.* [131], the rod equations (3.5) are discretized with an equidistant staggered grid to achieve a second order accuracy in space. As shown in Fig.3.1, the centroids of the cross sections are located at the edges of an element e which are denoted by a half-index, i.e. $\mathbf{c}_{e-\frac{1}{2}}$ and $\mathbf{c}_{e+\frac{1}{2}}$ with $e = 1, ..., N_\mathrm{e}$. The rotations of the cross sections are located between these centroids and are denoted by $\mathbf{q}_e$. Corresponding centroid velocities and quaternionic velocities are staggered identically and are given by $\dot{\mathbf{c}}_{e-\frac{1}{2}}$, $\mathbf{c}_{e+\frac{1}{2}}$ and $\dot{\mathbf{q}}_e$, respectively. After discretization the rod structure can be interpreted as a set of rigid *structural elements* connected by numerical joints along the arc length coordinate Z, as illustrated in Fig. 3.1.
The boundary conditions of the rod equations required at both ends of the rod, i.e. at $Z = 0$ and $Z = L$, are treated as follows. In case of freely movable unconstrained ends internal forces and internal moments vanish, which can simply be incorporated into the equations of motion discretized. Constrained and fixed ends of a rod correspond to Dirichlet conditions in terms of the center line, i.e. $\mathbf{c}_{\frac{1}{2}}$ or $\mathbf{c}_{N_\mathrm{e}+\frac{1}{2}}$, depending on the specific end to be fixed. The handling of predefined rotations is more difficult since no discrete quaternions are available at the lower end and the upper end of the rod due to the staggered discretization employed (see Fig.3.1). Instead, so-called ghost-quaternions are used, e.g. $\mathbf{q}_0$ at the lower end, determined in such a way that a desired rotation $\mathbf{q}_{\frac{1}{2}}$ is realized at $Z = 0$. Based on the well-known SLERP interpolation technique [213] – used here as an extrapolation technique to obtain ghost-values – the ghost-quaternion and the corresponding time derivative are given by

$$\mathbf{q}_0 = 2\,(\mathbf{q}_{\frac{1}{2}} \cdot \mathbf{q}_1)\,\mathbf{q}_{\frac{1}{2}} - \mathbf{q}_1 \qquad \text{and} \qquad \dot{\mathbf{q}}_0 = \frac{\partial \mathbf{q}_0}{\partial \mathbf{q}_1} \cdot \dot{\mathbf{q}}_1\,. \tag{3.7}$$

The ghost-quaternion $\mathbf{q}_{N_\mathrm{e}+1}$ at the upper end of the rod at $Z = L$ is computed analogously. Boundary conditions just mentioned also can be mixed, e.g. to realize a revolute joint, where the rod is fixed at one end but is able to rotate freely around this fixation.
The spatial discretization of the Cosserat equations via FDM results in a system of first-order ordinary differential equations (ODE) of the form

$$\dot{\mathbf{z}} = \mathbf{rhs}(\mathbf{z}, t), \quad \mathbf{z} = \left(\mathbf{c}_{\frac{1}{2}}, \dot{\mathbf{c}}_{\frac{1}{2}},\ \dot{\mathbf{q}}_1, \mathbf{q}_1,\ \mathbf{c}_{\frac{3}{2}}, \dot{\mathbf{c}}_{\frac{3}{2}},\ \dots\ ,\ \dot{\mathbf{q}}_{N_\mathrm{e}}, \mathbf{q}_{N_\mathrm{e}},\ \mathbf{c}_{N_\mathrm{e}+\frac{1}{2}}, \dot{\mathbf{c}}_{N_\mathrm{e}+\frac{1}{2}}\right)^\top. \tag{3.8}$$

Compared to other nonlinear differential equations ODEs are well understood and can be treated very efficient by optimized solvers to save computational time. Moreover, the present rod model is free of higher algebraic or transcendental functions which additionally reduces the computational effort [131]. As a result, it allows the simulation of multibody dynamics

with large numbers of rods, so that the model is well-suited for the specific requirements of the present FSI approach.
The time integration of system (3.8) can be done by an appropriate ODE-solver, adapted to the numerical properties of the ODE. Following recommendations of Lang et al. [131] the non-commercial solver RADAU5 [93, 91] is employed here for time integration. It is based on an implicit Runge-Kutta method of order 5 and is able to solve stiff problems. In principle, fully explicit solvers can be used as well, e.g. the non-commercial solver DOPRI5 [92, 91], provided the ODE has a moderate stiffness. In the present scenario, the numerical stiffness depends on the physical properties of the Cosserat rod and mainly is proportional to the rigidity of the rod and the speed of wave propagation. For rods of moderate stiffness focused here, RAUDAU5 turned out to be the best choice in terms of the computational effort.
To obtain the state vector $\mathbf{z}^{n+1}$ at the new time level $t^{n+1} = t^n + \Delta t$ from $\mathbf{z}^n$ at the previous time level t^n, the following system of equations is solved iteratively by RADAU5:

$$\tilde{\mathbf{z}}_i = \mathbf{z}^n + \Delta t \sum_{j=1}^{3} a_{ij}\, \mathbf{rhs}\left(\tilde{\mathbf{z}}_j,\, t^n + c_j \Delta t\right) \qquad \text{for} \quad i = 1,\, \ldots,3\,, \tag{3.9a}$$

$$\mathbf{z}^{n+1} = \mathbf{z}^n + \Delta t \sum_{j=1}^{3} b_j\, \mathbf{rhs}\left(\tilde{\mathbf{z}}_j,\, t^n + c_j \Delta t\right)\,, \tag{3.9b}$$

where the coefficients a_{ij}, b_j and c_j can be found in [93]. While computing, RADAU5 requires the Jacobian of the differential equation (3.8), i.e. $\mathbf{J} = \partial \mathbf{rhs}/\partial \mathbf{z}$, where an analytical derivation of $\mathbf{J}$ is laborious due to the nonlinear character of the rod equations (3.5). However, the RADAU5 package provides a FDM approximation of $\mathbf{J}$. It turned to be out, that this approximation performs very similarly to the analytical one and saves computational time in case of a fine spatial discretization of the rod, i.e. more degrees of freedom.
Successfully solving the differential equations (3.5) does not necessarily impose the constraint of unit length, i.e. $\|\mathbf{q}\| = 1$, required to describe rotations in space. As described in [131], the quaternion $\mathbf{q}$ drifts quadratically from this constraint which, however, can be counteracted by the projection

$$\mathbf{q} \leftarrow \mathbf{q}/\|\mathbf{q}\| \qquad \text{and} \qquad \dot{\mathbf{q}} \leftarrow \dot{\mathbf{q}} - (\mathbf{q}\cdot\dot{\mathbf{q}})\,\mathbf{q}\,, \tag{3.10}$$

applied after each time integration step for the entire set of quaternions $\mathbf{q}_e^{n+1}$, $e = 1, \ldots, N_\mathrm{e}$.

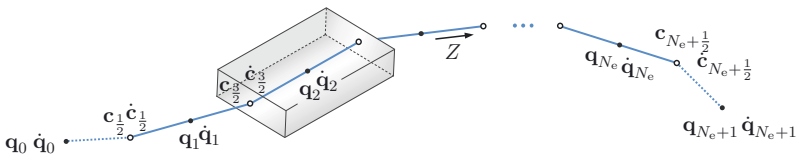

Figure 3.1: *Spatial discretization of the rod along the arc length Z by N_e elements of equal geometrical and material properties. Shown are discrete centroid positions $\mathbf{c}_{e-\frac{1}{2}}$ and velocities $\dot{\mathbf{c}}_{e-\frac{1}{2}}$, as well as the rotational degree of freedom represented by quaternions $\mathbf{q}_e$ and $\dot{\mathbf{q}}_e$, with $e = 1, \ldots, N_\mathrm{e}$. The dashed lines indicate the connection to ghost-quaternions $\mathbf{q}_0$ and $\mathbf{q}_{N_\mathrm{e}+1}$ and ghost-velocities $\dot{\mathbf{q}}_0$ and $\dot{\mathbf{q}}_{N_\mathrm{e}+1}$ required to impose the boundary conditions at both ends.*

3.3 Validation

The present fluid solver described in Section 3.1 was already employed and excessively validated in earlier works [118, 209, 211, 246]. Therefore, only the following validation case is presented here which covers the scope of applications focused in the present work, namely turbulent channel flows later interacting with highly flexible rods (see Chapter 6).
In terms of the validation of the structure solver, a huge amount of benchmark tests for the dynamic and static response of nonlinear rod models can be found in the literature. In this work three test configurations were selected, where one setup is used to validate the static response of the rod, the second test focuses on the application of co-rotating and fixed pressure loads, and the third test case captures the fully three-dimensional dynamic response of the rod. Supplementary validation studies are presented in Appendix A.

3.3.1 Turbulent channel flow

physical parameters:	
$\delta = 1\,\mathrm{m}$	channel half-width
$U = 1\,\mathrm{m/s}$	bulk velocity
$\nu_\mathrm{f} = 1.4531 \cdot 10^{-4}\,\mathrm{m^2/s}$	kinematic viscosity
dimensionless quantities:	
$Re_\delta = U\delta/\nu_\mathrm{f} \approx 6882$	Reynolds number
$Re_\tau = u_\tau\delta/\nu_\mathrm{f} \approx 395$	Reynolds number, based on friction vel. u_τ

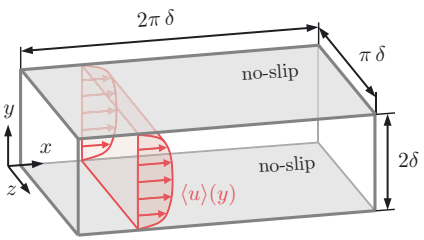

Figure 3.2: *Configuration of a turbulent channel flow driven by a spatially constant pressure gradient. In y-direction the channel is bounded by an upper and a lower no-slip wall, while the extension in streamwise and spanwise direction is assumed to be infinitely large. From a numerical point of view, this is approximated by periodic boundary conditions in x- and z-direction and a sufficiently large finite domain* $\Omega = [0; L_x] \times [0; L_y] \times [0; L_z]$ *with* $L_x = 2\pi\delta$, $L_y = 2\delta$ *and* $L_z = \pi\delta$, *so that statistical quantities are correctly covered [165], e.g. the time-averaged velocity profile* $\langle u \rangle(y)$.

Fig. 3.2 illustrates the configuration of a wall-bounded turbulent channel flow. Since the flow reveals a statistical stationarity and homogeneity in streamwise and spanwise direction the present validation is performed by means of temporally and spatially averaged quantities. These are the mean velocity profile $\langle u \rangle$ and relevant Reynolds stresses $\langle u'u' \rangle$, $\langle u'v' \rangle$ and $\langle w'w' \rangle$. The average of the fluid field $\langle \mathbf{u} \rangle = (\langle u \rangle, \langle v \rangle, \langle w \rangle)^\top$ is defined by

$$\langle \mathbf{u} \rangle(y) = \frac{1}{TL_zL_x} \int_0^T \int_0^{L_z} \int_0^{L_x} \mathbf{u}(\mathbf{x}, t)\ \mathrm{d}x\ \mathrm{d}z\ \mathrm{d}t\,, \tag{3.11}$$

where the velocity fluctuations $\mathbf{u}' = (u', v', w')^\top$ are obtained from the Reynolds decomposition of the instantaneous velocity field $\mathbf{u}$, i.e. $\mathbf{u} = \langle \mathbf{u} \rangle + \mathbf{u}'$. Velocities and Reynolds stresses labeled with a superscript $(.)^+$ are nondimensionalized with the friction velocity $u_\tau = \sqrt{\nu_\mathrm{f}\, \partial \langle u \rangle / \partial y\,|_{y=0}}$. In general, turbulent channel flows are fully characterized by one dimensionless quantity, usually given by the friction Reynolds number $Re_\tau = u_\tau\delta/\nu_\mathrm{f}$ or,

alternatively, by the bulk Reynolds number $Re_\delta = U\delta/\nu_\mathrm{f}$. Both are related via

$$Re_\delta = \int_0^{\delta^+ = Re_\tau} \langle u \rangle^+ \, \mathrm{d}y^+ \,, \tag{3.12}$$

with $y^+ = y\, u_\tau/\nu$ being the dimensionless wall coordinate, and $\delta^+ = y^+(y=\delta)$ the dimensionless channel width. In the present numerical approach a specific bulk Reynolds number $Re_\delta = U\delta/\nu$ is realized by a spatially constant but temporally variable volume force $\mathbf{f}_V = (f_V(t), 0, 0)^\top$ added to the momentum balance of the fluid (2.1a). By means of a PI-controller [118] the force $f_V(t)$ is dynamically adjusted to maintain a temporally constant bulk velocity

$$U = \int_\Omega u(\mathbf{x}, t) \, \mathrm{d}V = \text{const.} \,, \tag{3.13}$$

so that Re_δ is kept constant as well. Consequently, the friction velocity u_τ and the Reynolds number Re_τ are not adjusted and are a result of the simulation. Here, the reference simulation data of Moser et al. [165] at $Re_\tau = 392.24$ ($Re_\delta \approx 6682$) is used for validating the present fluid solver in both cases, a DNS and an LES.

In case of the DNS, the fluid domain Ω^f is discretized with $N_x \times N_y \times N_z = 256 \times 128 \times 256$ grid cells in x-, y- and z-direction, while the grid is refined towards the wall by means of a hyperbolic stretching in y-direction, i.e. $y_i = \delta\,\{1 - \tanh[\,\beta\,(1 - 2i/N_y)\,]/\tanh\beta\}$ with $i = 0, \ldots, N_y$. The stretching factor was chosen to be $\beta = 2$ which realizes a sufficiently fine resolution $y_1^+ \approx 1$ of the viscous sublayer. For the LES a much coarser grid is employed with $N_x \times N_y \times N_z = 64 \times 32 \times 64$, whereas the sublayer also is resolved with $y_1^+ \approx 1$, obtained for a stretching factor $\beta = 2.93$. The Smagorinsky constant is set to $C_s = 0.065$ as proposed in [77] for the present Re_τ. It is well known, that the standard Smagorinsky model causes non-physical values of the eddy viscosity ν_{sgs} in the near-wall region since the mean velocity gradient contributes to the eddy viscosity supposed to model turbulent fluctuations. For this reason, a Van Driest damping function $D(y^+) = 1 - \exp[-(y^+/25)^3]$ is applied which smoothly switches off ν_{sgs} near the wall [60]. Regarding the temporal discretization the time step size Δt is adjusted to realize a *CFL* number of 0.5 for both simulations. A physical time of 150 flow-through times $T_\mathrm{ft} = 2\pi\delta/U$ was simulated to reach statistical convergence of average quantities.

For $Re_\delta = 6882$ adjusted, the present DNS results in a friction Reynolds number of $Re_\tau \approx 390$ which is very close to the reference value of $Re_\tau \approx 392.24$ given by Moser *et al.* [165]. A slightly lower value of $Re_\tau \approx 380$ is computed by the LES. Fig. 3.3 presents the results of the averaged normalized velocity profile $\langle u \rangle^+$ and relevant normalized Reynolds stresses $\langle u'u' \rangle^+$, $\langle w'w' \rangle^+$ and $\langle u'v' \rangle^+$. Furthermore, the data is compared to the results obtained with a spectral method by Moser et al. [165], and compared to the data of Kawamura et al. [117, 1] which employed a second order finite-volume discretization. Obviously, the present DNS data nearly coincide with the results of Kawamura et al. [117, 1], while small differences occur in comparison to Moser *et al.* [165] for the peak region of $\langle u'u' \rangle^+$. Regarding the present LES the statistical data are represented sufficiently well, with slightly larger deviations in the peak region of $\langle u'u' \rangle^+$ and $\langle w'w' \rangle^+$. However, the much coarser discretization achieves a significant reduction of the computational effort to 0.3% of the effort required for the present DNS. In this context, the results obtained are very satisfactory.

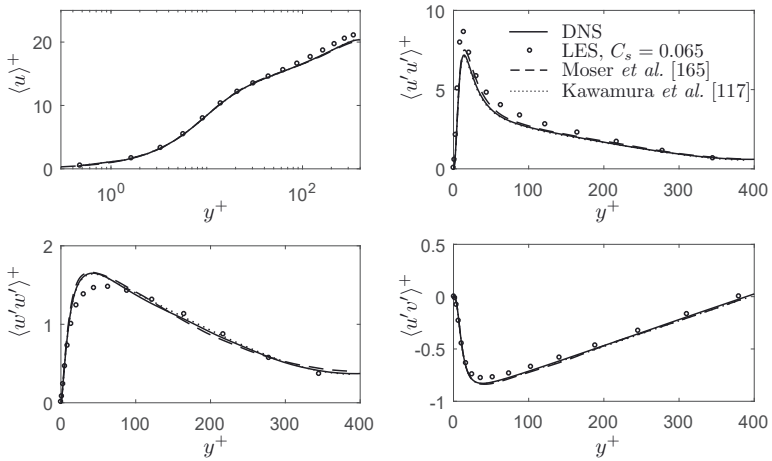

Figure 3.3: *Averaged normalized velocity profile* $\langle u \rangle^+$ *and relevant Reynolds stresses* $\langle u'u' \rangle^+$, $\langle w'w' \rangle^+$ *and* $\langle u'v' \rangle^+$ *at* $Re_\tau = 395$. *The present results of the DNS and the wall-resolving LES with a Smagorinsky constant of* $C_s = 0.065$ *are compared with the results obtained by Moser et al. [165] and the data of Kawamura et al. [117, 1].*

3.3.2 Cantilever subjected to a transversal load

$R = 1\,\mathrm{m}$	radial distance
$\phi = 45\,^\circ$	angle
$F = 0, 3, 6\,\mathrm{N}$	vertical loads
structure properties:	
$L = \pi/4\,\mathrm{m}$	rod length
$W = 0.01\,\mathrm{m}$	rod width (square)
$J = W^4/6$	polar moment
$E_\mathrm{s} = 10^9\,\mathrm{N/m^2}$	Young's modulus
$\nu_\mathrm{s} = 0$	Poisson's ratio

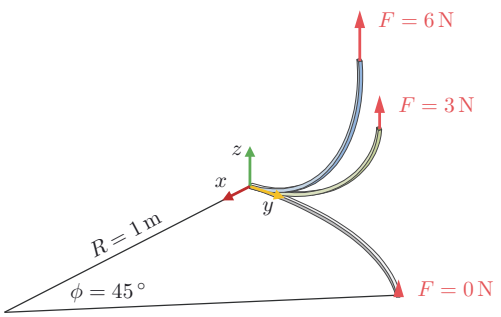

Figure 3.4: *Setup of the well-known configuration of a cantilever 45-degree bend proposed by Bathe and Bolourchi in 1979 [20]. The rod is clamped at one end and subjected to a transversal constant force* F *at the other end. Geometrical nonlinear effects yield a three-dimensional static response of the rod depending on the magnitude of* F *employed.*

The cantilever 45-degree bend scenario, proposed by Bathe and Bolourchi [20], is the most frequently applied setup used for benchmarking the three-dimensional static response of rod models. Furthermore, it is recommended by the National Agency for Finite Element Methods and Standards as a benchmark for geometric nonlinearities (NAFEMS, 3DNLG-5). As shown in Fig. 3.4 the initial shape of the rod is an arc of a circle of radius $R = 1\,\mathrm{m}$ located in the horizontal plane $z = 0$ of the global frame. Other geometrical and material properties of the

rod are provided in Fig. 3.4. At one end the rod is clamped to the plane $y = 0$ and is freely movable at the other end, while the free-end is subjected to a transversal tip force oriented in z-direction. Two different loads of constant magnitude $F = 3\,\mathrm{N}$ and $F = 6\,\mathrm{N}$ are employed in the present work, both yielding a different three-dimensional static equilibrium, as depicted in Fig. 3.4. Due to the curved rod shape all modes of deformation, i.e. extension, shear, bending and torsion, are geometrically nonlinear coupled resulting in a three-dimensional static response of the rod. The orientation of the tip cross section changes with increasing load while the force remains aligned in vertical direction of the global frame.
Since the present rod model is tailored for a dynamic response, a static equilibrium only can be obtained by introducing dissipative terms to the Cosserat rod equations. In principle, the internal viscous damping can be used for this purpose, but the equilibrium is reached more quickly with an external damping force $\overset{\triangledown}{\mathbf{f}} \propto -\dot{\mathbf{c}}$ and a damping moment $\overset{\triangledown}{\mathbf{m}} \propto -\dot{\mathbf{q}}$. Note, that the choice of the damping parameters affects the spatial path of the tip during deformation but does not change the static equilibrium. This confirms the path independence of the present rod model, as discussed by several authors [107, 202, 274]. Tab. 3.1 shows the equilibrium positions of the tip for different spatial resolutions of the rod, reaching from $N_\mathrm{e} = 8$ structural elements up to $N_\mathrm{e} = 256$. Already for a coarse resolution with 8 rod elements the deformation is captured very well and differs from the fine resolution with 256 by less than 1% for the loads applied here. Table 3.2 compares the converged results of the tip position to the values obtained by selected authors. Between the different numerical approaches, a slight variation of the solutions is observed with a maximum deviation of 2% from the averaged values. Compared to the other methods, the present results exhibit the smallest deviation from the mean values which is very satisfactory.

	$F = 3\,\mathrm{N}$			$F = 6\,\mathrm{N}$		
N_e	x_tip (cm)	y_tip (cm)	z_tip (cm)	x_tip (cm)	y_tip (cm)	z_tip (cm)
8	22.24	58.61	40.53	15.66	46.79	54.00
16	22.24	58.74	40.27	15.68	47.06	53.60
32	22.24	58.77	40.21	15.68	47.13	53.51
64	22.24	58.78	40.20	15.68	47.15	53.48
128	22.24	58.78	40.19	15.68	47.15	53.48
256	**22.24**	**58.78**	**40.19**	**15.68**	**47.15**	**53.48**

Table 3.1: *Numerical results of rod tip positions* $\mathbf{x}_\mathrm{tip} = (x_\mathrm{tip}, y_\mathrm{tip}, z_\mathrm{tip})^\top$ *for both employed magnitudes* $F = 3N$ *and* $F = 6N$ *as well as different spatial resolutions, i.e. number of structural elements* N_e.

	$F = 3\,\mathrm{N}$			$F = 6\,\mathrm{N}$		
	x_{tip} (cm)	y_{tip} (cm)	z_{tip} (cm)	x_{tip} (cm)	y_{tip} (cm)	z_{tip} (cm)
present ($N_{\mathrm{e}} = 256$)	**22.24**	**58.78**	**40.19**	**15.68**	**47.15**	**53.48**
Vetter et al. [256]	22.28	58.77	40.25	15.73	47.11	53.58
Li [141]	22.28	58.78	40.15	15.74	47.15	53.43
Zupan et al. [274]	22.28	58.78	40.16	15.74	47.15	53.43
Leung and Wong [137]	22.23	58.51	40.46	15.76	46.82	53.6
Li [140]	22.12	58.54	40.48	15.57	46.89	53.61
Rhim and Lee [200]	22.16	58.58	40.31	15.59	47.07	53.46
Crivelli and Felippa [49]	22.31	58.85	40.08	15.75	47.25	53.37
Lo [146]	22.3	58.8	40.1	15.8	47.2	53.4
Crisfield [48]	22.16	58.53	40.53	15.61	46.84	53.71
Sandhu *et al.* [206]	22.36	58.85	40.04	15.88	47.27	53.34
Cardona and Geradin [40]	22.14	58.64	40.35	15.55	47.04	53.50
Simo and Vu-Quoc [217]	22.33	58.84	40.08	15.79	47.23	53.37
Bathe and Bolourchi [20]	22.5	59.2	39.5	15.9	47.2	53.4
minimum value	22.12	58.51	39.5	15.55	46.82	53.34
maximum value	22.5	59.2	40.53	15.9	47.27	53.71
average value	**22.26**	**58.75**	**40.19**	**15.72**	**47.10**	**53.48**

Table 3.2: *Comparison of tip positions* $\mathbf{x}_{\mathrm{tip}} = (x_{\mathrm{tip}}, y_{\mathrm{tip}}, z_{\mathrm{tip}})^{\top}$ *at different loads* F*. The main part of the listed references was adopted from [256]. The present results exhibit the smallest deviation from the average values.*

3.3.3 Cantilever subjected to distributed loads

$F = 1, 3, \ldots, 25\,\mathrm{N}$	total load
$f = F/L$	distributed load
structure properties:	
$L = 0.5\,\mathrm{m}$	rod length
$W = 0.01\,\mathrm{m}$	rod width (square)
$E_{\mathrm{s}} = 1.2 \cdot 10^7\,\mathrm{N/m^2}$	Young's modulus
$\nu_{\mathrm{s}} = 0$	Poisson's ratio
dimensionless quantity:	
$FL^2/E_{\mathrm{s}}I = 1, 3, \ldots, 25$	load parameter

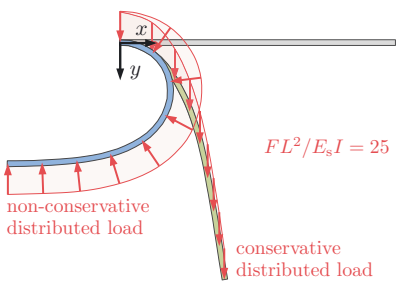

Figure 3.5: *Cantilever rod subjected to distributed conservative and non-conservative loads, as proposed by Kondoh and Atluri in 1987 [127]. For large load parameters* $FL^2/E_{\mathrm{s}}I$ *the deflection shapes are very different, as shown for* $FL^2/E_{\mathrm{s}}I = 25$*.*

The second test case shown in Fig. 3.5 is used to validate the response of the rod in terms of two different types of distributed loads, which are of crucial importance for fluid-structure interaction problems. The first load is spatially fixed and coincides with the y-direction in the present situation. The load acting on the rod is independent from the current deformation of

the rod and maintains its orientation. For example, this type of load is given by a gravitational load or buoyancy often considered in FSI problems. Furthermore, it counts to the conservative loads since the force distribution is expressible by a potential. The second type of distributed load is a non-conservative one, where its orientation depends on the current rod deformation. In this example, the force distribution remains locally perpendicular to the center line of the rod, such as a fluid pressure load acting on a structure in FSI problems. As stated in [140], for small loading parameters FL^2/E_sI the deflections are almost the same for conservative and non-conservative loads, while the deflections are very different for large FL^2/E_sI and, thus, large displacements. This emphasizes the importance of taking into account geometrically nonlinear effects in the rod model if large displacements are considered. The deformed shapes of the rod for a conservative and non-conservative load at a load parameter of value $FL^2/E_sI = 25$ are shown in Fig. 3.5. The tip position of the rod for various FL^2/E_sI and both load cases are given in Fig. 3.6. Furthermore, the results are compared to the original data of Kondoh and Atluri [127] and to a later simulation of Li [140]. Over the entire range of $FL^2/E_sI = 1, 3, ..., 25$ the present results are in very good accordance with the reference data.

load	conservative		non-conservative	
FL^2/E_sI	x_{tip}/L	y_{tip}/L	x_{tip}/L	y_{tip}/L
1	0.1251	0.9910	0.1241	0.9912
3	0.3622	0.9213	0.3411	0.9309
5	0.5628	0.7935	0.4976	0.8455
7	0.7121	0.6265	0.6031	0.7613
9	0.8049	0.4422	0.6745	0.6874
11	0.8451	0.2596	0.7243	0.6249
13	0.8420	0.9255	0.7603	0.5724
15	0.8071	-0.5085	0.7871	0.5281
17	0.7513	-0.1677	0.8077	0.4906
19	0.6840	-0.2585	0.8239	0.4584
21	0.6123	-0.3258	0.8370	0.4306
23	0.5411	-0.3731	0.8478	0.4064
25	0.4734	-0.4042	0.8568	0.3851

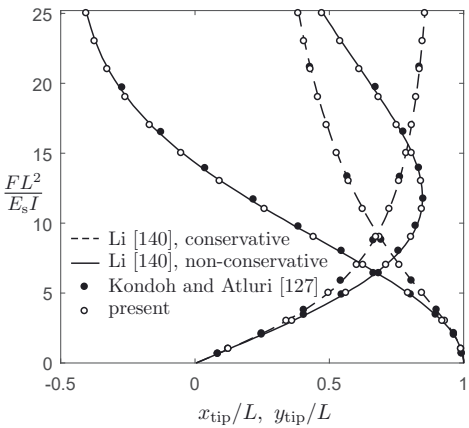

Figure 3.6: *Normalized tip positions of the rod* $\mathbf{x}_{tip}/L = (x_{tip}/L, y_{tip}/L)^\top$ *caused by a non-conservative and conservative distributed load of magnitude* FL^2/E_sI*. The present converged results, obtained with* $N_e = 256$*, are listed in the left table for selected load cases* FL^2/E_sI*. In the right graph, these results (black circle) are compared to the original data of Kondoh and Atluri [127] as well as to Li [140] which provided a continuous relation between the tip position and the load parameter (solid and dashed lines).*

3.3.4 Tumbling unconstrained rod

$L_x = 6\,\mathrm{m}$	horizontal distance
$L_z = 8\,\mathrm{m}$	vertical distance
$F(t) = 20\,\lambda(t)\,\mathrm{N}$	force along x-axis
$M_y(t) = 200\,\lambda(t)\,\mathrm{N}$	moment around z-axis
$M_z(t) = 100\,\lambda(t)\,\mathrm{N}$	moment around y-axis
structure properties:	
$L = 10\,\mathrm{m}$	rod length
inertia of cross section:	
$\rho_\mathrm{s} A = 1\,\mathrm{kg/m}$	
$\rho_\mathrm{s} I_\alpha = 10\,\mathrm{kg\,m}$	$\alpha = X, 2$
$\rho_\mathrm{s} J = 20\,\mathrm{kg\,m}$	
rigidities of cross section:	
$E_\mathrm{s} I_\alpha = G_\mathrm{s} J = 500\,\mathrm{Nm}^2$	*bending, torsion*
$E_\mathrm{s} A = G_\mathrm{s} J = 1 \cdot 10^4\,\mathrm{N}$	*extension, shear*

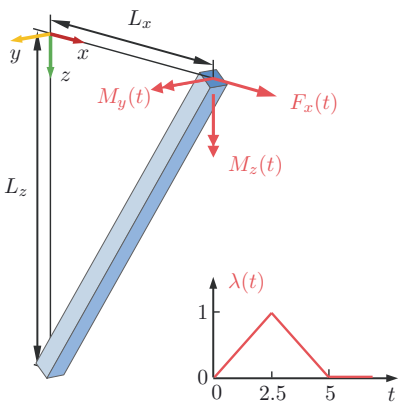

Figure 3.7: *Configuration of a spatially unconstrained flexible rod subjected to impulsive loads at one end, consisting of a conservative force $F_x(t)$ aligned in x-direction and two conservative moments M_y an M_z oriented along the y-direction and z-direction, respectively. The applied loads cause a complex three-dimensional dynamic response of the rod with large overall deflections. Note that gravitational effects are not considered in the present setup.*

The setup shown in Fig. 3.7 is used to demonstrate the ability of the rod model for the most complex situation of a dynamically three-dimensional response of the rod undergoing a large overall motion in space with a finite rod deformation. The problem first was proposed by Simo and Vu-Quoc in 1988 [218] and was employed to validate geometrically nonlinear rod models [259, 101, 99, 275, 216]. The initial condition is an unconstrained inclined rod positioned in the x-z plane. It is then subjected to a set of time dependent impulsive loads acting at one end of the rod, as depicted in Fig. 3.7. During the time interval $[0\,\mathrm{s}, 5\,\mathrm{s}]$, the force $F_x(t)$ causes a translational motion of the rod in x-direction, while the applied moment $M_y(t)$ yields a forward rotation around the y-axis. This planar motion is supplemented by an out-of plane motion induced by $M_z(t)$. At $t = 5\,\mathrm{s}$ the magnitude of the loads completely vanish and leave the rod in a three-dimensional motion, having certain similarities to a periodic "kayak-rowing" motion [218, 259], as illustrated in Fig. 3.8a. Since no internal or external viscous damping is considered in the present setup, the rod continues its motion without loss of energy, making the setup well-suited to test the long-term behavior of implemented rod models concerning the conservation of energy and momentum. As in the work of Simo *et al.* [216] this test was performed for the present implementation in a time interval of $[0\,\mathrm{s}, 500\,\mathrm{s}]$. Since the time integrator RADAU5 employed here is an energy conserving integration scheme, no loss of energy occurred during the simulation. Furthermore, the usage of quaternions for the rotational degree of freedom allows very large overall rotations of the rod without changing the properties of the numerical system, as already verified in [275].

The converged results of the center line of the rod, obtained with $N_e = 256$ and $\Delta t = 0.01\,\mathrm{s}$, are shown in Fig. 3.8 for selected instances in time. Furthermore, in Fig. 3.8b,c the deformed center lines are compared to the solutions of Hesse and Palacios [99] and Hsiao *et al.* [101], both are in very good agreement with the present results. While the results of Hesse and Palacios [99] coincide perfectly with the present observations, smaller deviations occur in comparison to Hsiao *et al.* [101]. A quantitative comparison to the original data published by Simo and Vu-Quoc [218] is not provided here since much larger deviations occur, which was already observed and reported by other authors [101, 99]. Hesse and Palacios [99] achieved a better match by increasing the torsional stiffness to $E_s I_\alpha = G_s J = 1 \cdot 10^3\,\mathrm{Nm}^2$, i.e. the rod appears to be much stiffer than the results presented.

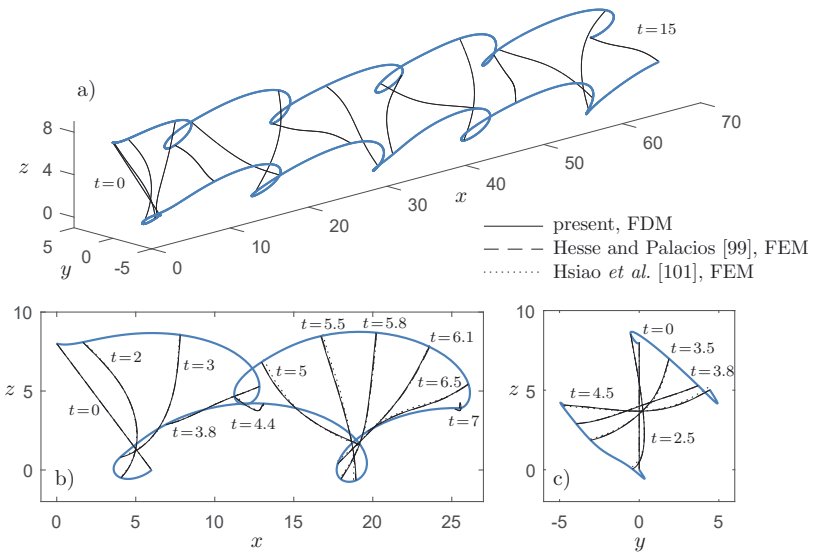

Figure 3.8: *Three-dimensional motion and deformation of the rod at selected times t. a) Perspective view of the center line of the rod (black lines) and trajectory of both rod ends (blue lines) as well as the corresponding projections b) on the $x-z$ plane and c) on the $y-z$ plane. The projection views provide a comparison of the present data to the results by Hesse and Palacios [99] and Hsiao et al. [101], both obtained with a finite element method. The converged results were obtained with $N_e = 256$ structural elements and a time step size of $\Delta t = 0.01\,\mathrm{s}$ as in [99].*

4 Numerical fluid-structure coupling

4.1 Fundamentals and state of the art

Clarification of terminology. During the last decades, various numerical approaches have been developed for the simulation of fluid-structure interactions, including the interaction with complex shaped rigid particles or flexible structures, e.g. rods, membranes, bubbles, etc. These numerical methods differ in the manner in which the fluid and the structure are coupled in time and space.

The *temporal coupling* can either be *monolithic*, defining a single discrete system comprising the fluid and the structure, or *partitioned*. With the partitioned approach, discrete equations for the fluid and the structure are solved separately and then coupled by an appropriate coupling algorithm. This strategy is versatile as it allows to use existing and optimized solvers. Hence, it is employed in most cases. The price to be paid is that the coupling can become unstable which requires substantial care and often generates problems. In this context, one can distinguish between *weak* and *strong* coupling strategies. With the former, also designated as *explicit* coupling schemes, the fluid and the structural part are solved once within each time step with an exchange of coupling quantities, such as the instantaneous fluid loads on the structure. This exchange is often performed in a sequential manner which allows a simple implementation. With this approach, however, it is not guaranteed that the kinematic and dynamic coupling condition at the interface are fulfilled accurately. In addition, weak coupling schemes become numerically unstable if structures are highly flexible and lightweight, so that the added mass effect of the fluid becomes important [73, 154]. Such kind of FSI problems strictly require a strong coupling strategy also termed implicit coupling. Then, the fluid and solid part are usually solved repeatedly, iterating within each time step until the coupling condition at the interface satisfies a certain convergence criterion. As demonstrated in the subsequent sections, an iterative procedure with a multiple exchange of the coupling quantities is not necessarily required to ensure numerical stability. However, some iteration between the fluid and structural part can achieve a more accurate satisfaction of the coupling conditions, comparable to monolithic FSI-methods.

In addition to the temporal coupling of the fluid and the structure part, both need to be spatially coupled at their common interface after discretization in space. The most common approach is to use a boundary fitted mesh to represent the structure within the fluid domain [261, 39, 97]. Here, the fluid and the structure grid share the same grid points at the fluid-structure interface, which enables a simple exchange of coupling quantities. As a result, however, the fluid grid has to be adjusted in time when structures move and deform in space. As an alternative to moving mesh techniques, approaches using a spatially uniform Eulerian background grid for the fluid part and a Lagrangian representation of the structures become increasingly popular [162, 222]. This is due to various advantages over moving mesh methods like algorithmic simplicity, higher efficiency of the background fluid solver, etc.

With a structure-independent, temporally constant fluid grid, the structures can be represented by various techniques, such as level-set (LS) methods [232, 47], volume-of-fluid (VOF) methods [100, 229, 183], phase field (PF) methods [5, 164] or immersed boundary methods [222, 239, 53, 125]. Especially for simulations of flow through or around complex mobile geometries, the immersed boundary method (IBM) has been applied with great success during the past decade. Closely related is the so-called fictitious domain method [87] which was developed within the FEM framework. As stated in [253], in the strong form the fictitious domain method does not differ from the immersed boundary method, but in the weak form when using an integral formulation of the FSI problem. Since these methods turned out to be well suited for scenarios with a large number of immersed mobile structures, e.g. particulate flows with thousands of particles [258, 121], the IBM approach is used in this work as well. This is reasonable, since the generation of an adapted grid is technically exceptionally difficult for scenarios with a large number of colliding slender structures considered here.

Immersed boundary methods for FSI problems. The IBM was originally introduced by Peskin [185, 186] for the simulation of blood flows in a beating heart. Later on, a variety of different IB approaches were developed in recent years differing in various technical aspects as reviewed in [162, 222]. IB methods share one property in common. While the fluid field is treated by an Eulerian description on a temporally constant grid, the immersed structures are described using a Lagrangian point of view. In the general case, the grids of the movable structures do not conform with the fixed grid of the fluid. At this point, the IBM offers a method to impose the coupling conditions (2.20), (2.18) on the fluid-structure interface Γ via an appropriate local (coupling) force $\mathbf{f}_\Gamma$ introduced into the momentum balance of the fluid and the structural equations of motion. From a numerical point of view, there are different approaches for the computation of this force, in which the various IBMs differ. Numerical stability and accuracy are decisive factors in this context.
Concerning the spatial imposition of the coupling conditions at the interface, IBMs are usually grouped into so-called *discrete forcing* schemes and *continuous forcing* schemes [162]. With the discrete forcing approach, the boundary conditions at the interface are imposed through the use of grid cells in the solid part. For each of these cells an interpolation scheme is derived that invokes the desired boundary condition at the interface [122, 162]. The treatment of zero-thickness structures with a discrete forcing requires special techniques [151]. In the continuous forcing approach, delta functions of compact support are used at the interface for the transfer of quantities between the fluid and the immersed structures. As described in the modeling Section 2.4, this approach is used in this work. A distinctive feature of a continuous forcing is, that the fluid-structure interface is represented by evenly distributed surface markers after spatial discretization of the physical problem [251, 119]. This avoids the identification of special grid points for the imposition of the coupling conditions, with the drawback that the interface is "smeared" over several cells of the fluid grid, typically three to four cells around each of the marker points. In this region the local coupling force is introduced in the momentum balance of the fluid to impose the no-slip condition at the fluid-structure interface. Due do its simplicity, stability and high efficiency, IBMs with continuous forcing are used preferably in large-scale simulations, e.g. disperse multiphase flows with rigid particles [258, 121] or bubbles [209].
Besides the different approaches used for the spatial coupling, the various IBMs differ in the manner in which the coupling force is computed in time, when a partitioned coupling approach is applied. Familiar techniques are *feedback forcing*, *discrete mass* and *momentum*

forcing as well as the so-called *direct forcing* [191]. The direct forcing approach is one of the most popular methods because of its increased stability.
In the literature several IB methods can be found, describing the fluid-structure interaction with movable rigid bodies, e.g. [86, 85, 119, 222, 126]. The description of classical fluid-structure interactions with elastic solid structures is less common, but has become increasingly important over the last decade. Most of these IBMs, however, were implemented and tested only with two-dimensional cases, e.g. in [10, 272, 269, 253, 201, 67, 255] without claim to completeness. Only few publications so far address truly three-dimensional scenarios. These can be divided into fluid-structure interactions with one-dimensional fiber-like structures [89, 31, 264], two-dimensional elastic membranes [134, 273, 263, 53] and volumetric elastic structures [271, 239, 125]. In some of these implementations, non-classical structure models are used, such as neutrally buoyant fibers and membranes in Le *et al.* [134], Griffith and Lim [89], Bhalla *et al.* [31] and Wiens and Stockie [263, 264], or a mass-spring network model in the work of de Tullio and Pascazio [53]. A classical continuum mechanical description of the structures was applied by Zhang *et al.* [271], Tian *et al.* [239], Zhu *et al.* [273] and recently by Kim *et al.* [125]. The methods mentioned, including IBMs for two-dimensional problems, are based on different coupling algorithms. Besides a few monolithic schemes [10, 253, 201, 255], most of the implementations are realized by means of a partitioned coupling approach. The latter range from non-iterative coupling schemes [272, 271, 269, 89, 67, 273, 263] and iterative strong coupling approaches [31, 239, 53], to improved non-iterative schemes with extended numerical stability [134, 125]. Sotiropoulos and Yang [222] provided a comprehensive overview of various IB approaches for the simulation of general FSI problems distinguishing between weak and strong coupling strategies. To the knowledge of the author, so far, no monolithic IBM has been developed for three-dimensional FSI problems with elastic solid structures.

Proposed coupling approach. The IBM developed in this work can be assigned to the group of IBMs with continuous direct forcing. A special component of this coupling scheme is a novel non-iterative semi-implicit direct forcing which combines the stability of monolithic methods with the advantages of partitioned weak approaches, mentioned above. Moreover, it concerns a general coupling strategy which enables the coupling of the Navier-Stokes equations with an arbitrary immersed structure, demonstrated for Cosserat rods here.
In contrast to other non-iterative coupling strategies, the main idea is not based on a stabilization technique, e.g. a relaxation technique [239, 53, 125], but on a semi-implicit time scheme for the structure motion. As a matter of fact, the coupling terms used to impose the coupling conditions, require some kind of implicit integration in time to ensure numerical stability [68]. It is shown here, that this is not only feasible by means of a global iteration between the fluid and structure part, but can also be achieved by an implicit integration of the coupling terms in the structure equations once per time step. These coupling terms are provided in a temporally continuous form enabling to solve the coupled structure equations by an arbitrary implicit time integration scheme. As a result, the coupling becomes independent of the discretization techniques employed for both subsolvers, which underlines the generality of the coupling strategy. It is referred to as semi-implicit coupling here, since only those coupling quantities are treated implicitly which have an effect on the stability of the time integration. Excluded from this are the structure positions constituting the fluid-structure interface Γ, which is treated fully explicitly in time. This minimizes an exchange of coupling quantities in one time step and reduces the overall computational time. The scheme developed is completely non-iterative and requires only a single bidirectional exchange of coupling

quantities between the fluid solver and the structure solver. A disadvantage resulting from this is a first-order accuracy of the coupling terms in time. However, for time step sizes at $CFL \approx 0.5$ usually employed in this work, the resulting errors remain reasonably small.

4.2 Temporal coupling using direct forcing

4.2.1 The direct forcing approach

Different variants of the immersed boundary method can be distinguished by the way in which the coupling force $\mathbf{f}_\Gamma$ in Eq. (2.1a) is computed. As already mentioned, a spatially continuous force $\mathbf{f}_\Gamma$, acting in an infinitesimally thin layer Λ (Fig. 2.4), is employed in the present work to impose the kinematic and dynamic coupling condition. In the IBM framework this approach is usually denoted as continuous forcing [162]. From a numerical point of view two aspects are decisive. First, the local force has to be evaluated in a time discrete manner to realize a coupling of fluid and structures, called temporal coupling here. Second, an appropriate approach is required for a spatial transfer of information between the fluid and the structure, each discretized in a different manner. While the temporal coupling is described in this section, the next section focuses on the spatial coupling. Finally, both approaches for temporal and spatial coupling are combined in Section 4.4, thus providing the complete coupling algorithm.

In the present work, the temporal coupling is realized by the direct forcing approach [163, 64, 251]. The basic idea of this approach is to incorporate the no-slip condition on Γ at a time discrete level to determine the coupling force within a certain time interval $t \in [t^n, t^{n+1}]$. According to the momentum balance (2.1a) the coupling force at $\mathbf{x} \in \Gamma$ is

$$\mathbf{f}_\Gamma = \frac{\partial \mathbf{u}}{\partial t} - \mathbf{rhs}\,, \tag{4.1}$$

where the right hand-side **rhs** includes the convective, pressure and viscous terms. The coupling force can then be obtained by integrating Eq. (4.1) with an arbitrary time-stepping scheme over the time interval $t \in [t^n, t^{n+1}]$, i.e.

$$\int_{t^n}^{t^{n+1}} \mathbf{f}_\Gamma \,\mathrm{d}t = \int_{t^n}^{t^{n+1}} \left(\frac{\partial \mathbf{u}}{\partial t} - \mathbf{rhs} \right) \mathrm{d}t = \mathbf{u}^{n+1} - \mathbf{u}^n - \int_{t^n}^{t^{n+1}} \mathbf{rhs} \,\mathrm{d}t\,, \tag{4.2}$$

with $\mathbf{u}^n$ and $\mathbf{u}^{n+1}$ being the fluid velocities at time level t^n and t^{n+1}, respectively. By incorporating the no-slip condition (2.20), $\mathbf{u}^{n+1}$ is replaced by the local desired velocity $\mathbf{u}_\Gamma^{n+1}$ of the interface Γ, yielding

$$\int_{t^n}^{t^{n+1}} \mathbf{f}_\Gamma \,\mathrm{d}t = \mathbf{u}_\Gamma^{n+1} - \mathbf{u}^n - \int_{t^n}^{t^{n+1}} \mathbf{rhs} \,\mathrm{d}t \qquad \forall\, \mathbf{x} \in \Lambda\,, \tag{4.3}$$

while $\mathbf{f}_\Gamma$ vanishes at locations $\mathbf{x} \notin \Lambda$. In the literature, this equation is usually converted into

$$\bar{\mathbf{f}}_\Gamma = \frac{1}{\Delta t} \int_{t^n}^{t^{n+1}} \mathbf{f}_\Gamma \,\mathrm{d}t = \frac{\mathbf{u}_\Gamma^{n+1} - \tilde{\mathbf{u}}}{\Delta t}\,, \tag{4.4}$$

where $\overline{\mathbf{f}}_\Gamma$ is the average coupling force applied over the time interval $t \in [t^n, t^{n+1}]$ and $\tilde{\mathbf{u}}$ is a shorthand for

$$\tilde{\mathbf{u}} = \mathbf{u}^n + \int_{t^n}^{t^{n+1}} \mathbf{rhs}\, \mathrm{d}t\,, \tag{4.5}$$

which is the preliminary velocity of the fluid obtained without accounting for the effect of the immersed boundary.

4.2.2 Modified equation of motion

As described in Section 2.4.1, the fluid-structure coupling is accomplished by two conditions, the kinematic coupling condition (2.20) and the dynamic coupling condition (2.18). Using the direct forcing method, the former is incorporated directly into the coupling force $\mathbf{f}_\Gamma$ imposing the no-slip condition in the fluid field, i.e. $\mathbf{u} = \mathbf{u}_\Gamma$ at $\mathbf{x} \in \Gamma$. In accordance with the dynamic coupling condition and the principle of *actio et reactio*, the coupling force $\mathbf{f}_\Gamma$ also appears in the equation of motion of the immersed boundary Γ. As a result, the motion of Γ and the coupling force (4.4) exhibit an implicit dependency, since $\mathbf{f}_\Gamma$ is a function of $\mathbf{u}_\Gamma^{n+1}$ at the new time level t^{n+1}. This becomes clearer when considering a general motion of Γ described by the differential equation

$$\dot{\mathbf{u}}_\Gamma = \mathbf{rhs}_\Gamma(\mathbf{u}_\Gamma, t) + \mathbf{f}_\Gamma \qquad \forall \mathbf{x} \in \Gamma, \tag{4.6}$$

with the right-hand side $\mathbf{rhs}_\Gamma$ describing the unconstrained motion of Γ. After time integration and under consideration of Eq. (4.4) the discrete motion is given by

$$\mathbf{u}_\Gamma^{n+1} = \mathbf{u}_\Gamma^n + \int_{t^n}^{t^{n+1}} \mathbf{rhs}_\Gamma(\mathbf{u}_\Gamma, t)\, \mathrm{d}t \;+\; \Delta t\, \overline{\mathbf{f}}_\Gamma(\mathbf{u}_\Gamma^{n+1}, \tilde{\mathbf{u}})\,. \tag{4.7}$$

Since the right-hand side depends on $\mathbf{u}_\Gamma^{n+1}$, this equation has to be solved implicitly in time with an appropriate time integrator. When using particular libraries, ODE integrators usually only provide an interface to the continuous version of the differential equation, e.g. $\dot{\mathbf{u}}_\Gamma = \mathbf{rhs}_\Gamma(\mathbf{u}_\Gamma, t)$, and not an already discrete version as given by Eq. (4.7). The user simply has to provide a continuous function of $\mathbf{rhs}_\Gamma(\mathbf{u}_\Gamma, t)$ to the solver while using it as a black-box without specific technical knowledge of the discretization scheme employed. To realize the direct forcing approach with a standard black-box ODE solver, a continuous version of Eq. (4.7) is required. While $\mathbf{rhs}_\Gamma(\mathbf{u}_\Gamma, t)$ is already known, the coupling force needs to be reformulated as $\mathbf{f}_\Gamma(\mathbf{u}_\Gamma, t)$ that continuously depends on time and on the interface velocity. Doing so, Eq. (4.7) can be expressed as a modified equation of motion of Γ

$$\dot{\mathbf{u}}_\Gamma = \mathbf{rhs}_\Gamma(\mathbf{u}_\Gamma, t) + \mathbf{f}_\Gamma(\mathbf{u}_\Gamma, t) \;=\; \mathbf{rhs}_{\Gamma,\mathrm{mod}}(\mathbf{u}_\Gamma, t)\,, \tag{4.8}$$

which can simply be passed to an arbitrary implicit ODE solver without need of knowledge about the time discretization technique. In the present work, the continuous variant of the coupling force is obtained by considering a linear behavior of the interface velocity within the given time interval, i.e.

$$\mathbf{u}_{\Gamma,\mathrm{lin}}(t) = \left(\mathbf{u}_\Gamma^{n+1} - \mathbf{u}_\Gamma^n\right) \frac{t - t^n}{\Delta t} + \mathbf{u}_\Gamma^n\,, \tag{4.9}$$

which can be rearranged into

$$\mathbf{u}_\Gamma^{n+1} = (\mathbf{u}_{\Gamma,\mathrm{lin}} - \mathbf{u}_\Gamma^n)\,\frac{\Delta t}{t - t^n} + \mathbf{u}_\Gamma^n\,, \tag{4.10}$$

such that the interface velocity at the new time level t^{n+1} is provided as a continuous function $\mathbf{u}_\Gamma^{n+1} = \mathbf{u}_\Gamma^{n+1}(\mathbf{u}_\Gamma, t)$. Using this formulation in combination with the direct forcing approach (4.4), the coupling force can be approximated by

$$\mathbf{f}_{\Gamma,\mathrm{lin}}(\mathbf{u}_\Gamma, t) = \frac{\mathbf{u}_\Gamma - \mathbf{u}_\Gamma^n}{t - t^n} + \frac{\mathbf{u}_\Gamma^n - \tilde{\mathbf{u}}}{\Delta t}\,. \tag{4.11}$$

As a crosscheck, the time integration of $\mathbf{f}_{\Gamma,\mathrm{lin}}$ for a linear slope of $\mathbf{u}_\Gamma(t) = \mathbf{u}_{\Gamma,\mathrm{lin}}(t)$ yields

$$\frac{1}{\Delta t}\int_{t^n}^{t^{n+1}} \mathbf{f}_{\Gamma,\mathrm{lin}}(\mathbf{u}_{\Gamma,\mathrm{lin}}, t)\;\mathrm{d}t \;=\; \bar{\mathbf{f}}_\Gamma = \frac{\mathbf{u}_\Gamma^{n+1} - \tilde{\mathbf{u}}}{\Delta t} \tag{4.12}$$

and, thus, reproduces the common direct forcing according to Eq. (4.4). Since the preliminary velocity $\tilde{\mathbf{u}}$ in $\mathbf{f}_{\Gamma,\mathrm{lin}}(\mathbf{u}_\Gamma, t)$ is computed for a particular time step Δt, the coupling force as well as the corresponding modified right-hand side of Eq. (4.8) is valid only for a specific time interval $t \in [t^n, t^{n+1}]$.
In general, the modified equations of motion (4.8) can be formulated for any kind of immersed boundaries, ranging from rigid bodies to deformable structures, by adding the continuous version of the coupling force $\mathbf{f}_{\Gamma,\mathrm{lin}}(\mathbf{u}_\Gamma, t)$ to the ODE describing the decoupled motion of Γ.

Application to Cosserat rod equations. In the present context, the motion of the immersed boundary Γ is described by the Cosserat rod equations (2.13) that contain external fluid forces $\overset{\triangledown}{\mathbf{f}}_\Gamma$ and external fluid moments $\overset{\triangledown}{\mathbf{m}}_\Gamma$, both related to the coupling force $\mathbf{f}_\Gamma$ via Eqs. (2.32a) and (2.32b), respectively. To apply the "black-box" technique via $\mathbf{f}_{\Gamma,\mathrm{lin}}$ just mentioned, the dependency of $\mathbf{u}_\Gamma$ in Eq. (4.11) must be expressed in terms of velocity quantities provided by the Cosserat rod, i.e. the linear velocity of the center line $\dot{\mathbf{c}}$ and the angular velocities represented by the quaternionic velocity $\dot{\mathbf{q}}$. According to the no-slip condition (2.21) the velocity at the interface Γ is given by

$$\mathbf{u}_\Gamma = \dot{\mathbf{c}} + \boldsymbol{\omega} \times \boldsymbol{\xi} \tag{4.13a}$$

$$\phantom{\mathbf{u}_\Gamma} = \dot{\mathbf{c}} + (2\,\dot{\mathbf{q}} * \overline{\mathbf{q}}) \times (\mathbf{q} * \boldsymbol{\xi}_0 * \overline{\mathbf{q}})\;, \tag{4.13b}$$

where in the second variant (4.13b) the angular velocity is expressed by means of quaternions via $\boldsymbol{\omega} = 2\,\dot{\mathbf{q}} * \overline{\mathbf{q}}$. Furthermore, the vector $\boldsymbol{\xi}$ can be rotated backwards into the local frame, so that $\boldsymbol{\xi} = \mathbf{q} * \boldsymbol{\xi}_0 * \overline{\mathbf{q}}$. Since $\boldsymbol{\xi}_0$ in the local reference frame is time-independent, the continuous coupling force (4.11) can be expressed as $\mathbf{f}_{\Gamma,\mathrm{lin}}(\dot{\mathbf{c}}, \dot{\mathbf{q}}, \mathbf{q}, t)$. Using this force, the related external fluid forces $\overset{\triangledown}{\mathbf{f}}_\Gamma$ (2.32a) and moments $\overset{\triangledown}{\mathbf{m}}_\Gamma$ (2.32b) can be approximated by

$$\int_\zeta \overset{\triangledown}{\mathbf{f}}_\Gamma\;\mathrm{d}Z \approx -\int_\Lambda \rho_\mathrm{f}\,\mathbf{f}_{\Gamma,\mathrm{lin}}(\dot{\mathbf{c}}, \dot{\mathbf{q}}, \mathbf{q}, t)\;\mathrm{d}V \tag{4.14a}$$

$$\int_\zeta \overset{\triangledown}{\mathbf{m}}_\Gamma\;\mathrm{d}Z \approx -\int_\Lambda \boldsymbol{\xi} \times \left[\rho_\mathrm{f}\,\mathbf{f}_{\Gamma,\mathrm{lin}}(\dot{\mathbf{c}}, \dot{\mathbf{q}}, \mathbf{q}, t)\right]\mathrm{d}V \tag{4.14b}$$

in the time interval $t \in [t^n, t^{n+1}]$.

4.2.3 Resulting coupling scheme

The modified direct forcing approach proposed in the previous Section can be summarized by the following steps:

1. Computation of the preliminary velocity $\tilde{\mathbf{u}}$ via Eq. (4.5) without accounting for any coupling to the immersed interface Γ.
2. Communication of the preliminary velocity $\tilde{\mathbf{u}}(\mathbf{x})$ at $\mathbf{x} \in \Gamma$ to the structure solver.
3. Computation of the interface velocity $\mathbf{u}_\Gamma^{n+1}$ at the new time level t^{n+1} by solving the equation of motion (4.8) implicitly, modified by the coupling force $\mathbf{f}_{\Gamma,\mathrm{lin}}$ (4.11).
4. Determination of the coupling force $\overline{\mathbf{f}}_\Gamma(\mathbf{x})$ at $\mathbf{x} \in \Gamma$ via Eq. (4.4) and communication of $\overline{\mathbf{f}}_\Gamma$ to the fluid solver.
5. Solving the Navier-Stokes equations (2.1) coupled to the immersed boundary Γ by $\overline{\mathbf{f}}_\Gamma$.

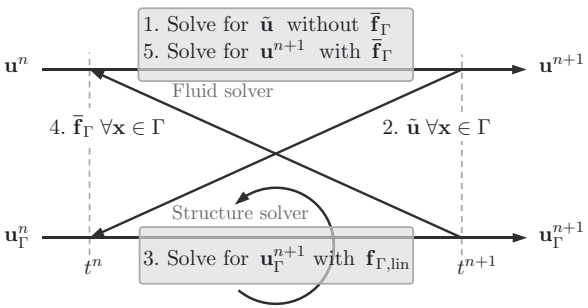

Figure 4.1: *Flowchart of the five steps to be performed for the temporal coupling of the fluid solver and the structure solver within one time step $t \in [t^n, t^{n+1}]$ by means of the direct forcing approach proposed here. The circular arrow illustrates the implicit nature of the solution procedure employed to solve for the structure motion.*

The implicit treatment of the modified equation of motion of the structure in step 3 corresponds to a strong coupling of fluid and structure and achieves numerical stability for arbitrary immersed objects. It can be solved by an iterative procedure, e.g. a Newton method or an implicit Runge-Kutta scheme, such as RADAU5 employed in the present work. As an alternative to an implicit treatment, the modified equations could be treated by an explicit integration scheme as well. When integrating the continuous coupling force $\mathbf{f}_\Gamma(\mathbf{u}_\Gamma, t)$ according to Eq. (4.11) with an explicit Euler scheme, e.g., it simplifies to

$$\frac{1}{\Delta t}\int_{t^n}^{t^{n+1}} \mathbf{f}_{\Gamma,\mathrm{lin}}(\mathbf{u}_{\Gamma,\mathrm{lin}}, t)\,\mathrm{d}t \quad \approx \quad \mathbf{f}_{\Gamma,\mathrm{lin}}(\mathbf{u}_{\Gamma,\mathrm{lin}}^n, t^n) = \frac{\mathbf{u}_\Gamma^n - \tilde{\mathbf{u}}}{\Delta t}\,. \tag{4.15}$$

Obviously, in contrast to the exact direct forcing (4.4), it is based on employing the interface velocity at the old time t^{n-1}. In this case the forcing scheme is equal to the well-known variants of an explicit IBM, proposed e.g. in [251, 119, 35]. It is known that these variants become

unstable, especially for lightweight immersed objects [119]. In addition, as demonstrated in previous works [246, 247], replacing $\mathbf{u}_\Gamma^{n+1}$ with $\mathbf{u}_\Gamma^n$ may result in a numerically inconsistent coupling, where the numerical solution does not converge to the monolithic solution by a spatial and temporal refinement. The solution only coincides with the monolithic solution if the mass ratio between the structure mass and the mass of the surrounding fluid layer Λ tends to infinity. However, for sufficiently large mass ratios the numerical error remains very small. For practical applications, the explicit direct forcing, based on $\mathbf{u}_\Gamma^n$, does not constitute any advantage over the present scheme in terms of implementation effort, numerical efficiency and accuracy. In other words, the present scheme combines the stability properties of strong coupling schemes with the efficiency and ease of implementation of weak coupling schemes.
The direct forcing scheme proposed here is derived for a spatially continuous configuration, sketched in Fig. 2.3. As a result, it is not restricted to immersed boundary methods and, in principle, can be applied to any other method, e.g. adapted mesh methods, where a no-slip constraint has to be imposed on the velocity field. The spatial discretization is an additional aspect of the coupling scheme which is discussed in the following section.

4.3 Spatial coupling via marker points

4.3.1 Lagrangian markers and volumes

In the framework of common IBMs the discrete elements of the structures do not coincide with the points of the Eulerian grid of the fluid. Hence, their coupling requires some technique to transfer information between both discrete representations. For this purpose, each zero-thickness rod is represented here by a set of discrete markers, so-called Lagrangian points, implementing this communication. The Lagrangian points $\mathbf{x}_l$ are evenly distributed over the fluid-structure interface Γ, as shown exemplarily for one structural rod element in Fig. 4.3. Furthermore, a two-dimensional sketch of the discretization of a rod embedded in the Eulerian background grid is shown in Fig. 4.2. As described in Section 2.4.3, the fluid-structure

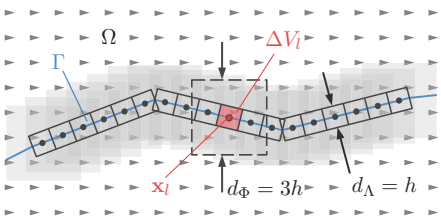

Figure 4.2: *Sketch of the spatial discretization employed by the immersed boundary method. The rod is represented by Lagrangian points $\mathbf{x}_l$. Each point is attributed a Lagrangian volume ΔV_l centered around $\mathbf{x}_l$. The union of all volumes constitutes a layer Λ of width $d_\Lambda = h$. The connection between the Lagrangian points $\mathbf{x}_l$ and the Eulerian grid $\mathbf{x}_{ijk}$ is realized by regularized delta functions, described below. The gray shaded area displays the cumulative spatial influence of all delta functions, one applied at each marker point. The dashed line represents the area of impact in the velocity field when the three-point delta function of Roma et al. [203] is employed. Note, that only the staggered grid for the velocity component u is shown to simplify the graphical exposition.*

coupling is realized by a distributive coupling force $\mathbf{f}_\Gamma$ acting in a small layer Λ around the interface Γ. While in the continuous formulation of the coupling force (2.30) the support of the corresponding delta function δ_V is infinitesimally small, i.e. $d_\Lambda \to 0$, in the discrete realization the thickness of the layer Λ has to be equal to the step size of the Eulerian grid, i.e. $d_\Lambda = h$. Hence, at least one marker point controls a volume equal to the volume of a fluid cell [251]. This means that each Lagrangian volume ΔV_l, associated to a marker point, has to be chosen smaller or equal to the size of the Eulerian fluid cells, i.e.

$$\Delta V_l = \Delta S_l \, h \leq h^3 \,, \tag{4.16}$$

where ΔS_l is the corresponding surface area attributed to a particular marker point. The volume of the entire layer, as the sum of all volumes ΔV_l, fulfills the condition

$$\sum_l \Delta V_l = S_\Gamma \, h \,, \tag{4.17}$$

with the surface area of the rod $S_\Gamma = \int_\Gamma \mathrm{d}S = \sum_l \Delta S_l$. Concerning Eq. (4.16) the corresponding number of Lagrangian marker points has to be $N_l \geq S_\Gamma / h^2$.

4.3.2 Regularized delta functions

In the general case, especially when rods are deformed, the Lagrangian points $\mathbf{x}_l$ on a rod and the Eulerian grid points $\mathbf{x}_{ijk}$, where the fluid motion is computed, do not coincide. Then a transfer of information is performed via a weighted sum of regularized delta functions δ_h. As common for the present type of IBM the three-dimensional function δ_h is generated by a tensor product of three one-dimensional functions δ_h^{1D}, so that

$$\delta_h(\mathbf{r}) \;=\; \delta_h^{\mathrm{1D}}(r_x) \;\, \delta_h^{\mathrm{1D}}(r_y) \;\, \delta_h^{\mathrm{1D}}(r_z) \tag{4.18}$$

with the distance vector $\mathbf{r} = (r_x, r_y, r_z)^\top = \mathbf{x}_l - \mathbf{x}_{ijk}$ between a Lagrangian marker and an Eulerian grid point. Furthermore, $\delta_h^{\mathrm{1D}}(r_x) = \Phi(r)/h$ and $r = r_x/h$, etc. The continuous function Φ is constructed so as to fulfill certain properties, e.g. moment conditions [186]. In Section 4.5, two frequently used delta functions are compared and tested for their suitability for the present IBM dealing with infinitely thin structures. The properties of various delta functions of different width and smoothness were studied by Yang *et al.* [268]. Here, the three-point version of Roma et al. [203]

$$\Phi_3(r) = \begin{cases} \frac{1}{6}\left(5 - 3|r| - \sqrt{-3(1-|r|)^2+1}\right) & , \, 0.5 \leq |r| \leq 1.5 \\ \frac{1}{3}\left(1 + \sqrt{-3|r|^2+1}\right) & , \, |r| < 0.5 \\ 0 & , \, \text{otherwise} \end{cases} \tag{4.19}$$

is employed, so that Φ_3 has a width of $d_\Phi = 3h$ as sketched in Fig. 4.2. This ensures a good balance between numerical efficiency and smoothing properties [119].
With the help of this delta function a transfer of an arbitrary vector quantity $\boldsymbol{\varphi}$ from the

Eulerian points $\mathbf{x}_{ijk}$ to the Lagrangian points $\mathbf{x}_l$ is accomplished by an interpolation via

$$\boldsymbol{\varphi}(\mathbf{x}_l) = \sum_{i=1}^{N_x} \sum_{j=1}^{N_y} \sum_{k=1}^{N_z} \boldsymbol{\varphi}(\mathbf{x}_{ijk})\, \delta_h(\mathbf{x}_{ijk} - \mathbf{x}_l)\, h^3\,, \tag{4.20}$$

e.g. to provide fluid velocities at the location of the interface Γ. The complementary operation is a transfer from Lagrangian to Eulerian points, often called spreading or regularization. It is defined by

$$\boldsymbol{\varphi}(\mathbf{x}_{ijk}) = \sum_{\mathbf{x}_l \in \Gamma_e} \boldsymbol{\varphi}(\mathbf{x}_l)\, \delta_h(\mathbf{x}_{ijk} - \mathbf{x}_l)\, \Delta V_l \tag{4.21}$$

and is commonly used to distribute the coupling force $\mathbf{f}_\Gamma$ to the Eulerian grid of the fluid, as described in Section 4.4 below.
Recognize, that the width of the regularized delta function d_Φ introduced in this section, and the thickness of the Lagrangian layer d_Λ of the previous section are two different aspects of the discretization scheme. The width d_Λ is required for the definition of appropriate forcing volumes ΔV_l associated to each forcing point. From a numerical point of view, this is the discrete realization of the support of the delta function δ_V in the continuous formulation of coupling force (2.30), and is uniquely defined by the discretization of the Eulerian grid. The second width d_Φ is an independent parameter and can be chosen "arbitrarily" by selecting a certain regularized delta function. It can be interpreted as the width of regularization regarding the spreading operation that serves to transfer momentum from the Lagrangian points to the Eulerian points. Due to the distributive nature of the momentum source $\mathbf{f}_\Gamma$ some regularization reduces or avoids jumps of $\mathbf{f}_\Gamma$ on the Eulerian grid and, thus, prevents numerical oscillations. Usually, interpolation and spreading are performed with the same delta function of width d_Φ, as it is the case in the present work.

4.4 Proposed coupling algorithm

Both approaches for temporal and spatial coupling of the Navier-Stokes equations (2.1) and the Cosserat rod equations (2.13) are now combined to a partitioned solution approach. It is realized in a fully explicit manner, which is exempt from any global iteration between the fluid part and the structure part. Analogous to Section 4.2.3, the coupling scheme consists of the following five steps executed once in each Runge-Kutta sub-step r. A compact overview of the proposed FSI scheme is provided in Appendix D.

1. Computation and interpolation of preliminary velocities. First, the preliminary velocity field $\tilde{\mathbf{u}}(\mathbf{x}_{ijk})$ is computed on the Eulerian grid points $\mathbf{x}_{ijk}$, according to Eqs. (4.5) and (3.1a) using the Runge-Kutta scheme applied here. Thereafter, the values $\tilde{\mathbf{u}}(\mathbf{x}_l^{r-1})$ located at the Lagrangian marker points of the previous time level $\mathbf{x}_l^{r-1}$ (Fig. 4.3) are interpolated from the Eulerian grid points $\mathbf{x}_{ijk}$ according to Eq. (4.20), so that

$$\tilde{\mathbf{u}}(\mathbf{x}_l^{r-1}) = \sum_{i=1}^{N_x} \sum_{j=1}^{N_y} \sum_{k=1}^{N_z} \tilde{\mathbf{u}}(\mathbf{x}_{ijk})\, \delta_h(\mathbf{x}_{ijk} - \mathbf{x}_l^{r-1})\, h^3\,. \tag{4.22}$$

2. Communication of preliminary quantities to the structure solver. According to the direct forcing approach described in Section 4.2, the values $\tilde{\mathbf{u}}$ on Γ are used to determine the coupling force $\mathbf{f}_\Gamma$ and thus are required to compute the fluid loads $\overset{\triangledown}{\mathbf{f}}_\Gamma$, $\overset{\triangledown}{\mathbf{m}}_\Gamma$ acting on the rod during motion. Therefore, the velocities $\tilde{\mathbf{u}}(\mathbf{x}_l^r)$ for N_l marker points need to be transferred to the corresponding structure solver. In order to realize a coupling to Cosserat rods these can be replaced by integral quantities $\tilde{\mathbf{p}}_e$, $\tilde{\mathbf{l}}_e$ (see Eqs. (4.24b) and (4.25b) below) for each rod element e. This drastically reduces the communication effort between the fluid and structure solver to 6 values per element, i.e. $6N_\mathrm{e}$ per rod in total.

3. Solving Cosserat rod equations modified by coupling terms. To realize the coupling to the surrounding fluid, the Cosserat rod equations (3.5a) are modified via the coupling terms (4.14a) and (4.14b). The corresponding discrete versions are given by

$$\overset{\triangledown}{\mathbf{f}}_{\Gamma,e}\,\Delta Z = -\sum_{\mathbf{x}_l\,\in\,\Gamma_e} \Delta m_l\;\mathbf{f}_{\Gamma,\mathrm{lin}}(\dot{\mathbf{c}},\dot{\mathbf{q}},\mathbf{q},t) \tag{4.23a}$$

$$\overset{\triangledown}{\mathbf{m}}_{\Gamma,e}\,\Delta Z = -\sum_{\mathbf{x}_l\,\in\,\Gamma_e} \Delta m_l\;\boldsymbol{\xi}_l \times \mathbf{f}_{\Gamma,\mathrm{lin}}(\dot{\mathbf{c}},\dot{\mathbf{q}},\mathbf{q},t) \tag{4.23b}$$

for an individual rod element $\Gamma_\mathrm{e} \subset \Gamma$ represented by Lagrangian marker points $\mathbf{x}_l$. Each marker covers a Lagrangian fluid layer mass $\Delta m_l = \rho_\mathrm{f}\, h\, \Delta S_l$. Assuming a rigid body motion of an element, as discussed in Section 3.2.2, the fluid force (4.23a) acting on Γ_e can be reformulated with $\mathbf{f}_{\Gamma,\mathrm{lin}}$ (4.11) as

$$\overset{\triangledown}{\mathbf{f}}_{\Gamma,e}\,\Delta Z = -\left[\frac{\mathbf{p}_\Gamma - \mathbf{p}_\Gamma^{r-1}}{t-t^{r-1}} + \frac{\mathbf{p}_\Gamma^{r-1} - \tilde{\mathbf{p}}}{2\alpha_r\,\Delta t}\right]_e \quad \text{with} \quad \mathbf{p}_{\Gamma,e} = \left[\mathbf{q}{*}(m\,\dot{\mathbf{c}}_0 + \boldsymbol{\omega}_0 \times \mathbf{s}_0){*}\overline{\mathbf{q}}\right]_e \tag{4.24a}$$

$$m_e = \sum_{\mathbf{x}_l\,\in\,\Gamma_e} \Delta m_l\,, \qquad \mathbf{s}_{0,e} = \sum_{\mathbf{x}_l\,\in\,\Gamma_e} \Delta m_l\,\boldsymbol{\xi}_{0,l}\,, \qquad \tilde{\mathbf{p}}_e = \sum_{\mathbf{x}_l\,\in\,\Gamma_e} \Delta m_l\,\tilde{\mathbf{u}}(\mathbf{x}_l^{r-1})\,, \tag{4.24b}$$

where the vector $\mathbf{p}$ designates the linear momentum of the fluid layer around an element e. Related quantities are the fluid layer mass m_e, the static moment of the layer $\mathbf{s}_{0,e}$ and the preliminary linear momentum $\tilde{\mathbf{p}}_e$ as an integral measure of $\tilde{\mathbf{u}}(\mathbf{x}_l^r)$, computed in the previous step. These quantities can be precomputed before solving the rod equations. Due to the staggered spatial discretization of the rod, the external forces $\overset{\triangledown}{\mathbf{f}}_\Gamma$ are considered at nodes with half-index, i.e. $e{+}\frac{1}{2} = \frac{1}{2}, \ldots N_{e+\frac{1}{2}}$ (Fig. 4.3). Here, $\overset{\triangledown}{\mathbf{f}}_{\Gamma,e+\frac{1}{2}}$ is approximated by the mean value of the fluid forces of both adjoining elements, i.e. $\overset{\triangledown}{\mathbf{f}}_{\Gamma,e+\frac{1}{2}} = (\overset{\triangledown}{\mathbf{f}}_{\Gamma,e} + \overset{\triangledown}{\mathbf{f}}_{\Gamma,e+1})/2$. In a similar manner, the velocities $\dot{\mathbf{c}}_e$, actually located at half-index, are estimated by $\dot{\mathbf{c}}_e = (\dot{\mathbf{c}}_{e+\frac{1}{2}} + \dot{\mathbf{c}}_{e-\frac{1}{2}})/2$. Analogous to the external fluid forces, the external moments acting on Γ_e are obtained via

$$\overset{\triangledown}{\mathbf{m}}_{\Gamma,e}\,\Delta Z = -\left[\frac{\mathbf{l}_\Gamma - \mathbf{l}_\Gamma^{r-1}}{t-t^{r-1}} + \frac{\mathbf{l}_\Gamma^{r-1} - \tilde{\mathbf{l}}}{2\alpha_r\,\Delta t}\right]_e \quad \text{with} \quad \mathbf{l}_{\Gamma,e} = \left[\mathbf{q}{*}(\mathbf{s}_0 \times \dot{\mathbf{c}}_0 + \boldsymbol{\mathcal{J}}_0{\cdot}\boldsymbol{\omega}_0){*}\overline{\mathbf{q}}\right]_e \tag{4.25a}$$

$$\boldsymbol{\mathcal{J}}_{0,e} = 0 \oplus \sum_{\mathbf{x}_l\,\in\,\Gamma_e} \Delta m_l\,[\boldsymbol{\xi}_{0,l}]_\times^\top{\cdot}\,[\boldsymbol{\xi}_{0,l}]_\times\,, \qquad \tilde{\mathbf{l}}_e = \sum_{\mathbf{x}_l\,\in\,\Gamma_e} \Delta m_l\,\boldsymbol{\xi}_l^n \times \tilde{\mathbf{u}}(\mathbf{x}_l^{r-1})\,, \tag{4.25b}$$

where $\mathbf{l}$ designates the angular momentum of the fluid layer. As for the linear momentum, the static moment of the layer $\mathbf{s}_{0,e}$, the quaternionic tensor of inertia $\boldsymbol{\mathcal{J}}_{0,e}$ and the preliminary angular momentum $\tilde{\mathbf{l}}_e$ can be precomputed.
In step 3 of the direct forcing coupling scheme (Fig. 4.1), the Cosserat rod equations (3.5) modified by $\overset{\triangledown}{\mathbf{f}}_{\Gamma,e}$ and $\overset{\triangledown}{\mathbf{m}}_{\Gamma,e}$ are solved implicitly for the new linear velocities of rod center line $\dot{\mathbf{c}}^r_{e-\frac{1}{2}}$ and the angular velocities $\boldsymbol{\omega}^r_e = 2\,\dot{\mathbf{q}}^r_e{}^{*}\overline{\mathbf{q}}^r_e$ by means of the quaternions $\mathbf{q}^r_e$, $\dot{\mathbf{q}}^r_e$.

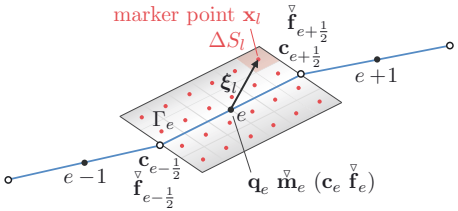

Figure 4.3: *Discrete structural rod element $\Gamma_e \subset \Gamma$ represented by uniformly distributed Lagrangian marker points $\mathbf{x}_l$, each covering a surface area ΔS_l. The vector $\boldsymbol{\xi}_l = \mathbf{x}_l - \mathbf{c}_e$ denotes the relative position of $\mathbf{x}_l$ with respect to the element center position $\mathbf{c}_e$. Due to the staggered spatial discretization the quaternions $\mathbf{q}_e$ and the external moments $\overset{\triangledown}{\mathbf{m}}_e$ are given at the element center, while the center line positions $\mathbf{c}_{e\pm1/2}$ and the external forces $\overset{\triangledown}{\mathbf{f}}_{e\pm1/2}$ are defined between two adjoining elements.*

4. Communication of coupling forces to the fluid solver. In the next step, the velocities $\dot{\mathbf{c}}^r_e = (\dot{\mathbf{c}}^r_{e+\frac{1}{2}} + \dot{\mathbf{c}}^r_{e-\frac{1}{2}})/2$ and $\boldsymbol{\omega}^r_e$ at the new Runge-Kutta time level are communicated to the fluid solver. Based on these velocities the corresponding interface velocity of a rod element e is computed via

$$\mathbf{u}^r_{\Gamma_e}(\mathbf{x}^{r-1}_l) = \dot{\mathbf{c}}^r_e + \boldsymbol{\omega}^r_e \times \boldsymbol{\xi}^{r-1}_l \,. \tag{4.26}$$

With the preliminary velocities $\tilde{\mathbf{u}}(\mathbf{x}^{r-1}_l)$ computed in step 1, the coupling force located at an individual Lagrangian point then is given by

$$\overline{\mathbf{f}}_\Gamma(\mathbf{x}^{r-1}_l) = \frac{\mathbf{u}^r_\Gamma(\mathbf{x}^{r-1}_l) - \tilde{\mathbf{u}}(\mathbf{x}^{r-1}_l)}{2\alpha_r\,\Delta t}\,, \tag{4.27}$$

according to Eq. (4.4). Here, $\overline{\mathbf{f}}_\Gamma$ is formulated with the preliminary velocity $\tilde{\mathbf{u}}\,(\mathbf{x}^{r-1}_l)$ using the marker location $\mathbf{x}^{r-1}_l$ at the old time level $r-1$, which amounts to a semi-implicit treatment of the coupling force.

5. Spreading of coupling forces and reintegration of NSE. In a final step, the remaining equations of the fractional step scheme (3.1b)-(3.1c) are solved to obtain the new fluid velocity field $\mathbf{u}^r$ and the pressure field p^r. Herein, the Helmholtz equation (3.1b) includes $\mathbf{f}_\Gamma(\mathbf{x}_{ijk})$, so that the fluid motion now is constrained by the immersed boundary Γ. Since the coupling forces $\overline{\mathbf{f}}_\Gamma(\mathbf{x}^{r-1}_l)$ computed in step 4 are only provided at the Lagrangian points $\mathbf{x}^{r-1}_l$, they are distributed to the Eulerian grid points $\mathbf{x}_{ijk}$ via the spreading operation (4.21), i.e.

$$\overline{\mathbf{f}}_\Gamma(\mathbf{x}_{ijk}) = \sum_{\mathbf{x}_l \in \Gamma_e} \overline{\mathbf{f}}_\Gamma(\mathbf{x}^{r-1}_l)\;\delta_h(\mathbf{x}_{ijk} - \mathbf{x}^{r-1}_l)\,\Delta V_l \,. \tag{4.28}$$

4.5 Numerical study of convergence

4.5.1 Test configuration

physical parameters:	
$H = 1\,\mathrm{m}$	channel height
$\rho_\mathrm{f} = 100\,\mathrm{kg/m^3}$	fluid density
$\nu_\mathrm{f} = 0.005\,\mathrm{m^2/s}$	kinematic viscosity
$U = 1\,\mathrm{m/s}$	shear velocity
dimensionless quantities:	
$Re_{\frac{H}{2}} = 100$	Reynolds number
	$Re_{\frac{H}{2}} < Re_\mathrm{crit} = 600$ [51]
numerical parameters:	
$L_x = L_y = L_z = H$	domain size (cubic)
$N_x = N_y = N_z = 8 \cdot 2^i$	number of grid cells, $i \geq 0$
$\Delta x = 1/N_x$	step size of Eulerian grid
$\Delta x_l = 2^{-i}/17$	step size of Lagrangian grid
$\phi = \arctan(8/15)$	rotation of Lagrangian grid

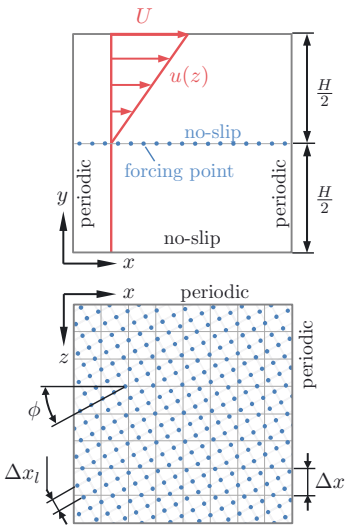

Figure 4.4: *Planar shear flow driven by a constant shear velocity U at the top of the fluid domain. The no-slip condition is imposed by a layer of uniformly distributed forcing points located at $y = H/2$. Below this plane the fluid remains at rest. The present setup is used to analyze the convergence behavior of the direct forcing approach employed at the layer of forcing points.*

The convergence behavior of the proposed direct forcing IBM is assessed by a simple steady planar shear flow. The computational domain extends over a height H, with a no-slip condition $\mathbf{u} = \mathbf{0}$ at the bottom and a moving wall with $\mathbf{u} = (U, 0, 0)^\top$ at the top. Positioning an interface Γ at $y = H/2$ mimics a solid structure of vanishing thickness and is addressed as immersed wall here. This results in the exact solution for the x-component of the velocity

$$u(y) = \begin{cases} 0\,, & y \leq \frac{H}{2} \\ U\,(2y - H)\,, & \frac{H}{2} < y \leq H\,, \end{cases} \tag{4.29}$$

while the pressure is uniform, i.e. $p = \mathrm{const}$. The boundary conditions at $y = 0$ and $y = H$ are imposed on the Eulerian grid as usual Dirichlet conditions. The no-slip condition at $y = H/2$, instead, is imposed by a layer of forcing points arranged as a two-dimensional Cartesian grid of spacing Δx_l. The layer is rotated by an angle of $\phi = \arctan(8/15)$ around the y-axis, to achieve a high degree of variation between the arrangement of the forcing points and the discretization of the fluid domain, as it is the case for freely movable structures.
Due to the kink in the velocity profile at $y = H/2$ the hydrodynamic stresses $\boldsymbol{\sigma}$ are different on both sides of the interface Γ. According to Eq. (2.27), the jump in $\boldsymbol{\sigma}$ is associated to a fluid load acting on Γ. For the present configuration this load simplifies to

$$\int_\Gamma \boldsymbol{\sigma}^+ \cdot \mathbf{n}\,\mathrm{d}S - \int_\Gamma \boldsymbol{\sigma}^- \cdot \mathbf{n}\,\mathrm{d}S \;=\; \tau_\mathrm{w} H^2\,\mathbf{e}_x \tag{4.30}$$

and, thus, is solely determined by the shear stress $\tau_w = 2\,\rho_\mathrm{f}\nu_\mathrm{f}\,U/H$ in the streamwise direction acting on the upper side of the immersed wall. In terms of the present direct forcing IBM, each forcing point $\mathbf{x}_l$ acts against this shear to impose the no-slip condition at $y = H/2$. Using Eq. (4.23a), with $\mathbf{u}_\Gamma = \mathbf{0}$ at the immersed wall, the shear force acting on Γ can be approximated numerically by

$$\tau_\mathrm{w} H^2 \mathbf{e}_x \;\approx\; \mathbf{f}_\mathrm{w} = \sum_{r=1}^{3} \sum_{\mathbf{x}_l \in \Gamma} \Delta m_l\, \tilde{\mathbf{u}}(\mathbf{x}_l)/\Delta t\,, \tag{4.31}$$

with $\Delta m_l = \rho_\mathrm{f}\,\Delta x\,(\Delta x_l/H)^2$ for the present spatial arrangement of the forcing points. Since the components of the fluid loads in y- and z-direction vanish, the relation between the wall shear and the direct forcing is given by $\tau_\mathrm{w} \approx \mathbf{f}_\mathrm{w} \cdot \mathbf{e}_x/H^2$. The following convergence analysis bases on the relative error between the theoretical value of the wall shear and the numerical approximation

$$\epsilon = \frac{\mathbf{f}_\mathrm{w} \cdot \mathbf{e}_x}{\tau_\mathrm{w} H^2} - 1\,. \tag{4.32}$$

4.5.2 Numerical parameters

To determine numerically the spatial and the temporal convergence rate, the error was computed over a wide range of grid step sizes $\Delta x \in \{1/8, 1/16, 1/32, 1/64\}$ and Courant numbers $CFL \in \{1, 0.5, 0.25, ..., 1/2^6, 0.01\}$. The spatial distribution of the forcing points, controlled by $\Delta_l = \text{const.}$, is adapted to the step size of the Eulerian grid, so that $\Delta_l/\Delta x = 8/17 \approx 0.5$ for any Δx. Besides the temporal and spatial resolution the error is also influenced by the delta function employed for interpolation of the preliminary velocity $\tilde{\mathbf{u}}$ to the Lagrangian positions $\mathbf{x}_l$, as well as for spreading the IBM force $\mathbf{f}_\Gamma$ to the Eulerian grid points $\mathbf{x}_{ijk}$. Two different delta functions are tested in the present study, which are frequently employed in continuous direct forcing schemes [186, 251, 268, 119, 246]. One is the three-point delta function Φ_3 of Roma *et al.* [203] and the other the four-point delta function Φ_4 proposed by Peskin [186]. Both functions are compared in Fig. 4.5.

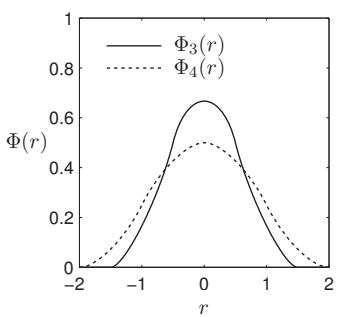

3-point delta function of Roma et al. [203]:

$$\Phi_3(r) = \begin{cases} \frac{1}{6}\left(5 - 3|r| - \sqrt{-3(1-|r|)^2+1}\right) & ,\ 0.5 \le |r| \le 1.5 \\ \frac{1}{3}\left(1 + \sqrt{-3|r|^2+1}\right) & ,\ |r| < 0.5 \\ 0 & ,\ \text{otherwise} \end{cases} \tag{4.33}$$

4-point delta function of Peskin [186]:

$$\Phi_4(r) = \begin{cases} \frac{1}{8}\left(5 - 2|r| - \sqrt{-7+12|r|-4|r|^2}\right) & ,\ 1 \le |r| \le 2 \\ \frac{1}{8}\left(3 - 2|r| + \sqrt{1+4|r|-4|r|^2}\right) & ,\ |r| < 1 \\ 0 & ,\ \text{otherwise} \end{cases} \tag{4.34}$$

Figure 4.5: *The two variants of delta functions studied in this work, the three-point delta function $\Phi_3(r)$ of Roma et al. [203], defined in Eq.* (4.33)*, as well as the four-point delta function $\Phi_4(r)$ of Peskin [186], defined in Eq.* (4.34)*.*

4.5.3 Results and discussion

The convergence behavior obtained for Φ_3 and Φ_4 in the given range of spatial and temporal resolutions is shown in Fig. 4.6 using ϵ from Eq. (4.32). Selected values of the corresponding errors ϵ_3 and ϵ_4, respectively, are provided in Table 4.1.

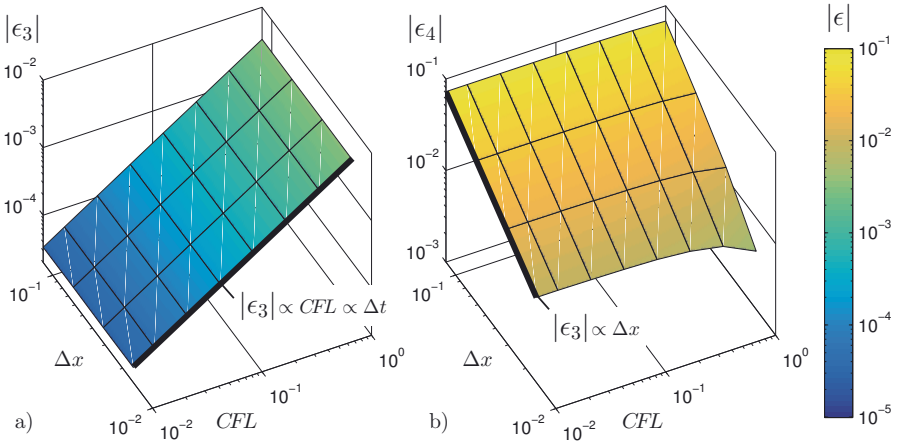

Figure 4.6: *Temporal and spatial convergence of the present direct forcing–IBM in a range of* $\Delta x \times CFL = \{1/8, 1/16, 1/32, 1/64\} \times \{1, 0.5, 0.25, ..., 1/2^6, 0.01\}$. *Shown are the relative errors* ϵ_3 *and* ϵ_4 *according to Eq.* (4.32) *obtained from simulations with the three-point delta function* Φ_3 *and the four-point delta function* Φ_4, *respectively.*

$1/\Delta x$	$1/CFL$	$1/\Delta t$	$\lvert\epsilon_3\rvert$	$\lvert\epsilon_4\rvert$
8	64	512	$5.248 \cdot 10^{-5}$	$7.275 \cdot 10^{-2}$
16	64	1024	$5.237 \cdot 10^{-5}$	$3.509 \cdot 10^{-2}$
32	64	2048	$5.196 \cdot 10^{-5}$	$1.731 \cdot 10^{-2}$
64	64	4096	$5.040 \cdot 10^{-5}$	$8.510 \cdot 10^{-3}$
64	32	2048	$1.022 \cdot 10^{-4}$	$8.433 \cdot 10^{-3}$
64	16	1024	$2.086 \cdot 10^{-4}$	$8.295 \cdot 10^{-3}$
64	8	512	$4.194 \cdot 10^{-4}$	$8.026 \cdot 10^{-3}$

Table 4.1: *Relative errors* ϵ *of the wall shear stress* τ_w *for selected grid step sizes* Δx *and time step sizes* Δt *(*$CFL = U\Delta t/\Delta x$*). Listed are the errors* ϵ_3 *and* ϵ_4 *obtained with the 3-point delta function* Φ_3 *and the 4-point delta function* Φ_4, *respectively.*

Obviously, the convergence behavior is quite different for the two delta functions selected. While the three-point version exhibits a first order convergence in time for any spatial discretization, the four-point version shows the opposite behavior, i.e. a first order convergence in space for any *CFL* number. This is explained as follows: The total numerical error of the

present direct forcing IBM can be traced back to two sources. On one hand, the temporal part of the error results from the direct forcing approach which is used to estimate the amplitude of the coupling force at each forcing point. Due to its time splitting the method exhibits first order accuracy in time $\mathcal{O}(\Delta t)$. A theoretical proof is provided in Appendix C. On the other hand, the spatial part of the total error stems from the delta functions used for the interpolation and spreading step. While an evaluation of numerical errors for the spreading operation at least seems to be ambitious, the accuracy of an interpolation by means of delta functions is well understood. By increasing the width of support additional constraints can be incorporated, so that higher moments of Φ and its smoothness are conserved [186, 268]. As stated in [145], the moment order controls the accuracy in the low frequency range, while the smoothing order suppresses a possible Gibbs phenomenon that may corrupt convergence. A simple two-point linear hat-function, for example, exhibits a discontinuity in its first derivative that often leads to spatial oscillations in the solution [112].
In fact, the convergence rate of the approximation depends on both, the smoothness of the approximating function as well as the smoothness of the function to be approximated. In the present IBM framework $\boldsymbol{\sigma}$ exhibits a jump at the interface Γ, so that $\mathbf{u}(\mathbf{x})$ is not differentiable at $\mathbf{x} \in \Gamma$. As a consequence, the rate of spatial convergence reduces to $\mathcal{O}(\Delta x)$ for any delta function, regardless of the support of Φ [30, 186]. Moreover it turns out, that a wider support increases the spatial error compared to a more narrow delta function. As shown in Fig. 4.6, the errors obtained for Φ_4 with four-point support are increased by at least one order of magnitude compared to Φ_3 with three-point support. The total error ϵ_4 is dominated by spatial interpolation and spreading errors of order $\mathcal{O}(\Delta x)$, while temporal errors, resulting from the direct forcing approach, are much smaller and just not recognizable. On the contrary, for Φ_3 spatial errors are negligibly small compared to the temporal splitting error, so that ϵ_3 mainly converges with $\mathcal{O}(\Delta t)$.
In the present work, the three-point function of Roma *et al.* [203] is preferred as it constitutes a good balance between accuracy, numerical efficiency and smoothing properties. Indeed, for commonly used grid step sizes Δx spatial errors are considerably smaller than obtained for different four-point delta functions, e.g. the function of Peskin [186] presented here. Furthermore, the numerical effort is reduced significantly with a three-point support since it exponentially increases with the width of support. For instance, while the four-point support requires $4^3 = 64$ Eulerian fluid nodes for an interpolation in the three-dimensional case, the three-point support requires only $3^3 = 27$ fluid nodes. Especially for a large number of immersed objects and their representation by a sufficient number of forcing points $\mathbf{x}_l$, the interpolation and spreading operation may occupy a substantial part of the overall computation time and, thus, should be reduced if possible.
At this stage it should be noted that Beyer and Leveque [30] developed a four-point delta function which enables a second order accurate approximation for functions of class C^0 by means of an extrapolation technique. This strategy seems very promising, even if the transferability to the present direct forcing IBM needs to be verified. The so-called immersed interface method [138, 143] overcomes this issue by introducing jump conditions directly into the discretized Navier-Stokes equations which, however, comes along with other technical challenges.

4.6 Parallelization technique

4.6.1 General approach

In terms of the simulation of large-scale FSI problems focused here parallelization is essential. On the one hand, a large number of structures needs to be handled in an appropriate way and, on the other hand, the fluid part requires an enormous amount of computational effort and physical memory when performing direct numerical simulations and large eddy simulations. In such cases the overall computational load is distributed to an available number of processing units, e.g. central processing units (CPUs), graphics processing units (GPUs) or heterogeneous systems combining different kinds of processing technologies. The present parallelization approach is designed for multi-CPU machines in the order of several thousands processors. In the context of multi-CPU concepts, two different approaches have been established in the recent years, the Open Multi-Processing standard (OpenMP) [50, 181] and the Message Passing Interface standard (MPI) [74, 166]. While the former strategy needs a physically shared memory of the CPU cluster, the MPI standard bases on an explicit message passing and, thus, is well suited for clusters with distributed physical memory. Above a certain number of processors on a cluster the shared memory concept is not technical feasible, so that OpenMP only is suitable for a moderate number of processors. Especially for numerical applications dealing with several thousand CPUs the distributed memory concept with communication by an explicit message passing is the most efficient way and offers the best scalability. In the present approach the message passing concept is employed in different ways for the fluid part, the structure part as well as their interaction, to achieve an optimal and efficient use of available computational resources.

4.6.2 Fluid solver and structure solver

As described in Section 3.1, the basic fluid solver is adopted from Kempe *et al.* [119, 118] including the concept of parallelization which reveals an excellent performance in case of massively parallel computers. A detailed study of performance is reported in [118]. The approach is based on a domain decomposition strategy, where the entire fluid domain Ω is decomposed into a number of subdomains, equal to the number of processors allocated on the machine. As a consequence, the numerical solution of the spatially discretized Navier-Stokes equations require an exchange of information across the borders of connected subdomains, e.g. to compute local velocity gradients or pressure gradients etc. In the present approach this exchange is realized by means of a ghost-cell technique, where the quantities of interest are communicated between two bordering subdomains via additional ghost-cells located at their common boundary. All ghost cells of one subdomain coincide with the corresponding physical cells of the other subdomain. For the second order finite volume approach used here, the width of the ghost-cell reduces to a layer of only one cell, which also minimizes the required time of communication. Whenever a local subdomain requires values of their neighborhood, e.g. to compute gradients, a communication is performed by means of MPI. In order to save implementation time for this task, the solver makes use of modern libraries such as the Portable Extensible Toolkit for Scientific computations (PETSc) [13, 12, 14] and the library of High Performance Preconditioners (Hypre) [132, 65], both based on MPI. Hypre provides far advanced solvers used here for the parallel computation of the Helmholtz equation (3.1b) and the Poisson equation (3.1c), both parts of the fractional step scheme (3.1)

employed here. Solving these linear systems consumes the major part of the overall computational time, so that optimized solvers become of crucial importance. Besides the domain decomposition, PETSc is also used for parallel data input and data output, strictly required for large-scale applications since the fluid data easily reaches several gigabytes of storage per instant in time.
The structure part is parallelized by a simpler approach, well suited for FSI problems with a large number of individual structures. Usually, the solution procedure for a single rod is less time consuming, while the bottleneck arises due to the huge amount of structures. Consequently, the rods are distributed among the available processors, so that the dynamics of each Cosserat rod is computed by a single processor. This is reasonable as it avoids decomposition of the individual structural problem (3.8) solved efficiently by the non-commercial ODE-solver RADAU5 [91], as described in Section 3.2.2.

4.6.3 Coupling scheme

In addition to the parallel computation of the separated fluid and structure part, their coupling needs an appropriate strategy of parallelization. As described in Section 4.4, the coupling requires several subsequent steps. First, the preliminary velocity $\tilde{\mathbf{u}}_\Gamma(\mathbf{x}_{ijk})$ located at the Eulerian grid points is interpolated to the Lagrangian markers $\mathbf{x}_l$ on the rod. Secondly, based on $\tilde{\mathbf{u}}_\Gamma(\mathbf{x}_l)$ the coupling force $\mathbf{f}_\Gamma(\mathbf{x}_l)$ is evaluated and, in a final step, spread back to the Eulerian grid to obtain $\mathbf{f}_\Gamma(\mathbf{x}_{ijk})$. In the present work, the interpolation, evaluation and spreading operation are performed by the associated structural rod element, were the marker points $\mathbf{x}_l$ are located. This spatial decomposition by means of rod elements enables an efficient parallel treatment of these three steps, which is realized here by a so-called master and slave strategy [250, 118]. Each single processor, dedicated to a decomposed subdomain, only treats those elements located geometrically in the corresponding subdomain. Such elements are called master elements. In some situations, an element may belong to two or more adjoining subdomains at the same time. While one processor/subdomain contains this element as a master the other subdomains assign it as a slave element. Fig. 4.7 illustrates the scenario for two discretized rods, whose elements are distributed over four subdomains.

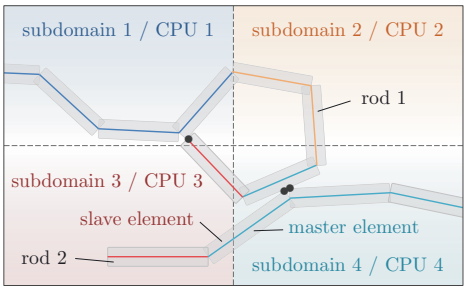

Figure 4.7: *Parallelization by means of a domain decomposition, illustrated with four subdomains. The master elements of the rods are dyed with the color of the associated subdomain. Rod 1 and rod 2 are solved by different CPUs, e.g. CPU 1 and CPU 2 to spread the computational effort. At the positions identified by black dots, several rod elements are in contact. Such collisions are treated by a collision model.*

Using the master-slave concept on CPU clusters with distributed memory, the following communication steps need to be carried out by means of MPI:

1. *Interpolation of velocities:* Concerning Eq. (4.22), $\tilde{\mathbf{u}}(\mathbf{x}_{ijk})$ is interpolated at the Lagrangian marker $\mathbf{x}_l^{r-1}$ on a specific element e at time $t = t^{r-1}$. As described above, the motion of a Cosserat rod is computed by the same processor during the entire simulation. As a result, the rod is not necessarily located in the associated subdomain of the CPU. Thus, the latest geometrical properties of each element, i.e. center line position $\mathbf{c}_e^{r-1}$ and rotation $\mathbf{q}_e^{r-1}$, need to be communicated to the processors where the corresponding master element is located. If a master element is part of two subdomains, these information are further communicated from the master process to the adjoining slave process. With $\mathbf{c}_e^{r-1}$ and $\mathbf{q}_e^{r-1}$ the Lagrangian coordinates $\mathbf{x}_l^{r-1}$ can be reconstructed for each master and slave element which, afterwards, are used to determine $\tilde{\mathbf{u}}(\mathbf{x}_l^{r-1})$. Using Eq. (4.22), the velocity at $\mathbf{x}_l^{r-1}$ is obtained by the sum over the Eulerian points $\mathbf{x}_{ijk}$ belonging to the stencil of the delta function δ_h. To obtain correct values in cases where the stencil is treated by different subdomains, the data obtained for the slaves are sent back to the corresponding master and gathered there. Hence, each master provides the complete set of $\tilde{\mathbf{u}}(\mathbf{x}_l^{r-1})$.

2. *Evaluation of coupling force:* Lagrangian velocities are related to the external fluid loads $\overset{\triangledown}{\mathbf{f}}_\Gamma$, $\overset{\triangledown}{\mathbf{m}}_\Gamma$ required by each structure solver to compute for the next time level $t = t^r$. According to Eqs. (4.24)-(4.25), these fluid loads contain $\tilde{\mathbf{p}}_e$ and $\tilde{\mathbf{l}}_e$ obtained from sums over $\tilde{\mathbf{u}}(\mathbf{x}_l^{r-1})$ on an element e. Therefore, the sums are computed for each master element and communicated to the responsible structure solver, where these quantities are employed to solve for the motion at $t = t^r$. Then, the updated rod data ($\mathbf{c}_e^r$, $\dot{\mathbf{c}}_e^r$, $\mathbf{q}_e^r$ and $\dot{\mathbf{q}}_e^r$) are sent back to the master processes. Note, that $\mathbf{c}_e^r$ and $\mathbf{q}_e^r$ are reused for the subsequent interpolation step and do not need to be communicated twice. Based on the current motion, the interface velocities $\mathbf{u}_\Gamma(\mathbf{x}_l^{r-1})$ are computed via Eq. (4.26) for each master element. Finally, these are used to evaluate the coupling forces $\bar{\mathbf{f}}_\Gamma(\mathbf{x}_l^{r-1})$ according to Eq. (4.27).

3. *Spreading of coupling force:* After evaluating the coupling forces, these are sent to adjoining slave processes by the master process. In a last step, the Lagrangian coupling forces $\mathbf{f}_\Gamma(\mathbf{x}_l)$ are distributed on the Eulerian grid by the spreading operation (4.28) yielding $\mathbf{f}_\Gamma(\mathbf{x}_{ijk})$. This source term then is employed in the Helmholtz equation (3.1b) to obtain the constrained velocity field of the fluid.

4.6.4 Collision handling

Especially in fluid-structure interaction problems dealing with a large number of densely arranged rods, these may collide with each other as shown in Fig. 4.7. For this purpose, an own collision model designed for Cosserat rods was developed, presented in Chapter 5 below. It is parallelized with the already described master-slave concept, so that the processor handling the fluid-structure coupling also performs the contact detection and the computation of the collision response between the master elements. Possible collisions of elements belonging to different subdomains are treated as collisions between master and slave elements. The information required for such kind of collisions is exchanged between the subdomains involved.

4.7 Validation and results

4.7.1 Turek & Hron's benchmark problem

		FSI-1	FSI-2	
fluid properties:				
L_x	m	2.5	2.5	channel length
L_y	m	0.41	0.41	channel height
ρ_f	kg/m^3	10^3	10^3	fluid density
ν_f	m^2/s	10^{-3}	10^{-3}	kin. viscosity
U	m/s	**0.2**	**1**	mean velocity
structure properties:				
D	m	0.1	0.1	diameter
L	m	0.35	0.35	rod length
T	m	0.02	0.02	rod thickness
ρ_s	kg/m^3	$\mathbf{10^3}$	$\mathbf{10^4}$	structure density
ν_s	–	0.4	0.4	Poisson's ratio
E_s	MPa	1.4	1.4	Young's modulus
dimensionless quantities:				
Re_D	–	20	100	Reynolds number
$\rho_\mathrm{s}/\rho_\mathrm{f}$	–	1	10	density ratio

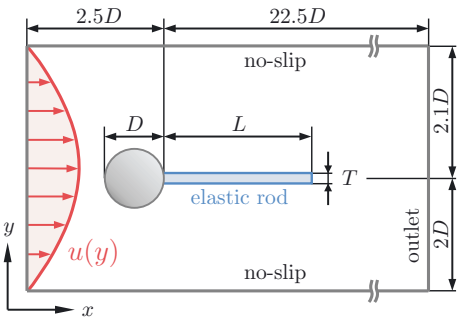

Figure 4.8: *Setup of the FSI benchmark problem proposed by Turek and Hron [248] (not to scale). Depending on the set of parameters, the rod responds with a steady deflection (FSI-1) or with a periodic oscillation, excited by vortices shed from the cylinder (FSI-2).*

The two-dimensional benchmark of Turek and Hron [248] shown in Fig. 4.8 is the most commonly used test case for validating and comparing FSI approaches. The physical setup is defined in the laminar regime of an incompressible Newtonian fluid, while the elastic rod structure responds with large deflections under the influence of the fluid loads. The latter is attached to the downstream side of a rigid circular cylinder, with its center at $(0.2\,\mathrm{m}, 0.2\,\mathrm{m})^\mathrm{T}$. The horizontal expansion of the domain L_x is large enough to avoid any influence of the outflow condition on the behavior of the rod [248]. Furthermore, the immersed object is intentionally positioned slightly above the midspan of the domain to predefine the structure deflection in the initial transient phase of the motion. At the inlet boundary a time-dependent velocity is imposed, which is defined by

$$\frac{u(y,t)}{U} = \begin{cases} u^* \sin(\pi/4\, t^*) & , t^* < 20 \\ u^* & , \text{otherwise} \end{cases} \tag{4.35}$$

with the parabolic profile $u^* = 6y^*(1-y^*)$, the mean velocity $U = 2/3\ u(y^* = 1/2,\, t^*)$, the dimensionless vertical coordinate $y^* = y/L_y$ and the dimensionless time $t^* = t\,U/D$. At the outlet boundary a convective outflow condition is applied, while the remaining boundaries are defined as no-slip walls, including the fluid-solid interface of the cylinder and the rod.

The present FSI model differs in some respects from the common model assumptions, required for this benchmark. First, a zero-thickness approximation of the fluid-structure interface is used here, so that the coupling conditions are imposed at the midline of the rod. Second, the elastic structure is modeled by a one-dimensional Cosserat rod model, in contrast to the two-dimensional models commonly used in the literature.
Nonetheless, simulations were conducted for the benchmark cases FSI-1 and FSI-2, with the associated material properties provided in Fig. 4.8. While the first case results in a small stationary deflection of the rod (Fig. 4.9a,b), the solution of case FSI-2 exhibits an unsteady behavior in which the vortices shed from the cylinder excite a periodic oscillation of the rod (Fig. 4.9c,d). In order to study the convergence behavior of the present FSI-solver and to achieve grid independence of the simulation results, five simulations with different grid resolutions were performed for each test case. Table 4.2 provides an overview of all resolutions used. The rate of convergence q is estimated via Richardson extrapolation [70] yielding

$$q_{2h} = \log_2\left(\frac{\epsilon_{8h} - \epsilon_{4h}}{\epsilon_{4h} - \epsilon_{2h}}\right) , \tag{4.36}$$

where e.g. ϵ_{2h} is the relative error of resolution $2h$ with respect to the finest resolution h, i.e. $\epsilon_{2h} = \varphi_{2h}/\varphi_h - 1$ for an arbitrary quantity φ. The results of the convergence test are listed in Tab. 4.2. As expected, the rate of convergence q is around 1 which is a consequence of the direct forcing approach and the use of regularized delta functions for the interpolation and spreading operation, as demonstrated in Section 4.5. At coarser resolution levels the asymptotic range is apparently not reached, so that orders larger than 1 can be observed. The converged simulation results obtained with the finest resolution are used for a quantitative comparison with the reference data of Turek and Hron [248], shown in Fig. 4.10 and Tab. 4.3.

level	$\Delta t/10^{-4}$s	$\Delta x/10^{-4}$m	$L/\Delta x$	N	N_e
$16h$	4	1	35	10250	5
$8h$	2	0.5	70	41000	10
$4h$	1	0.25	140	164000	20
$2h$	0.5	0.125	280	656000	40
h	0.25	0.0625	560	2624000	80

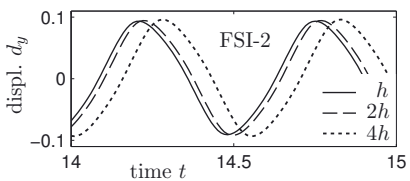

FSI-1	ϵ_{16h}	ϵ_{8h}	ϵ_{4h}	ϵ_{2h}	q_{4h}	q_{2h}	q_h
displacem. d_x	$1.66 \cdot 10^{-1}$	$7.43 \cdot 10^{-2}$	$3.06 \cdot 10^{-2}$	$9.90 \cdot 10^{-3}$	1.06	1.08	1.07
displacem. d_y	$1.38 \cdot 10^{-1}$	$4.87 \cdot 10^{-2}$	$1.79 \cdot 10^{-2}$	$5.69 \cdot 10^{-3}$	1.53	1.34	1.10

FSI-2		ϵ_{16h}	ϵ_{8h}	ϵ_{4h}	ϵ_{2h}	q_{4h}	q_{2h}	q_h
d_y	mean	$3.63 \cdot 10^{-1}$	$2.07 \cdot 10^{-2}$	$8.88 \cdot 10^{-3}$	$2.91 \cdot 10^{-3}$	4.85	0.99	1.04
	ampl.	$2.45 \cdot 10^{-1}$	$1.06 \cdot 10^{-1}$	$4.37 \cdot 10^{-2}$	$1.42 \cdot 10^{-2}$	1.16	1.08	1.05
	freq.	$-7.19 \cdot 10^{-2}$	$-2.35 \cdot 10^{-2}$	$-6.59 \cdot 10^{-3}$	$-1.79 \cdot 10^{-3}$	1.51	1.82	1.42

Table 4.2: *Upper left table: Resolution levels with corresponding time step size Δt and grid step size Δx. Additionally, the number of grid cells $N = N_x \times N_y$ and number of structural rod elements N_e are listed. Lower tables: Convergence study concerning the cases FSI-1 and FSI-2, with the relative errors ϵ_h and the rate of convergence q defined by Eq. (4.36). Upper right figure: Vertical tip displacement d_y in the periodic regime, FSI-2, for the 3 finest resolutions $4h$, $2h$ and h.*

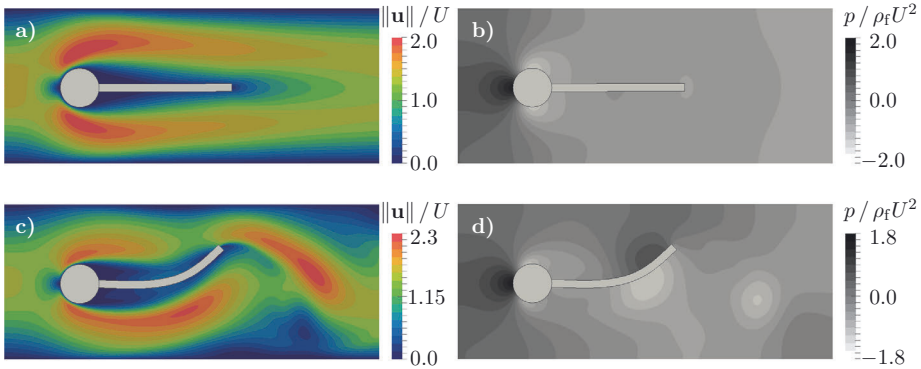

Figure 4.9: *Contour plots of the instantaneous normalized velocity $\|\mathbf{u}\|/U$ (a,c) and normalized pressure $p/\rho_f U^2$ (b,d) for the steady-state case FSI-1 (a,b) and the periodic case FSI-2 (c,d). The latter case FSI-2 shows the instant of maximum vertical deflection of the rod.*

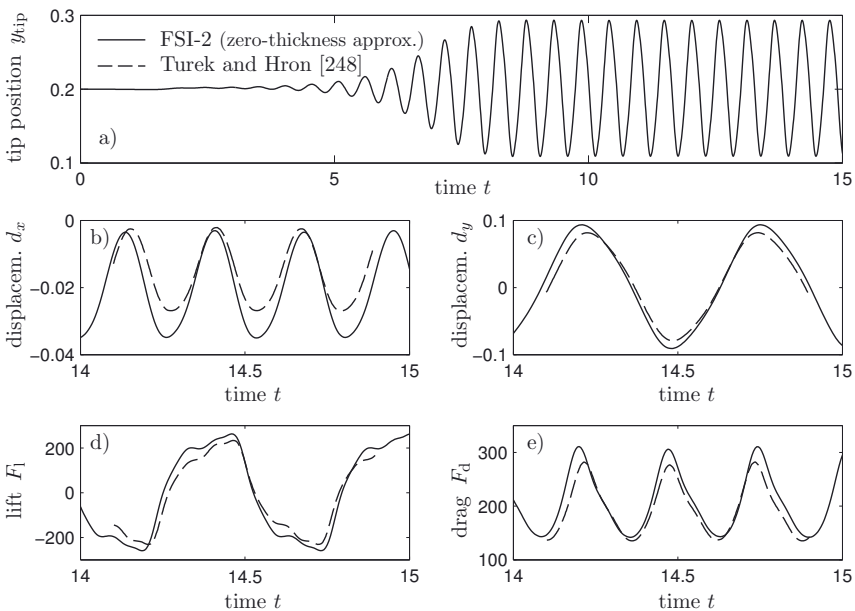

Figure 4.10: *Present simulation results (solid lines) of case FSI-2 compared with the reference data of Turek and Hron [248] (dashed lines). The upper graph a) shows the initial transient of the vertical tip position y_{tip} (not provided in [248]). The temporal evolution of b) the horizontal tip displacement d_x, c) the vertical tip displacement d_y, d) the lift force F_l and e) the drag force F_d are shown for a selected time interval of 1 second in the periodic phase.*

FSI-1	d_x (mm)	d_y (mm)	F_d (N)	F_l (N)
Present IBM, zero-thickness approx.	0.0204	0.9370	13.596	0.6604
Reference (ALE) Turek and Hron [248]	0.0227	0.8209	14.295	0.7638
rel. error (%)	-10.1	14.1	-4.9	-13.5

FSI-2	d_x (mm)	d_y (mm)	F_d (N)	F_l (N)
Present IBM, zero-thickness approx.	-18.95 ± 15.91 [3.66]	1.27 ± 92.16 [1.84]	226.42 ± 84.47 [3.66]	1.53 ± 261.13 [1.84]
IBM of Bhardwaj and Mittal [32]	–	– ± 92 [1.9]	178 ± – [–]	–
IBM of Tian *et al.* [239]	–	– ± 78 [1.9]	205.5 ± – [–]	–
Reference (ALE) Turek and Hron [248]	-14.58 ± 12.44 [3.8]	1.23 ± 80.6 [2.0]	208.83 ± 73.75 [3.8]	0.88 ± 234.20 [2.0]
rel. error (%)	29.9 ± 27.9 [-3.7]	3.3 ± 14.3 [-8.0]	8.4 ± 14.5 [-3.7]	73.9 ± 11.5 [-8.0]

Table 4.3: *Horizontal and vertical tip displacements d_x and d_y as well as drag force F_d and lift force F_l of the entire immersed object, i.e. cylinder and rod. In case FSI-2 the time-dependent periodic quantities are provided in the form $m \pm a\,[f]$, with the mean value m, the amplitude a and the frequency f. The present simulation results are compared with the reference data of Turek and Hron [248] and with IBM simulations of Bhardwaj and Mittal [32] and Tian et al. [239].*

The present IBM approach qualitatively captures the behavior of the coupled system in both scenarios, the steady state solution in case FSI-1 and the periodic solution in case FSI-2. From a quantitative point of view, however, larger deviations can be observed in comparison to the reference data of Turek and Hron [248]. For example, the relative errors obtained for FSI-2 are up to approximately 15% for the amplitudes of the drag and lift forces and up to 28% for the amplitudes of the tip displacement. The sources of these differences are manifold. As already shown in [249], different discretization schemes and coupling procedures may produce slightly different solutions. This reference provides a cross-comparison between strongly coupled partitioned approaches and monolithic approaches, based mainly on an arbitrary Lagrangian-Eulerian (ALE) method for the fluid part and an FEM for the structure part [249, 159]. As an example, Turek and Hron [248] used a fully implicit, monolithic ALE-FEM approach, while Bletzinger [249] combined a Lattice-Boltzmann method on a fixed Eulerian fluid grid with an FEM for the structure part. Differences up to 50% for the drag and lift forces, and in the range of 10% for the displacements were obtained [249]. The present FSI-solver contains additional model assumptions which also affect the numerical solution. First, the rod structure is represented by a one-dimensional Cosserat rod model. In [249] only Bletzinger used a similar rod model (Reissner-Mindlin shell model), leading to errors in the order of 10%, which is comparable to the present results. Second, the

zero-thickness representation of the rod in the fluid field used here seems to be a quite rough approximation. One obvious consequence is that larger tip deflections are predicted in the simulations, which in turn causes slightly increased drag forces on the rod at maximum tip deflection. Finally, it is known that the present type of IBM usually overestimates the drag of immersed boundaries [35]. This is caused by the regularized delta functions employed to "spread" the coupling forces from the Lagrange markers to the Eulerian grid (see Section 4.3.2). The spreading leads to a sort of diffuse interface with the fluid which marginally increases the effective diameter of the cylinder. As a result, its drag is slightly overestimated.

4.7.2 Wall & Ramm's FSI problem

fluid properties:	
$L_x = 19.5\,\text{cm}$	channel length
$L_y = 13\,\text{cm}$	channel height
$\rho_\text{f} = 1.18 \cdot 10^{-3}\,\text{g/cm}^3$	fluid density
$\eta_\text{f} = 1.82 \cdot 10^{-4}\,\text{g/(cm s)}$	dyn. viscosity
$U = 51.3\,\text{cm/s}$	bulk velocity
structure properties:	
$W = 1\,\text{cm}$	square width
$L = 4\,\text{cm}$	rod length
$T = 0.06\,\text{cm}$	rod thickness
$\rho_\text{s} = 0.1\,\text{g/cm}^3$	structure density
$\nu_\text{s} = 0.35$	Poisson's ratio
$E_\text{s} = 2.5 \cdot 10^6\,\text{g/(cm s}^2\text{)}$	Young's modulus
$k_\text{s} = 5/6$	shear correction
dimensionless quantities:	
$Re_W \approx 333$	Reynolds number
$\rho_\text{s}/\rho_\text{f} \approx 85$	density ratio

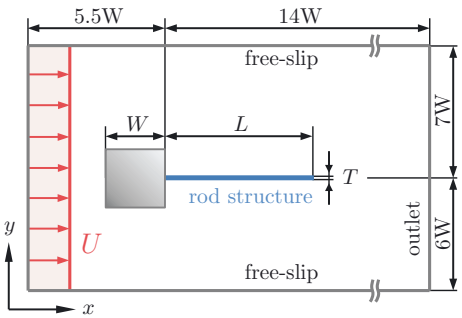

Figure 4.11: *Setup according to Wall and Ramm's FSI benchmark problem [261, 260] (not to scale). A slender elastic rod is mounted on an immobile square shaped obstacle submerged into a uniform flow. At the present Reynolds number of $Re_W = UW/\nu_\text{f} \approx 333$ vortices are shed from the square, which excite a periodic oscillation of the rod.*

The FSI benchmark of Turek and Hron [248] presented in the previous section is an improved version of the FSI problem proposed by Ramm and Wall [261, 260] several years earlier. Both configurations base on the same physical phenomenon, a vortex-induced oscillation of a flexible rod in the wake of an immobile obstacle in laminar flow. Besides different material parameters for the fluid and the structure, an alternative shape of the obstacle is used. In the original setup of Ramm and Wall, the slender flexible structure is attached to the downstream end of a square shaped body, while in [248] a circular shape is used. Moreover, the thickness of the rod is significantly smaller, which is better suited to validate the

present IBM using a zero-thickness representation of the rod structure. The definition of the FSI benchmark is provided in Fig. 4.11. Initially, the structure is at rest while a uniform and temporally constant bulk velocity of $U = 51.3\,\mathrm{cm/s}$ is applied instantaneously at the inlet at time $t = 0$. The corresponding Reynolds number is $Re_W = \rho_\mathrm{f} U W/\eta_\mathrm{f} \approx 333$ based on the square width W and the bulk velocity U. At the outlet a convective outflow condition is imposed, and the lateral boundaries are modeled as free-slip walls.

In the original setup of Ramm and Wall [261] the obstacle with the rod is positioned symmetrically at the midspan of the domain, so that numerical instabilities of the fluid flow cause a transition to a periodic motion of the rod. The time of the first occurrence of such instabilities can vary significantly between different numerical methods, which complicates a cross-comparison of the associated simulation results. Similar to the benchmark of Turek and Hron [248] the domain is slightly enlarged in vertical direction here, so that the symmetry of the domain is broken. This small geometrical change triggers a well-defined initial instability which initiates the transition phase. The amplitude and frequency of the subsequent steady oscillation are barely affected by this modification.

In the work of Ramm and Wall [261] the present configuration was used only as a phenomenological study of such kind of FSI problems without any convergence study. The results should not be considered as an exact solution, even if the principle physical behavior is reproduced [260]. In general, this benchmark is less popular and commonly used as a qualitative validation of numerical strategies for FSI, e.g. in [226] where only a short time interval was simulated without reaching the steady oscillation state. Other groups slightly changed the material properties and performed simulations at a lower Reynolds number of $Re_W = 204$ instead of $Re_W = 333$ [266, 103]. This complicates a cross-comparison between the different numerical approaches. To date, only few studies provide data for quantitative comparison, as the one of Dettmer and Perić [56], for example. They carried out simulations with various structure models, even with a zero-thickness approximation of the rod in the fluid which indeed is atypical. Most authors, however, model the rod via the regular structure equations (2.4), denoted as *continuum models* here.

The fluid domain shown in Fig. 4.11 is discretized by a Cartesian, equidistant grid with the same grid step size in x- and y-directions. To assess the convergence behavior, three simulations with different grid resolutions were performed (Fig. 4.12). Here, the step size of the fine grid corresponds to $L/\Delta x = 640$ equidistant grid cells over the length of the rod L. The resolution of the coarsest mesh is given by $L/\Delta x = 160$ cells. In terms of the temporal

level	$\Delta t/10^{-4}\mathrm{s}$	$\Delta x/10^{-1}\mathrm{cm}$	$L/\Delta x$	N	N_e
$4h$	1	0.25	160	405600	20
$2h$	0.5	0.125	320	1622400	40
h	0.25	0.0625	640	6489600	80

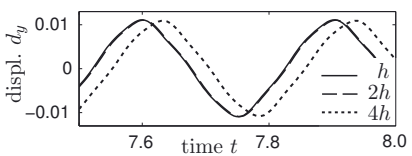

Figure 4.12: *Selected time step sizes Δt and grid step sizes Δx used to assess the temporal and spatial convergence. In addition, the resulting number of grid cells $N = N_x \times N_y$ and number of structural rod elements N_e are listed in the table. The right figure shows the vertical tip displacement d_y obtained for different resolutions.*

discretization a constant time step was used, determined such that $CFL \approx 0.5$. Figure 4.13 shows the temporal evolution of the vertical tip displacement $d_y(t)$ for different grid resolutions, compared with the result of Dettmer and Perić [56]. Especially with the coarse grid resolution of $L/\Delta x = 160$, the initial transient of the oscillation agrees well with the reference data, while the fine resolution of $L/\Delta x = 640$ differs slightly more. These results indicate that the grid resolution used by Dettmer and Perić [56] is not fine enough to guarantee grid independence. In fact, they used only two adapted meshes of different spatial resolutions, the finest having about $L/\Delta x \approx 100$ cells over the rod length. Although temporal convergence has been demonstrated in [56], no spatial convergence study was presented.
The long term response of the rod is shown in Fig. 4.14. Obviously, the transition phase to the steady-state oscillation is finished after a time period of approximately 2 s. Then, the rod oscillates with an amplitude of 1.1 cm and a frequency of 3.29 Hz, where the motion is dominated by the first natural bending mode. Fig. 4.15 shows a snapshot of the oscillation at the instant of maximum vertical deflection of the rod. Different numerical structure models were studied by Dettmer and Perić [56], ranging from a large strain continuum model to a small strain rod model. Depending on the model applied, the dominant first mode oscillation is superposed by a second mode of higher frequency. The displacement plot in Fig. 4.13 shows that such second mode oscillations also occur with the present Cosserat rod model ($t > 2.5$ s), but with smaller amplitudes compared to the small strain continuum model of Dettmer and Perić [56]. Tab. 4.4 provides a cross-comparison between the present IBM and

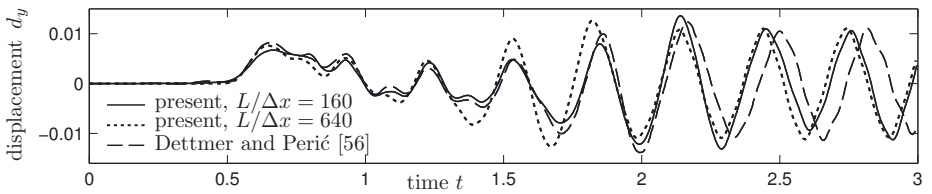

Figure 4.13: *Vertical tip displacement d_y during the initial transition phase. The results obtained for the coarse resolution ($L/\Delta x = 160$) and the fine resolution ($L/\Delta x = 640$) are compared to the data of Dettmer and Perić [56] (picked case: fine grid, small strain continuum structure model).*

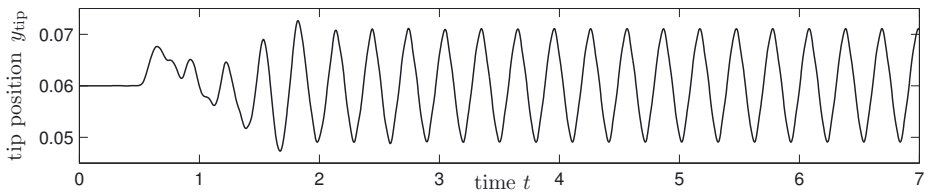

Figure 4.14: *Long-term response of the rod shown for the vertical tip position y_{tip}. After an initial transition phase of approximately 2 seconds the rod oscillates with temporally constant amplitudes of* 1.1 cm *and a frequency of* 3.29 Hz.

selected numerical approaches from the literature. Each numerical approach reproduces the expected periodic behavior of the coupled system. However, deviations in the order of 10% can be observed for the oscillation amplitude and frequency. Hübner *et al.* [103] showed how different stable periodic solutions can arise when different initial conditions are imposed. In the present study it was observed that the spatial resolution has a noticeable impact on the dynamic behavior. A very fine spatial discretization must be used to reach convergence, especially with regard to the initial transient phase.

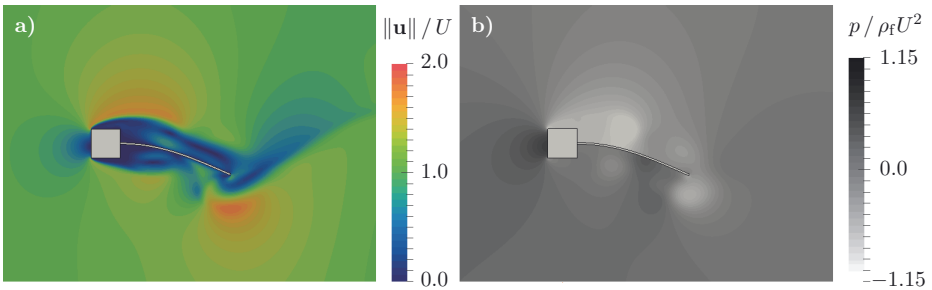

Figure 4.15: *Instantaneous solution of the FSI problem according to Wall and Ramm [261] at the time of maximum vertical deflection of the rod. a) Contour plot of normalized velocity magnitude* $\|\mathbf{u}\|/U$*, and b) normalized pressure field* $p/\rho_f U^2$*. Clearly visible are the suction side (negative pressure, light gray) and the pressure side (positive pressure, dark gray), generating a positive lift force on the structure. The light pressure region at the tip indicates the growth of an individual vortex.*

numerical method	IBM present	IBM Kamensky *et al.* [113]	ALE Kamensky *et al.* [113]	ALE Baudille & Biancolini [22]	ALE Dettmer & Perić [56]		
structure model	Cosserat rod (zero-thickness)	shell	shell	continuum	beam	continuum (small strain)	**average**
ampl. (cm)	**1.10**	1.3	≈ 1	≈ 1	1.24	1.29	**1.15**
freq. (Hz)	**3.29**	3.2	3.2	3.18	3.08	2.96	**3.15**

Table 4.4: *Oscillation amplitudes and frequencies of vertical tip-displacement* d_y *obtained by different authors using either an IBM with a fixed background grid or an ALE method with a moving adapted mesh. Moreover, different structure models were applied in these works, ranging from non-reduced three-dimensional continuum models to one-dimensional rod models. Each structure model is formulated geometrically exact and thus is able to represent large rod deflections.*

4.7.3 Flexible rod in cross flow

$g = 981\,\mathrm{cm/s^2}$	grav. acceleration
fluid properties (water):	
$L_x = 20\,\mathrm{cm}$	channel length
$L_y = 16\,\mathrm{cm}$	channel height
$L_z = 16\,\mathrm{cm}$	channel width
$\rho_\mathrm{f} = 1\,\mathrm{g/cm^3}$	fluid density
$\nu_\mathrm{f} = 0.01\,\mathrm{cm^2/s}$	kin. viscosity
$U = 3.6 \ldots 32\,\mathrm{cm/s}$	bulk velocity
structure properties (foam material):	
$L = 5\,\mathrm{cm}$	rod length
$W = 1\,\mathrm{cm}$	rod width
$T = 0.2\,\mathrm{cm}$	rod thickness
$\rho_\mathrm{s} = 0.67\,\mathrm{g/cm^3}$	structure density
$\nu_\mathrm{s} = 0.4$	Poisson's ratio
$E_\mathrm{s} = 50\,\mathrm{N/cm^2}$	Young's modulus
dimensionless quantities:	
$Re_L = 360 \ldots 3200$	Reynolds number
$\rho_\mathrm{s}/\rho_\mathrm{f} = 0.67$	density ratio

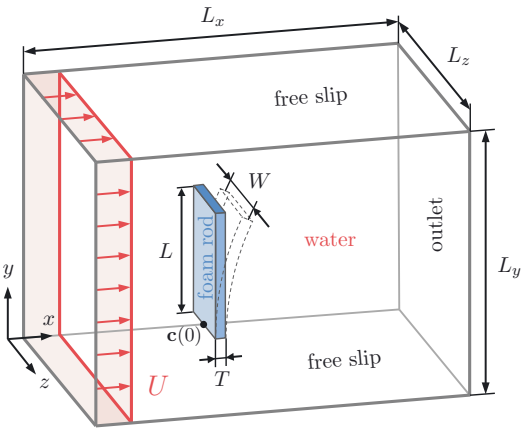

Figure 4.16: *Benchmark configuration of a flexible rod made out of foam material subjected to a uniform cross flow (not to scale) according to the experimental work of Luhar and Nepf [150].*

The configuration shown above was experimentally studied by Luhar and Nepf [150] and is well suited as a benchmark problem for steady-state fluid-structure interactions. In contrast to the previous two benchmarks the interaction is pressure dominated as the blade is oriented perpendicular to the mean flow. To provide a uniform flow over the entire length of the rod, it is positioned above the boundary layer of the channel bottom. In the experiment this is realized with the aid of a thin steel rod. The latter is connected to a load sensor which simultaneously measures the integral hydrodynamic force acting on the rod. The structure responds by a large almost steady deflection to the applied fluid load and the wake generated past the rod is three-dimensional and turbulent (Fig. 4.17).
The laboratory flume used in the experiment is approximated here by a bounded rectangular fluid domain of size $[0; L_x] \times [0; L_y] \times [0; L_z]$ with $L_x = 20\,\mathrm{cm}$, $L_y = 16\,\mathrm{cm}$ and $L_z = 16\,\mathrm{cm}$. Within the domain, the lower end of the rod is positioned at $\mathbf{c}(Z=0) = (5\,\mathrm{cm}, 5\,\mathrm{cm}, 8\,\mathrm{cm})^\mathrm{T}$. Test simulations with different domain sizes have shown that this domain is sufficiently large and does not affect the flow around the rod by boundary effects. At the four lateral boundaries of the domain a free-slip rigid lid condition is applied. The inlet velocity is set to a constant bulk velocity U, while a convective outflow condition is used at the outlet. The fluid domain is discretized by $N_x \times N_y \times N_z = 200 \times 160 \times 160$ cells in total, which corresponds to $W/\Delta x = 10$ grid cells over the width of the structure W. In addition, a finer resolution of $W/\Delta x = 20$ is used to verify grid independence. The rod is discretized by $N_\mathrm{e} = 20$ struc-

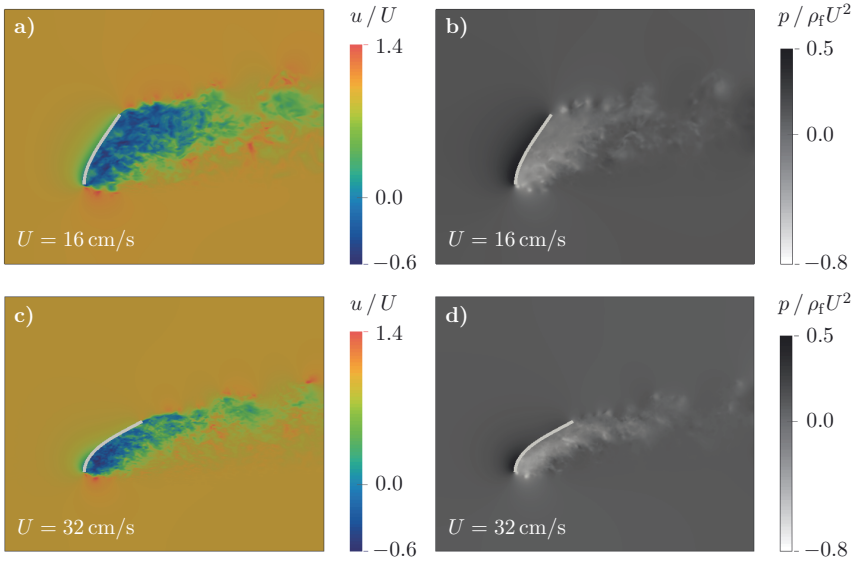

Figure 4.17: *Instantaneous flow around the rod in the center plane, $z = 8\,\mathrm{cm}$, for two bulk velocities U. a) Streamwise velocity component u for $U = 16\,\mathrm{cm/s}$. b) Pressure field for $U = 16\,\mathrm{cm/s}$. d) Streamwise velocity component u for $U = 32\,\mathrm{cm/s}$. d) Pressure field for $U = 32\,\mathrm{cm/s}$.*

tural elements, while $N_e = 40$ is employed for the fine resolution. Regarding the temporal discretization a constant time step size was chosen, yielding $CFL \approx 0.5$. This, for example, results in a time step size of $\Delta t = 1 \cdot 10^{-3}\,\mathrm{s}$ at a bulk velocity of $U = 16\,\mathrm{cm/s}$ and a grid resolution of $W/\Delta x = 10$.

In order to validate the FSI-solver over a wide range of Reynolds numbers $Re_L = UL/\nu_f$, simulations were carried out for 8 bulk velocities ranging from $U = 3.6\,\mathrm{cm/s}$ ($Re_L = 360$) up to $U = 32\,\mathrm{cm/s}$ ($Re_L = 3200$). Figure 4.18 shows a comparison between the present simulation results and the experimental data of Luhar and Nepf [150] over the entire range of bulk velocities U. In addition, the results are compared with a similar IBM simulation carried out by Tian *et al.* [239] for $U = 16\,\mathrm{cm/s}$. With regard to the average drag force F_d, the present results show an excellent agreement with the experimental data over the entire range of bulk velocities U. Small differences can be observed for the deflection shape of the rod, shown in Fig. 4.18b for a selected velocity of $U = 16\,\mathrm{cm/s}$. Compared to the experimental observation, the rod is slightly more deflected in the simulation. One possible reason can be assigned to the values of the material parameters provided in [150]. Measurement uncertainties of more than 10% may be expected for the Young's modulus E_s and the density ρ_s of the foam material. An additional source of the deviations obtained can be related to the isotropic linear-elastic constitutive relations applied here to simulate a rod made out of non-isotropic foam material. At this point, a hyperelastic material model, e.g. a neo-Hookean material, would be better suited. Despite these minor uncertainties in the properties of the experimental setup, the present results show reasonably good agreement with the reference, thus providing another validation of the approach.

U (cm/s)	3.6	7.1	11	14	16	22	27	32
F_d (mN)	0.5	1.9	4.3	6.4	7.5 (7.6)	10.9	13.7	16.0 (16.1)

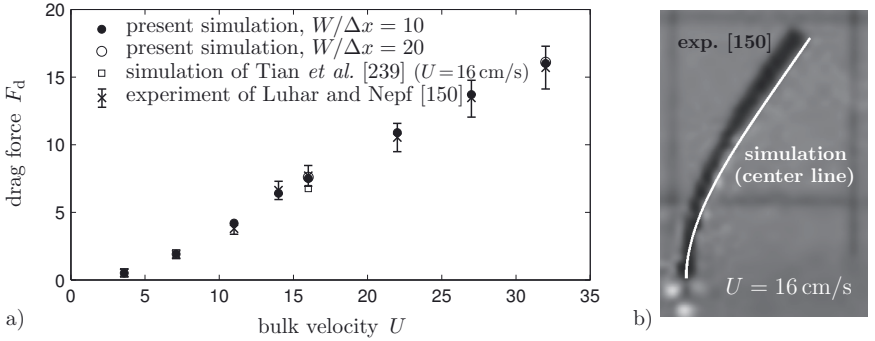

Figure 4.18: *Upper Table: Average drag force F_d at different bulk velocities U ranging from $U = 3.6\,\mathrm{cm/s}$ up to $U = 32\,\mathrm{cm/s}$. For the simulations performed over the entire range of U a grid resolution of $W/\Delta x = 10$ was used. To verify convergence of F_d, a finer grid resolution of $W/\Delta x = 20$ was employed at $U = 16\,\mathrm{cm/s}$ and $U = 32\,\mathrm{cm/s}$ as well (values in brackets). a) Drag force F_d plotted against the bulk velocity U. The present results are compared with the experimental data of Luhar and Nepf [150] and to the simulation results of Tian et al. [239]. b) Comparison of the average rod shape between the experiment (dark blurred line) and the present simulation (white line) at a velocity of $U = 16\,\mathrm{cm/s}$.*

5 Collision model for Cosserat rods

5.1 Fundamentals and state of the art

In cases, where rod structures are close to each other, the collision response strongly influences the physical behavior of the entire system, so that it must be accounted for. For this purpose, an own collision model was developed, which is able to treat a simultaneous collision of a large number of individual Cosserat rods. From a physical point of view, each individual collision causes a local deformation of the structures involved at and closely around the contact region where the structures touch, as well as a dissipation of energy due to internal friction inside the structures and external friction between them. The simulation of these processes requires very high temporal and spatial resolution and can be accomplished only in rare cases, when just a very small number of structures is involved. If, as in the present work, the focus lies on a larger scale, e.g. the macroscopic collective motion of interacting structures, the collision response and the structures need to be modeled to a higher degree by incorporating assumptions or empirical laws. By taking advantage of geometrical or material properties, three-dimensional high-resolution models can be simplified to "reduced-order" models, as already realized in terms of the structure part to obtain the Cosserat rod equations (Section 2.3.2). Selected levels of abstraction used to simulate collision processes of rods are shown in Fig. 5.1, where case c) constitutes the subject in this chapter.

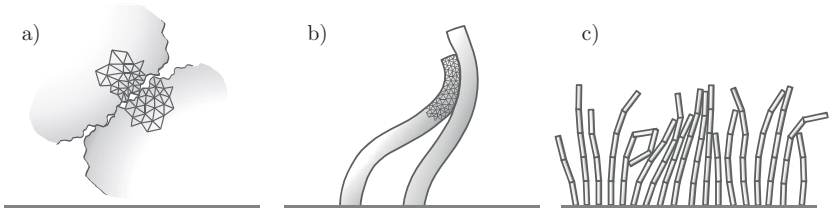

Figure 5.1: *Different levels of abstraction in the description of collision processes: a) Resolution of local deformation and friction mechanisms during a collision of two rods. b) Resolution of deformation and modeling friction in tangential space. c) Representation of structures by one-dimensional model. Deformation due to collision and frictional effects are modeled.*

Clarification of terminology. Primarily, each collision model counteracts against an interpenetration of two interacting structures by means of a contact force oriented in the direction normal to the contact surface. Therefore, the contact force acts in the *normal space* of the contact surface, which is often denoted as *contact space* [63, 223]. Correspondingly, friction forces act in the *tangent space* of the contact surface. Friction models are further

classified into models for static and kinetic friction, where in the latter case the structures slide along each other in tangent space. Depending on the kind of relative motion, kinetic friction models are classified into models for sliding, spinning and rolling friction [90]. In case of vanishing relative motion, the interacting structures stick to each other due to static friction. The situation where structures are completely at rest while interacting is usually called *contact* or more precisely *static contact*. In contrast, the term *collision* actually describes a dynamic interaction. In the literature, the term collision model and contact model, is often used as an umbrella term, including dynamic collisions as well as static contact with or without consideration of frictional effects and also covers the numerical treatment. Some numerical approaches treat collision and contact in a uniform way [161, 120], other methods separate them to avoid common related problems, e.g. spurious vibration [90].
In the present work the term *collision model* is used for a model representing the entire physical response of at least two dynamically or statically interacting structures. In cases where a distinction becomes important, a dynamic interaction is termed *dynamic collision*, while a static response is denoted as *static contact*. However, the term *contact* is also often used to point out a relation to the contact surface, e.g. contact space, contact point or contact force. Furthermore, the proposed collision model distinguishes between a collision response in the *normal space* and the *tangent space* of the contact surface, while the latter is modeled by an appropriate *friction model*.

Collision models for rods. In contrast to developments of rod theories and rod models, there exist only few works on the representation of collisions of rod-like structures. These almost belong exclusively to the field of computer graphics. Early simulations of contacting or colliding rod-like structures were published by Lenoir *et al.* [136] and Phillips *et al.* [188], where material torsion were not resolved. Besides the works related to rod models, similar collision models were proposed for comparable reduced-order structures, e.g. models for cloth [36, 238, 228]. Indeed, rods and membranes share the common property that inconsistent penetrations must be avoided, in particular where dealing with visualizations. In these papers two different approaches are used to formulate contact forces, which can be taken as a classification of presently existing methods. One comprises penalty methods, the other termed non-penetration methods or constraint-based methods in subsequent papers [188, 42, 223, 27, 256]. As stated in [223] this terminology can be misleading, since also penalty methods are employed to handle constraints.
In general, penalty methods and constraint-based methods are employed to model the collision response between arbitrary structures. The following remarks focus on rod structures considered in the present work. However, the described properties of both approaches are generally valid for any other kind of colliding structures.
Penalty methods relate the contact forces to a measure of interpenetration, e.g. the penetration depth of two colliding structures. Such methods are simple by construction, but an appropriate stiffness of a penalty-spring and often also a penalty-damper have to be prescribed. Such penalty collision models were applied to the simulation of rod-like structures by Lenoir *et al.* [136], Bertails *et al.* [28, 27] and Vetter *et al.* [256]. In case of constraint-based methods, position constraints or velocity constraints are incorporated into the motion of the colliding structures, which avoids mutual interpenetration, as employed by Phillips *et al.* [188] and Choe *et al.* [42]. Spillmann *et al.* [225, 224] proposed a collision model for Cosserat rods that combines the accuracy and physical correctness of a constraint-based method with the efficiency of a penalty method. Based on the penetration depth of two rods, a spring force

is computed that exactly compensates this penetration. This can be interpreted as a special constraint regarding positions.
Rod models usually assume rigidity of cross sections, so that any collision model has to handle the rigid part in an appropriate way. In general, for rigid bodies no deformation of the structure is considered and, as a result, the level of abstraction of ongoing collisions is high which saves computational time. By neglecting any deformation process, the contact force instantaneously changes the momentum of the colliding structures. As stated in [223], that is why collision handling of rigid bodies is a famous and difficult problem. Furthermore, due to the rigid body assumption the momentum is transferred instantaneously through the colliding structures. As a consequence, simultaneous collisions of numerous structures become a global problem. Such *multiple collision* regions further complicate a simulation and require special numerical techniques. In case of penalty methods an artificial elasticity is introduced, so that the problem remains a local problem for a simultaneous collision, but disproportionately small time steps are required to ensure numerical stability and physical correctness [25, 223].
To date, there exists a huge amount of literature on collision modeling for rigid bodies. In the field of multibody dynamics, effects of any surrounding fluid are mostly neglected as the focus usually lies on the interaction of rigid and elastic bodies. In the recent past, many studies on collision handling for rigid bodies were published in the field of computer graphics resulting in major progress in terms of the handling of numerous simultaneously colliding structures under consideration of friction. The renowned work by Guendelman *et al.* from 2003 [90] proposed an impulse-based collision model, where the non-penetration constraints are satisfied by imposing corrective impulsive forces, that discontinuously modify the velocities of the colliding structures. These impulses are computed globally by means of an iterative procedure, which enables a simulation of a multiple collision of rigid bodies at the same time. Comparable strategies belonging to the group of constraint-based collision models were proposed by Bender and Schmidt 2006 [24] and Tonge *et al.* 2012 [243]. Pure penalty methods were also used in rigid body dynamics and other applications [98, 61, 234], but with limited success due to several disadvantages, such as reduced physical justification and the difficulty of specifying an appropriate stiffness constant [224].
Unlike collisions of rigid bodies, a collision model for soft deformable structures only requires to handle the non-penetration constraint and no further instantaneous transfer of momentum. Multiple simultaneous collisions still yield local problems, since the compression and decompression during the collision process is resolved and thus also the transfer of momentum between the structures. As usual, the constraint at the contact surface can be achieved by constraint-based methods and penalty methods [224, 223].

5.1.1 Penalty versus constraint-based methods

Regarding the collision modeling the Cosserat rod combines features of deformable structures and rigid bodies. While single rod elements behave like rigid bodies the interaction between the elements captures the deformability of the rod. Such a hybrid form requires an appropriate collision model able to describe both effects. In principle, for any structure - deformable or rigid - an interpenetration must be avoided during the collision process. As already mentioned, this is accomplished either by penalty methods or by constraint-based methods. In the following, advantages and disadvantages of both methods are weighted against each other, and the more suitable approach is chosen in terms of the present situation.

Penalty methods. Penalty methods are based on a spring-like force which is proportional to a measure of interpenetration and provide a temporal continuous contact force. In contrast to that, constraint-based methods instantaneously correct a violation of non-penetration. This generates discontinuous contact forces which are more difficult to handle from a numerical point of view. A further advantage of penalty methods is the simple implementation, since a penetration between two colliding structures is often easily accessible. On the other hand, the estimation of the spring constant is very complicated and sometimes described as "black art" [160]. For few scenarios, mostly involving single collisions of similar shaped structures such as spheres of equal size, the stiffness can be calibrated and assumed constant. In some enhanced approaches the spring constant is recomputed for each single collision using additional ordinary differential equations to capture the collision constraint in normal direction [120, 198]. The situation is complicated in the general case of simultaneous multiple collisions of arbitrary shaped structures. The stiffness of the penalty spring may have to vary considerably to avoid excessive penetration, as illustrated in Fig. 5.2. Maintain-

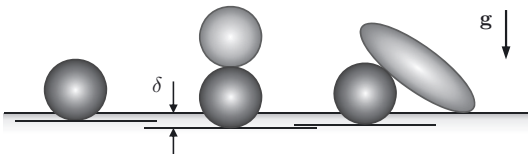

Figure 5.2: *Static contact of a single dark sphere with a wall modeled by a penalty method. When using a global predefined spring constant the penalty depth δ can vary considerably depending on the particular situation.*

ing a uniform global behavior, i.e. a comparable penetration depths, with a global choice of the stiffness constant is impossible in general cases. Instead, dynamic quantities of the colliding structures, such as inertia, external loads etc., need to be used to derive an appropriate spring for each individual collision. As a result, such a penalty method looses the advantage of an easy implementation and, furthermore, is almost indistinguishable from a constraint-based method. Indeed, as stated by Baraff [17], the penalty method converts the constrained problem to an unconstrained problem where simply the deviations from the constraint are penalized. As a result, satisfaction of the constraint is encouraged but not strictly enforced. For three-dimensional convex structures this approximation is permitted, since minor penetrations are barely of influence. In contrast, for thin shells or cloth excessive interpenetration results in sizable intersections of structures and influence the physical behavior, which must be avoided. To overcome this problem, often the spring constant is significantly increased to keep an interpenetration reasonably small. However, large stiffness causes stiff behavior of the underlying differential equations of motion, which often become numerically unstable or at least require very small time steps to the detriment of efficiency of large-scale simulations.

Constraint-based methods. As an alternative to the penalty approach, constraint-based methods incorporate the non-penetration constraints directly in the equations of motion of the colliding structures. The main difference is that constraint-based methods avoid an interpenetration and hence might better just be termed non-penetration methods. Furthermore, non-penetration methods do not require additional parameters, e.g. a spring constant, and

are able to handle the general case of multiple simultaneous collisions of different structures. A disadvantage is the increased effort required for their implementation.
The methodology of a constraint-based collision response can be applied to both, deformable and rigid structures, which is important for Cosserat rods sharing both properties. For deformable structures the collision response is usually resolved in space and time. The collision constraints solely have to realize the non-penetration of both structures at the contact surface so that any normal relative velocity vanishes after contact, i.e. $v'_{\mathrm{n}} = 0$. Here, v_{n} is the normal relative velocity at the moment of first contact and v'_{n} the normal relative velocity after collision. Especially for rigid bodies the compression and decompression during the collision process, intentionally, is not resolved but is accounted for by collision constraints. In this case, the constraint for the relative velocity is given by $v'_{\mathrm{n}} = -e\, v_{\mathrm{n}}$, where e is the coefficient of restitution modeling the influence of viscoelastic processes of deformation during the collision (see *Poisson's hypothesis* below). Obviously, the velocity constraints for deformable structures are a subset of the constraints for rigid bodies with $e = 0$. Static contact between resting structures with $v'_{\mathrm{n}} = v_{\mathrm{n}} = 0$ is included as well. The constraint-based approach can, therefore, be applied to a general class of problems, including dynamic collisions and static contact for arbitrary structures. Moreover, frictional forces acting in the tangent space also can be modeled by constraints which further extends the field of application of the approach. Due to the generality of constraint-based methods this strategy is followed here.

Numerical aspects. From a mathematical point of view the motion of colliding structures constitutes a system of constrained differential equations, more precisely inequality-constrained differential equations since only the interpenetration has to be avoided but not a separation [17]. In case of frictionless collision the non-penetration constraints can be formulated as a so-called linear complementary problem (LCP) [18], whose solution is NP-hard [223]. Similar systems of inequality-constrained differential equations result for cases where friction is considered but are considerably more complex, and the efficient numerical treatment of such kinds of problems is still subject of ongoing research [223, 16].
From a different point of view, an overall system of constrained differential equations usually can be divided into coupled subsystems. Especially in the field of collision handling each subsystem is represented by the equations of motion of a single structure. The coupling of these subsystems is described by collision constraints. In general, coupled systems can be treated numerically by the monolithic and the partitioned coupling approach, analogous to the coupling of fluid and structure equations. In the former case, the constraints are directly incorporated into the system of equations and the entire coupled system is numerically treated as a whole. With partitioned coupling the subsystems remain separated, while the constraints are realized by an exchange of coupling quantities. In case of collision modeling, these can be interpreted as contact forces. From a mathematical point of view, the contact forces play the role of Lagrange multipliers [34, 25].
The clear advantage of partitioned coupling is that it allows simple implementation by a combination of existing and optimized solvers for the coupled subsystems, i.e. solvers for the unconstrained equations of motion. The collision constraints are incorporated as contact forces, which are treated as common external forces. Hence, the collision response can be switched on as a modular feature, simply by adding the contact forces to the equations of motion. On the other hand, monolithic approaches generally yield high numerical accuracy and good stability, even for large time step sizes. In the present work the partitioned approach is used since the collision model for Cosserat rods proposed here can be applied to

other structures as well without further development effort. The somewhat reduced numerical accuracy is compensated by using a slightly smaller time step size.
Ensuring numerical stability of partitioned coupling approaches is not an easy task. If the coupling force is solely formulated in terms of quantities at the old time level, the coupled problem may become numerically unstable, so that these coupling strategies are often termed weak coupling approaches [156, 154]. To ensure stability the coupling must contain an implicit part, i.e. the contact force has to be formulated with consideration of quantities at the new time level. This usually requires an iterative procedure between the coupled subsystems or at least multiple executions of each subsolver within one time step.
For this purpose predictor-corrector methods are often employed and are widely used in the field of constraint simulations [223]. In a predictor step, the equations of motion are solved without constraints, so that the intermediate solution violates the constraints. Afterwards, a corrective force, an acceleration or a momentum transfer can be computed by means of the predicted solution and the desired constraints. In the correction step, the equations of motion are integrated in time again, now incorporating of the corrective forces which act against the violation of the constraints, so that these are met at the new time level. Using an appropriate temporal discretization with a time step size Δt the constraint is not exactly met at the end of the time step in the general case of nonlinear equations of motion, such as for Cosserat rods, but exhibits a splitting error. As stated in [223], the numerical error is linear dependent on Δt (see section 5.5, below). For linear equations of motion of rigid bodies, in contrast, the constraints are met exactly.
In principle, the predictor-corrector strategy can be applied multiple times within a time step to reduce the numerical error and the violation of the constraint, using the solution of the first correction step as a predictor for the second iteration step, and so on. On the other hand, a major objective is to minimize the required number of iterations, since the multiple solution of the subsystems drastically increases the computational effort. Regarding collision handling of rigid bodies or more complex structures like shells or membranes, the one-step predictor-corrector strategy seems to be sufficient and has been employed frequently, not only in the community focusing on collisions. Indeed, in the present framework of the immersed boundary method, the predictor-corrector strategy is called “direct forcing” and used to impose constraints on the velocity field of a fluid (Section 4.2).

5.1.2 Proposed collision model

The collision model proposed is suitable for rigid and deformable structures making it well suited for Cosserat rods including both properties. It follows the well-established constraint-based strategy, where the constraints are imposed by iteratively computed impulsive forces [161, 90, 24]. The collision model is able to represent frictional effects as well as lubrication effects and does not separate static contact and dynamic collisions. This is achieved by defining the contact force in the geometrical center of the contact region, which avoids spurious vibrations. Moreover, the model is able to handle multiple simultaneous collisions and, hence, is well-suited for simulations of large numbers of interacting elastic rods. Besides the computation of contact forces, each collision model must involve a strategy for collision detection which becomes computationally expensive for complex shaped structures. To respond to this need, an efficient algorithm for estimating the distance between two rods is proposed as well.

The entire procedure required to compute the collision response between the structures involved consists of the following four steps:

1. Detection of possible contacts between the simulated rod structures. More precisely, contact detection between the structural elements given by the spatial discretization detailed in Section 5.2.
2. Calculation of the collision response between colliding pairs of two elements, called single collision. This is detailed in Section 5.3.2.
3. Determining the collision response for multiple simultaneous collisions when more than two elements are in contact at the same time. The underlying linear complementary problem is solved by an iterative procedure based on the treatment of single collisions as described in Section 5.3.3.
4. Solving the equations of motion for each Cosserat rod with additional collision loads obtained by step 1-3.

With this approach, the collision is treated fully explicitly in time in a simple staggered manner, visualized in Fig. 5.3.

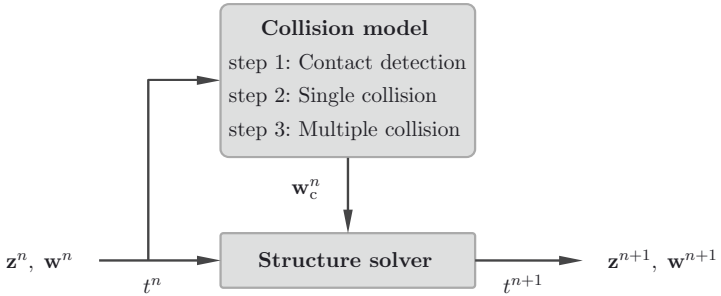

Figure 5.3: *Flowchart of the coupling strategy between the collision model and the structure solver. Shown is the exchange of data within one time step $t \in [t^n, t^{n+1}]$. At time level t^n the state of the rod element $\mathbf{z}^n$, including the velocities, and the external loads $\mathbf{w}^n$ acting on the rod element are transferred to the collision module. With the given quantities the collision loads $\mathbf{w}_c$ are calculated successively by executing step 1 up to step 3. Afterwards, $\mathbf{w}_c^n$ is communicated to the structure solver, where $\mathbf{z}^{n+1}$ and $\mathbf{w}^{n+1}$ at the next time level t^{n+1} are calculated.*

5.2 Contact detection

5.2.1 General approach

Often, the contact detection is identified as the bottleneck in terms of the computational time, so that substantial work has been done in this field, comprehensively reviewed by Van den Bergen [252]. As described in Section 4.6, a spatial subdivision is used, where the entire computational domain as well as the rods are divided into smaller parts, i.e. subdomains and structural elements, where each subdomain fully or partially contains a number of rod elements. Due to the relatively small number of elements in a subdomain, the spatial distance

between them can be computed in an efficient way. If the distance decreases below a critical value the collision response between the colliding structures is computed afterwards. The contact detection between the Cosserat rods is divided into two steps: 1. The determination of collision pairs each consisting of two structural elements. 2. The calculation of the contact point for each collision pair.

5.2.2 Collision pairs

According to the spatial discretization explained in Section 3.2.2, each Cosserat rod consists of N_e structural elements. Let E be the set of all elements within the computational domain and S the set of all rod structures. At the beginning of every time step each element $e \in E$ is checked for an ongoing impact with another element, i.e. that the distance between two elements decreases below a critical value. As a restriction, at most one colliding element $e_\mathrm{c} \in E$ per structure $s \in S$ is detected for the element e, i.e.

$$e_\mathrm{c}: \quad E \times S \to E, \;\; (e,s) \mapsto e_\mathrm{c}\,, \tag{5.1}$$

where e_c satisfies the condition of the smallest distance

$$\forall \;\; \tilde{e} \in s \backslash o: \quad d_\mathrm{sp}(e,e_\mathrm{c}) \leq d_\mathrm{sp}(e,\tilde{e})\,. \tag{5.2}$$

Here, $d_\mathrm{sp}(e,\tilde{e})$ is the distance between two conceived spheres enveloping element e and $\tilde{e}$. The set $o = \{e, ...\}$ consists of excluded elements, e.g. e itself or elements that are too far away to be in contact with e, i.e. $d_\mathrm{sp} > d_\mathrm{crit} \geq 0$. In the rare case of an ambiguity of e_c one of these is chosen at random. After all pairs of elements are detected by using the approximated distance d_sp, a more precise distance d between the elements is evaluated by a different algorithm defined below. Pairs which do not fulfill the condition $d \leq d_\mathrm{crit}$ are deleted from the list of detected pairs. For all remaining pairs the collision response is computed.

5.2.3 Distance and contact point

Each pair consists of two structural elements. Since the rods are restricted to a strip shape in the present case, their thickness is much smaller than their width and their length. Hence, the structural elements are geometrically well approximated by the center plane bounded by the width and length of the element. This greatly simplifies the contact detection and evaluation of the smallest distance between two elements. Nevertheless, the determination of the exact distance and contact point is challenging due to numerous possible arrangements of both elements. Here, an iterative procedure is used to evaluate the two nearest points $\mathbf{x}_e$ and $\mathbf{x}_{\tilde{e}}$ on the center planes of element e and $\tilde{e}$, presented in Alg. 5.1. Since the colliding elements have a finite thickness $T > 0$ the corresponding vector $\mathbf{d} = \mathbf{x}_e - \mathbf{x}_{\tilde{e}}$ overestimates the distance between e and $\tilde{e}$, as shown in Fig. 5.4b. Taking into account the individual thickness of both elements the true distance is given by

$$d = \|\mathbf{d}\| - (T_e + T_{\tilde{e}})/2\,, \tag{5.3}$$

while the common contact point is approximated by

$$\mathbf{x}_\mathrm{c} = \mathbf{x}_e + \frac{T_e}{T_e + T_{\tilde{e}}}\,(\mathbf{x}_{\tilde{e}} - \mathbf{x}_e)\,. \tag{5.4}$$

Note, that $\mathbf{x}_c$ only coincides with the exact contact point if the distance is $d = 0$, i.e. both elements touch each other.
The main idea of the distance search algorithm is to iterate $\mathbf{x}_e^k$ and $\mathbf{x}_{\tilde{e}}^k$ until the solution is converged. Initially, $\mathbf{x}_e^0$ and $\mathbf{x}_{\tilde{e}}^0$ are set to the center point position of the corresponding element. Then, $\mathbf{x}_e^k$ is orthogonally projected by an operation $\mathcal{P}$ to the plane of the other element. This gives the smallest distance between $\mathbf{x}_e^k$ and the element $\tilde{e}$ and thus $\mathbf{x}_{\tilde{e}}^{k+1} = \mathcal{P}[\mathbf{x}_e^k, \tilde{e}]$ is a good estimation for the distance so far. If the projected point lies outside the bounded plane of $\tilde{e}$, it is projected back to the element borders, so that $\mathbf{x}_{\tilde{e}} \leftarrow \mathcal{B}[\mathbf{x}_{\tilde{e}}, \tilde{e}]$, with the bounding operation $\mathcal{B}$. Within the same iteration step this cut orthogonal projection (COP) is done for the second element in the same way.
The proposed procedure only detects one smallest distance. In some cases a line segment or a surface area define the region of smallest distance, e.g. if both element planes are parallel to each other. Assuming that the collision force acting equally distributed in the contact region an equivalent single force can be found which acts at an appropriately chosen contact point $\mathbf{x}_c$. This point is well-defined by the geometric center of the contact region. The latter can be obtained by a projection of the element borders onto a virtual plane which is perpendicular to the vector $\mathbf{d}$, see Fig. 5.4b. Then, the contact region is given by the intersection area of both projections. By using the Sutherland-Hodgman algorithm [233] the borders of the intersection area can be easily extracted. Last but not least the geometric center has to be calculated.

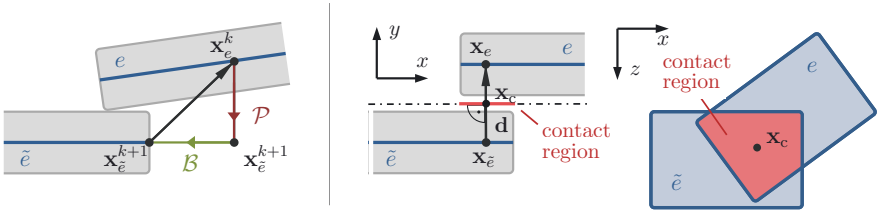

a) kth iteration of contact point $\mathbf{x}_{\tilde{e}}^{k+1}$ *b)* $\mathbf{x}_c$ *and* $\mathbf{d}$ *in geometrical center of contact region*

Figure 5.4: *Determination of contact point* $\mathbf{x}_c$ *and distance vector* $\mathbf{d} = \mathbf{x}_e - \mathbf{x}_{\tilde{e}}$ *between two colliding elements* e *and* $\tilde{e}$*. Basically, the algorithm consists of two parts. a) An iterative procedure to determine one smallest distance part of the contact region, using a projection operation* $\mathcal{P}$ *followed by a bounding operation* $\mathcal{B}$ *in each iteration cycle. b) In cases of a contact region of smallest distance, computation of the geometrical and correction of* $\mathbf{x}_c$ *and* $\mathbf{d}$*.*

For reasons of efficiency, an arbitrary contact point within the contact region is chosen in several different methods, e.g. an edge point of the elements [90]. However, if the contact point is not corrected to the geometrical center position, a moment acts on the colliding structure which is followed by a rotational motion. In the next time step the contact point is moved and usually an opposite moment results due to the collision response, and so on. By using the geometrical center as the contact point a much more stable behavior can be expected. As a consequence the *jitter* effect, i.e. spurious vibrations, can be reduced. Furthermore, the contact pressure acting at the contact region is treated more physically by using an equivalent single force acting at the geometrical center position.

foreach *colliding pair* e,$\tilde{e}$ **do**
  initialize $\mathbf{x}_e^0$, $\mathbf{x}_{\tilde{e}}^0$
  while *iteration* **do**
    project $\mathbf{x}_e^k$ to plane of $\tilde{e}$:
    $\mathbf{x}_{\tilde{e}}^{k+1} = \mathcal{P}[\mathbf{x}_e^k, \tilde{e}]$
    if $\mathbf{x}_{\tilde{e}}^{k+1}$ *outside* $\tilde{e}$ **then**
      bound $\mathbf{x}_{\tilde{e}}^{k+1}$ to plane of $\tilde{e}$:
      $\mathbf{x}_{\tilde{e}}^{k+1} = \mathcal{B}[\mathbf{x}_{\tilde{e}}^{k+1}, \tilde{e}]$
    end
    $\mathbf{x}_e^{k+1}$ analog
  end
end

Algorithm 5.1: *Determination of contact points* $\mathbf{x}_e$ *and* $\mathbf{x}_{\tilde{e}}$ *as well as the distance vector* $\mathbf{d}$ *between two colliding elements* e, $\tilde{e}$.

5.3 Constraint-based collision model

5.3.1 Role of rod elements for collision handling

From a numerical point of view, each structural element of the discretized Cosserat rod (Fig. 3.1) may be regarded as a rigid body influenced by external and internal loads [131]. Forces and moments due to an ongoing collision between elements can simply be added to the external loads. The advantage is that existing and well established collision models for rigid bodies can be used. Conversely, models for rigid bodies can easily be extended to deformable structures, which are discretized by structural elements.
In the following, the collision model is derived in terms of such discrete structural elements. The corresponding equations of motion for a single element, shown in Fig. 5.5, are given by

$$\mathbf{M} \cdot \partial_t \mathbf{z} = \mathbf{w} \tag{5.5}$$

$$\partial_t \mathbf{y} = \mathbf{z}\,, \tag{5.6}$$

with the twist $\mathbf{z} = [\mathbf{v}, \boldsymbol{\omega}]^\top$ representing the velocity of the element by its linear velocity $\mathbf{v} = \partial_t \mathbf{c}$ and its angular velocity $\boldsymbol{\omega}$. According to the staggered discretization of the structures, the element center point is defined as $\mathbf{c} = (\mathbf{c}_{i-1} + \mathbf{c}_i)/2$, the geometrical mean of the vertex positions $\mathbf{c}_{i-1}$ and $\mathbf{c}_i$. The angular velocity is $\boldsymbol{\omega} = 2\,\partial_t \mathbf{q}_i {}^* \overline{\mathbf{q}}_i$, with the quaternion $\mathbf{q}_i$ at the center point position $\mathbf{c}$. The motion of the body is affected by forces $\mathbf{f}$ and moments $\mathbf{m}$, which are combined to the wrench $\mathbf{w} = [\mathbf{f}, \mathbf{m}]^\top$. Since each element is part of a Cosserat rod, $\mathbf{w}$ captures internal stresses due to a deformation of the rod and external fluid loads $\overset{\triangledown}{\mathbf{f}}$, $\overset{\triangledown}{\mathbf{m}}$ caused by the fluid-structure interaction. Gravitational forces are included in the wrench as well, if present in the problem considered. Here, the wrench acts at the center $\mathbf{c}$, so that no other moment is generated by $\mathbf{f}$. The inertia of the element is combined to the inertia matrix

$\mathbf{M} = m\,\mathbb{I} \oplus \mathbf{I}$, with the identity matrix $\mathbb{I}$, the mass of the element m and its tensor of inertia $\mathbf{I}$.

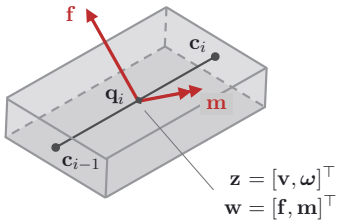

Figure 5.5: *Structural element of a discretized Cosserat rod. It is connected to further elements at the vertex positions* $\mathbf{c}_{i-1}$ *and* $\mathbf{c}_i$*, as shown in Fig. 3.1. The rotation of an element is represented by a quaternion* $\mathbf{q}_i$ *at the geometrical center. Each element may be regarded as a rigid body, where its linear velocity* $\mathbf{v}$ *and angular velocity* $\boldsymbol{\omega}$ *are determined by the force* $\mathbf{f}$ *and moment* $\mathbf{m}$ *acting on the center of mass. Velocities and loads are combined to the twist* $\mathbf{z}$ *and the wrench* $\mathbf{w}$*, respectively.*

5.3.2 Single collision

Two structural elements are in contact if the smallest distance d is less than a critical distance, i.e. $d \leq d_{\text{crit}}$. In that case, the collision response between the colliding elements is computed by the present collision model. The situation of a pair of elements is shown in Fig. 5.6. As described by Mirtich and Canny [161] three assumptions are commonly made to estimate the collision response, which are described in the following.

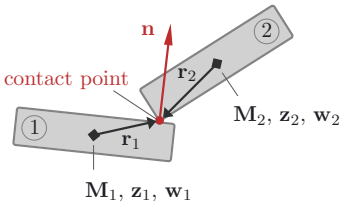

Figure 5.6: *Single collision between two elements, labeled with 1 and 2. Both elements touch each other in a contact region, here a contact point, as one special case. The orientation of the collision force is given by the normal vector* $\mathbf{n}$ *pointing from element 1 to element 2. The vector* $\mathbf{r}$ *pointing from the element center to the contact point, the geometrical center of the contact region. The motion of each rigid element is defined by an inertia matrix* $\mathbf{M}$*, the twist* $\mathbf{z}$ *and a wrench* $\mathbf{w}$*, which determine the collision response.*

Assumption 1: Infinitesimal collision time. The time scale of collision processes between the structures is much smaller than the long-term behavior, often focused in dynamic simulations. The more restrictive assumption of an infinitesimally small collision time results in two simplifications. First, the position and orientation of the colliding structures can be treated as constant over the period of collision and the collision model only acts on the velocities of the structures. Second, for an infinitesimally collision time the collision force has an impulsive nature (high amplitude over a very short time) which causes an instantaneous change of the velocities of dynamically colliding structures. Due to the discontinuous

change of the velocities, the collision response can be described more easily by a change of momentum of the structures between the state before, and the state after the collision. The impulsive collision force then is replaced by a transfer of momentum. In the literature this transfer of momentum is usually called collision impulse, with its unit being mass times velocity [36, 84, 90, 24, 234, 243]. This term is also used in the present work. Employing both simplifications the equations of motion (5.5), (5.6) of the two elements simplify to

$$\mathbf{z}_1' = \mathbf{z}_1 + \mathbf{M}_1^{-1}\cdot(\mathbf{w}_1\,\Delta t_\mathrm{c} + \mathbf{i}_1) \tag{5.7a}$$

$$\mathbf{z}_2' = \mathbf{z}_2 + \mathbf{M}_2^{-1}\cdot(\mathbf{w}_2\,\Delta t_\mathrm{c} + \mathbf{i}_2)\,, \tag{5.7b}$$

with the twist $\mathbf{z}$ before, and $\mathbf{z}'$ after the period of collision $\Delta t_\mathrm{c} \to 0$ due to the effect of the resulting collision impulse wrench $\mathbf{i} = [\mathbf{p}, \mathbf{l}]^\top$, including the linear momentum $\mathbf{p}$ and the angular momentum $\mathbf{l}$. Since only a linear momentum acts at the contact point, the angular momentum can be expressed by $\mathbf{p}$ using the vector $\mathbf{r}$, which connects the element center with the contact point (Fig. 5.6). Therefore, the impulse wrenches are given by

$$\mathbf{i}_1 = -\mathbf{C}_1^\top\cdot\mathbf{p} \tag{5.8a}$$

$$\mathbf{i}_2 = \quad \mathbf{C}_2^\top\cdot\mathbf{p}\,, \tag{5.8b}$$

with the matrix $\mathbf{C} = (\mathbb{I}, [\mathbf{r}]_\times)$ defining the relation between the linear and angular momentum. Recall, that the term $[\mathbf{r}]_\times$ is the skew matrix of the radius vector $\mathbf{r}$, such that $[\mathbf{r}]_\times\cdot\mathbf{p} = \mathbf{r}\times\mathbf{p}$. To estimate the required impulse $\mathbf{p}$, two further assumptions are necessary.

Assumption 2: Poisson's hypothesis. As mentioned above, the complex collision process is commonly not resolved in time. According to [161] Poisson's hypothesis is an approximation of that process, capturing the basic behavior with a compression and a restitution phase. By means of the normal relative contact velocity v_n at the contact point the Poisson's hypothesis states

$$v_\mathrm{n}' = -e\,v_\mathrm{n}\,. \tag{5.9}$$

The elastic behavior involving, e.g., internal friction is simply captured by the restitution coefficient $e \in [0, 1]$ which describes the ratio of the normal relative velocity after the impact, v_n', and before the impact, v_n. While for $e = 1$ the collision is modeled as perfectly elastic, for $0 \leq e < 1$ some kinetic energy is dissipated during the collision process and the collision is inelastic. In case of $e = 0$ the collision is perfectly plastic. In this case the kinetic energy is fully dissipated and the structures do not move apart after the impact, so that the relative velocity $\mathbf{v}_\mathrm{r} = \mathbf{v}_{\mathrm{c},2} - \mathbf{v}_{\mathrm{c},1}$ is $\mathbf{v}_\mathrm{r} = 0$. For each element the normal relative contact velocity is given by $v_\mathrm{n} = \mathbf{v}_\mathrm{r}\cdot\mathbf{n}$, where $\mathbf{n}$ is the vector in normal direction pointing from element 1 to element 2 (Fig. 5.6). The corresponding velocity at the contact point is related to the twist $\mathbf{z}$, i.e. $\mathbf{v}_\mathrm{c} = \mathbf{v} + \boldsymbol{\omega}\times\mathbf{r} = \mathbf{C}\cdot\mathbf{z}$.

Assumption 3: Coulomb friction model. In addition to the relations in normal direction the model needs to be supplemented with focus in tangential direction. Two regimes can be distinguished: Static friction for non-moving structures which are in contact, and kinetic friction, where the structures slide on each other with a relative tangential velocity $v_\mathrm{t} \neq 0$. Coulomb's law of friction states that the kinetic friction is independent of the sliding velocity v_t. Furthermore, the friction force in tangential direction is proportional to the normal part of the contact force. The Coulomb friction model, written in terms of the normal linear

impulse $\mathbf{p}_\mathrm{n} = p_\mathrm{n}\,\mathbf{n}$ and tangential linear impulse $\mathbf{p}_\mathrm{t} = p_\mathrm{t}\,\mathbf{t}$ reads

$$v_\mathrm{t} = 0 \quad \Leftrightarrow \quad p_\mathrm{t} \leq \mu_\mathrm{s}\, p_\mathrm{n} \quad \text{(sticking)} \tag{5.10}$$

$$v_\mathrm{t} \neq 0 \quad \Leftrightarrow \quad p_\mathrm{t} = \mu_\mathrm{k}\, p_\mathrm{n} \quad \text{(sliding)}\,, \tag{5.11}$$

where μ_s, is the coefficient of static friction and μ_k, the coefficient of kinetic friction, with $\mu_\mathrm{s} \geq \mu_\mathrm{k}$. The tangential velocity is given by $v_\mathrm{t} = \mathbf{v}_\mathrm{r} \cdot \mathbf{t}$, where the unit vector $\mathbf{t}$ identifying the sliding direction in the tangent space of the contact region. It is approximated by $\mathbf{t} = -\mathbf{v}_\mathrm{t}/\|\mathbf{v}_\mathrm{t}\|$, with the tangential part of the initial relative velocity $\mathbf{v}_\mathrm{t} = \mathbf{v}_\mathrm{r} - (\mathbf{v}_\mathrm{r} \cdot \mathbf{n})\,\mathbf{n}$.

Using the above assumptions the impulse $\mathbf{p}$ can be derived by following the strategy of Guendelman *et al.* [90]. First, it is assumed that the colliding elements stick at the contact point in tangential direction, i.e. $v'_\mathrm{t} = 0$. Along with Poisson's hypothesis $v'_\mathrm{n} = -e\, v_\mathrm{n}$, the impulse $\mathbf{p}$ has to cause a change in the relative velocity

$$\Delta\mathbf{v} = \mathbf{v}_\mathrm{r} - \mathbf{v}'_\mathrm{r} \tag{5.12a}$$

$$= \mathbf{v}_\mathrm{r} + e\,(\mathbf{v}_\mathrm{r} \cdot \mathbf{n})\,\mathbf{n}\,, \tag{5.12b}$$

where $\mathbf{v}_\mathrm{r} = \mathbf{C}_2 \cdot \mathbf{z}_2 - \mathbf{C}_1 \cdot \mathbf{z}_1$. With the equations of motion (5.7a), (5.7b) for the twists $\mathbf{z}_1$ and $\mathbf{z}_2$ together with the definition of the impulse wrenches (5.8a), (5.8b) the impulse for the sticking mode then is

$$\mathbf{p} = \mathbf{p}_\mathrm{w} - \mathbf{K}^{-1} \cdot \Delta\mathbf{v}\,, \tag{5.13}$$

where $\mathbf{K} = \mathbf{C}_2 \cdot \mathbf{M}_2^{-1} \cdot \mathbf{C}_2^\top + \mathbf{C}_1 \cdot \mathbf{M}_1^{-1} \cdot \mathbf{C}_1^\top$ is the symmetric positive definite system matrix and $\mathbf{p}_\mathrm{v} = -\mathbf{K}^{-1} \cdot \Delta\mathbf{v}$ imposes the required velocity constraint in terms of $\Delta\mathbf{v}$, commonly used in collision models without consideration of external loads. The effects of external loads $\mathbf{w}$, such as the gravitational acceleration, are captured by $\mathbf{p}_\mathrm{w} = -\Delta t_\mathrm{c} \mathbf{K}^{-1} \cdot (\mathbf{C}_2 \cdot \mathbf{M}_2^{-1} \cdot \mathbf{w}_2 - \mathbf{C}_1 \cdot \mathbf{M}_1^{-1} \cdot \mathbf{w}_1)$. As required, $\mathbf{p}$ achieves the sticking of both elements in tangential direction. If it is inside the friction cone, i.e. $p_\mathrm{t} \leq \mu_\mathrm{s}\, p_\mathrm{n}$ according to (5.10), $\mathbf{p}$ is a sufficient collision impulse. Otherwise, the structures will slide on each other and the collision impulse needs to be adjusted. For the sliding mode (5.11) the impulse takes the form

$$\mathbf{p} = p_\mathrm{n}\,\mathbf{n} + p_\mathrm{t}\,\mathbf{t} \tag{5.14a}$$

$$= p_\mathrm{n}\,(\mathbf{n} + \mu_\mathrm{k}\,\mathbf{t})\,. \tag{5.14b}$$

Using Eq. (5.13) the normal part of $\mathbf{p}$ can be obtained by

$$p_\mathrm{n} = \frac{\mathbf{K} \cdot \mathbf{p}_\mathrm{w} \cdot \mathbf{n} \;-\; \Delta\mathbf{v} \cdot \mathbf{n}}{\mathbf{K} \cdot (\mathbf{n} + \mu_\mathrm{k}\,\mathbf{t}) \cdot \mathbf{n}} \tag{5.15a}$$

$$= \; p_\mathrm{w,n} + p_\mathrm{v,n} \tag{5.15b}$$

ensuring that the normal velocity constraint $\Delta\mathbf{v} \cdot \mathbf{n}$ is conserved after changing the tangential part of $\mathbf{p}$ in case of sliding, similar to [90] but taking into account the external loads $\mathbf{w}$.
In the derivations (5.13), (5.15b) it is assumed that both external loads $\mathbf{w}$ as well as the initial relative velocity $\mathbf{v}_\mathrm{r}$ cause an interpenetration of the colliding structures, e.g. if a single structure vertically collides with a wall under additional influence of gravity. The collision impulse has to overcome both, the velocity difference and the gravitational load. Accordingly, both derived impulses $\mathbf{p}_\mathrm{w}$ and $\mathbf{p}_\mathrm{v}$ act against this interpenetration, so that $\mathbf{p}_\mathrm{w} \cdot \mathbf{n} > 0$ and

$\mathbf{p}_\mathrm{v}\cdot\mathbf{n} > 0$. From a mathematical point of view, Eq. (5.13) also allows negative values $\mathbf{p}_\mathrm{w}\cdot\mathbf{n} < 0$ and $\mathbf{p}_\mathrm{v}\cdot\mathbf{n} < 0$. However, such impulses are non-physical since separating structures can not transfer momentum or forces. Hence, any collision impulse must not be attractive, i.e. $\mathbf{p}\cdot\mathbf{n}>0$ for arbitrary computed impulses $\mathbf{p}$, which is usually termed Signorini condition [223, 243]. To fulfill this condition the parts $p_\mathrm{w,n}$ and $p_\mathrm{v,n}$ in Eq. (5.15b) are modified to

$$p_\mathrm{w,n} = \begin{cases} \frac{\mathbf{K}\cdot\mathbf{p}_\mathrm{w}\cdot\mathbf{n}}{\mathbf{K}\cdot(\mathbf{n}+\mu_\mathrm{k}\,\mathbf{t})\cdot\mathbf{n}}, & \text{if} \quad \mathbf{p}_\mathrm{w}\cdot\mathbf{n} > 0 \\ 0, & \text{otherwise} \end{cases} \quad \text{and} \quad p_\mathrm{v,n} = \begin{cases} \frac{\mathbf{K}\cdot\mathbf{p}_\mathrm{v}\cdot\mathbf{n}}{\mathbf{K}\cdot(\mathbf{n}+\mu_\mathrm{k}\,\mathbf{t})\cdot\mathbf{n}}, & \text{if} \quad \mathbf{p}_\mathrm{v}\cdot\mathbf{n} > 0 \\ 0, & \text{otherwise} \end{cases} . \tag{5.16}$$

A pseudo code of the model for a single collision with tangential friction is given in Alg. 5.2.

foreach *single collision* **do**

relative velocity:
$\mathbf{v}_\mathrm{r} = \mathbf{C}_2\cdot\mathbf{z}_2 - \mathbf{C}_1\cdot\mathbf{z}_1$

velocity difference:
$\Delta\mathbf{v} = \mathbf{v}_\mathrm{r} + e\,(\mathbf{v}_\mathrm{r}\cdot\mathbf{n})\,\mathbf{n}$

impulses for sticking:
$\mathbf{p}_\mathrm{w} = -\mathbf{K}^{-1}\cdot\Delta t_\mathrm{c}\,(\,\mathbf{C}_2\cdot\mathbf{M}_2^{-1}\cdot\mathbf{w}_2 - \mathbf{C}_1\cdot\mathbf{M}_1^{-1}\cdot\mathbf{w}_1)$
$\mathbf{p}_\mathrm{v} = -\mathbf{K}^{-1}\cdot\Delta\mathbf{v}$
$\mathbf{p} = \mathbf{p}_\mathrm{w} + \mathbf{p}_\mathrm{v}$

check friction cone:
$p_\mathrm{n} = \mathbf{p}\cdot\mathbf{n}$
$p_\mathrm{t} = \|\mathbf{p} - p_\mathrm{n}\,\mathbf{n}\|$

if $p_\mathrm{t} > \mu_\mathrm{s}\,p_\mathrm{n}$ **then**

tangential vector:
$\mathbf{v}_\mathrm{t} = \mathbf{v}_\mathrm{r} - (\mathbf{v}_\mathrm{r}\cdot\mathbf{n})\,\mathbf{n}$
$\mathbf{t} = -\mathbf{v}_\mathrm{t}/\|\mathbf{v}_\mathrm{t}\|$

impulses for sliding:
$\mathbf{p}_\mathrm{w} = \frac{\mathbf{K}\cdot\mathbf{p}_\mathrm{w}\cdot\mathbf{n}}{\mathbf{K}\cdot(\mathbf{n}+\mu_\mathrm{k}\,\mathbf{t})\cdot\mathbf{n}}\,(\mathbf{n}+\mu_\mathrm{k}\,\mathbf{t})$
$\mathbf{p}_\mathrm{v} = \frac{\mathbf{K}\cdot\mathbf{p}_\mathrm{v}\cdot\mathbf{n}}{\mathbf{K}\cdot(\mathbf{n}+\mu_\mathrm{k}\,\mathbf{t})\cdot\mathbf{n}}\,(\mathbf{n}+\mu_\mathrm{k}\,\mathbf{t})$

end

prevent attraction:
if $\mathbf{p}_\mathrm{w}\cdot\mathbf{n} \le 0$ **then** $\mathbf{p}_\mathrm{w} = \mathbf{0}$
if $\mathbf{p}_\mathrm{v}\cdot\mathbf{n} \le 0$ **then** $\mathbf{p}_\mathrm{v} = \mathbf{0}$

corrected collision impulse:
$\mathbf{p} = \mathbf{p}_\mathrm{w} + \mathbf{p}_\mathrm{v}$

end

Algorithm 5.2: *Computation of the collision impulse* $\mathbf{p}$ *for a single collision between a pair of structural elements including tangential friction. Non-physical attractive impulses are avoided, i.e.* $\mathbf{p} = \mathbf{0}$ *if* $\mathbf{p}\cdot\mathbf{n} \le 0$ *for any* $\mathbf{p}$ *(Signorini condition).*

5.3.3 Multiple collision

In some cases, e.g. numerous densely arranged structures, more than two structural elements are in contact at the same impact time. The corresponding collision response of each element, hence, depends on the reaction of the others. This scenario is called multiple collision. As for a single collision, the multiple collision must satisfy the Signorini condition, which means that any collision force only acts if the contact is not separating and thus the collision impulse (5.13) must not be attractive, i.e. $\mathbf{p} \cdot \mathbf{n} > 0$. The mechanical equations to be solved for a collision in combination with the Signorini condition result in an optimization problem, known as linear complimentary problem (LCP). Further information in this regard can be found in [243]. Here, the LCP is numerically treated by an iterative projected Gauß-Seidel method (PGSM) [243] in which an additional projection step is used to satisfy the Signorini condition. A pseudo code of the PGSM is shown in Alg. 5.3. This approach is advantageous

while *iteration* **do**
  foreach *colliding pair* **do**
    relative velocity:
    $\mathbf{v}_\mathrm{r} = \mathbf{C}_2 \cdot \mathbf{z}_2^{k-1} - \mathbf{C}_1 \cdot \mathbf{z}_1^{k-1}$
    velocity difference:
    $\Delta\mathbf{v} = \mathbf{v}_\mathrm{r} + e\,(\mathbf{v}_\mathrm{r} \cdot \mathbf{n})\,\mathbf{n}$
    current total impulse:
    $\Delta\mathbf{p}_\mathrm{w} = -\mathbf{K}^{-1} \cdot \Delta t_\mathrm{c}\,(\,\mathbf{C}_2 \cdot \mathbf{M}_2^{-1} \cdot \mathbf{w}_2^{k-1} - \mathbf{C}_1 \cdot \mathbf{M}_1^{-1} \cdot \mathbf{w}_1^{k-1})$
    $\Delta\mathbf{p}_\mathrm{v} = -\mathbf{K}^{-1} \cdot \Delta\mathbf{v}$
    $\mathbf{p} = \mathbf{p}_\mathrm{w}^{k-1} + \Delta\mathbf{p}_\mathrm{w} + \Delta\mathbf{p}_\mathrm{v}$
    corrective impulses:
    $\mathcal{S}\,[\mathbf{p}, \Delta\mathbf{p}_\mathrm{w}, \Delta\mathbf{p}_\mathrm{v}]$
    corrective impulse wrenches:
    $\Delta\mathbf{i}_\mathrm{w1} = -\mathbf{C}_1^\top \cdot \Delta\mathbf{p}_\mathrm{w} \qquad \Delta\mathbf{i}_\mathrm{w2} = \mathbf{C}_2^\top \cdot \Delta\mathbf{p}_\mathrm{w}$
    $\Delta\mathbf{i}_\mathrm{v1} = -\mathbf{C}_1^\top \cdot \Delta\mathbf{p}_\mathrm{v} \qquad \Delta\mathbf{i}_\mathrm{v2} = \mathbf{C}_2^\top \cdot \Delta\mathbf{p}_\mathrm{v}$
    update collision quantities:
    $\mathbf{p}_\mathrm{w}^k = \mathbf{p}_\mathrm{w}^{k-1} + \Delta\mathbf{p}_\mathrm{w}$
    $\mathbf{w}_{1,2}^k = \mathbf{w}_{1,2}^{k-1} + \Delta\mathbf{i}_{\mathrm{w}1,2}/\Delta t_\mathrm{c}$
    $\mathbf{z}_{1,2}^k = \mathbf{z}_{1,2}^{k-1} + \mathbf{M}_{1,2}^{-1} \cdot \Delta\mathbf{i}_{v1,2}$
    $\mathbf{i}_{1,2}^k = \mathbf{i}_{1,2}^{k-1} + \Delta\mathbf{i}_{\mathrm{w}1,2} + \Delta\mathbf{i}_{\mathrm{v}1,2}$
  end
end

Algorithm 5.3: *Projected Gauß-Seidel method (PGSM) to solve linear complimentary problem (LCP) in case of a multiple collision. The operator $\mathcal{S}$ represents a common single collision between the pair of elements, given in Alg. 5 2. The initial conditions of the iteration are $\mathbf{p}_\mathrm{w}^0 = \mathbf{0}$, $\mathbf{i}_{1,2}^0 = \mathbf{0}$, $\mathbf{w}_{1,2}^0 = \mathbf{w}_{1,2}^n$ and $\mathbf{z}_{1,2}^0 = \mathbf{z}_{1,2}^n$, where $\mathbf{z}^n$ and $\mathbf{w}^n$ are the twists and external loads of each element before the collision at time $t = t^n$. After reaching convergence at kth subcollision the total collision wrench $\mathbf{w}_\mathrm{c}^n = \mathbf{i}^k/\Delta t_\mathrm{c}$ of a collided element is passed to the structure solver, as sketched in Fig. 5.3.*

because only a sufficient model for single collisions between two structures is required, as the one presented in Section 5.3.2. The solution then is obtained by iterating over all pairs of elements which are in contact. It is assumed that all pairs are colliding one after another, called *subcollision*. Since there is no difference between a subcollision and a single collision, Alg. 5.2 can be applied to each subcollision. Provided the collision time of a single collision is infinitesimal both the monolithic solution of the LCP and a sequential solution by the PGSM are equivalent.

It is well known, that Gauß-Seidel methods are not easy to handle in parallel and require special techniques for their parallelization [243]. Here, a simpler approach is used. The LCP is performed only on one processor per time step. After the solution is found iteratively, the required data of collision impulses are communicated back to the processors where the corresponding rod structure is treated. Although this is not the most efficient way, regarding the FSI problems simulated in the present work, the PGSM needs much less computational effort compared to the overall computing time.

During the iteration the impulse wrench $\mathbf{i}$ acting on a colliding element is incrementally updated by a corrective impulse $\Delta\mathbf{i}$ in each subcollision, i.e. $\mathbf{i}^k = \mathbf{i}^{k-1} + \Delta\mathbf{i}$ with $\mathbf{i}^0 = \mathbf{0}$. As for a single collision, the impulse wrench is split into two parts $\mathbf{i} = \mathbf{i}_\mathrm{w} + \mathbf{i}_\mathrm{v}$. While $\mathbf{i}_\mathrm{w}$ represents the collision response on external loads $\mathbf{w}$, the part $\mathbf{i}_\mathrm{v}$ is the response to dynamically colliding structures. This distinction is essential, because external loads and velocity differences yield a different collision response and, correspondingly, need to be treated by different constraints as illustrated by the two limiting cases. In the special case of pure external loads and zero velocity the collision impulse is $\mathbf{i} = \mathbf{i}_\mathrm{w}$, e.g. for a simultaneous multiple static contact under the influence of gravity. Neglecting tangential effects, the zero velocity of the structures then has to be conserved to avoid an interpenetration. Therefore, the conceived momentum due to external loads $\hat{\mathbf{i}} = \mathbf{w}\Delta t_\mathrm{c}$ has to be compensated by $\mathbf{i}$, so that $\mathbf{i}\cdot\mathbf{n} = -\hat{\mathbf{i}}\cdot\mathbf{n}$. In the opposite case of a pure dynamic collision with a relative approaching velocity $\mathbf{v}_\mathrm{r}\cdot\mathbf{n} > 0$ and without external loads, the collision impulse is $\mathbf{i} = \mathbf{i}_\mathrm{v}$. For a fully elastic collision, captured by a restitution coefficient $e = 1$, the collision impulse has to overcome at most twice the impulse at the impact $\hat{\mathbf{i}} \sim \mathbf{v}_\mathrm{r}$ to invert the approaching velocity, i.e. $\mathbf{i}\cdot\mathbf{n} = -(1+e)\,\hat{\mathbf{i}}\cdot\mathbf{n}$. Consequently, for $e > 0$ the constraints are different for static and dynamic collisions, which requires a different treatment of $\mathbf{i}_\mathrm{w}$ and $\mathbf{i}_\mathrm{v}$.

Furthermore, due to the assumption of infinitesimally small collision time, $\Delta t_\mathrm{c} \to 0$, (Section 5.3.2) it is assumed that external loads do not change the linear and angular velocity of the structures when solving the LCP, i.e. $\mathbf{z}^k = \mathbf{z}^0$ for any $\mathbf{i}_\mathrm{w}$. However, external loads significantly affect the contact pressure between colliding structures and, hence, the tangential motion due to frictional effects. In addition, external loads are transferred to other contacted structures. For example, in case of a vertical stack of contacted structures under gravity the lowest structure is influenced by the weight of each structure above. To solve this "static" part of the collision response, the external load is updated during the PGSM by an impulse wrench $\mathbf{i}_\mathrm{w}^k = \mathbf{i}_\mathrm{w}^{k-1} + \Delta\mathbf{i}_\mathrm{w}$, i.e.

$$\mathbf{w}^k = \mathbf{w}^0 \quad + \quad \mathbf{i}_\mathrm{w}^k/\Delta t_\mathrm{c} \tag{5.17a}$$

$$= \mathbf{w}^{k-1} + \Delta\mathbf{i}_\mathrm{w}/\Delta t_\mathrm{c}\,, \tag{5.17b}$$

with the initial external wrench $\mathbf{w}^0 = \mathbf{w}^n$ before the collision at time $t = t^n$. Analogously, the impulse at the contact point of two colliding structures is $\mathbf{p}_\mathrm{w}^k = \mathbf{p}_\mathrm{w}^{k-1} + \Delta\mathbf{p}_\mathrm{w}$. As a counterpart, the dynamics of the colliding structures is influenced by impulses $\mathbf{i}_\mathrm{v} \sim \mathbf{v}_\mathrm{r}$ causing a change

of the relative velocity $\mathbf{v}_\mathrm{r}$ after each single collision. During the PGSM, the twist $\mathbf{z}$ for the kth subcollision of an element, updated by $\mathbf{i}_\mathrm{v}^k = \mathbf{i}_\mathrm{v}^{k-1} + \Delta\mathbf{i}_\mathrm{v}$, is given by

$$\mathbf{z}^k = \mathbf{z}^0 \quad + \mathbf{M}^{-1}\cdot\mathbf{i}_\mathrm{v}^k \tag{5.18a}$$

$$= \mathbf{z}^{k-1} + \mathbf{M}^{-1}\cdot\Delta\mathbf{i}_\mathrm{v}\,, \tag{5.18b}$$

where $\mathbf{z}^0 = \mathbf{z}^n$ is the twist before the collision. After the impulses $\mathbf{i}_\mathrm{w}$ and $\mathbf{i}_\mathrm{v}$ of each element are converged the corresponding collision wrenches $\mathbf{w}_\mathrm{c} = (\mathbf{i}_\mathrm{w} + \mathbf{i}_\mathrm{v})/\Delta t_\mathrm{c}$ are passed to the structure solver. The theory above and the resulting collision model are developed for a collision time $\Delta t_\mathrm{c} \to 0$. Since the structure solver is discretized in time with a finite time step Δt the collision time is selected to be equal to this time step, i.e. $\Delta t_\mathrm{c} = \Delta t$. This yields a first-order accurate approximation of the equations of motion (5.5), (5.6) in time.

5.3.4 Numerical stability

Due to the simple, fully explicit formulation of the collision loads with communication between the structures once per time step the collision model is a first-order accurate approximation in time, as described in Section 5.3.2. Outside the stability region the model is unstable and the simulation terminated. In that case the time step size is decreased or, in other words, the exchange of information between the colliding structures. Also the spatial discretization can influence the stability. Increasing the number of elements per structure often has a positive effect. It was experienced that the most efficient and simplest way to avoid stability problems is to increase the internal viscous damping of the structures which is a material parameter. In most of the simulations without viscous damping, the resulting dynamics of the colliding rods is not realistic, even if the simulation is stable. This is not really a problem, since every real structure loses energy due to dissipation processes, especially during collision event, where high deformation rates result in an increased damping.

5.3.5 Coefficient of restitution for Cosserat rods

The Cosserat rod model combines features of deformable structures and rigid bodies. While the cross sections of the rod behave perfectly rigid the interaction between them captures the deformability of the rod. As a result, a longitudinal collision (Fig. 5.7a) strongly differs from a lateral collision (Fig. 5.7b) because of the anisotropic nature of the Cosserat rod. Nonetheless, the constraint-based collision model can be applied for both cases using the general constraint (5.9), where the coefficient of restitution e is of crucial importance.
For a collision in longitudinal direction, the collision response is resolved in time and space by the structure solver. The collision constraints solely have to realize the non-penetration of both structures at the contact surface so that any normal relative velocity during contact vanishes. Starting from the beginning of contact the rod is deformed and internal energy is stored. The stored energy is released and the rod structure moves away from the wall with the same or a lower velocity, depending on the internally dissipated amount of energy. During a finite contact time, the corresponding contact force is continuous in time (see Fig. A.14) which seems to contradict the infinitesimal contact time $\Delta t_\mathrm{c} \to 0$ and the impulsive nature of the collision force, assumed in Section 5.3.2. Nevertheless, such impulsive forces can also be

used to impose the required non-penetration constraint for a resolved finite collision process. This is done by applying a series of impulses during contact, where each impulse enforces the required constraint $v_\mathrm{n}' = 0$ and avoids a mutual penetration. From a numerical point of view, the collision model applies one impulse per time step Δt until the rod moves away from the wall. In [161] this technique is called micro-collision impulses.
On the contrary, a lateral collision only needs infinitesimally small time due to the assumption of rigid cross sections. The deformation of the cross sections during a collision is not resolved but is captured by the restitution coefficient $e \in [0, 1]$ depending on internal dissipation. The impulsive collision force causes a discontinuous change in the normal relative velocity according to the constraint $v_\mathrm{n}' = -e\, v_\mathrm{n}$.
Obviously, the velocity constraint $v_\mathrm{n}' = 0$ for a resolved longitudinal collision is a subset of the general constraint $v_\mathrm{n}' = -e\, v_\mathrm{n}$ for a lateral collision. This also means, that the general constraint can be used for both cases with only the coefficient of restitution e being adjusted. While for a longitudinal collision $e = 0$ is mandatory to enforce zero relative velocity, the coefficient of restitution has to be adapted in case of a lateral collision. Here, this is done by introducing a corrected coefficient of restitution e_corr which depends on the angle of incidence ϕ, illustrated in Fig. 5.7c.

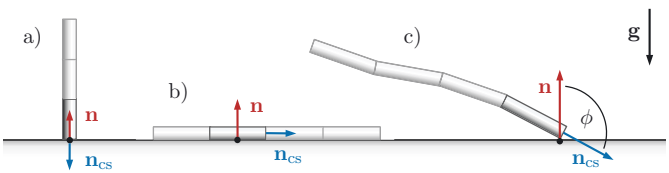

Figure 5.7: *Collision of a Cosserat rod with a wall in a) longitudinal direction b) lateral direction and c) oblique direction. The angle of incidence ϕ is defined between* $\mathbf{n}$*, the unit normal vector pointing in direction of the contact force, and* $\mathbf{n}_\mathrm{cs}$*, the normal vector of the cross section.*

The ratio between e_corr and $e \in [0, 1]$ is given by

$$\frac{e_\mathrm{corr}}{e} = H_\epsilon[\cos(\phi_\mathrm{crit}) - |\cos(\phi)|] \,, \tag{5.19}$$

where H_ϵ is an appropriate smoothed unit step function, e.g. $H_\epsilon(x) = \frac{1}{2} + \frac{1}{\pi} \arctan\left(\frac{x}{\epsilon}\right)$, with a smoothing parameter $0 < \epsilon \ll 1$ set to $\epsilon = 10^{-3}$ here. For a longitudinal collision with $\phi = 0$ (or $\phi = \pi$), the ratio is $e_\mathrm{corr}/e = 0$, whereas for a lateral collision with $\phi = \pi/2$, the ratio gives $e_\mathrm{corr}/e = 1$. The critical angle ϕ_crit specifies for which angles the collision process is resolved by the Cosserat rod model. In the present work it was chosen to be $\phi_\mathrm{crit} = \pi/8$, i.e. the collision process is resolved if the angle of inclination is at most $22.5\,^\circ$.

5.4 Lubrication model

The collision model presented so far provides a simple model for dry collisions between rods under influence of external loads such as gravitational loads. For fluid-structure interaction problems considered here the collision response is further influenced by external fluid loads. Especially the dynamics of the fluid film between two approaching structures plays an important role in modeling wet collisions. This so-called lubrication process influences the normal as well as the tangential collision response. In the former case the fluid film between the two approaching structures drains out which yields an additional damping during collision. In case of a pure tangential relative motion of the structures the generated shear flow results in an additional viscous friction, which also has a dampening effect on the collision. In particular in large-scale simulations, the lubrication of thin fluid films can not be resolved by the present numerical approach using a temporally constant fluid grid, since each fluid film needs a sufficiently fine spatial resolution, which would drastically increase the overall computational effort. In order to avoid this, the lubrication is only resolved by the fluid solver until the chosen grid size Δx is not fine enough to capture the ongoing drainage process or the shear flow between the colliding rods. Spatially unresolved lubrication processes and corresponding fluid loads are then modeled by an appropriate lubrication model which has to be adjusted to the geometrical properties of the colliding structures, e.g. lubrication models for spheres [120] or ellipsoids [8]. To the knowledge of the author, no lubrication models for rod-like geometries were published in the literature so far. The lubrication model proposed here is based on a velocity-proportional damping, which is the simplest approach to capture the influence of lubrication. The associated lubrication force $\mathbf{f}_{\mathrm{lub}}$ is given by

$$\mathbf{f}_{\mathrm{lub}} = D_{\mathrm{n}}\,\mathbf{v}_{\mathrm{n}} - D_{\mathrm{t}}\,\mathbf{v}_{\mathrm{t}}\,, \tag{5.20}$$

where $\mathbf{v}_{\mathrm{n}} = (\mathbf{v}_{\mathrm{r}} \cdot \mathbf{n})\,\mathbf{n}$ is the part of the relative velocity of both approaching elements in normal direction, and $\mathbf{v}_{\mathrm{t}} = \mathbf{v}_{\mathrm{r}} - \mathbf{v}_{\mathrm{n}}$ the part in tangential direction. Determining the damping constants D_{n} as well as D_{t} is a formidable task, since the lubrication process can vary considerably with the relative orientation between the structural elements. In principle, the damping constants D_{n} and D_{t} must depend on the contact region, where a larger contact area A_{c} results in a higher damping rate. Assuming a small thickness h of the fluid film and a parallel orientation of the elements, both damping constants can be derived analytically. According to [15], the damping parameter D_{n} in case of an approach in normal direction is given by

$$D_{\mathrm{n}} = \rho_{\mathrm{f}}\,\nu_{\mathrm{f}}\left(\frac{A_{\mathrm{c}}}{h}\right)^{2}\frac{\beta(1)}{h}\,, \tag{5.21}$$

with $\beta(\kappa = 1) = 0.42$ and $\kappa = W/L$ the relation between the lateral and longitudinal expansion of the contact surface. As a first approximation, it is assumed that $W = L = \sqrt{A_{\mathrm{c}}}$, i.e. the contact surface almost has a square shape. For a pure tangential relative motion, the corresponding damping constant is [190]

$$D_{\mathrm{t}} = \rho_{\mathrm{f}}\,\nu_{\mathrm{f}}\,\frac{A_{\mathrm{c}}}{h}\,. \tag{5.22}$$

Both damping constants should be considered only as a rough estimation. The situation is more complex in the general case, where the colliding elements are approaching in normal and tangent space simultaneously. In the present model, this situation is taken into account

by a simple superposition of both parts. Nevertheless, the estimation allows an access to the correct order of magnitude of the lubrication forces and, furthermore, the model works very well for pure normal and tangential lubrication as demonstrated in Section A.9. As mentioned above, the model is derived for elements oriented in parallel during a collision which does not hold in the general case. In order to apply the model to cases with inclined elements, the spatially varying film thickness h is approximated by a constant film thickness $\overline{h}$, defined as the average of h over the contact region (see Fig. 5.8b). If $\overline{h}$ is larger than a critical film thickness h_{crit}, the ongoing lubrication is resolved by the fluid solver. Otherwise, in a range of $0 < \overline{h} \leq h_{\text{crit}}$ the lubrication process is modeled according to Eq. (5.20). As proposed in [120], the critical distance is set to $h_{\text{crit}} = 4\Delta x$.
With the damping constants defined by Eqs. (5.21) and (5.22) the velocity-proportional lubrication force (5.20) reads

$$\mathbf{f}_{\text{lub}} = \rho_{\text{f}}\, \nu_{\text{f}}\, \frac{A_{\text{c}}}{h} \left[\beta(1) \frac{A_{\text{c}}}{h^2}\, \mathbf{v}_{\text{n}} - \mathbf{v}_{\text{t}} \right] , \tag{5.23}$$

while the corresponding lubrication wrenches are

$$\mathbf{w}_{\text{lub},1} = -\mathbf{C}_{lub,1}^{\top} \cdot \mathbf{f}_{\text{lub}} \tag{5.24a}$$

$$\mathbf{w}_{\text{lub},2} = \quad \mathbf{C}_{lub,2}^{\top} \cdot \mathbf{f}_{\text{lub}} \, . \tag{5.24b}$$

By analogy with the modeling of dry collisions, the matrix $\mathbf{C}_{\text{lub}} = (\mathbb{I}, [\mathbf{r}_{\text{lub}}]_{\times})$ defines the relation between the force $\mathbf{f}_{\text{lub}}$ and the resulting angular momentum generated by $[\mathbf{r}_{\text{lub}}]_{\times}\mathbf{f}_{\text{lub}}$. The vector $\mathbf{r}_{\text{lub}}$ is pointing from the element center to the point of attack of the lubrication force. As shown in Fig. 5.8b, a lubrication process and a dry collision response do not have to exclude themselves. In this case, the lubrication wrenches $\mathbf{w}_{\text{lub}}$ must be added to the wrenches $\mathbf{w}_{\text{c}}$, computed for a dry collision (see Section 5.3.3), to provide the total collision response on the rods.

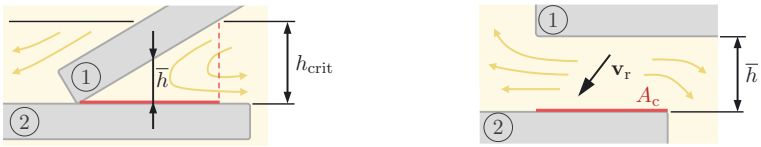

a) combination of dry contact and lubrication *b) pure lubrication process*

Figure 5.8: *Ongoing lubrication of a fluid film (yellow shaded area) between two structural elements a) without any dry contact and b) with contact between the rod elements. The distance $\overline{h}$ denotes an average thickness of the fluid film within the red colored contact region of area A_{c}. If $\overline{h}$ is larger than the critical distance, i.e. $\overline{h} > h_{\text{crit}}$, the lubrication process is assumed to be resolved by the fluid solver, while for $\overline{h} \leq h_{\text{crit}}$ the process is modeled by the proposed lubrication model.*

5.5 Validation and results

5.5.1 Newton's cradle

coefficient of restitution:
$e = 0,\ 1$

initial conditions:
$x_1|_{t=0} = 0\,\mathrm{m}$
$v_1|_{t=0} = 1\,\mathrm{m/s}$
$x_{2-5}|_{t=0} = 0.45\ \ldots\ 0.6\,\mathrm{m}$
$v_{2-5}|_{t=0} = 0\,\mathrm{m/s}$

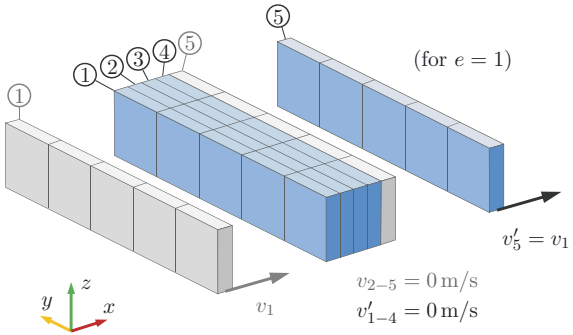

Figure 5.9: *Newton's cradle consisting of five laterally colliding rods. With an initial velocity v_1, rod 1 strikes a bundle of four rods, which are in contact and at rest. For $e = 1$ the force is transmitted through the rods, by which rod 5 moves away with velocity v_1, while rod 1 to 4 remain at rest.*

Newton's cradle is a common benchmark of multiple simultaneous collisions between rigid bodies, but can also be applied to Cosserat rods as shown in Fig. 5.9. Five rods are considered, all having equal properties. The first, rod 1, approaches the others, tightly packed and immobile, with velocity v_1. At the impact time $t = 0.4\,\mathrm{s}$, rod 1 hits the bundle of resting rods. This, indeed, is a multiple collision, since the corresponding collision response of each structure depends on the reaction of the other rods. As described in Section 5.3.3, the solution can be obtained by solving the underlying linear complimentary problem. Here, the LCP is solved by iterating over all single pairs which are in contact using the PGSM (Alg. 5.3). Due to conservation of momentum and kinetic energy rod 1 relays its velocity to rod 2, provided no energy is dissipated, i.e. $e = 1$. Because of the sequence of structures in contact, the process continues to each successive pair until rod 5 moves away with a velocity of $v_5' = v_1$. Here, two simulations were conducted, one with a coefficient of restitution $e = 1$, the other with $e = 0$. The simulations with the present collision model reproduce the theoretical results perfectly well, as shown in Fig. 5.10. Supplementary validation can be found in Appendix A.

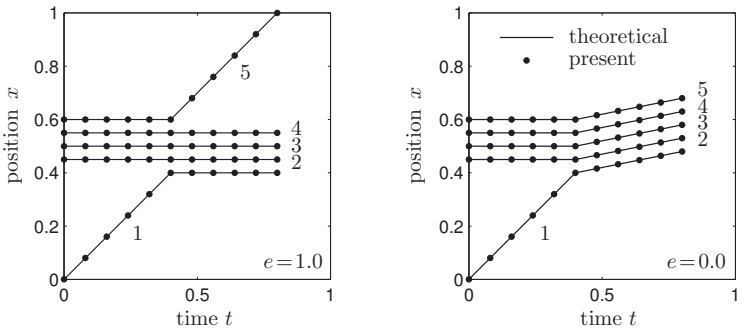

Figure 5.10: *Temporal evolution of rod positions during the collision process, for a coefficient of restitution $e = 1$ (left) and $e = 0$ (right). The rods are labeled from 1 up to 5.*

5.5.2 Ring-shaped rods

$g = 10\,\mathrm{m/s^2}$	gravitational acceleration
$N_\mathrm{s} = 27$	number of structures
structure properties:	
$L = 0.5\,\mathrm{m}$	length
$W = 0.04\,\mathrm{m}$	width
$T = 0.01\,\mathrm{m}$	thickness
$\rho_\mathrm{s} = 1000\,\mathrm{kg/m^3}$	mass density
$E_\mathrm{s} = 1 \cdot 10^6\,\mathrm{N/m^2}$	Young's modulus
$G_\mathrm{s} = 1 \cdot 10^6\,\mathrm{N/m^2}$	shear modulus
	effective viscosities:
$c_\mathrm{e} = 1 \cdot 10^{-2}\,\mathrm{Ns}$	*extension*
$c_\mathrm{s} = 1 \cdot 10^{-2}\,\mathrm{Ns}$	*shearing*
$c_\mathrm{b} = 2 \cdot 10^{-5}\,\mathrm{Ns\,m^2}$	*bending*
$c_\mathrm{t} = 2 \cdot 10^{-5}\,\mathrm{Ns\,m^2}$	*torsion*
collision parameters:	
$e = 0$	coef. of restitution
$\mu_\mathrm{s} = 0.3$	coef. of static friction
$\mu_\mathrm{k} = 0.3$	coef. of kinetic friction

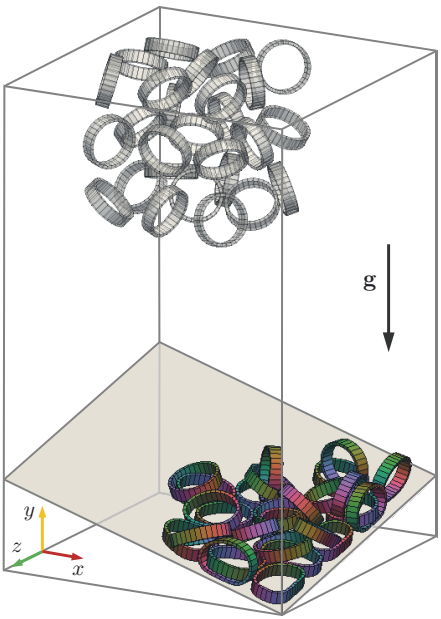

Figure 5.11: *Multiple collision of* 27 *ring-shaped rods. Initially, an array of* $3 \times 3 \times 3$ *rods are positioned at the top of the domain, where each rod is randomly oriented in space (transparent rods). Due to gravity the rods fall down on an inclined plane and collide with each other. Afterwards, the accumulation of contacted rods slides down the wall and comes to rest at the lower corner of the domain (colored rods).*

The configuration of numerous ring-shaped rods shown in Fig. 5.11 is used to test the collision model for multiple simultaneous collisions with a large variety of local collision scenarios. At the top of the domain an array of 27 structures is initialized. Each ring-shaped structure has a randomly generated orientation in space. The positions were chosen such that the center of the rings form an equidistant $3 \times 3 \times 3$ cubic lattice. Under the influence of gravity the rings fall down on an inclined planar wall. The chosen elasticity is quite small which results in large deformations of several rings due to collisions with walls or other rings. Moreover, self-collisions also occur in that case. An internal damping is added to the structure motion, so that all rings come to rest in the lower corner of the domain which allows to test the representation of static contact of structures. Shortly after the rings have reached the inclined wall the ring layers of different initial height collide with each other. Here, very complex dynamic collisions occur between two or more elastic rings. They slide down the plane and come to rest due to the influence of friction and internal dissipation with many structures being in static contact, as shown in Fig. 5.12a. This is a special case where the collision modeling generates difficulties. Because many rings are in contact at the same time the

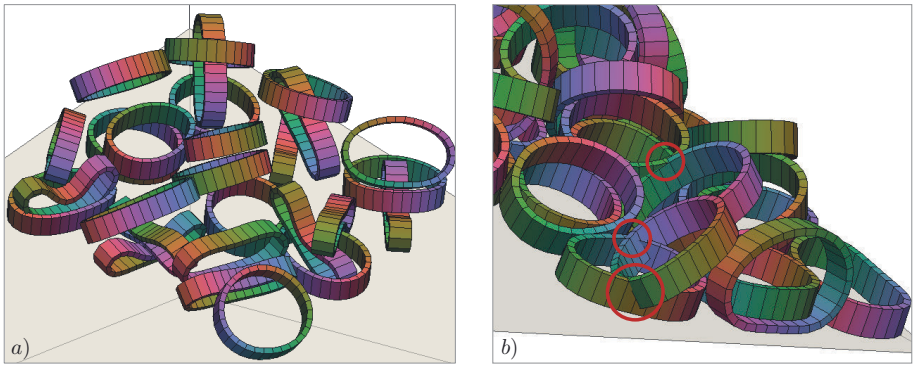

Figure 5.12: *Snapshot of colliding rods. a) Shortly after all rods impinged on the inclined wall, b) long after the rods came to rest at the lower corner of the domain. Large time steps Δt or non-converged solutions of the LCP may result in intersection of rods (red circles). The shown results were obtained with $\Delta t = 1 \cdot 10^{-4}$ s and a limitation of the PGSM to 10 iterations. Coloring of the rods according to their arc length.*

corresponding LCP has to be solved iteratively by the PGSM. When stopping the iterations before reaching convergence, e.g. in case where the iteration limit is exceeded, the resulting energy in the system can vary considerably between two time steps. This can cause some structures near rest to wiggle around their equilibrium. This unphysical effect is called *jitter* and is a common problem in the field of collision modeling for rigid bodies [243]. A further effect of an insufficient number of iterations is that the rods may intersect. The amount of intersection also is affected by the time discretization. By continuously applying impulses to impose the contact-constraints the numerical splitting error may accumulate and cause, e.g., significant intersections of rods after several time steps (Fig. 5.12, b). All identified problems mainly occur in case of resting contacts where the collision model operates in each time step and the error accumulation becomes important. In contrast to that, a dynamic collision between two rod is treated only by one collision impulse, so that numerical errors are negligible.

By appropriately decreasing the time step size and iterating the LCP until convergence the majority of jittering and intersections can be avoided. Especially in real time applications where a reduction of time step size and number of iterations is limited, more sufficient strategies are inevitable. Several techniques are proposed in the literature, e.g. the so-called *sleeping-method* which avoids jittering, where the structures near rest are simply temporarily removed from the simulation [243]. A similar strategy to avoid intersections is proposed in [90] where a *contact graph* is used in combination with a *shock propagation algorithm* that separates dynamic collisions and static contact.

5.5.3 Array of rods

$g = 10\,\mathrm{m/s^2}$	gravitational acceleration
$U = 1\,\mathrm{m/s}$	velocity of tube
$N_\mathrm{s} = 181$	number of structures

structure properties:

$L = 0.4\,\mathrm{m}$	length
$W = 0.04\,\mathrm{m}$	width
$T = 0.01\,\mathrm{m}$	thickness
$\rho_\mathrm{s} = 1000\,\mathrm{kg/m^3}$	mass density
$E_\mathrm{s} = 3 \cdot 10^5\,\mathrm{N/m^2}$	Young's modulus
$G_\mathrm{s} = 1 \cdot 10^5\,\mathrm{N/m^2}$	shear modulus
	effective viscosities:
$c_\mathrm{e} = 1\,\mathrm{Ns}$	*extension*
$c_\mathrm{s} = 1\,\mathrm{Ns}$	*shearing*
$c_\mathrm{b} = 1 \cdot 10^{-5}\,\mathrm{Ns\,m^2}$	*bending*
$c_\mathrm{t} = 1 \cdot 10^{-5}\,\mathrm{Ns\,m^2}$	*torsion*

collision parameters:

$e = 0$	coef. of restitution
$\mu_\mathrm{s} = 0.2$	coef. of static friction
$\mu_\mathrm{k} = 0.2$	coef. of kinetic friction

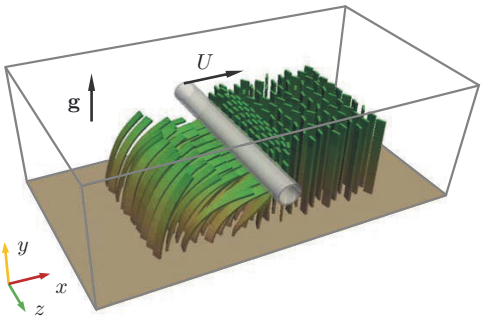

Figure 5.13: *Setup of densely arranged simplified aquatic plants, called canopy. The artificial canopy consists of* 181 *straight rods pinned to a wall in a staggered manner. The cross-section of each rod is randomly rotated around the y-axis. A glass tube is moved through the array of artificial plants which yields multiple simultaneous collisions between them. Coloring of the rods according to their arc length.*

A final setup is considered to illustrate the potential of the present collision model for complex fluid-structure interactions. The configuration addressed here is a simplified model of a dense submerged canopy in a river flow, focused in chapter 6. Due to the dense arrangement of the plants numerous collisions occur between them. In some real configurations a characteristic vortex pattern traveling in streamwise direction and causes a wavy collective bending of the rods, called *monami* [169]. The present study focuses on the collision process and does not represent any fluid. To generate a similar motion of the structures a glass tube is moved through the array of rods in x-direction. The rods are buoyant, as real plants, and internal dissipation by structural viscosity is added to make the dynamic behavior realistic. The array consists of 181 single plants which are arranged in a staggered manner with 10 rows of 10 and 9 rows of 9 structures. Furthermore, each rod is rotated by a randomly generated small angle around the y-axis.
At the beginning the structures are at rest. The glass tube moves with a constant velocity U through the artificial canopy which yields numerous collisions between the rods and the

tube, as well as between two or more rods. After the tube has left the canopy each structure shows a pendulum like motion due to the chosen values for buoyancy and rigidity. Because the structures do not oscillate synchronously in x-direction, a kind of a collision front is generated that moves through the canopy, similar to the *monami* phenomena (Fig. 5.14). During the entire simulation, all collisions are treated correctly by the proposed collision model. To get a converged solution of the LCP, the average number of iterations is about 15 after the glass tube has left the canopy. In the presence of the tube more rods are in contact at the same time such that the PGSM needs more iterations of about 50.

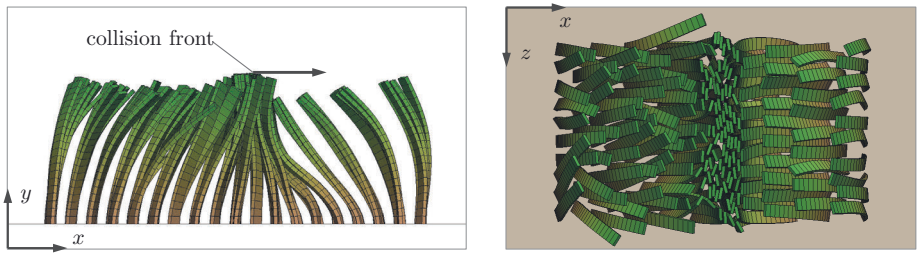

Figure 5.14: *Instantaneous situation of the artificial canopy after the glass tube has left the domain. Due to the phase shift between the induced pendulum-like motion of each rod, a collision front is generated and travels through the canopy, with numerous multiple simultaneous collisions. Coloring of the rods according to their arc length.*

6 Application to canopy flows

6.1 Introduction

The long-term goal beyond this work is to gain a deeper understanding of the physics behind the interaction of numerous slender rods with turbulent fluid flow. The present numerical method is designed especially for such configurations and enables to generate physical data from simulations beyond reach of other numerical and experimental studies. In the present work, the FSI approach is applied to simulate a unidirectional flow over flexible aquatic plants, a so-called canopy flow.
Aquatic plants are essential for the ecological quality of aquatic ecosystems and constitute a key topic due to their abundance and their various roles on different scales, ranging from the quality of drinking water taken from the local river to the large-scale impact on climate change. At river scale, canopies cause a reduction of velocity, sediment erosion, concentration of pollutants, etc. [168, 192, 33]. Recently, a new inter-disciplinary research area called "Hydrodynamics of aquatic ecosystems" is emerging due to the relevance and challenges of the topic [174].

Classification and terminology. Nepf [169] provides a comprehensive overview on canopy flows, which are usually classified into atmospheric and aquatic canopies. The rigidity of atmospheric plants, e.g. cereal plants, is usually higher compared to aquatic plants since aquatic canopies are supported by buoyancy to act against gravity in the competition for sunlight. Consequently, the deflection of single plants is smaller in case of atmospheric canopies [197, 62]. Due to the lower rigidity aquatic plants accommodate drag by changing their geometry while subjected to hydrodynamic loads, commonly termed as reconfiguration [257, 52]. This reconfiguration again modifies the impact on the fluid motion which constitutes a strongly coupled two-way fluid-structure interaction.
An additional classification is conducted by the submergence depth of canopies. Atmospheric canopies reveal no sharp upper boundary so that the submergence is very high. In aquatic canopies, however, the situation is more complex where the water depth is finite and usually restricted to moderate depths. Indeed, in case of higher depths the sunlight required for plant growth does not reach the ground. Based on the ratio between the water depth H and the height of plants after reconfiguration L^*, it is distinguished between deep submergence with $H/L^* > 10$, and shallow submergence with $H/L^* < 5$ which is common in aquatic systems [169]. While deeply submerged canopies show similarities to atmospheric canopies for sufficiently large ratios H/L^*, shallow submergence is characterized by substantially different turbulent structures [171].
Another important parameter is the density of the canopy, depending on the spacing between individual plants and the frontal area of a plant subject to the flow. Obviously, the behavior of sufficiently sparse canopies coincide with common boundary layer flows. However, dense

canopies generate a pronounced mixing layer at their top making the flow prone to Kelvin-Helmholtz instabilities [169]. Analysis of corresponding turbulent structures in dense shallow canopies of rigid elements showed that the flow is dominated by strong sweep and ejection events in the mixing layer [176]. Depending on the degree of reconfiguration of vegetation elements, the interaction between these coherent structures and the canopy results in different flow patterns [41, 175]. In this regard, the Cauchy number Ca is an important dimensionless number to distinguish between different types of vegetation. It is defined as

$$Ca = \frac{(\rho_f/2)\, U^2\, C_d\, WL}{E_s I / L^2}\,, \tag{6.1}$$

with the bulk velocity U, the drag coefficient C_d, the width W, the length L and the flexural rigidity $E_s I$ of an individual vegetation element. The Cauchy number represents the ratio between drag forces and elastic restoring forces, so that a high degree of reconfiguration relates to large values of Ca. Different mechanisms of fluid-structure interaction can be observed with increasing Ca, as illustrated in Fig. 6.1. Coherent structures generated by

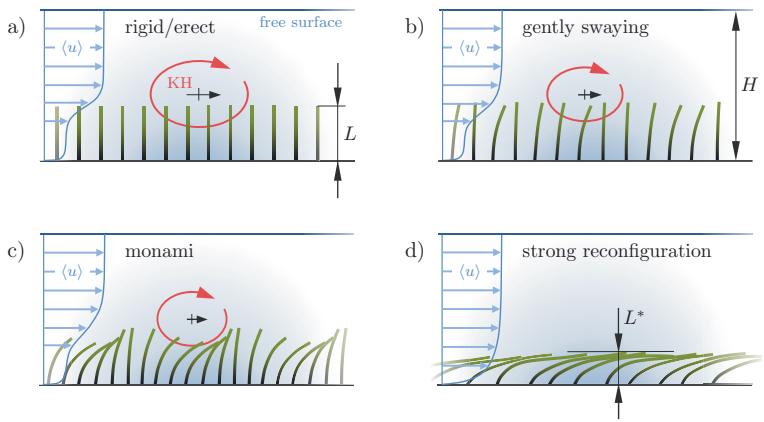

Figure 6.1: *Influence of Cauchy number Ca on the FSI of dense shallowly submerged canopies according to [176, 178]. a) For Ca = 0 vegetation elements (green) remain erect while a mixing layer is generated at top of the canopy. Kelvin-Helmholtz (KH) vortices (red) are convected in streamwise direction. b) At a certain value of Ca the elements start to sway independently with small amplitudes, called gently swaying. c) For larger Ca the elements are more reconfigured and exhibit highly coherent waving motion, called monami phenomenon (Japanese: mo = aquatic plant, nami = wave [3, 179]). d) Very large Ca result in a substantial reconfiguration with elements mainly aligned in streamwise direction. A mixing layer and corresponding KH-vortices are suppressed since the canopy top is fully covered by reconfigured elements. This prevents any momentum exchange in vertical direction.*

the shear layer are only one part of a particular hierarchy of scales observed in submerged canopies (Fig. 6.13, below). These range from the sub-plant scale over the wake on plant-scale, up to the shear layer generated on canopy scale and the scales of the boundary layer above

the canopy. Additionally, in natural rivers aquatic plants are often separated in patches, so that the patch scale is also important for some processes [174]. To date, the coexistence and interaction of different scales is not fully understood and constitutes a major challenge for experimental studies and numerical investigations.

Experimental studies on canopy flows. Due to the wide range of scales in aquatic canopies experimental studies range from field studies in real rivers to laboratory experiments with abstracted model canopies. The former generally address the patch scale or larger scales [230, 174] while smaller scales are generally not addressed since this is more convenient in a laboratory flume. Here, model canopies can be made of natural plants [106, 193], but due to the difficulties of conducting long term experiments with living plants and in order to focus on the fundamental effects, most of the studies in flumes have been conducted with model plants [167, 81, 265, 176, 220]. As demonstrated in [150, 205] model plants are indeed able to capture the behavior of living plants, e.g. drag forces and reconfiguration, and are usually shaped as cylinders or thin blades. Furthermore, the flexural rigidity of model plants can simply be adopted to a desired Cauchy number Ca and the corresponding regime of interest (Fig. 6.1). Shallow canopies made of rigid cylinders or blades were experimentally studied by [173, 176, 149, 178], while flexible model plants are employed in [83, 176, 153, 33]. As an example, Ghisalberti and Nepf [83] model each plant by a rigid stem which supports highly flexible plastic blades, mimicking the typical morphology of eelgrass.
Unfortunately, obtaining spatially detailed measurements inside the canopy is particularly difficult due to limited optical access. This also holds for data acquisition of the plant motion. Thus, most of the experimental studies mentioned above focused on drag forces, exerted by the canopy on the flow in relation to the reconfigured canopy height. Only very few experimental studies of flexible canopies were undertaken dealing with simultaneous measurements of blade motion and fluid flow, e.g. the study of Okamoto and Nezu [175, 178]. This is, however, a prerequisite for a deeper understanding of hydrodynamic processes in canopy flows. Consequently, data acquisition must be complemented by numerical studies which are discussed in the following.

Numerical simulations of canopy flows. Depending on the scales of interest different numerical models were employed for the simulation of canopy flows. In most cases it is sufficient to use a homogenized model representation of individual plants, especially when interested in average quantities, such as mean velocity profiles, Reynolds stresses etc. For atmospheric canopies, solving the Reynolds-averaged Navier-Stokes (RANS) equations using a homogenized drag is state of the art [19]. In submerged aquatic canopies, however, the reconfiguration is larger so that the RANS approach must be supplemented with deformable canopies [254, 58]. When interested in the nature of coherent structures, eddy-resolving approaches, e.g. LES, are employed to resolve large-scale coherent vortex structures. For the sake of simplicity, canopies can be still modeled as a time-independent homogeneous continuum. Shaw and Schumann [212] were the first in this direction who proposed a drag force proportional to the canopy density. A time-dependent flexible homogenized canopy in an LES was realized by Dupont *et al.* [62] for an atmospheric grain field.
Besides homogenized representation of vegetation, LES have also been used to study channel flows with resolved but only rigid structures. Several studies of rough walls made of a matrix of differently shaped obstacles have already attracted attention [155, 114, 227]. Further work in this direction, but with a clear focus on aquatic canopy flow, was undertaken in the group

of Nezu [177] simulating an experiment with rigid blades conducted in the same group [173]. Due to the fine spatial and temporal resolution required for these investigations, resolving simulations of the fluid-structure interaction in canopy flows are extremely costly, especially when reliable statistical data is accumulated over a longer time interval.
The fluid-structure coupling can be established by very different approaches ranging from methods using body-fitted grids to immersed boundary techniques [39]. Especially for the latter group it is comparatively easy to impose boundary conditions for complex time-dependent geometries, as it is the case for flexible structures of low rigidity which may even bend around each other during motion. In the literature only a few works can be found simulating the flow over arrays of flexible structures mimicking a canopy-like geometry. For instance, Yang *et al.* [267] employed an IBM to performed two-dimensional simulations of the flow around 16 rigid cylinders mounted elastically to the bottom wall. Yusuf *et al.* [270] computed the flow around 10 triangular and round structures undergoing only small deformations in a uniform cross-flow by means of an adapted mesh technique. Recently, IBM were combined with structure solvers able to represent large deformations [222, 239, 125], e.g. the IBM of Kim *et al.* who applied the method to a single flexible blade in cross-flow [125] (see validation Section 4.7.3). To date, only two numerical studies could be found in the literature where a larger number of highly flexible structures was simulated. To the knowledge of the author, the work of Marjoribanks [152, 153] provides the most advanced simulation of an entire canopy with up to 300 individual flexible elements in cross-flow. The geometrical description of the structures is relatively crude and the fluid load was computed using a simple local drag law. Furthermore, the level of resolution is below the state of the art for simulations of canopies made of rigid structures [177] or simulations of a single flexible structure undergoing large deformation [239]. Another work is [78], but the agreement with the experiment is not convincing. The lack of numerical studies demonstrates that simulating an entire canopy with individual structures being resolved is methodologically highly complex. With the present FSI approach this gap is closed and highly resolved simulations of canopies with hundreds of structures are possible. The LES of a selected model canopy is presented in the following sections. Already a first analysis of the data obtained delivers new insights into the nature of coherent structures in canopy flows, presented in Section 6.3.4.

6.2 Model canopy and numerical setup

6.2.1 Choice of model canopy

$g = 9.81\,\mathrm{m/s^2}$	grav. acceleration
fluid properties (open water channel):	
$H = 21\,\mathrm{cm}$	channel height
$\rho_\mathrm{f} = 1000\,\mathrm{kg/m^3}$	fluid density
$\nu_\mathrm{f} = 1 \cdot 10^{-6}\,\mathrm{m^2/s}$	kin. viscosity
$U = 0.2\,\mathrm{m/s}$	bulk velocity
structure properties (OHP slides):	
$L = 70\,\mathrm{mm}$	rod length
$W = 8\,\mathrm{mm}$	rod width
$T = 0.1\,\mathrm{mm}$	rod thickness
$\Delta S = 32\,\mathrm{mm}$	rod spacing
$\rho_\mathrm{s} = 1400\,\mathrm{kg/m^3}$	structure density
$E_\mathrm{s} = 4.8 \cdot 10^9\,\mathrm{N/m^2}$	Young's modulus
dimensionless quantities:	
$Re_H = 42000$	Reynolds number
$\rho_\mathrm{s}/\rho_\mathrm{f} = 1.4$	density ratio
$Ca \approx 17$	Cauchy number

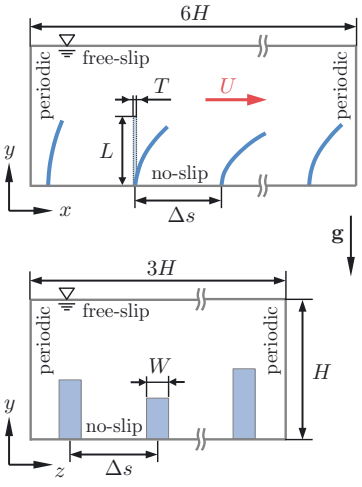

Figure 6.2: *Shallowly submerged canopy modeled as an array of flexible rectangular rods made out of polyester overhead projector (OHP) slides with fixation on the bottom plate (same spacing ΔS in x- and z-direction), corresponding to the experimental setup of [176] with an overview over the physical parameters.*

As mentioned above, artificial model canopies consisting of abstracted plants are able to capture the behavior of living plants as well as fundamental effects appearing in real canopy flows. The present numerical approach is optimized for zero-thickness rod structures with spatially constant properties. For this reason the model canopy chosen here is represented by an array of strip-shaped rods of vanishing thickness fixed to the bottom wall in a well-defined square arrangement, as sketched in Fig. 6.2. As a further simplification, all rods are of equal size and equal material properties to minimize the degrees of freedom of the model configuration. Even in case of this high level of abstraction the present setup is defined by 11 physical parameters, resulting in 8 independent dimensionless numbers. To find appropriate sets of parameters covering the physics of real canopies at different regimes is a formidable task. However, identical or similar types of artificial canopies were already focused in several laboratory experiments and thus provide appropriate parameter combinations for different flow regimes, e.g. those shown in Fig. 6.1. Here, the values of physical parameters were chosen according to the experimental work of Okamoto and Nezu [176] who studied a variety of shallowly submerged model canopies. All experiments were conducted in a tilting flume having a length of 10 m and a width of 0.4 m. The vegetation elements were made out of polyester overhead projector (OHP) transparencies and arranged over a length of 9 m in streamwise direction and the full channel width. In the following, the OHP slides are briefly referred to as blades.

Mean velocity profiles and Reynolds stress distributions are provided in [176] for different submergence depths and Cauchy numbers, making the experiment ideally suited for a direct comparison with the simulation. Here, one case at a moderate Ca was selected as it exhibits the *monami* phenomenon (Fig. 6.1c), i.e. a strong relation of coherent structures and an organized wavelike plant deflection. Related three-dimensional turbulent structures are very difficult to measure, so that the present simulation data can be used to ascertain physical mechanisms behind this phenomenon. The Reynolds number, based on the bulk velocity U and the channel height H, is $Re = UH/\nu_\mathrm{f} = 42000$ and the Cauchy number $Ca = 6\,\rho_f U^2 L^3/E_\mathrm{s} T^3 \approx 17$ which is obtained from Eq. 6.1 with a rectangular cross section of the blades and a drag coefficient of $C_\mathrm{d} = 1$. The density ratio is $\rho_s/\rho_f = 1.4$ which is different from many aquatic species which have gas-filled sacs or material densities below that of water, so that buoyancy may also act as a restoring force [170]. All relevant geometrical and material properties of the fluid and the blades are given in Fig. 6.2.
Regrettably, several important parameters were not provided in the paper of Okamoto and Nezu [176], but could be partially reconstructed by the present author from previous publications of the same group [173]. For instance, the number of blades fixed to the channel bottom as well as their spacings in streamwise and spanwise direction are missing. Two years earlier, Nezu and Sanjou used an equal spacing of $\Delta S = 32\,\mathrm{mm}$ in a very similar experimental setup with an array of rigid blades and a frontal area per canopy volume of $a = W/\Delta S^2 \approx 7.8\,\mathrm{m}^{-1}$. Since this value is nearly equivalent to the value provided for the present setup with flexible blades, it is assumed that an equal spacing of 32 mm was also used in [176]. Another issue concerns the material properties of the OHP transparencies, especially the mass density ρ_s and the flexural rigidity $E_\mathrm{s}I$. While ρ_s is missing in [176], the rigidity is provided with a value of $E_\mathrm{s}I = 7.3 \cdot 10^{-5}\,\mathrm{Nm}^2$. For rectangular cross sections with $I = WT^3/12$ the Young's modulus then should be $E_\mathrm{s} = 109.5 \cdot 10^9\,\mathrm{N/m}^2$. This is typical for metallic materials but far too high for OHP transparencies usually made of thermoplastic polymer materials, e.g. polyvinyl chloride (PVC) or polyethylene terephthalate (PET). As a consequence, the value of the Young's modulus E_s was adjusted here in a preliminary simulation using an iterative procedure taking the average reconfigured height of the deflected blades $\langle L^* \rangle$ as the target. With a value of $\langle L^* \rangle / L = 0.8$ given in [176] the Young's modulus then resulted to be $E_\mathrm{s} = 4.8 \cdot 10^9\,\mathrm{N/m}^2$. Especially for PVC, PET or similar polymers a wide range for E_s can be found in the literature ranging from $E_\mathrm{s} = 2.4 \cdot 10^9\,\mathrm{N/m}^2$ up to $E_\mathrm{s} = 11 \cdot 10^9\,\mathrm{N/m}^2$ [242, 38, 26, 96, 237], depending on the specific material composition and the thermo-mechanical treatment during manufacturing. Thus, the value of $E_\mathrm{s} = 4.8 \cdot 10^9\,\mathrm{N/m}^2$ obtained iteratively for the blades seems realistic. The mass density of PVC and PET ranges from $\rho_s = 1300\,\mathrm{kg/m}^3$ up to $1450\,\mathrm{kg/m}^3$ [242, 79]. On this basis, a value of $\rho_s = 1400\,\mathrm{kg/m}^3$ is used here.

6.2.2 Numerical setup

With a water depth of 0.21 m the measurement zone was positioned 7 m downstream of the leading edge of the artificial canopy in [173, 176] to ensure a fully developed and uniform canopy flow. Side wall effects could be excluded since a two-dimensional mean flow was observed in preliminary experiments [173]. From a numerical point of view, resolved simulations of the entire transition zone are technically not feasible. In order to keep the computational effort within reasonable limits the size of the computational domain is set to $L_x \times L_y \times L_z = 1.28\,\mathrm{m} \times 0.21\,\mathrm{m} \times 0.64\,\mathrm{m}$ ($\approx 6H \times H \times 3H$) in x-, y-, z-direction which is

around one seventh of the experimental canopy in x-direction. Since time-dependent inlet conditions of the developed canopy flow are not known a periodic boundary condition is used in the streamwise direction instead. As described in Section 3.3.1, the flow then is driven by a spatially constant volume force, dynamically adjusted in time to realize a temporally constant bulk velocity $U = 0.2\,\mathrm{m/s}$ and thus a fully developed flow after an initial transient. In contrast to the experimental setup a periodic condition is also employed in the spanwise direction, to circumvent side wall effects on the flow. A no-slip condition is imposed at the bottom wall of the channel, while the water surface is approximated by a free-slip rigid lid condition. The computational domain is discretized by cubic cells of size $\Delta x = 0.625\,\mathrm{mm}$, i.e. $W/\Delta x = 12.8$ grid cells over the blade width yielding about 700 million grid cells in total. To model the subgrid scale a Smagorinsky constant of $C_s = 0.15$ is chosen, as already employed by [177] for an LES of canopy flows over rigid blades. The flexible blades considered here are fixed to the bottom wall in a square arrangement defined by a distance $\Delta S = 32\,\mathrm{mm}$ in the x- and z-direction, corresponding to an array of 40×20 structures. Each of the 800 rods are discretized by 30 elements of equal size in longitudinal direction. Regarding the temporal discretization, the time step size is $\Delta t = 4 \cdot 10^{-4}\,\mathrm{s}$ yielding a *CFL* number of approximately 0.5. All relevant numerical parameters are summarized in Tab. 6.1.

domain size	$L_x \times L_y \times L_z = 1.28\,\mathrm{m} \times 0.21\,\mathrm{m} \times 0.64\,\mathrm{m}$
number of grid cells	$N_x \times N_y \times N_z = 2048 \times 336 \times 1024$
grid step size	$\Delta x = 6.25 \cdot 10^{-4}\,\mathrm{m}$
number of rods	$N_\mathrm{s} = 800$
elements per rod	$N_\mathrm{e} = 30$
time step size	$\Delta t = 4 \cdot 10^{-4}\,\mathrm{s}$ $(CFL \approx 0.5)$
Smagorinsky constant	$C_\mathrm{s} = 0.15$

Table 6.1: *Overview over numerical parameters used for the present LES.*

6.2.3 Sensitivity of numerical parameters

All results presented in this chapter are converged and thus are independent from the numerical parameters listed in Tab. 6.1. This is demonstrated by means of a sensitivity analysis, performed for the mean velocity profile $\langle u \rangle$ and the Reynolds stress $\langle u'v' \rangle$.
To validate the suitability of the grid employed, a grid refinement study was performed. The results are presented in Fig. 6.3a. It is obvious that the data from the second finest and finest grid are very close and the same holds for the Reynolds stresses. This demonstrates that the finest grid, employed for the main study below, provides reliable results. It is in line with the results obtained in Section 4.7.3 above, where already a slightly coarser mesh with $W/\Delta x = 10$ provides sufficiently accurate results for the drag of a single blade. Note, that the finest resolution with $W/\Delta x = 12.8$ grid cells over the blade width is at the very edge of what is technically feasible because the instantaneous flow has to be simulated over a certain duration to be developed and to accumulate statistics. Indeed, just a further halving of the grid spacing would yield 5.6 billion grid cells which would currently be too costly.
The influence of the domain size was studied in a second test where both the streamwise extent L_x and the spanwise extent L_z were varied simultaneously by doubling and halving the values listed in Tab. 6.1. As shown in Fig. 6.3b these variation in domain size results only in minor differences. This supports the assumption that the domain size of $6H \times H \times 3H$ chosen

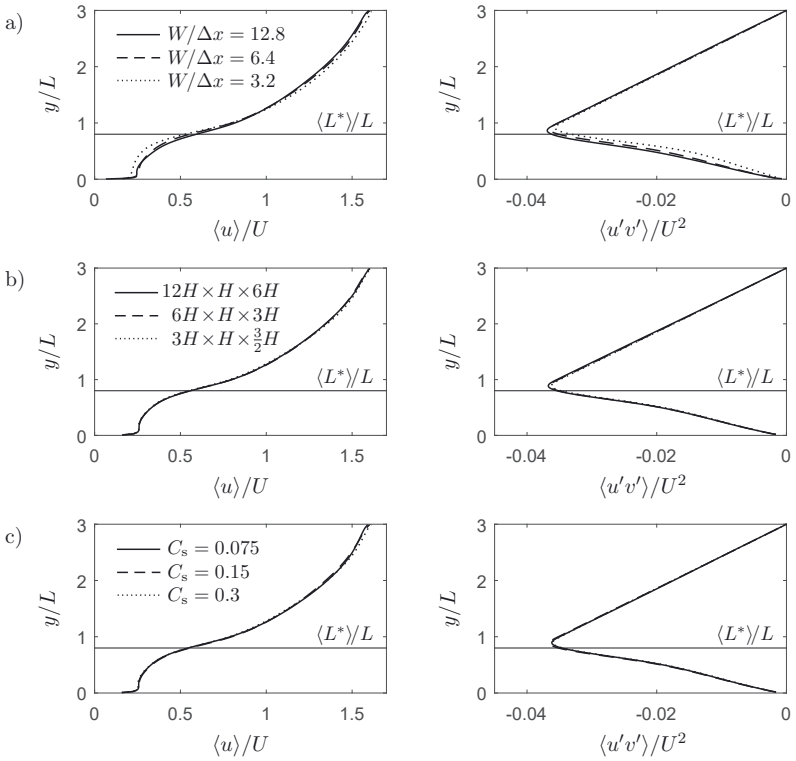

Figure 6.3: *Sensitivity of numerical parameters on the average velocity profile $\langle u \rangle / U$ (left column) and Reynolds stress profile $\langle u'v' \rangle / U^2$ (right column). Shown are the influence of a) the grid resolution $W/\Delta x$, b) the extent of the computational domain $L_x \times H \times L_z$ and c) the value for the Smagorinsky constant C_s. The tests were performed with the numerical setup defined in Tab. 6.1 where, however, a coarser grid with $W/\Delta x = 6.4$ was used for b) and c). The horizontal line corresponds to the average reconfigured canopy height $\langle L^* \rangle / L = 0.8$.*

for data production is able to resolve most of the coherent structures on canopy scale and log-layer scale. Indeed, in a usual channel flow without vegetation elements the extensions of the domain should be at least $6H \times H \times 3H$, which is the proper size to resolve large scale, coherent turbulent structures [124]. In the present case, in addition, the canopy obstructs the lower part of the channel by about 27% which increases the rate of the effective extend of the open channel flow.

Another test was conducted with different values of the Smagorinsky constant C_s, using $C_s = 0.15$ together with half of this value and twice this value. As demonstrated in Fig. 6.3c the results obtained practically coincide, so that $C_s = 0.15$ was retained. For this value the subfilter-activity [80] exhibits maximum values of $\nu_{\text{sgs}}/(\nu_{\text{sgs}} + \nu_{\text{f}}) \approx 0.9$ located in the mixing layer. The spatially averaged value on the fine grid is $\langle \nu_{\text{sgs}}/(\nu_{\text{sgs}} + \nu_{\text{f}}) \rangle \approx 0.19$.

Note, that the number of elements $N_{\text{e}} = 30$ per rod structure and $CFL = 0.5$ were kept constant in all test simulations. Their independence was verified by two additional simulations using $N_{\text{e}} = 60$ and $CFL = 0.2$, respectively (not shown here).

6.3 Data analysis and physical interpretation

6.3.1 Mean velocity profile and Reynolds stresses

The simulation results of the turbulent velocity field $\mathbf{u}(\mathbf{x}, t)$ are first analyzed in terms of the mean velocity profile $\langle \mathbf{u} \rangle$ and Reynolds stresses $\langle \mathbf{u}' \otimes \mathbf{u}' \rangle$. These quantities result from a Reynolds decomposition of the velocity field $\mathbf{u} = \langle \mathbf{u} \rangle + \mathbf{u}'$, i.e. the decomposition into a mean component

$$\langle \mathbf{u} \rangle(y) = \frac{1}{L_x L_z T} \int_0^{L_x} \int_0^{L_z} \int_0^{T} \mathbf{u}(\mathbf{x}, t) \, \mathrm{d}x \, \mathrm{d}z \, \mathrm{d}t \tag{6.2}$$

averaged over a time period T and in both homogeneous directions x and z, and a fluctuating component $\mathbf{u}'(\mathbf{x}, t) = (u', v', w')^T = \mathbf{u}(\mathbf{x}, t) - \langle \mathbf{u} \rangle(y)$. Using these definitions, the Reynolds stresses can be expressed as

$$\langle \mathbf{u}' \otimes \mathbf{u}' \rangle = \langle \mathbf{u} \otimes \mathbf{u} \rangle - \langle \mathbf{u} \rangle \otimes \langle \mathbf{u} \rangle \,, \tag{6.3}$$

which is used here for their computation by a simple averaging of $\langle \mathbf{u} \rangle$ and $\langle \mathbf{u} \otimes \mathbf{u} \rangle$ during runtime of the simulation.

The results for the mean velocity profile and relevant Reynolds stresses obtained from simulation are given in Fig. 6.4. Moreover, the profile $\langle u \rangle$ and the turbulent shear stress $\langle u'v' \rangle$ are compared to the experimental data of Okamoto and Nezu [176]. The comparison shows that the mean streamwise velocity component $\langle u \rangle$ is slightly underestimated inside the canopy region while, due to continuity, it is slightly overestimated above the canopy in the free-flow region. The height of the inflection point of the velocity profile and the velocity magnitude at this location are very well captured by the simulation. Basically, this can be expected since the position of the inflection point coincides with the average reconfigured canopy height $\langle L^* \rangle$ [171] which was adjusted in the simulation to the experimental observation to estimate the correct rigidity $E_\mathrm{s}I$ of the blades (see previous Section 6.2). In terms of the Reynolds stress $\langle u'v' \rangle$ the simulation results are in good agreement with the experiment. Especially, the minimum of $\langle u'v' \rangle$ and its y-position are very close to the experimental observation. Near the channel bed the measurements behave differently up to a height of about $0.5L$. In the free-flow region above the canopy $\langle u'v' \rangle$ behaves linearly, as required by the momentum balance. The experimental data, however, match this behavior only with some deviation. Hence, it must be assumed that the experimental statistics are not fully converged. A further source of deviations obtained for $\langle u \rangle$ and $\langle u'v' \rangle$ can be assigned to the way how the flow is driven through the channel. In the experiment a tilting flume is used where the bulk velocity is adjusted by the inclination of the flume. The drag generated by the canopy varies slightly in time due to a time-dependent reconfiguration of individual blades, as shown in Fig. 6.6 below. As a result, the bulk velocity may also vary in time within the measurement zone, so that $U = 0.20\,\mathrm{m/s}$ provided in [176] must be interpreted as a time-averaged value. However, this value is kept entirely constant during the present simulation by means of a PI-controller as described in Section 3.3. In the present scenario the spatially averaged canopy height $\langle L^* \rangle_\mathrm{E}$, i.e. the ensemble average over all 800 rods, varies with amplitudes of at most 4% of $\langle L^* \rangle$. Thus, the differences between experiment and simulation should be comparatively small which is reflected by the comparison shown in Fig. 6.4.

As described in [207] and references therein [189, 83], the canopy flow over the entire channel height can be divided into three zones (see Fig. 6.13 below) exhibiting different unique phys-

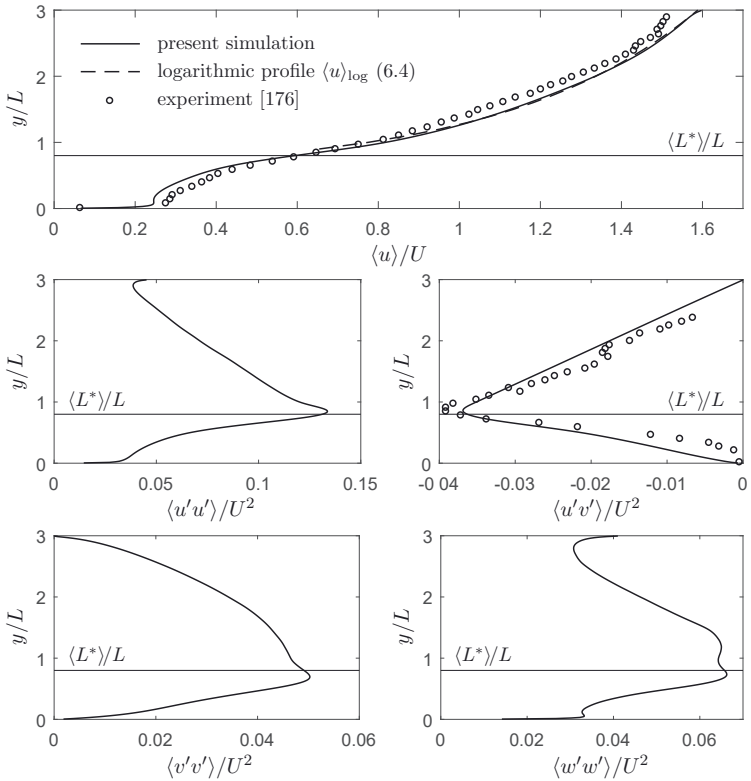

Figure 6.4: *Normalized mean velocity profile $\langle u \rangle / U$ and non-vanishing Reynolds stresses $\langle u'u' \rangle$, $\langle u'v' \rangle$, $\langle v'v' \rangle$ and $\langle w'w' \rangle$ normalized by U^2 (observe the different ranges). The present results are compared to the experimental data of [176] identified by black circles. The temporally and spatially averaged height of the canopy with the blades being deflected by the flow is $\langle L^* \rangle / L = 0.8$, represented by the horizontal black line. The mean velocity profile is well fitted by a logarithmic profile concerning Eq.* (6.4) *in the free-flow region above the canopy.*

ical properties. These zones are usually classified by means of the mean velocity profile $\langle u \rangle$ and the Reynolds stress component $\langle u'v' \rangle$. The bottom region is termed *emergent zone* and it extends from the channel bottom to the upper limit of the wake zone defined as the elevation of 10% of $\langle u'v' \rangle_{\min}$ [171]. Here, the flow is dominated by wakes of individual vegetation elements, so that a vertical momentum transfer is comparably small. The velocity profile is characterized by a regular boundary layer at the bottom followed by a layer of almost constant velocity, which is well-captured by the present simulation.
The subsequent zone is termed *mixing layer zone* including the upper canopy region and the lower part of the free-flow region for $y \lessapprox 2\langle L^* \rangle$ [169]. The velocity profile exhibits an inflection point at the canopy edge as a result of the shear layer generated in this zone. As a result, the flow prone to Kelvin-Helmholtz instabilities and turbulent fluctuations evolve to form large-scale coherent structures, which is an essential precondition to trigger the

monami phenomenon [197, 176, 219]. In particular, the maximum absolute Reynolds stress $-\langle u'v'\rangle_{\min}$, located slightly above the average canopy height $\langle L^*\rangle$, signifies how strong u'- and v'-fluctuations are correlated in this region. Since the extremal value of $\langle u'v'\rangle$ is negative, positive fluctuations u' are strongly correlated to negative fluctuations v' and *vice versa*. Such events are called sweeps ($u' > 0$, $v' < 0$) and ejections ($u' < 0$, $v' > 0$), respectively, and were identified as the main mechanism for momentum transfer between the canopy and the free-flow region [184]. In contrast to unobstructed channel flows the vertical momentum transfer associated with sweeps and ejections is much more pronounced, possibly causing a vertical displacement of the water surface. In the present numerical setup the water surface is modeled by a free-slip rigid lid boundary condition. Consequently, vertical velocity components $\langle v\rangle$ are fully suppressed and redirected in the tangential space of the upper boundary. As shown in Fig. 6.4 this causes seemingly non-physical strong peaks in terms of $\langle u'u'\rangle$ and $\langle w'w'\rangle$ at the surface at $y/L = 3$. Even if the present numerical model is not able to capture a vertical displacement of the water surface, it is suspected that the influence on the flow below and especially the mixing layer of interest here is negligibly small. This is supported by the fact, that the present velocity profile for $y \gtrapprox 2\langle L^*\rangle$ obeys the classical log-law of rough boundary layers, as observed by several authors, e.g. [111, 169, 207]. This third layer, located above the mixing layer, is commonly designated as *log layer (log-law) zone*, by reason of the fact that the velocity profile can be well approximated by

$$\langle u\rangle_{\log}(y) \;=\; \frac{U_\tau}{\kappa}\,\ln\!\Big(\frac{y-y_{\mathrm{m}}}{y_0}\Big)\,, \tag{6.4}$$

with the von Kármán constant $\kappa = 0.4$, the displacement height y_{m}, the roughness height y_0 and the friction velocity U_τ. The latter velocity can be expressed in terms of the Reynolds stress $\langle u'v'\rangle$ at the canopy edge, i.e. $U_\tau^2 = -\langle u'v'\rangle|_{\langle L^*\rangle} \approx -\langle u'v'\rangle|_{\min}$, which gives $U/U_\tau \approx 5.2$ in the present case. According to [172], the displacement height is $y_{\mathrm{m}} = \langle L^*\rangle - \delta/2$, with $\delta \approx \langle u\rangle / \frac{\mathrm{d}\langle u\rangle}{\mathrm{d}y}|_{\langle L^*\rangle}$ and seems to increase proportionally to the average canopy height with $y_{\mathrm{m}}/\langle L^*\rangle \approx 0.78$ [176]. The present simulation yields a value of $y_{\mathrm{m}}/\langle L^*\rangle \approx 0.69$. The roughness height in terms of the frontal canopy area per volume $a = W/\Delta S^2 = 7.8125\,\mathrm{m}^{-1}$ was estimated to be about $y_0 = 0.049\,a^{-1}$, which lies in the range of $y_0 = (0.04 \pm 0.02)a^{-1}$ for submerged canopies [169]. Furthermore, $y_0/\langle L^*\rangle = 0.112$ which is consistent with the value of 0.11 obtained in [171].

6.3.2 Average blade deflection and fluctuations

As for the fluid velocity field a decomposition is performed for the array of blades represented as a spatially discrete field $\mathbf{x}(s;Z,t) = (\mathsf{x},\mathsf{y},\mathsf{z})^T$, defined by $\mathbf{x} = \mathbf{c}_s - \mathbf{c}_{s,0}$. Here, $\mathbf{c}_s = \mathbf{c}_s(Z,t)$ is the time-dependent center line of an individual rod, with $s \in \mathbb{N}$, $1 \le s \le N_{\mathrm{s}}$, and $\mathbf{c}_{s,0} = \mathbf{c}_s(0,0)$ its position of fixation on the bottom plate. The mean component is given by

$$\langle\mathbf{x}\rangle(Z) = \frac{1}{T}\int_0^T \langle\mathbf{x}(s;Z,t)\rangle_{\mathrm{E}}\,\mathrm{d}t\,, \tag{6.5}$$

with the ensemble average over the set of all $N_{\mathrm{s}} = 800$ rods

$$\langle\mathbf{x}\rangle_{\mathrm{E}}(Z,t) = \frac{1}{N_{\mathrm{s}}}\sum_{s=1}^{N_{\mathrm{s}}}\mathbf{x}(s;Z,t)\,. \tag{6.6}$$

Non-vanishing components $\langle \mathsf{x} \rangle$ and $\langle \mathsf{y} \rangle$ of the mean blade profile are given in Fig. 6.5. Moreover, relevant fluctuations $\langle \mathsf{x}'\mathsf{x}' \rangle$, $\langle \mathsf{x}'\mathsf{y}' \rangle$, and $\langle \mathsf{y}'\mathsf{y}' \rangle$ are shown in Fig. 6.5 in order to assess the specific type of oscillation, e.g. mode 1 bending or mixed-mode bending. Statistical data of the OHP-strip motion were not acquired in the experiment [176], so that a comparison with the simulation results can not be provided here.

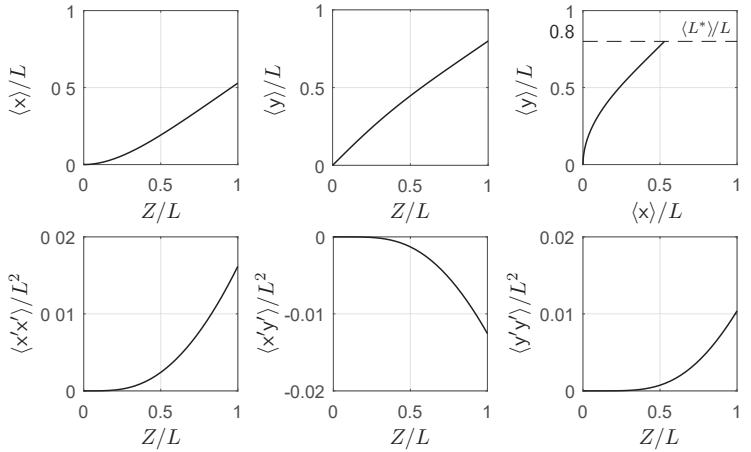

Figure 6.5: *Normalized components $\langle \mathsf{x} \rangle / L$ and $\langle \mathsf{y} \rangle / L$ of the average center line of the blades and corresponding fluctuating components $\langle \mathsf{x}'\mathsf{x}' \rangle / L^2$, $\langle \mathsf{x}'\mathsf{y}' \rangle / L^2$, and $\langle \mathsf{y}'\mathsf{y}' \rangle / L^2$.*

While the center line of the blades shows a well-pronounced reconfiguration in the streamwise direction, no lateral reconfiguration is obtained in the homogeneous spanwise direction. As indicated by the fluctuations plotted in Fig. 6.5, the motion of the blades appears to be characterized by a mode 1 bending. If the rods were to oscillate, for instance, with a second bending mode of significant magnitude, the functions $\langle \mathsf{x}'\mathsf{x}' \rangle$, $\langle \mathsf{x}'\mathsf{y}' \rangle$ and $\langle \mathsf{y}'\mathsf{y}' \rangle$ would have inflection points at some arc length $0 < Z \leq L$. All fluctuations are of the same order of magnitude. This indicates that the motion in the x- and y-direction is strongly coupled, which is naturally the case as a forward bending of the blade in the x-direction will induce a y-deflection. The component $\langle \mathsf{z}'\mathsf{z}' \rangle$ completely vanishes, which implies that the rods do not undergo any lateral motion.

Fourier analysis of blade motion In the *monami* regime studied here the blades oscillate between an almost upright shape and a maximum deflection of approximately 50% of their length. The periodic features of this motion can be identified with the aid of an ensemble averaged Fourier spectrum of the rod height $L^*(s;t) = \mathsf{y}(s; Z = L, t)$, i.e.

$$\langle |\widehat{L}^*| \rangle_{\mathrm{E}} = \frac{1}{N_{\mathrm{s}}} \sum_{s=1}^{N_{\mathrm{s}}} |\widehat{L}^*|_s \,, \tag{6.7}$$

where the spectrum $|\widehat{L}^*|_s$ of each rod s is evaluated by means of a windowed fast Fourier transform (FFT) applying the Hann window function [231]. Here, L^* is chosen as an appropriate measure of the oscillation since the rod motion is dominated by a mode 1 bending. Any other

material point on the rod describes an equivalent motion with only a less pronounced amplitude. It should be noted, that in Eq. (6.7) the ensemble average is performed intentionally for the magnitudes of individual FFTs, i.e. $\langle|\widehat{L}^*|\rangle_\mathrm{E}$. In contrast, the magnitude of the averaged complex FFTs, i.e. $|\langle\widehat{L}^*_s\rangle_\mathrm{E}|$, nearly vanishes since the phase information strongly varies between each individual rod motion. Figure 6.6b shows the averaged spectrum $\langle|\widehat{L}^*|\rangle_\mathrm{E}(f/f_\mathrm{ft})$, where the frequency f is normalized by the flow through frequency $f_\mathrm{ft} = 1/T_\mathrm{ft}$ as the inverse of the flow through time of the channel $T_\mathrm{ft} = U/L_x$. The averaged spectrum shows mainly a

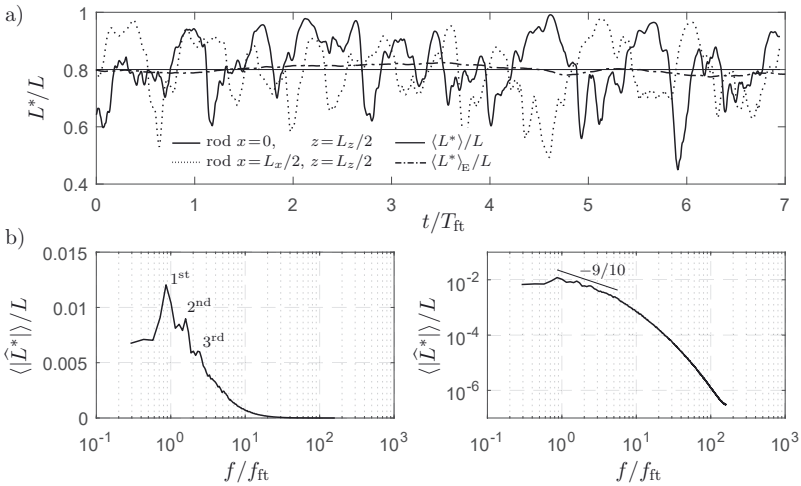

Figure 6.6: *a) Temporal evolution of tip height L^* of two individual rods (black solid line and dashed line) and ensemble averaged height $\langle L^*\rangle_\mathrm{E}$ (black dotdashed line). b) Averaged Fourier spectrum $\langle|\widehat{L}^*|\rangle_\mathrm{E}(f)$ in semi-logarithmic scale (left) and double-logarithmic scale (right), where $|\widehat{L}^*|$ is the windowed-FFT of L^*. The frequency axis is normalized by the flow through frequency $f_\mathrm{ft} = U/L_x$.*

continuous shape with a slope of approximately $\langle|\widehat{L}^*|\rangle/L \propto (f/f_\mathrm{ft})^{-9/10}$ for frequencies f/f_ft storing about 70% of the total energy. A well-pronounced dominant frequency peak can be observed at $f_1 \approx 0.86\, f_\mathrm{ft}$ accompanied by two harmonics of lower energy at $f_2 \approx 2f_1$ and $f_3 \approx 3f_1$ indicating a periodic rod motion. Indeed, as shown in Fig. 6.6a for two individual blades, the rods exhibit an oscillatory behavior with reconfigurations mainly in the range of $0.6 < L^*/L < 1$. At more or less regular time intervals the rods abruptly incline and show a strong reconfiguration with heights down to $L^*/L = 0.4$ which is half of the average canopy height. Statistically, such events happen with a frequency of $f_1 \approx 0.86\, f_\mathrm{ft}$.
As described above the blades mainly oscillate with a mode 1 bending. The corresponding natural frequency can be estimated by [95]

$$f_\mathrm{n} = \frac{1.875^2}{2\pi}\sqrt{\frac{E_\mathrm{s}I}{mL^3}}\,, \tag{6.8}$$

with the flexural rigidity $E_\mathrm{s}I$ and the mass of the oscillating system $m = m_\mathrm{s} + m_\mathrm{add}$ including the mass of the blade m_s and the added mass of the surrounding fluid m_add. The latter can

be estimated by means of potential theory which gives $m_{\mathrm{add}} = \frac{\pi}{4}\rho_f W^2 L$ for the present blade geometry [59]. The ratio between the frequency f_1 and the natural frequency of the first bending mode f_{n} is an important indicator of the physical cause of the periodic motion of the blades. If the large oscillation amplitude observed in the *monami* regime is due to a resonant system created by the fluid and the structures, the natural frequency of the blades should be almost equal to the frequency of the entire excited system, i.e. $f_1/f_{\mathrm{n}} \approx 1$. If, on the other hand, the blades behave like passive objects, simply following an external periodic excitation by the fluid, their natural frequency can be expected to be much smaller than the lowest dominant frequency observed in the system, i.e. $f_1/f_{\mathrm{n}} \ll 1$. Using Eq. (6.8) the frequency ratio is $f_1/f_{\mathrm{n}} \approx 0.15$, indicating that the dominant frequency does not result from a mechanical resonance between the fluid and the blades. It is rather that the blades react to the external excitation by the fluid, e.g. by coherent structures acting on the blades at regular time intervals. Okamoto and Nezu [173, 176] did indeed observe that the flow in sufficiently dense shallow canopies is dominated by sweep and ejection events at the canopy edge. The unique feature of canopies in the *monami* regime is, that their flexible blades react nearly instantaneously with large displacements to an increased momentum transfer caused by such events. Concurrently, the blades are sufficiently stiff to enable a momentum transfer in the mixing layer required to generate sweeps and ejections. This transfer is inhibited if the flexibility is too high, as illustrated in Fig. 6.1d.

From a different point of view, for small frequency ratios f_1/f_{n} vegetation elements are capable of following the surrounding fluid motion and, thus, can be employed to detect or visualize coherent structures. In cases where the ratio f_1/f_{n} does not completely vanish a small time delay between the excitation by fluid and the response of the blade may be expected. To quantify this delay for the present scenario, an additional simulation with a single blade in a cross flow swaying periodically with f_1 was performed. As shown in Fig. 6.7, the blade responds with only a slight time delay of $\Delta t/T_{\mathrm{ft}} \approx 0.04$. This further supports the fact that the reconfiguration of the blades is a simple reaction to an increased vertical momentum transfer, generated by sweep and ejection events. Several researchers suggest that sweeps and ejections appear periodically in time [11]. For the present configuration this presumption can be confirmed since the averaged spectrum of the blades clearly contains periodic features.

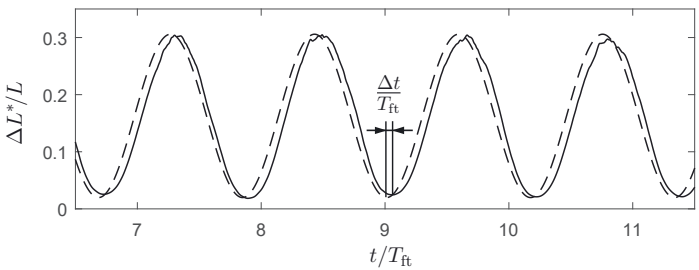

Figure 6.7: *Large eddy simulation of a single OHP-strip subjected to a swaying bulk velocity* $u(t)/U = 1/2\,\{1 + 1/2\,\sin(2\pi f_1 t)\}$ *with* $f_1 = 0.86 f_{\mathrm{ft}}$. *All parameters are equivalent to the present simulation with 800 OHP-strip, but a smaller computational domain of size* $3L \times H \times 2L$ *was used. This figure shows the simulation results of the normalized tip displacement in y-direction* $\Delta L^*/L = 1 - L^*/L$ *over time* t/T_{ft} *(solid line). The response of the rod with respect to the bulk velocity* U_1 *(dashed line, amplitude adapted) is slightly delayed in time with* $\Delta t/T_{\mathrm{ft}} \approx 0.04$.

6.3.3 Two-point correlations

In order to characterize coherent structures on the canopy scale, responsible for an organized motion of the blades, a two-point correlation analysis was performed for both the fluid velocity as well as the reconfiguration of the blades. The autocorrelation of the streamwise velocity fluctuation u' is defined as

$$\rho_{uu}(r_x, y, r_z) = \frac{\langle\, u'(\mathbf{x},t)\, u'(\mathbf{x}+\mathbf{r},t)\,\rangle}{\sqrt{\langle\, u'(\mathbf{x},t)\, u'(\mathbf{x},t)\,\rangle\, \langle\, u'(\mathbf{x}+\mathbf{r},t)\, u'(\mathbf{x}+\mathbf{r},t)\,\rangle}} \tag{6.9}$$

based on the fields $u'(\mathbf{x},t)$ and $u'(\mathbf{x}+\mathbf{r},t)$, the latter shifted by the distance vector $\mathbf{r} = (r_x, 0, r_z)^\top$ in the horizontal plane utilizing the periodicity of the computational domain in the r_x- and r_z-direction. Due to averaging in time and homogeneous directions (see Eq. (6.2)), the correlation coefficient ρ_{uu} is a function of the streamwise distance $r_x/L_x \in [-0.5, 0.5]$ ($L_x \approx 6H$), the vertical coordinate y and the spanwise distance $r_z/L_z \in [-0.5, 0.5]$ ($L_z \approx 3H$). Analogous to ρ_{uu} for the fluid velocity fluctuations, a correlation coefficient $\rho_{L^*L^*}$ is defined for the fluctuation of the canopy height, i.e. $\mathsf{y}'(s,L,t) = L^{*\prime}(s,t) = L^*(s,t) - \langle L^* \rangle$. It is given by

$$\rho_{L^*L^*}(r_x, r_z) = \frac{\langle\, L^{*\prime}(s,t)\, L^{*\prime}(s+s_r,t)\,\rangle}{\sqrt{\langle\, L^{*\prime}(s,t)\, L^{*\prime}(s,t)\,\rangle\, \langle\, L^{*\prime}(s+s_r,t)\, L^{*\prime}(s+s_r,t)\,\rangle}}\,, \tag{6.10}$$

where $s_r = r_x\, L_z/\Delta S^2 + r_z/\Delta S + 1$ with $s_r \in \mathbb{N}$ realizes a shifting between the blades in streamwise direction via $r_x/L_x \in \{-\frac{1}{2}, -\frac{1}{2}+\frac{\Delta S}{L_x}, \ldots, \frac{1}{2}\}$ and in spanwise direction via $r_z/L_z \in \{-\frac{1}{2}, -\frac{1}{2}+\frac{\Delta S}{L_z}, \ldots, \frac{1}{2}\}$. The averaging is performed according to Eq. (6.5).
Figure 6.8a shows different contour plots of ρ_{uu} in two vertical planes $r_x = 0$ and $r_z = 0$, respectively, as well as in the horizontal plane located at $y/H = 0.5$. Elongated regions with a high degree of correlation ($|\rho_{uu}| > 0.2$) can be observed, indicating the presence of streamwise velocity streaks above the canopy edge at a height of approximately $0.5H$. Indeed, high-speed (HS) velocity streaks, i.e. regions with $u' > 0$, and low-speed (LS) velocity streaks with $u' < 0$ are also clearly identifiable in the instantaneous velocity field, as shown in Fig. 6.11 for one selected instant in time. Statistically, a single streak extends over a length of approximately $2H$ in the streamwise direction and $0.75H$ in the spanwise direction, identified from the local minimum of $\rho_{uu}(r_x, H/2, 0)$ and $\rho_{uu}(0, H/2, r_z)$, respectively (Fig. 6.9). An influence of the domain size could be excluded by a supplementary simulation using a larger computational domain of size $12H \times H \times 6H$ discretized with a coarser spatial resolution of $W/\Delta x = 6.4$. The change from positive to negative values of $\rho_{uu}(0, H/2, r_z)$ indicates that HS–streaks are accompanied laterally by LS–streaks and *vice versa*. Moreover, a periodic pattern of alternating positive and negative correlation appears for $\rho_{uu}(r_x, H/2, r_z)$ extending over the entire horizontal plane, having certain similarities to a checkerboard pattern. However, from a statistical point of view, the periodicity is less pronounced since ρ_{uu} nearly vanishes already at $r_x/H = 3$ and $r_z/H = 1.5$. This implies, that a pairing of HS–streaks and LS–streaks is more of a local event, while a global regular periodic pattern is less probable.
As described in the previous section, the flexible blades react nearly instantaneously with large displacements to an increased momentum transfer caused, e.g. by sweeps and ejections. It can be expected that in regions with $u' > 0$ the blades tend to be more reconfigured due to an increased drag, while being more erect in regions with $u' < 0$. As shown in Fig. 6.8, this is also reflected by the two-point correlation of the local blade reconfigura-

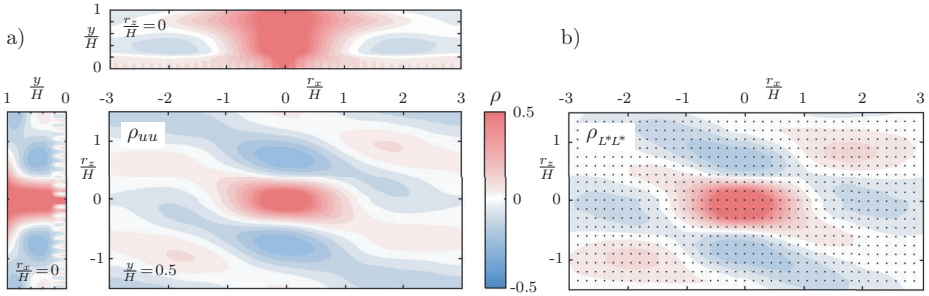

Figure 6.8: *Contours of two-point correlation coefficients at different planes located at $y/H=0.5$, $r_x/H=0$ and $r_z/H=0$. a) Correlation of velocity fluctuations in streamwise direction ρ_{uu} and b) correlation of the height of reconfigured vegetation elements $\rho_{L^*L^*}$. At the black dots the blades are fixed to the bottom plate.*

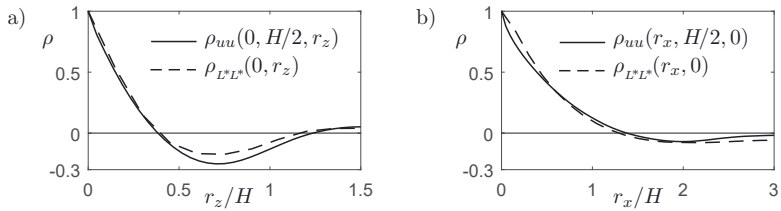

Figure 6.9: *Two-point correlation coefficient ρ_{uu} of velocity fluctuations u' and $\rho_{L^*L^*}$ concerning the canopy height L^* a) along r_z in spanwise direction and b) along r_x in streamwise direction.*

tions $\rho_{L^*L^*}(r_x, r_z)$ which is obviously very similar to the results obtained for $\rho_{uu}(r_x, H/2, r_z)$. The cross-correlation coefficient of both autocorrelations gives a value of approximately 0.89, which further emphasizes a strong coupling between velocity streaks and the reconfiguration of blades. Since velocity streaks act in a certain range in space, the blades react by a reconfiguration in groups which is also indicated by the elongated regions of positive or negative $\rho_{L^*L^*}$. Analogous to the streaks, these separated regions extend over a length of $2H \approx 13\Delta S$ in the streamwise direction and $0.75H \approx 5\Delta S$ in the spanwise direction, which corresponds to an array of about 13×5 blades in which, statistically, a group of blades undergoes a large reconfiguration, being accompanied by a group of erect blades and *vice versa*. While the instantaneous deflection of blades of course departs from their statistical behavior, it is predominantly organized in groups, as visualized in Figure 6.11 where the instantaneous blade deflection is colored according to the respective normalized tip elevation L^*/L for a selected instant in time.

The relation between velocity streaks and the reconfiguration of blades found here, agrees with experimental observations of Ghisalberti and Nepf [81, 82]. They noticed that a waving of blades is clearly confined to longitudinal "monami channels" (velocity streaks here), where the blade motion in one channel is out of phase with the motion in the adjacent channels. Moreover, it was found in that reference as well that these flow structures persist even when the flexible blades are replaced by rigid vegetation elements.

6.3.4 Coherent structures

The *monami* phenomenon, observed for the present set of parameters, is characterized by an organized large-amplitude oscillation of groups of blades at different locations in the channel. The present simulation shows these well-separated regions of different blade deflection as they travel through the canopy (Fig. 6.11, left). This indicates the presence of coherent structures on canopy scale since a large reconfiguration of blades is a reaction to an increased local transfer of momentum, as demonstrated in the previous Section 6.3.3. The relation between momentum transfer and the *monami* phenomenon was already studied by Ghisalberti and Nepf in 2002 [81]. They found that the vertical transport of momentum is dominated by coherent vortices advected downstream which cause the wavy motion of the canopy [81, 176]. However, the exact nature of coherent structures and vortices in canopy flows is still not fully understood and remains to be investigated. The most common model of coherent structures is based on the existence of a straight horizontal KH–vortex generated at the canopy edge by a mechanism similar to the KH–instability in the mixing layer [173, 176, 169]. On the other hand, as recently shown in [219], the hydrodynamic instability in the *monami* regime seems to differ from the traditional KH–instability due to the presence of vegetation elements. The KH–model usually provides only a two-dimensional explanation of dominant coherent structures, but does not consider the three-dimensional features to be expected in turbulent channel and canopy flows. Indeed, as suggested in [173] for aquatic canopies and in [71, 72] for terrestrial canopies, the turbulence in canopy flows is rather dominated by a complicated three-dimensional large-scale motion of the fluid with sweeps, ejections and roller vortices as the dominant contributions at the canopy edge. For terrestrial canopies, Finnigan *et al.* [72] elucidated the three-dimensional formation of vortices and accompanying sweep and ejection events. In that work, they deduced the eddy structures by means of conditional averaging of the flow field, using canopy pressure maxima as a trigger to identify the structure location. Based on the averaged results, they found a dual-hairpin eddy structure which appears as a combination of a "head-up" (HU) and a "head-down" (HD) hairpin vortex (Fig. 6.10b). In between the counter-rotating legs of the corresponding hairpin, an ejection or a sweep is generated. Despite the different physical properties, a comparable sys-

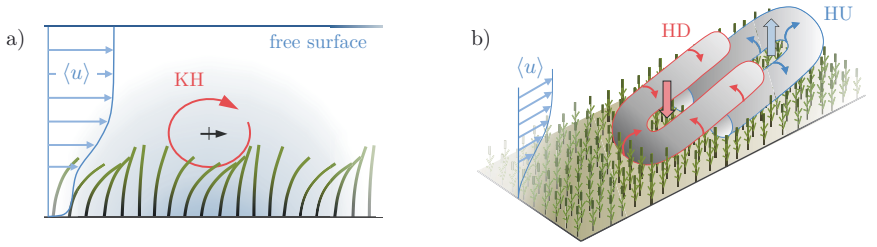

Figure 6.10: *Different models of vortices responsible for the monami phenomenon. a) Common model of a two-dimensional Kelvin-Helmholtz vortex generated in the mixing layer at the canopy edge. b) Dual-hairpin eddy model according to observations by [72, 69] for terrestrial canopies. The vortex structure consists of "head-up" (HU) and "head-down" (HD) hairpin vortices aligned in streamwise direction. Due to the counter-rotating legs of the hairpins the HU–vortex generates an ejection (broad blue arrow), while the HD–hairpin generates a sweep (broad red arrow). The smaller arrows indicate the motion due to self-induction.*

tem of eddy structures appears to manifest itself in aquatic canopies. Similar to the strategy of [72] conditional averaging of the present fluid fields was performed in the present study, defined as

$$\langle \mathbf{u} \rangle_{\mathrm{c}}(\mathbf{x}) = \frac{1}{|\mathcal{C}|} \sum_{(\mathbf{x}_{\mathrm{c}},t_{\mathrm{c}})\in\mathcal{C}} \mathbf{u}(\mathbf{x}+\mathbf{x}_{\mathrm{c}},t_{\mathrm{c}})\,, \tag{6.11}$$

where the tupel $(\mathbf{x}_{\mathrm{c}},t_{\mathrm{c}})$ is an element of the set

$$\mathcal{C} = \{(\mathbf{x}_{\mathrm{c}},t_{\mathrm{c}}) \mid \forall \mathbf{x} \text{ with } \|\mathbf{x}-\mathbf{x}_{\mathrm{c}}\| < R : \mathcal{A}(\mathbf{x}_{\mathrm{c}},t_{\mathrm{c}}) \leq \mathcal{A}(\mathbf{x},t_{\mathrm{c}}) < \mathcal{A}_{\mathrm{th}}\} \tag{6.12}$$

defining all locations in the fluid domain $\mathbf{x}_{\mathrm{c}} = (x_{\mathrm{c}},0,z_{\mathrm{c}})^{\top} \in \Omega$ at times $t_{\mathrm{c}} \in [0,T]$ which fulfill a certain averaging condition $\mathcal{A}(\mathbf{x}_{\mathrm{c}},t_{\mathrm{c}}) < \mathcal{A}_{\mathrm{th}}$ with a predefined threshold $\mathcal{A}_{\mathrm{th}} \in \mathbb{R}$. The condition has to be adapted to the kind of events to be detected, e.g. pressure minima used in the work of Finnigan *et al.* [72]. All detected locations $\mathbf{x}_{\mathrm{c}}$ exhibit the minimum value with respect to the condition function $\mathcal{A}$, i.e. $\mathcal{A}(\mathbf{x}_{\mathrm{c}},t_{\mathrm{c}}) \leq \mathcal{A}(\mathbf{x},t_{\mathrm{c}})$ in a circular region $\|\mathbf{x}_{\mathrm{c}}-\mathbf{x}\| < R$ around $\mathbf{x}_{\mathrm{c}}$ for all $\mathbf{x} = (x,0,z)^{\top} \in \Omega$. The radius R defines the approximate spatial extension of an event to be detected. In the present context, the value $R = 0.75H$ was chosen, according to the extent of dominant structures obtained from the two-point correlations ρ_{uu} and $\rho_{L^*L^*}$ investigated in Section 6.3.3. The total number of events detected in the domain Ω over the time interval $[0,T]$ is given by the cardinality of $\mathcal{C}$, denoted as $|\mathcal{C}| \in \mathbb{N}$. Since the present LES provides resolved data for the fluid motion and the blade motion, conditional averaging is performed simultaneously for both data sets by means of the same condition. As a consequence, only those locations $\mathbf{x}_{\mathrm{c}} \in \Omega$ are permitted that coincide with a fixation point $\mathbf{c}_{s,0} = \mathbf{c}_s(Z=0,t=0)$ of a structure s, i.e. $\mathbf{x}_{\mathrm{c}} = \mathbf{c}_{s_{\mathrm{c}},0}$. Using this relation the associated conditional averaging for the array of blades $\mathbf{x}(s;Z,t)$ is given by

$$\langle \mathbf{x} \rangle_{\mathrm{c}}(s,Z) = \frac{1}{|\mathcal{C}|} \sum_{(\mathbf{x}_{\mathrm{c}},t_{\mathrm{c}})\in\mathcal{C}} \mathbf{x}(s+s_{\mathrm{c}},t_{\mathrm{c}})\,. \tag{6.13}$$

In this work, the local deflection of the blades was used to define the averaging condition requesting $L^*(\mathbf{x}_{\mathrm{c}},t_{\mathrm{c}})/L < 0.55$. The result is shown in Fig. 6.12, along with a visualization of the vortical structure obtained via the λ_2 criterion [108]. In contrast to the observations of Finnigan *et al.* [72] no dual-hairpin was observed, but only the HD–hairpin with a strong and pronounced sweep at the low-end between both counter-rotating legs. This demonstrates the strong correlation between sweeps and an increased reconfiguration of the blades, already mentioned in the previous sections. As a result, nearly equivalent averaged fields $\langle \mathbf{u} \rangle_{\mathrm{c}}$ and $\langle \mathbf{x} \rangle_{\mathrm{c}}$ were obtained when using sweep events $(u' > 0, v' < 0)$ as alternative averaging conditions with values of $u'v'/U^2 < -0.16$ in the horizontal plane $y/L = 0.65$.

Besides the HD–hairpin observed for the averaged fluid field, Fig. 6.12 shows eddy structures for an arbitrary instant in time, visualized by iso-surfaces of negative pressure fluctuation $p'/(\rho_{\mathrm{f}}U^2) = \text{const}$. Obviously, well pronounced HD–hairpins can not be found in the instantaneous flow fields which appears to be more irregular. Instead, KH-like eddies of different intensity seem to be formed in the mixing layer, especially in regions of large blade deflection, as suggested by the KH–model. One example of a strongly pronounced KH–vortex is shown in Fig. 6.13a. As demonstrated by the two-point correlations presented in Section 6.3.3, these regions generally appear in conjunction with longer HS–streaks with $u' > 0$ and are bounded laterally by LS–streaks with $u' < 0$ (Fig. 6.11, right). A deeper analysis of the data reveals that hairpin–like vortices are generated on top of a LS–streak (Fig. 6.13b).

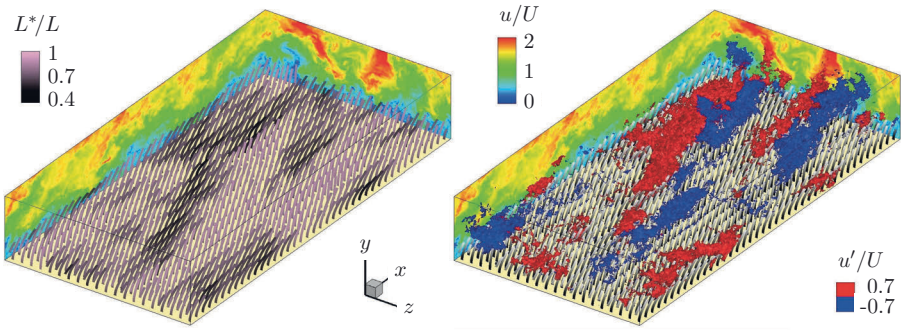

Figure 6.11: *Both visualizations show the instantaneous, streamwise velocity component u/U in the vertical planes $z = 0$ and $x = 6H$, at the same arbitrary instant in time $t = \tilde{t}$. In addition, the left figure shows the array of deflected blades colored with the respective normalized tip elevation L^*/L. While some groups of blades are deflected by up to 50% of the blade length, other groups stand up quite vertically. In the right figure regions of positive and negative velocity fluctuation $u' = \pm 0.7\,U$ are highlighted by iso-surfaces in red and blue, respectively.*

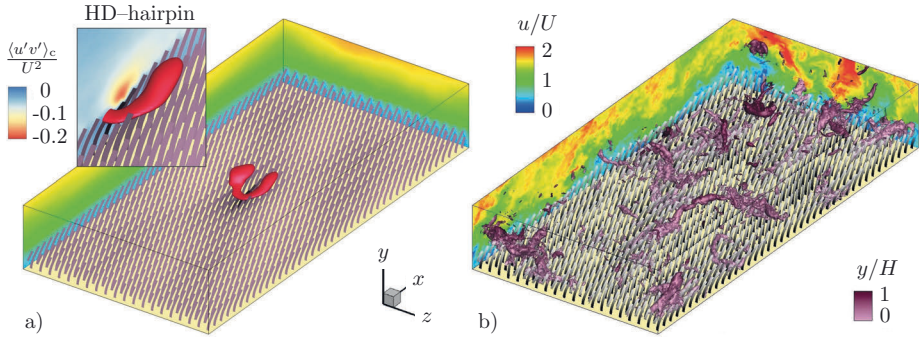

Figure 6.12: *a) Conditionally averaged fluid field $\langle u \rangle_c/U$, where the events of high deflection are used as a trigger for an ensemble average. The flow fields have been transferred horizontally such that the reference blade of highest deflection is located in the middle of the channel. The region centered around the trigger blade reveals a HD–hairpin which is about $3\Delta S$ wide, visualized by an iso-surface of $\lambda_2 = -2.5\,\mathrm{s}^{-2}$. Between the counter-rotating legs of the hairpin a sweep is generated, which yields a global minimum of the conditionally averaged Reynolds stress $\langle u'v' \rangle_c/U^2$ above the blade of highest deflection. In contrast to the work of [72] no HU–hairpin occurs in combination with the HD–hairpin, as depicted in Fig. 6.10b. b) Coherent vortex structures visualized by pressure iso-surfaces at a value $p'/(\rho_f U^2) = -0.2$ at the same instant in time $t = \tilde{t}$ as in Fig. 6.11. A number of well separated eddies is observed ranging from the interior of the canopy far into the free-flow region. The iso-surfaces are colored by the vertical position y/H. In the bottom region of the vortices the blades are generally highly deflected.*

Especially this relation between LS–streaks and hairpins is a common feature of the turbulence in smooth channel flows. In fact, as discussed in Section 6.3.1 the free-flow region in shallow canopies behaves similarly to the boundary layer in smooth channels. A certain resemblance of coherent structures should be expected as well. This is supported by observations in [173], who stated that the turbulence and coherent structures in the free-flow region are quite similar to boundary layers rather than mixing layers.

6.3.5 Proposed model of coherent structures

The analysis of the fluid data revealed that different coherent structures can be observed at different heights in the channel. These range from turbulent wakes of the vegetation elements, over KH–like structures in the mixing layer zone, up to turbulent structures known from regular boundary layers in the free-flow region. It can, therefore, be suspected that the nature of coherent structures in canopies appears as a superposition of the different zones with corresponding turbulent mechanisms and structures. Recall that from an average point of view the canopy flow is well described by a simple three-zone model dividing the flow into an *emergent zone*, a *mixing layer zone* and a *log-layer zone* proposed in [207] (Fig. 6.13). This division is also reflected in terms of turbulence mechanisms, so that the basic idea of the three-zone model is reconsidered here and enhanced by the three-dimensional nature of coherent structures. As it turned out, the interaction between these zones may generate some unique turbulent features which do not occur in regular mixing layers and boundary layer flows. The three zones can be characterized as follows:

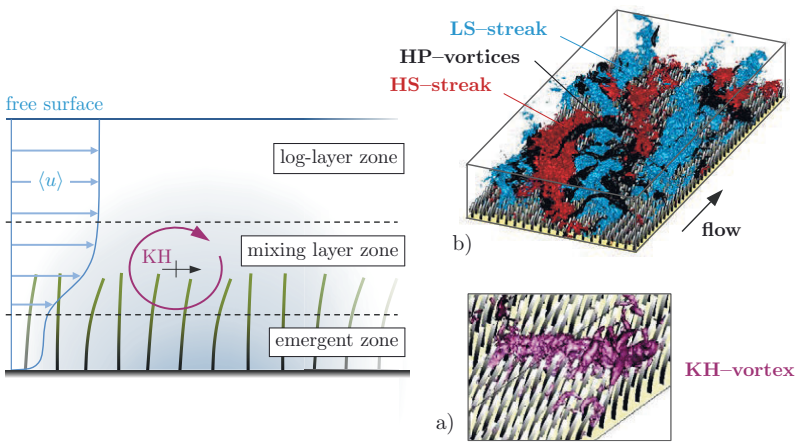

Figure 6.13: *Three-zone model of an aquatic submerged canopy flow according to [207]. The lower emergent zone is characterized by the turbulent wake of individual plants, similar to the wake shown in Fig. 4.17 for a single blade in cross-flow. In the mixing layer zone the flow prone to instabilities and turbulent fluctuations evolve to form coherent structures, e.g. KH–vortices and velocity streaks shown in Fig. a) and b), respectively. In the subsequent log-layer zone the free flow behaves very similarly to a boundary layer flow without vegetation. Here, common coherent structures are HS–streaks, LS–streaks and hairpin (HP) vortices on top of the LS–streaks. Observe the similarity of Fig. b) and Fig. 26 in [54].*

Emergent zone. The flow in the emergent zone is dominated by wakes of individual vegetation elements (Fig. 4.17). These are characterized by small-scale vortices on plant-scale which have a destabilizing impact on the mixing layer above. Furthermore, as observed in rough channel flows [2], the vortex shedding from single roughness elements can also support the generation of hairpin vortices. Nonetheless, the outer interaction with the mixing layer is limited due to the comparably small vertical transfer of momentum [81].

Mixing layer zone. For sufficiently dense canopies a pronounced shear layer in the upper region of the canopy is generated by the drag of vegetation elements [169]. Here, the flow is prone to instabilities of KH type and turbulent fluctuations evolve to form large-scale KH–vortices, as shown in Fig. 6.13a. At the leading edge of the eddy high momentum fluid is transferred from the free-flow zone towards the canopy, whereas at the trailing edge low momentum fluid is transferred upwards [214]. The KH–vortex is advected in streamwise direction while the blades beneath respond with a large reconfiguration. The analysis of two-point correlations revealed that regions of large blade deflection are accompanied by an increased streamwise velocity $u' > 0$ at the canopy edge (Fig. 6.14a). Laterally adjacent regions of lower velocity $u' < 0$ contain statistically less reconfigured blades compared to the mean blade deflection.

Log-layer zone. In the log-layer zone above the mixing layer the fluid behaves similarly to a classical boundary layer without vegetation [173]. In boundary layers of smooth channels the flow is characterized by alternating streaky regions of high velocity (HS–streaks) and low velocity (LS–streaks) where sweeps and ejections are dominant contributions. As a common basic structure, hairpin vortices of different sizes, ages and aspect ratios coexist and occur as clusters aligned in the streamwise direction [4, 55]. The clusters serve to pump fluid away from the channel bottom (ejection), consequently accumulating low speed fluid between them (LS–streak, Fig. 6.14a), often referred to as multiple ejection bursts [235, 55]. The present simulation clearly shows such bursts on top of the canopy indicating the similarity with coherent structures in boundary layers (Fig. 6.13b).

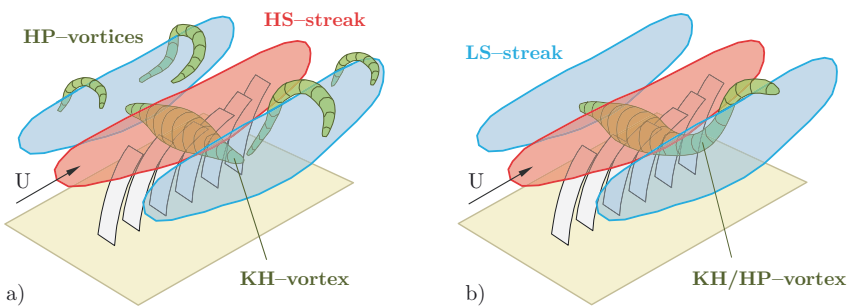

Figure 6.14: *Model system of coherent structures on canopy scale. a) A group of blades (depicted as a single column here) is strongly reconfigured in a HS–streak region, where the flow is prone to instabilities and turbulent fluctuations, both evolve to form KH–vortices. A HS–streak is accompanied laterally by LS–streak regions. These are populated by HP–vortices which pump fluid away from the canopy edge. b) Merging of KH–vortex and HP-vortex to a Kelvin–Helmholtz hairpin (KH/HP) vortex. An instantaneous snapshot of a selected KH/HP–vortex is shown in Fig. 6.15a.*

Unique turbulent features. The common coherent structures just mentioned can not be assigned completely to a specific zone. Rather, it appears that dominant turbulent features of the zones overlap and thus interact in the transition region. Especially HS–streaks and LS–streaks reach from the mixing layer deep into the free-flow zone and thus are dominant contributions in both zones. While the flow in the mixing layer tends to form KH–vortices in HS–streak regions, clusters of hairpins can be observed on top of LS–streaks in the log-layer zone. In the transition zone these vortical structures regularly interact with each other. Since KH–vortices and hairpins exhibit the same sense of rotation, they are able to merge to form KH/HP–vortices, as illustrated in Fig. 6.14b. This type of vortex appears to be a unique turbulent structure in sufficiently dense shallow canopy flows. One selected instantaneous KH/HP–vortex is shown in Fig. 6.15b. It is presumed that the merging of these two vortices increases the intensity of the associated HS-streak resulting in the formation of particularly strong sweeps. This in turn leads to a particularly pronounced reconfiguration of the canopy with deflections of single blades down to $L^*/L = 0.4$ (Fig. 6.6a).
The shape of the KH/HP–vortex discovered allows an interesting conclusion on the conditional average, which was performed to extract coherent flow structures responsible for a *monami*. Similar to the observations of Finnigan *et al.* [72], a symmetric HD–hairpin vortex was obtained (Fig. 6.10b). However, in the present instantaneous flow fields HD–hairpins were not observed. Instead, it appears that instantaneous eddies are shaped more like KH-vortices, hairpins and KH/HP–vortices of which the latter cause particularly strong reconfigurations of the blades. This suggests that the symmetric "two-legged" HD–hairpin appears as a "statistical" artifact since the conditional average does not distinguish between differently directed "one-legged" KH/HP–eddies. Indeed, since each HS–streak borders on adjacent LS–streaks the eddy-formation is equiprobable on both sides, but not strictly arranged in pairs opposite to each other.

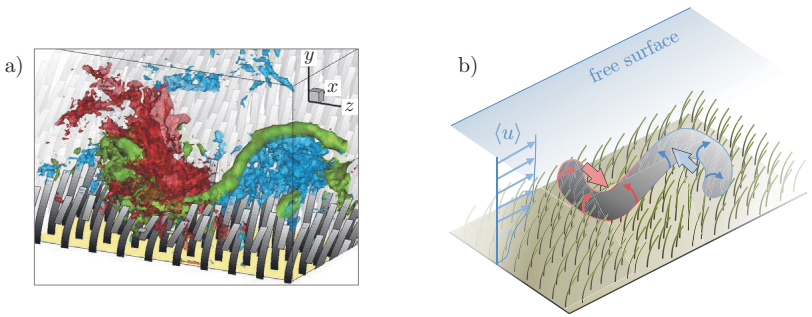

Figure 6.15: *a) Instantaneous KH/HP–vortex visualized by green pressure iso-surfaces at a value of $p'/\rho_f U = 0.2$. Regions of positive and negative velocity fluctuations $u' = \pm 0.7\,U$ are represented by iso-surfaces in red and blue, respectively. b) Schematic illustration of KH/HP–vortex dyed in gray on top of the canopy edge inclined in streamwise direction. The small red and blue arrows indicate the direction of rotation. The lower "head" of the vortex (KH part framed in red) accelerates the fluid and causes a vertical momentum transfer (broad red arrow) into the canopy region. At the same time the fluid is decelerated by the upper "head" (HP part framed in blue), which in addition pumps fluid away from the canopy edge (broad blue arrow).*

7 Conclusions

With regard to both research aims defined at the beginning, the corresponding two parts of this thesis can be summarized as follows:

Numerical method for slender rods in flow. The main contribution of the present work is the development of a numerical method suited for fluid-structure interactions of large numbers of slender flexible rods in turbulent flow. The underlying physical model was tailored to this kind of FSI using appropriate model assumptions and simplifications. While the fluid flow is modeled as usual by the three-dimensional Navier-Stokes equations, the motion of the slender structures is described by an enhanced one-dimensional rod model, the so-called geometrically exact Cosserat rod model. Based on these continuous models for fluid and structure, both partitioned problems were discretized in space and time using existing optimized approaches. The basic fluid solver was adopted from the in-house code PRIME, originally implemented by Kempe [118, 119]. Concerning the structure solver, the associated Cosserat rod equations were discretized according to recommendations of Lang *et al.* [131], who proposed a performance-optimized variant. In order to describe the interaction of fluid and structure, the associated solvers were coupled by an own semi-implicit coupling scheme based on an IBM with continuous forcing. It combines the stability of monolithic methods with advantages of partitioned approaches, such as computational efficiency. As a special feature, the coupling is exempt from any global iteration between the fluid part and the structure part, usually performed to ensure numerical stability of partitioned FSI-solvers. In contrast to other non-iterative coupling strategies, the main idea is not based on a stabilization technique, e.g. a relaxation technique, but on a semi-implicit integration of the coupling terms in the structural equations of motion. It is referred to as semi-implicit coupling here, since only those coupling quantities are treated implicitly which have an effect on the stability of the time integration. Excluded from this are structure positions, constituting the fluid-structure interface. As a result, the proposed coupling scheme requires only a single bidirectional exchange of information between the fluid solver and the structure solver, so that the computing time per individual Cosserat rod could be reduced to a minimum. This makes the developed numerical method highly efficient and particularly suitable for large-scale configurations with a very large number of deformable rods. The method was successfully validated for various test cases with single elastic rods in flow, including the well-known two-dimensional benchmark of Turek and Hron [248], its predecessor case of Ramm and Wall [261, 260], and a three-dimensional setup of a flexible blade in cross flow according to an experiment of Luhar and Nepf [150].
Besides the development and implementation of the basic FSI-solver, a key part of this work was the extension of the method to the regimes of densely arranged rods prone to collisions. For this purpose, an own constraint-based collision model was developed, tailored to the properties of Cosserat rods. It is able to represent frictional effects, lubrication, as well as multiple simultaneous collisions. The latter feature is particularly difficult, since Cosserat

rods share properties of rigid and deformable objects. As known from the collision modeling of pure rigid bodies, multiple simultaneous collisions become a global problem. While this is often solved monolithically by a global system of constraint equations of motion, the present approach uses a simpler partitioned formulation where the collision handling and the numerical treatment of the structure motion are clearly separated. This allows an easy modular implementation of the collision model into existing FSI-solvers, so that both parts can be executed in a simple staggered manner.
The numerical method presented has a wide range of applications. In the framework of this thesis it was utilized to gain fundamental insights into the physics of aquatic canopy flows, summarized in the subsequent section. Perspectively, the FSI-solver could also be applied to more technical flows, e.g. fiber suspensions important for paper manufacture, polymer melts and composite materials [244, 264], or piezo-electric blades in oscillating flow used for energy harvesting [182]. Especially for such configurations the present numerical method is designed: the fluid-structure interaction of slender rods in turbulent flow.

Application to canopy flows. In a second part of this work, the proposed FSI-solver was employed to simulate the flow through an artificial aquatic canopy according to an experimental setup of Okamoto and Nezu [176]. The corresponding abstracted canopy consisted of 800 regularly arranged strip-shaped blades, coupled to the fluid in the framework of an LES. Very good agreement with the experimental data was found for the mean velocity profile and Reynolds stresses. Moreover, the organized wave-like motion of the model plants in the *monami* regime was captured as well. Supplementing the experimental study of Okamoto and Nezu [176], the high-resolution data obtained from the simulations were analyzed to gain fundamental information on the three-dimensional nature of coherent structures in dense aquatic canopies. These new insights contributed to an enhanced understanding of the flow-biota interaction in canopy flows, such as the mechanism behind the *monami* phenomenon. It was observed that in the present type of canopy flow, the nature of coherent structures appears as a superposition of common turbulent features and mechanisms. These range from turbulent wakes of the vegetation elements in the emergent zone, over Kelvin-Helmholtz vortices generated in the mixing layer zone, up to velocity streaks and hairpins in the free-flow zone above the canopy. As it turned out, the interaction between these zones may generate unique turbulent structures which do not occur in regular mixing layers and boundary layers. Of particular importance here is the merge of Kelvin–Helmholtz vortices at the canopy edge and hairpins located on top of the low-speed streaks in the free-flow region. Since both vortices exhibit the same sense of rotation, their pairing promotes the formation of particularly strong sweeps, which in turn lead to large reconfigurations of the model plants. This appears to be a key mechanism driving the wavy motion of the canopy in the *monami* regime. To extract statistically significant information in this context, conditional averaging of the flow field was performed, using locally increased blade deflections as a trigger to identify pronounced coherent structures. Based on the averaged results, a symmetric "head-down" hairpin vortex was observed on top of the most deflected blade. It is accompanied by a strong sweep between its counter-rotating legs which supports the strong correlation between sweeps and local reconfigurations of the canopy. These "head-down" hairpins were not observed in the instantaneous flow fields. Instead, instantaneous eddies are rather shaped like Kelvin-Helmholtz vortices, hairpins and their combinations. This suggests that the symmetric hairpin obtained from the conditional average emerges as a "statistical" artifact, since the predefined condition does not distinguish between differently directed instantaneous eddies.

Future work on this topic should employ a more sophisticated averaging condition, which is able to classify different types of vortices. Additionally, time instances before and after the detected event could be recorded and averaged using the same condition as a trigger. This would improve the understanding of involved dynamic processes responsible for a particular event, e.g. a pronounced reconfiguration of the canopy. The variation of physical parameters, e.g. the rigidity of the model plants and its arrangement, will further elucidate the physical behavior. First studies in this direction revealed that Kelvin–Helmholtz vortices, velocity streaks and hairpins can also be observed in case of immobile rigid blades and more flexible blades. Moreover, configurations with spatially randomly distributed blades show a remarkably similar behavior, suggesting that the turbulent mechanisms discovered in this thesis are "universal" properties of aquatic flows trough sufficiently dense canopies.
Further research questions concerning aquatic canopy flows are addressed in the DFG-ANR project ESCaFlex (*Experiments and simulations for the study of submerged aquatic canopies consisting of long flexible blades*), currently conducted in an international collaboration of TU Dresden with scientists from the Université Claude Bernard Lyon 1. The vision here is to generate a detailed understanding of hydrodynamic processes in high-Cauchy number canopies, and to derive information relevant for aquatic ecosystems. This will be achieved through complementary experimental and numerical efforts, employing the FSI-solver developed in this thesis to realize the simulation part of the project.

Appendices

A Supplementary validation studies

This section provides supplementary validation studies for the present Cosserat rod model and the corresponding collision model. These are ordered with increasing complexity ranging from a simple static deformation up to an unsteady three-dimensional motion and deformation of the rod. In terms of the collision model, the focus lies on wall collisions of a single rod and its behavior under the influence of frictional effects.

A.1 Pure extension, shear, bending and torsion

$L = 10\,\mathrm{m}$	rod length
$W = 1\,\mathrm{m}$	rod width (square)
$E_\mathrm{s} = 1200\,\mathrm{N/m^2}$	Young's modulus
$G_\mathrm{s} = 600\,\mathrm{N/m^2}$	shear modulus
$k_\mathrm{s} = 5/6$	shear correction

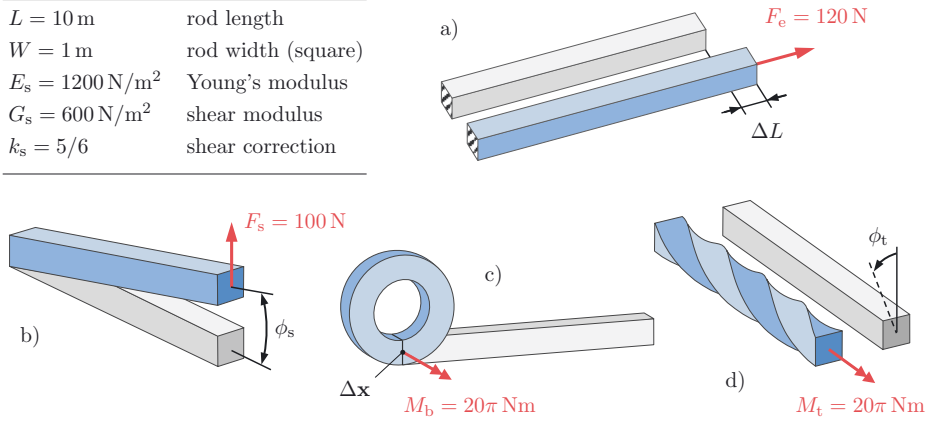

Figure A.1: *Cantilever rod fully anchored at one end (dashed area in a), hidden areas in other cases) and subjected to a) extensional force b) shear force c) bending moment d) torsional moment at the opposite rod end. While the gray colored rods represent unloaded cases, the blue colored rods show deformed configurations.*

Figure A.1 shows the four principal modes of deformation, i.e. extension, shear, bending and torsion. In each mode, the rod is subjected to an appropriate load which ensures the decoupling of the other modes.
In terms of the longitudinal deformation (Fig. A.1a) a tensile loading is validated, since a compressive loading may result in a bifurcation buckling problem. In this case, the other modes of deformation would be involved due to the nonlinear character of the Cosserat rod model. The rod elongation ΔL is related to the extensional force subjected via $F_\mathrm{e} = E_\mathrm{s} A\, \varepsilon$, with the cross sectional area $A = W^2$ and the strain $\varepsilon = \Delta L / L$ as a normalized elonga-

tion. The force of magnitude $F_\mathrm{e} = 120\,\mathrm{N}$ applied here causes a longitudinal displacement of $\Delta L = 1\,\mathrm{m}$ for the values of the parameters listed in Fig. A.1.
In contrast to the other deformation modes, a pure shear is not feasible by a load applied at the tip of the rod. The shear generated by a lateral force (Fig. A.1b) always is accompanied by a lateral bending. Here, the undesirable bending is suppressed by increasing the second moment of area ad hoc to $I = 1 \cdot 10^{20}\,\mathrm{m}^4$, so that the displacement caused by the resulting bending moment is negligible small. The lateral part of the displacement caused by the shear load $F_\mathrm{s} = 100\,\mathrm{N}$ then is given by $L\tan(\phi_\mathrm{s}) = 2\,\mathrm{m}$ for the present setup and can be completely attributed to shear deformation. The shear angle ϕ_s and the shear force F_s are connected via $F_\mathrm{s} = G_\mathrm{s} k_\mathrm{s} A_k \tan(\phi_\mathrm{s})$, where $k_\mathrm{s} A$ is the shear corrected cross sectional area.
A pure bending without shear can be realized by a moment M_b subjected to the tip of the rod (Fig. A.1c). It is given by $M_\mathrm{b} = E_\mathrm{s} I\,\kappa_\mathrm{b}$, now with the geometrically correct second moment of area $I = W^4/12$ and the curvature of the rod due to bending κ_b. In the depicted case the rod is deformed to a closed circle which results in a constant curvature of $\kappa_\mathrm{b} = 2\pi/L$. With $M_\mathrm{b} = 20\pi\,\mathrm{Nm}$ chosen here, the tip position $\mathbf{x}_\mathrm{tip}$ coincides with the clamping point, so that the magnitude of the tip displacement is $\|\Delta\mathbf{x}_\mathrm{tip}\| = L$.
Finally, a pure torsion (Fig. A.1d) is achieved by a torsional moment $M_\mathrm{b} = G_\mathrm{s} J\,\kappa_\mathrm{t}$, with the polar moment of area $J = 2I = W^4/6$ and the torsional curvature $\kappa_\mathrm{t} = \phi_\mathrm{t}/L$. With a moment of $M_\mathrm{t} = 20\pi\,\mathrm{Nm}$ applied to the rod, it is twisted by an angle of $\phi_\mathrm{t} = 2\pi$.
The results obtained from the simulations are presented in Tab. A.1. In case of extension

N_e	ϵ_e	ϵ_s	ϵ_b	ϵ_t
8	$-0.2907 \cdot 10^{-14}$	$-0.3389 \cdot 10^{-11}$	0.2392	2.2970
16	$-0.1292 \cdot 10^{-14}$	$-0.9702 \cdot 10^{-11}$	$0.2712 \cdot 10^{-1}$	0.2590
32	0.0000	0.0000	$0.4718 \cdot 10^{-2}$	$0.4571 \cdot 10^{-1}$
64	0.0000	0.0000	$0.1048 \cdot 10^{-2}$	$0.1030 \cdot 10^{-1}$
128	0.0000	0.0000	$0.2538 \cdot 10^{-3}$	$0.2515 \cdot 10^{-2}$
256	0.0000	0.0000	$0.6292 \cdot 10^{-4}$	$0.6264 \cdot 10^{-3}$

Table A.1: *Relative errors ϵ for different spatial resolutions, i.e. number of elements N_e. The errors for the different modes of deformation are computed with the following reference values: The displacement $\Delta L = 1\,\mathrm{m}$ caused by the extensional force F_e, the shear angle $\phi_\mathrm{s} = \arctan(2/10)$ caused by the shear force F_s, the magnitude of the tip displacement $\|\Delta\mathbf{x}_\mathrm{tip}\| = L$ caused by the bending moment M_b, and the torsional angle $\phi_\mathrm{t} = 2\pi$ caused by the torsional moment M_t.*

and shear the numerical solutions exactly reproduce the theoretical predictions. However, a spatial discretization of the rod causes small numerical errors in case of a pure bending and a pure torsion. This results from the numerical approximation of curvatures, i.e. κ_b and κ_t, by means of discrete quaternions (see Appendix D, Eq. (D.2h)). The relative errors, ϵ_b and ϵ_t, listed in Tab. A.1 reveal that the numerical estimation of curvature used in the present model is of second order accuracy. This confirms the spatial convergence behavior stated by Lang et al. [131].

A.2 Physical pendulum

$g = (1470 + \frac{1}{3})\ \mathrm{m/s^2}$	gravity
$L = 10\,\mathrm{m}$	rod length
$W = 1\,\mathrm{m}$	rod width (square)
$E_\mathrm{s} = 1 \cdot 10^{15}\,\mathrm{N/m^2}$	Young's modulus
$G_\mathrm{s} = 1 \cdot 10^{15}\,\mathrm{N/m^2}$	shear modulus
$\phi_0 = \pi/2$	initial inclination

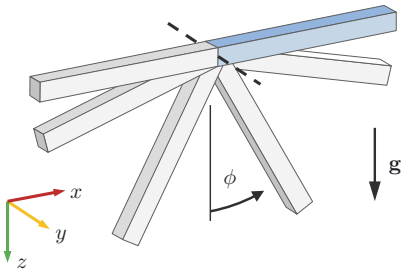

Figure A.2: *Oscillation of a rigid physical pendulum about a fixed rotation axis under the influence of gravity. Initially, at time $t = 0$, the rod (blue) is at rest and oriented in x-direction with an angular displacement of $\phi_0 = \phi(t = 0)$.*

In case of large-angle oscillations of the pendulum the differential equation of motion is nonlinear. According to [23], the temporal evolution of the angular displacement is given by

$$\phi(t) = 2\arcsin\left\{\mathrm{sn}\left[\mathrm{K}\left(\sin^2\frac{\phi_0}{2}\right) - \omega\, t\,;\, \sin^2\frac{\phi_0}{2}\right]\sin\frac{\phi_0}{2}\right\}\,, \qquad \omega = \sqrt{\frac{gL}{2I}}, \tag{A.1}$$

where $\mathrm{K}(m)$ is the complete elliptical integral of the first kind, and $\mathrm{sn}(u; m)$ is the Jacobi elliptic function with $u, m \in \mathbb{R}$. Especially for the present rod the second moment of area is $I = (W^2 + (2L)^2)/12$ with respect to the rotation axis. The period of oscillation is defined by $T = 4\,\mathrm{K}\big(\sin^2(\phi_0/2)\big)/\omega$ which is approximately $T \approx 0.5\,\mathrm{s}$ for the present parameter values listed in Fig. A.2. To realize a rigid pendulum, both elastic moduli of the Cosserat rod are sufficiently large to suppress deformations. Note, that with increasing moduli E_s and G_s the numerical problem becomes stiffer so that the numerical effort increases rapidly. Figure A.3 provides a comparison between the analytical prediction of the oscillation and the simulation results obtained with a spatial discretization of $N_e = 32$ rod elements. The maximum numerical deviation from the theoretical solution ϕ is less than 0.5°.

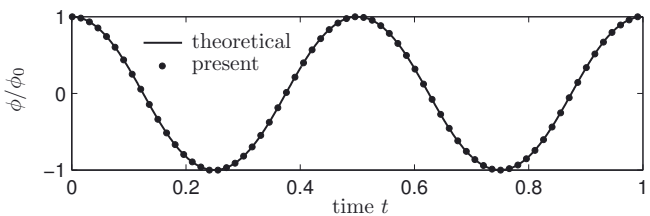

Figure A.3: *Normalized angular displacement ϕ/ϕ_0 over time t. The theoretical solution* (A.1) *is compared with the numerical solution obtained for $N_e = 32$ rod elements.*

A.3 Swinging rubber rod

$g = 9.81\,\mathrm{m/s^2}$	gravity
$L = 1\,\mathrm{m}$	rod length
$R = 5\,\mathrm{mm}$	rod radius
$\rho_\mathrm{s} = 1100\,\mathrm{kg/m^3}$	mass density
$E_\mathrm{s} = 5 \cdot 10^6\,\mathrm{N/m^2}$	Young's modulus
$\nu_\mathrm{s} = 0.5$	Poisson's ratio

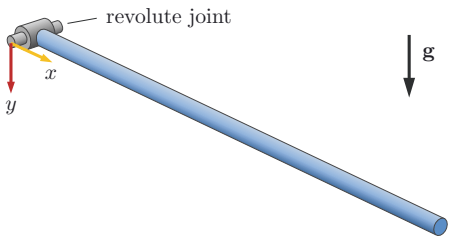

Figure A.4: *Setup of a slender, circular rubber rod supported by a revolute joint at one end (not to scale). Initially, the rod is aligned in x-direction and exposed to the field of gravity.*

Figure A.4 shows the setup of a highly flexible, slender rod describing a pendulum-like motion under the influence of gravity. In contrast to the rigid physical pendulum studied in Section A.2 deformations now become important and significantly affect the motion. This benchmark was initially introduced by Lang et al. [131] and used for a comparison with the commercial FEM-solver Abaqus. They demonstrated the outstanding accuracy of the rod model even for coarse spatial resolutions, especially with $N_\mathrm{e} = 10$ equal sized elements in the present test case. Later, Schulze et al. [210] took up the setup for a validation of different numerical Cosserat rod models, while retaining a spatial discretization of 10 elements. Figure A.5 presents a cross-comparison of the previous results and the present simulation. Especially in the initial phase of the oscillation the dynamic behavior reveal a very good agreement with the reference data. At later stages in time, however, small deviations can be

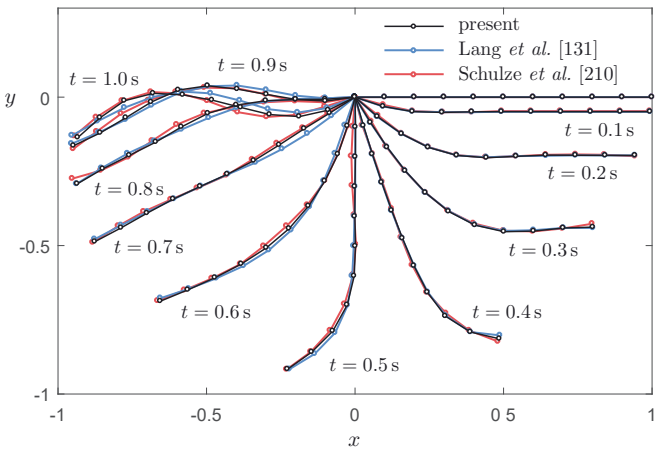

Figure A.5: *Temporal evolution of the rubber rod under the influence of gravity. Shown are the center lines of the rod at selected instances in time. The present results (black lines) are compared to the data of Lang et al. [131] (blue lines) and the results obtained by Schulze et al. [210] (red lines).*

observed between the different simulations. This is caused by a temporal accumulation of numerical errors resulting from differences in the numerical scheme employed to discretize the continuous Cosserat rod. Although the numerical model proposed by Lang et al. [131] is implemented in the present work, both solutions do not coincide against all expectations. This can be explained by slight modifications of the model applied by Lang et al. [144], in order to improve the accordance between the Cosserat rod model and the FEM-solution obtained with Abaqus. In terms of the present setup the best agreement was obtained with the following two modifications. One is the decoupling of internal shear forces and internal extensional forces which both are coupled by default in the Cosserat rod model. The second one is the implementation of an improved mass matrix instead of common lumped mass matrix, where the mass of the rod is concentrated at the discretization nodes which slightly affects inertia properties especially for coarse spatial discretizations with few elements. The numerical rod model of Schulze et al. [210] also differs in terms of discretization techniques applied here. Contrary to the present approach, the rod is discretized in a non-staggered fashion, where translational and rotational degrees of freedom coincide at the same node. Furthermore, they use a recursive order-n multibody system (MBS) formulation of the underlying physical rod model. In this context, the only small deviations obtained for the different numerical approaches are entirely satisfactory.

A.4 Vibration of simply supported rod

$L = 10\,\mathrm{m}$	rod length
$A = 1\,\mathrm{m}^2$	cross sectional area
$I = 0.1\,\mathrm{m}^4$	second moment of area
$\rho_\mathrm{s} = 1\,\mathrm{kg/m}^3$	mass density
$E_\mathrm{s} = 1 \cdot 10^4\,\mathrm{N/m}^2$	Young's modulus
	shear moduli:
$G_\mathrm{s} = 1 \cdot 10^4\,\mathrm{N/m}^2$	*shear deformable*
$G_\mathrm{s} = 1 \cdot 10^7\,\mathrm{N/m}^2$	*shear stiff*

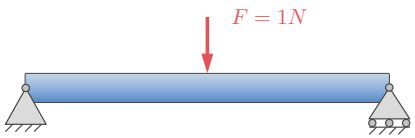

Figure A.6: *Simply supported rod pinned at one end to a revolute joint, while the other end is supported by a roller. At time $t = 0$ a force F is abruptly subjected to the mid-span causing a vibration of the rod.*

The forced vibration of a simply supported straight rod, shown in Fig. A.6, is a common benchmark for a dynamic response of rods since an analytical solution exists for very small vibration amplitudes, i.e. linear kinematics. In that case, the temporal evolution of the vertical displacement d_y at the mid-span of the rod can be expressed by a series expansion [195]

$$d_y(L/2,t) = \frac{2F}{\rho_\mathrm{s} A L} \sum_{n=1,\,n\ \mathrm{odd}}^{\infty} \frac{1-\cos(\omega_n t)}{\omega_n} \qquad \text{with} \qquad \omega_n = \left(\frac{n\pi}{L}\right)^2 \sqrt{\frac{E_\mathrm{s} I}{\rho_\mathrm{s} A}}\,, \tag{A.2}$$

and the natural frequencies ω_n for odd $n \in \mathbb{N}$. The period of the dominating first mode is $T_1 = 2\pi/\omega_1 \approx 2.013\,\mathrm{s}$. Figure A.6 provides all relevant geometrical and material properties which were adopted from Zupan *et al.* [275]. In this reference, a shear modulus of

$G_s = 1 \cdot 10^4\,\mathrm{N/m^2}$ was used for a comparison to the theoretical solution of a completely shear stiff rod. In contrast to [275], in the present work the rod behaves shear deformable for $G_s = 1 \cdot 10^4\,\mathrm{N/m^2}$. This causes a slight sagging of the rod during vibration and, furthermore, alters the oscillation frequency. As a consequence, the present simulation results do not agree with the analytical prediction (A.2) that, of course, does not take into account any shear effects. To allow, however, a comparison to the shear stiff oscillation the shear modulus was increased by two orders of magnitude to $G_s = 1 \cdot 10^7\,\mathrm{N/m^2}$. Note, that a further increase of G_s would have no impact on the oscillation, but increases the computational effort since the underlying equations become much stiffer. Figure A.7 shows the oscillation obtained for two different shear moduli as well as the theoretical solution of the shear stiff rod. For $G_s = 1 \cdot 10^7\,\mathrm{N/m^2}$ the present solution almost coincide with the theoretical expectations regarding oscillation amplitudes and frequency. As presented in Fig. A.8 this already applies to a coarse spatial resolution of $N_e = 16$ elements which barely differs from the finest resolution with $N_e = 128$ elements. The time step size was automatically adjusted by RADAU5 to hold a set relative tolerance of $1 \cdot 10^{-8}$, so that the temporal discretization error is negligibly small. The table depicted in Fig. A.8 shows that with increasing number of elements N_e the period of the first bending mode converges to $T_1 = 2.023\,\mathrm{s}$. This value slightly underestimates the theoretical value $T_{1,\mathrm{ref}} = 2.013\,\mathrm{s}$ and yields an error of $\epsilon = -0.5\,\%$ which does not completely vanish. This behavior also was observed by Lang *et al.* [131] who reported that remaining

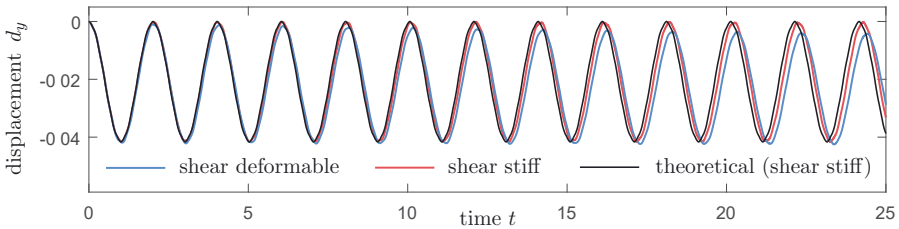

Figure A.7: *Temporal evolution of the vertical displacement $d_y(L/2, t)$ for both the shear deformable rod at $G_s = 1 \cdot 10^4\,\mathrm{N/m^2}$ and the shear stiff rod at $G_s = 1 \cdot 10^7\,\mathrm{N/m^2}$. The present results obtained with $N_e = 128$ are compared to the theoretical solution* (A.2) *of a shear stiff vibration.*

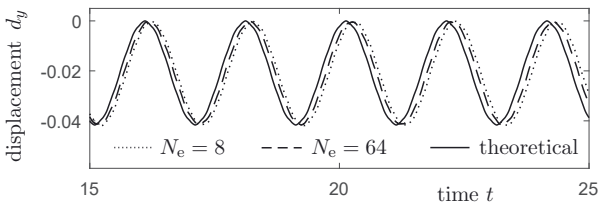

N_e	T_1 in s	ϵ
16	2.029	−0.0079
32	2.024	−0.0056
64	2.024	−0.0053
128	2.023	−0.0050

Figure A.8: *Vertical displacement u at the mid-span of the vibrating shear stiff rod for different spatial resolutions ranging from $N_e = 16$ to $N_e = 128$ elements. The period of the first bending mode converges to a value of $T_1 = 2.023\,\mathrm{s}$ which yields an error of $\epsilon = -0.5\,\%$ to the theoretical value $T_{1,ref} = 2.013\,\mathrm{s}$ concerning Eq.* (A.2)*. The values of T_1 for different resolutions were evaluated by means of an FFT (fast Fourier transform).*

deviations seems to be influenced by the spatial discretization technique [144]. Another potential cause may be attributed to the difference of the underlying differential equations. As already mentioned in Section A.1, a lateral bending is accompanied by shear if the rod is subjected to a lateral force, as it is the case in the present situation. Consequently, the corresponding parts for shear and bending in the Cosserat rod equations are geometrically coupled. In this regard it is presumed, that even for very large shear moduli the Cosserat rod model does not completely coincide with the Euler-Bernoulli rod equation solved to obtain Eq. (A.2). This is evidenced by two further simulations. Besides the bending oscillation, a pure extensional vibration and a pure torsional vibration were validated by similar setups. In these cases, the natural frequencies converged to the theoretical values, since the corresponding part of the Cosserat rod equations are decoupled from the other deformation modes and are equivalent to the underlying differential equations of the reference solutions.

A.5 Spin-up maneuver

$L = 10\,\mathrm{m}$	rod length
$A = 6 \cdot 10^{-3}\,\mathrm{m}^2$	cross sectional area
$I = 3 \cdot 10^{-6}\,\mathrm{m}^4$	2nd moment of area
$\rho_\mathrm{s} = 200\,\mathrm{kg/m}^3$	mass density
$E_\mathrm{s} = 14/3 \cdot 10^9\,\mathrm{N/m}^2$	Young's modulus
$G_\mathrm{s} = 2 \cdot 10^9\,\mathrm{N/m}^2$	shear modulus
$k_\mathrm{s} = 5/6$	shear correction

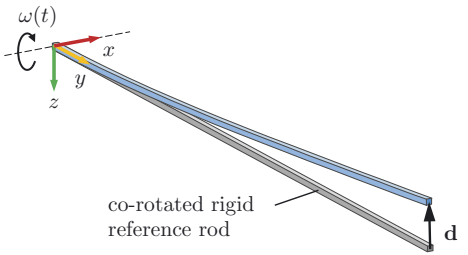

Figure A.9: *Spin-up maneuver proposed by Simo and Vu-Quoc [218]. An initially straight rod, pinned at one end, is rotated around the x-axis with a prescribed time-dependent angular velocity $\omega(t)$. The part of pure deformation during rotation, denoted as $\mathbf{d} = (d_y, d_z)^\top$, is obtained by subtracting the rigid body motion from the overall motion of the rod.*

The kind of setup shown in Fig. A.9 initially was proposed by Kane *et al.* [115, 116] to illustrate the importance of geometrical exactness of rod models. They showed, how linearized kinematics may lead to very non-physical results, e.g. the destabilization of physically stable systems [115, 217]. Shortly after, Simo and Vu-Quoc [217, 218] adopt this type of motion to study the behavior of their rod model in case of finite vibrations coupled to large overall motions of the rod. In the present work, the material and geometrical properties are consistent to this configuration. It is known as Spin-up maneuver, and has established as a standard test for nonlinear kinematics of rods. As illustrated in Fig. A.9, one end of the rod is pinned to a revolute joint that prescribes an angular velocity around the x-axis

$$\omega(t) = \frac{90}{t_\mathrm{ref}} \begin{cases} \frac{t}{t_\mathrm{ref}} - \frac{1}{2\pi} \sin\left(2\pi \frac{t}{t_\mathrm{ref}}\right), & 0 \le t < t_\mathrm{ref} \\ 1, & t \ge t_\mathrm{ref} \end{cases} \tag{A.3}$$

with the reference time $t_\mathrm{ref} = 15\,\mathrm{s}$. The other end moves freely in space and exhibits a large overall motion due to the rotation imposed. During the acceleration phase $t < t_\mathrm{ref}$, the rod is spun up from rest and largely deforms due to inertia effects. After this initial

deflection for $t > t_{\text{ref}}$, the rod rotates with a constant angular velocity $\omega = 90/t_{\text{ref}}$. During this phase of steady rotation, it vibrates with small amplitudes while it is straightened by centrifugal force. In addition, this force causes a centrifugal stiffening of the rod so that it oscillates with increased natural frequencies [218]. Figure A.10 shows the time-histories of displacements $\mathbf{d} = (d_y, d_z)^\top$ computed with respect to the co-rotated reference rod (Fig. A.9). The present simulation results are compared to those obtained by Simo and Vu-Quoc [218], both qualitatively coincide with each other. A cross-comparison is provided in Tab. A.2.

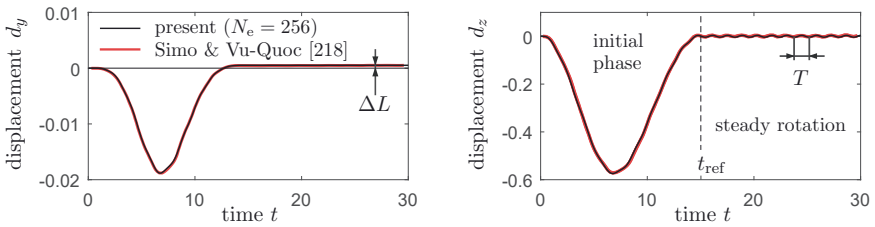

Figure A.10: *Temporal evolution of the displacement components d_y and d_z. During the phase of steady rotation, the centrifugal force causes an rod elongation of $\Delta L = 0.514 \cdot 10^{-3}$ m. Simultaneously, the rod oscillates laterally with a period of $T = 1.393$ s. The present results, fully converged for $N_e = 256$ elements, are compared to the reference data of Simo and Vu-Quoc [218].*

	$d_{y,\max}$ in m	$d_{z,\max}$ in m	ΔL in m	T in s
present ($N_e = 256$)	$-0.188 \cdot 10^{-1}$	-0.574	$0.514 \cdot 10^{-3}$	1.393
Clerici [44]	$-0.190 \cdot 10^{-1}$	-0.580	$0.514 \cdot 10^{-3}$	1.417
Simo & Vu-Quoc [218]	$-0.188 \cdot 10^{-1}$	-0.575	$0.514 \cdot 10^{-3}$	1.410
theoretical [44]	–	–	$0.514 \cdot 10^{-3}$	1.392

Table A.2: *Cross-comparison of maximal displacement $\mathbf{d}_{\max} = (d_{y,\max}, d_{z,\max})^\top$ during the initial transient, as well as the longitudinal elongation ΔL and period of oscillation T during the steady-state phase. Present converged results are compared to the data of Simo and Vu-Quoc [218] (values taken from [44]) and to the simulation results obtained by Clerici [44]. Theoretical expectations were provided in [217, 44].*

The values of maximal deflection $d_{y,\max}$ and $d_{z,\max}$ during the acceleration phase are equivalent to the reference data of Simo and Vu-Quoc [218]. The centrifugal elongation is also well captured and in agreement with the theoretical value of [217]

$$\Delta L = L\left(\frac{\tan(aL)}{aL} - 1\right) \qquad \text{with} \qquad a = \omega\sqrt{\frac{\rho_s}{E_s}}, \tag{A.4}$$

resulting in $\Delta L = 0.514 \cdot 10^{-3}$ m for the present set of parameters listed in Fig. A.9. The period of lateral oscillation in the steady phase was determined by means of an FFT analysis to $T = 1.393$ s, which reveals a slight deviation from the reference data of about 1.5%. However, it almost perfectly reproduces the theoretical value of $T = 1.392$ s obtained with the Rayleigh-Ritz method by Clerici [44].

A.6 Lateral collision

coefficient of restitution:

$e = 0,\ 0.5,\ 1$

initial conditions:

$v|_{t=0} = v = -5\,\mathrm{m/s}$

$y|_{t=0} = 1\,\mathrm{m}$

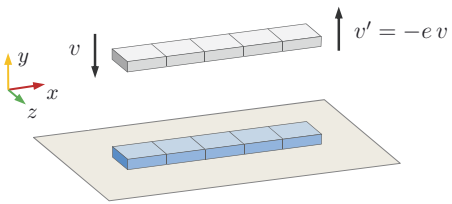

Figure A.11: *Setup of a straight rod laterally collides with a wall. After the rod is collided with an impact velocity of v, it bounces back with velocity v', depending on the coefficient of restitution e.*

The configuration shown in Fig. A.11 is chosen to validate a pure lateral collision of Cosserat rods. In this respect, there is no difference between the collision of two rods or the collision of a rod with a static wall. The latter can simply be represented by a Cosserat rod of huge size with infinite inertia.
As described in Section 5.3.5, a longitudinal collision strongly differs from a lateral collision because of the anisotropic nature of the Cosserat rod model. In the latter case, the collision force acts parallel to the cross sections which are assumed to be rigid. The elastic behavior such as internal friction is simply captured by the restitution coefficient $e \in [0, 1]$, validated for the three cases $e = 0,\ 0.5,\ 1$ with the present setup. According to Fig. A.12 the results of the simulations reproduce the expected theoretical behavior for different coefficients of restitution e.

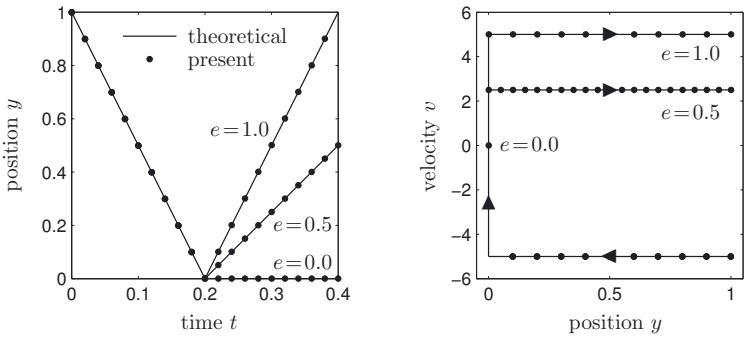

Figure A.12: *Lateral collision of a straight rod with a wall for different coefficients of restitution e. Shown are the temporal evolution of the rod position y (arbitrary point on the underside of the rod) and the corresponding phase portrait. The present simulation perfectly matches the theoretical behavior.*

A.7 Longitudinal collision

structure properties:

$L = 1\,\mathrm{m}$	length
$A = 0.01\,\mathrm{m}^2$	cross sectional area
$\rho_\mathrm{s} = 1000\,\mathrm{kg/m}^3$	mass density
$E_\mathrm{s} = 4 \cdot 10^5\,\mathrm{N/m}^2$	Young's modulus

coefficient of restitution:

$e = 0$

initial conditions:

$v|_{t=0} = v = -5\,\mathrm{m/s}$

$y|_{t=0} = 1\,\mathrm{m} + \xi$

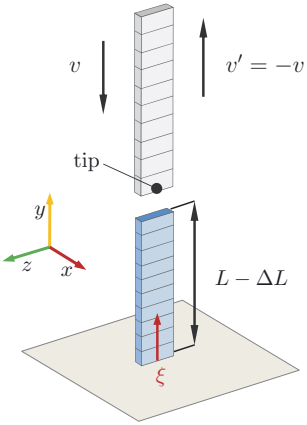

Figure A.13: *Configuration of a straight rod colliding longitudinally with a wall. After the rod has come into contact with the wall at an impact velocity of v, it performs a compression up to a length of $L - \Delta L$ followed by an expansion phase. Even if the coefficient of restitution is $e = 0$, the rod separates and moves away from the wall with $v' = -v$ after the expansion phase.*

The setup sketched in Fig. A.13 was chosen to test a pure longitudinal collision of the Cosserat rod. The rod approaches the wall with a constant velocity v. Thereafter, at the time of first contact the rod compresses until all kinetic energy is stored as internal elastic energy within the rod. Since the collision is elastic here, the rod decompresses in the same way and moves away from the wall with a uniform velocity of $v' = -v$. For the period of contact $t \in [t_\mathrm{c}, t_\mathrm{c} + \Delta t_\mathrm{c}]$ the wave solution reveals the longitudinal compression of the rod [208]

$$\Delta l\,(\xi, t) = -\frac{L\,v}{c} \sum_{n=1}^{\infty} \frac{8 \sin(\Pi_n\,\xi) \sin(\Pi_n\,ct)}{\pi^2\,(2n-1)^2}\,, \tag{A.5}$$

with $\Pi_n = (n - 1/2)\,\pi/L$ and $c = \sqrt{E_\mathrm{s}/\rho_\mathrm{s}}$ the speed of sound. During the time of contact the corresponding contact force at the tip is given by

$$f_\mathrm{c} = -E_\mathrm{s} A \left.\frac{\partial \Delta l}{\partial \xi}\right|_{\xi=0} = \frac{E_\mathrm{s} A\,v}{c} \tag{A.6}$$

and thus has a constant value over the time interval $\Delta t_\mathrm{c} = 2L/c$. The maximal contraction is $\Delta L = \Delta l\,(L, \Delta t_\mathrm{c}/2) = L/4$. As discussed in Section 5.3.5, the collision process is resolved by the Cosserat rod model for a pure longitudinal collision. In that case, a restitution coefficient of $e = 0$ is mandatory to enforce a zero relative velocity between the rod and the wall and to avoid mutual penetration. For the example studied here, the collision model enforces the boundary condition $\Delta l|_{\xi=0} = 0$ for the underlying wave equation whose solution during the period of contact is given by Eq. (A.5). After the rod contacts the wall the collision process is resolved in time and space by the structure solver.
The results of the simulation are in good agreement with the theoretical solution, as shown in Fig. A.14. The motion of the rod is reproduced correctly during the entire collision process

including approach, contact and rebound. Due to numerical inaccuracies a wave of small amplitude remains after the rod has left the wall. The corresponding oscillations can be seen in the velocity plot of Fig. A.14. It is assumed that the abrupt jump in the contact force leads to errors due the time integration by the structure solver. It was observed, that the frequency of the remaining wave scales with $1/\Delta t$, while the amplitude decreases with the time step size which is indicative of a purely numerical effect. Since there is no internal viscous damping in this test case, the wave remains for all time.
A convergence study is shown in Fig. A.14d. Here, a simultaneous reduction of the time step Δt and the number of elements N_e were performed. The coarsest resolution is $\Delta t = 20 \cdot 10^{-4}\,\mathrm{s}$ and $N_\mathrm{e} = 25$, while the finest resolution is $\Delta t = 2.5 \cdot 10^{-4}\,\mathrm{s}$ and $N_\mathrm{e} = 200$. Depending on the time step size the rod slightly penetrates the wall. For the coarsest resolution with $\Delta t = 20 \cdot 10^{-4}\,\mathrm{s}$ the penetration depth is less than $0.015L$ and decreases linearly with Δt. In other words, the model is of first order accuracy, as discussed in Section 5.1.1.

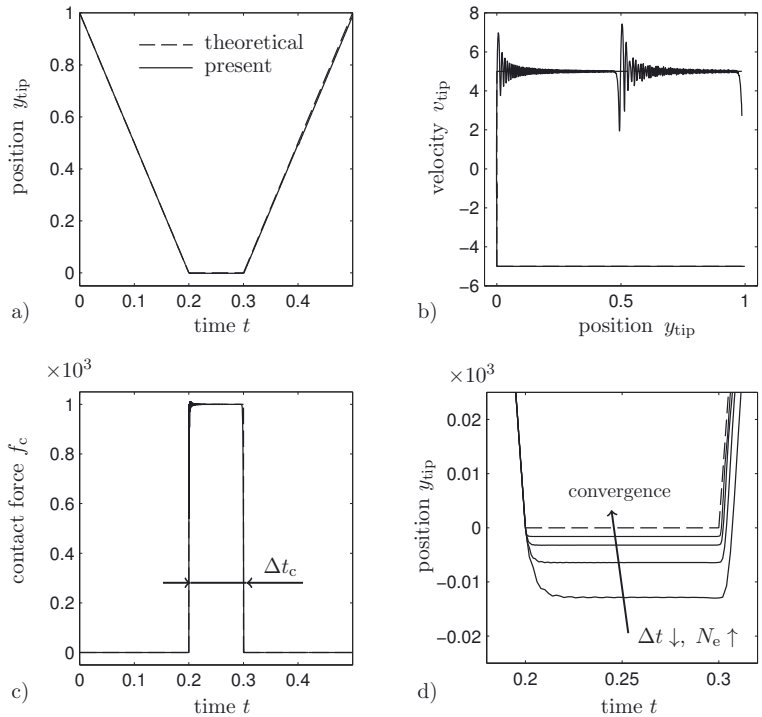

Figure A.14: *Longitudinal collision of a straight Cosserat rod with a wall obtained with a time step* $\Delta t = 2.5 \cdot 10^{-4}\,\mathrm{s}$ *and* $N_\mathrm{e} = 200$ *rod elements. Shown are the temporal evolution of a) tip position* y_tip*, b) corresponding phase portrait and c) contact force* f_c *according to Eq.* (A.6)*. d) Zoom of tip position* y_tip *for different resolutions. The coarsest resolution is* $\Delta t = 20 \cdot 10^{-4}\,\mathrm{s}$ *and* $N_\mathrm{e} = 25$*, while the finest resolution is* $\Delta t = 2.5 \cdot 10^{-4}\,\mathrm{s}$ *and* $N_\mathrm{e} = 200$*. The successive refinement shows an overall first order accuracy.*

A.8 Sliding on an inclined plane

$g = \sqrt{2}\,\mathrm{m/s^2}$ gravitational acceleration
$\phi = 45\,^\circ$ angle of inclination

coefficients of friction:
$\mu_\mathrm{k} = 0.5$ *kinetic friction*
$\mu_\mathrm{s} \lesseqgtr 1$ *static friction*

initial conditions:
$s|_{t=0} = s_0$
$\dot{s}|_{t=0} = 0$

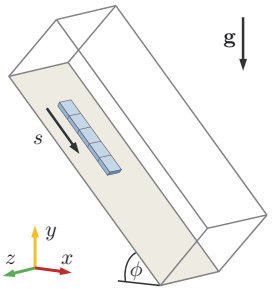

Figure A.15: *Configuration of a straight rod sliding on a plane inclined by an angle ϕ. Depending on the value of the coefficient of static friction μ_s the rod remains at rest for $\mu_\mathrm{s} < 1$, while the rod slides down the plane for $\mu_\mathrm{s} \geq 1$.*

The proposed collision model includes a simple model for tangential friction. The setup shown in Fig. A.15 is used to validate both, a static contact where the structures remain at rest, as well as the dynamic case considering tangential friction forces that influence the rod motion. As in the other test cases, the inclined wall is represented by a Cosserat rod of huge size with infinite inertia. In principle, the friction model is suitable for a general dynamic collision or static contact between two or more rods. Contrary to the general case, the dynamic behavior of the rod is theoretically accessible for the present configuration. If the coefficient of friction is $\mu_\mathrm{s} \geq 1$ the normal contact force is larger than the downhill force and the rod remains at rest (sticking mode), with the value of ϕ chosen here. For $\mu_\mathrm{s} < 1$ the rod starts to accelerate, counteracted by kinetic friction forces (sliding mode). In the latter

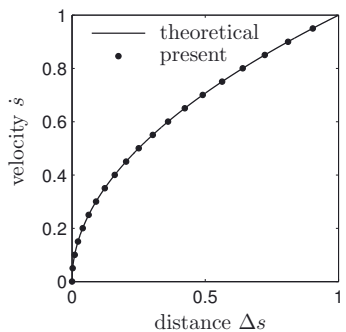

Figure A.16: *Phase portrait of a sliding rod on an inclined plane with $\mu_\mathrm{s} < 1$. Compared are the results of the present simulation (dots) with the theoretical expectation (line).*

case, the velocity of the rod is given by $\dot{s} = \sqrt{\Delta s}$, where $\Delta s = s - s_0$ represents the covered distance, and s_0 the position of the rod at time $t = 0$. Fig. A.16 shows the sliding velocity $\dot{s}$ over distance Δs. The present simulation reproduces the theoretical behavior obtained for the proposed Coulomb friction model. The rod remains immobile in case of $\mu_\mathrm{s} \geq 1$.

A.9 Sliding on a viscous fluid film

$g = \sqrt{2}\,\mathrm{m/s^2}$ gravitational acceleration
$\phi = 45\,^\circ$ angle of inclination

structure properties:
$m = 10\,\mathrm{kg}$ mass
$A_\mathrm{c} = 0.2\,\mathrm{m^2}$ contact area

fluid properties:
$\mu_\mathrm{f} = 1\,\mathrm{N\,s/m^2}$ dynamic viscosity
$h = 0.02\,\mathrm{m}$ film thickness

initial conditions:
$s|_{t=0} = s_0$
$\dot{s}|_{t=0} = 0$

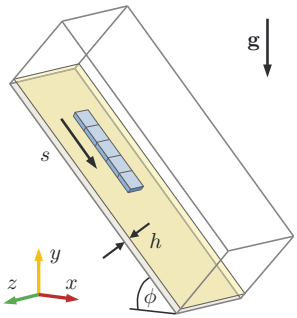

Figure A.17: *Setup of a straight rod sliding on a thin fluid film down a plane, inclined by an angle ϕ. Initially, the rod is at rest and starts to accelerate under the influence of gravity, while the fluid film acts against this motion due to viscous friction at the contact surface of area A_c.*

As described in Section 5.4, the present collision model provides a simple lubrication model to capture the influence of the fluid film between colliding rods. The configuration shown in Fig. A.17 is used to validate the lubrication model in the case of a pure tangential relative motion between the rod and a wall. Driven by the downhill force $f_\mathrm{dh} = m\,g\sin(\phi)$ the rod starts to accelerate along the inclined wall in s-direction, counteracted by viscous friction of the fluid. Compared to the sliding velocity of the rod $\dot{s}$, the proper motion of the fluid film can be neglected for small h. In this case, a linear shear layer is generated between the rod and the wall, where a uniform force distribution $f_\mathrm{lub}/A_\mathrm{c} = \eta_\mathrm{f}\,\dot{s}/h$ acts on the bottom side of the rod against the direction of motion. With the values of the parameters listed in Fig. A.17, the equation of motion along s is given by $\ddot{s} = 1 - \dot{s}$ with the initial position $s(t=0) = s_0$. The theoretical solution of the covered distance $\Delta s = s(t) - s_0 = t - 1 + e^{-t}$ is well captured by the numerical results, obtained with the present lubrication model. Fig. A.18 shows the sliding velocity $\dot{s}$ over the covered distance Δs.

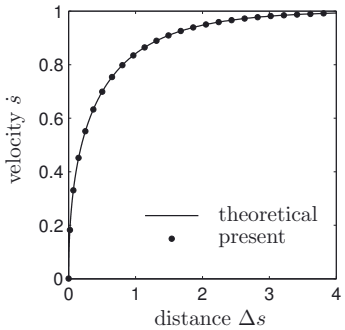

Figure A.18: *Phase portrait of a sliding rod on a viscous fluid film, given by $\dot{s} + \ln(1-\dot{s}) = -\Delta s$. Compared are the results of the present simulation (dots) with the theoretical expectation (line).*

B Model reduction of the Cosserat rod

The nonlinear Cosserat rod equations (2.13) describe the rod motion with six degrees of freedom, which are coupled nonlinearly due to the geometrically exact representation of the kinematic relations. The numerical treatment of these equations is not trivial and requires special techniques, as described in Section 3.2. This is also reflected by an increased computational effort. In this context, the question arises whether the rod equations can be simplified further to save computational time without loss of physical plausibility. The following two modifications are suitable for the present rod model, accompanied by advantages and disadvantages:

Linearization of kinematic relations: Especially for infinitesimally small displacements and rotations the rod equations can be linearized in space. Lagrangian and Eulerian configuration coincide while the individual measure of strains for axial extension, bending and torsion geometrically decouple. As a result, the corresponding parts of the Cosserat rod equations decouple as well and can be treated separately. The FSI problems considered here are dominated by a bending deformation. The corresponding part of the linearized Cosserat equations simplifies to the common Euler-Bernoulli beam equation or, if shear deformability is essential, to the Timoshenko beam equation. Other modes have a limited impact on the overall dynamic response and can be neglected. In a regime of small displacements the use of the Euler-Bernoulli equation drastically reduces the computational effort and is thus the optimal choice. However, if the model is employed in the regime of finite displacements and rotations, the following aspects arise:

- In the general case, when nonlinear kinematics become important, the deformation modes do not decouple and interact with each other. Consider, for instance, the scenario shown in Fig. B.1. When subjecting a straight rod to an external bending moment $\mathring{\mathbf{m}}$ at one end, it moves in space until a static equilibrium is reached. In the linear Euler-Bernoulli equation an internal axial tension is not considered which causes a non-physical elongation of the rod in case of large lateral displacements, as illustrated in Fig. B.1. However, such geometrical reconfigurations of the rod play a crucial role in some physical phenomena. By neglecting geometrical changes in shape, interesting physical effects could be suppressed inadvertently.
  Some advanced Euler-Bernoulli equations incorporate additional constrains preventing any artificial elongations of the rod. In principle, this contradicts a spatial linearization since geometrically nonlinear effects are taken into account again. Furthermore, solving constrained differential equations is more challenging, as described below.

- Linear Euler-Bernoulli beam models assume conservative loads that are laterally subjected to the rod. Longitudinal components of the load caused by geometrical changes of the rod are not considered. Furthermore, non-conservative or co-rotated loads (see Section 3.3.3),

which change their orientation depending on the current rod shape, e.g. pressure loads, are not accounted for by geometrically linearized rod models. Obviously, at very small displacements conservative and non-conservative forces coincide, so that geometrical errors remain small. For large displacements, however, the error due to geometrical changes may have a strong impact on the dynamic response.

Even if the computational effort can be reduced drastically when using geometrically linearized rod equations, the simulation results may exhibit non-physical effects, especially for larger displacements. However, this regime can not be precluded for the FSI problems considered in the present work. For this reason, a linearization of the kinematic relations is not performed here.

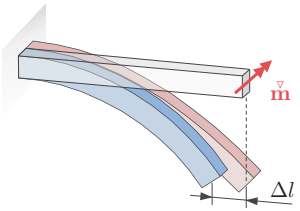

Figure B.1: *Straight clamped rod subjected to an external moment. Compared are the results of the static equilibrium obtained with the Euler-Bernoulli beam model (red rod) and with the Cosserat rod model (blue rod). For large displacements the linear Euler-Bernoulli model causes an artificial elongation of the rod since geometrical nonlinearities are not considered.*

Additional kinematic constraints for axial tension and shear: The FSI problems considered here are dominated by a large-scale bending of rods accompanied by torsion in some cases. These so-called "soft" degrees of freedom of the deformation mainly determine the dynamic behavior of the rod. External loads usually are not sufficiently large to yield an elongation or a shear deformation. This means that the "stiff" degrees of freedom, i.e. axial tension and shear, can be neglected in terms of the overall motion of the rod. In other words, the rods behave in an almost shear-stiff and inextensible manner. Consequently, the corresponding degrees of freedom can be canceled by appropriate kinematic constraints in the Cosserat rod equations. As described in [131], the constraints $\mathbf{r}_X \cdot \mathbf{c}' = \mathbf{r}_Y \cdot \mathbf{c}' = 0$ inhibit lateral shearing of the rod while the cross sections remain normal to the center line ζ. The Cosserat rod equations turn into the equations of the nonlinear Euler-Bernoulli beam. An inextensible Euler-Bernoulli beam additionally imposes the constraint $\|\mathbf{c}'\| = 1$, which inhibits an elongation of the rod along the arc length coordinate Z. The degrees of freedom required for the inextensible Euler-Bernoulli beam are half in number compared to the Cosserat equations. At first glance, this safes further computational time. However, as demonstrated in [131], an incorporation of inextension constraints is numerically challenging and does not necessarily reduce the computational effort, although the degrees of freedom are reduced. For this reason, no additional constraints are imposed in the present Cosserat rod model.

C Convergence of direct forcing method

This section provides a derivation of the rate of convergence of the direct forcing method employed to impose the velocity constraint

$$\mathbf{u}(\mathbf{x},t) = \mathbf{u}_\Gamma(\mathbf{x},t) \qquad \forall \mathbf{x} \in \Gamma \tag{C.1}$$

for a velocity field $\mathbf{u} = \mathbf{u}(\mathbf{x},t)$ on an embedded boundary Γ. The velocity field satisfies the differential equation

$$\frac{\partial \mathbf{u}}{\partial t} = \mathbf{rhs}(\mathbf{u},t) + \mathbf{f}_\Gamma, \tag{C.2}$$

where $\mathbf{rhs}(\mathbf{u},t)$ is the right-hand side of the momentum balance of the fluid, and $\mathbf{f}_\Gamma$ the forcing term used to realize the constraint (C.1). According to the direct forcing approach it is given by

$$\overline{\mathbf{f}}_\Gamma = \frac{1}{\Delta t}\int_{t^n}^{t^{n+1}} \mathbf{f}_\Gamma \,\mathrm{d}t = \frac{\mathbf{u}_\Gamma^{n+1} - \tilde{\mathbf{u}}}{\Delta t}\,, \tag{C.3}$$

where $\overline{\mathbf{f}}_\Gamma$ is a temporally constant force acting within a given time interval $[t^n, t^{n+1}]$ with $\Delta t = t^{n+1} - t^n$. As described in Section 4.5 the forcing (C.3) can be derived directly from the differential equation (C.2) via the fundamental theorem of calculus and incorporating the velocity constraint (C.1) on each discrete instant in time, i.e. $\mathbf{u}^{n+1} = \mathbf{u}_\Gamma^{n+1}$. The velocity $\tilde{\mathbf{u}}$ is a shorthand for

$$\tilde{\mathbf{u}} = \mathbf{u}^n + \int_{t^n}^{t^{n+1}} \mathbf{rhs}(\mathbf{u},t)\,\mathrm{d}t\,, \tag{C.4}$$

which is obtained by integrating Eq. (C.2) in time over the interval $[t^n, t^{n+1}]$ without accounting for the effect of the immersed boundary and can be interpreted as a predictor velocity. The magnitude of the force defined by Eq. (C.3) is simply determined by the deviation of the predicted velocity $\tilde{\mathbf{u}}$ from the desired velocity $\mathbf{u}_\Gamma$. After integration of Eq. (C.2) accounting for the forcing term $\overline{\mathbf{f}}_\Gamma$, the constraint (C.1) is imposed with a certain numerical accuracy. In the following the remaining numerical error $\boldsymbol{\epsilon} = \mathbf{u}^{n+1} - \mathbf{u}_\Gamma^{n+1}$ is derived analytically to assess the rate of convergence. For this purpose, first the direct forcing scheme (C.1)-(C.4) is reformulated as a more general iterative forcing procedure

$$\mathbf{u}^{k,n+1} = \mathbf{u}^{k,n} + \int_{t^n}^{t^{n+1}} \mathbf{rhs}(\mathbf{u}^k,t)\,\mathrm{d}t + \overline{\mathbf{f}}_\Gamma^k\,\Delta t \tag{C.5a}$$

$$\overline{\mathbf{f}}_\Gamma^{k+1} = \overline{\mathbf{f}}_\Gamma^{k} + \frac{\mathbf{u}_\Gamma^{n+1} - \mathbf{u}^{k,n+1}}{\Delta t}\,, \tag{C.5b}$$

where $\mathbf{u}^k$ represents the velocity field of the kth iteration step with $k = 0, \ldots, N_{\text{iter}}$ and $N_{\text{iter}} \geq 1$ the number of iteration steps employed to impose the velocity constraint (C.1).

Note, that $\overline{\mathbf{f}}_\Gamma^k$ with $\overline{\mathbf{f}}_\Gamma^0 = \mathbf{0}$ only affects the velocity at time level t^{n+1}, so that the velocity at time t^n does not change during the iteration, i.e. $\mathbf{u}^{k,n} = \mathbf{u}^n$. Especially for $N_{\text{iter}} = 1$ the procedure consists of two subsequent steps, which is equivalent to the common non-iterative direct forcing scheme (C.1)-(C.4) above. The predictor velocity $\tilde{\mathbf{u}}$ concerning Eq. (C.4) is computed at $k = 0$, so that $\tilde{\mathbf{u}} = \mathbf{u}^{0,n+1}$ in the iterative procedure.
Here, the rate of convergence p is derived more generally for the kth iteration step, where it is obtained that $p = k$ and, thus, the numerical error decreases with increasing number of iterations N_{iter}, i.e. $\boldsymbol{\epsilon} \propto \Delta t^{N_{\text{iter}}}$. The numerical error between the desired boundary velocity $\mathbf{u}_\Gamma^{n+1}$ and the velocity $\mathbf{u}^{k,n+1}$ after k iterations is defined by

$$\boldsymbol{\epsilon}^k = \mathbf{u}^{k,n+1} - \mathbf{u}_\Gamma^{n+1} = -\Delta t \left(\overline{\mathbf{f}}_\Gamma^{k+1} - \overline{\mathbf{f}}_\Gamma^k \right) , \tag{C.6}$$

where the right expression directly results from definition (C.5b). In order to demonstrate that $\boldsymbol{\epsilon} \propto \Delta t^{N_{\text{iter}}}$, the velocity $\mathbf{u}^{k,n+1}$ in (C.6) is represented by its Taylor series expansion, i.e.

$$\mathbf{u}^{k,n+1} = \mathbf{u}^{k,n} + \Delta t \left.\frac{\partial \mathbf{u}^k}{\partial t}\right|_{t^n} + \frac{\Delta t^2}{2} \left.\frac{\partial^2 \mathbf{u}^k}{\partial t^2}\right|_{t^n} + \mathcal{O}\left(\Delta t^3\right) \tag{C.7a}$$

$$= \mathbf{u}^{k,n} + \Delta t \left(\mathbf{rhs}(\mathbf{u}^{k,n}, t^n) + \overline{\mathbf{f}}_\Gamma^k \right) + \frac{\Delta t^2}{2} \left.\frac{\partial^2 \mathbf{u}^k}{\partial t^2}\right|_{t^n} + \mathcal{O}\left(\Delta t^3\right) , \tag{C.7b}$$

where $\mathcal{O}\left(\Delta t^3\right)$ is the truncation error which increases proportionally with Δt^3. In (C.7b) the first derivative $\partial \mathbf{u}^k / \partial t$ is replaced by the right-hand side of the differential equation (C.2). Therefore, $\partial \mathbf{u}^k / \partial t$ includes the temporally constant force $\overline{\mathbf{f}}_\Gamma^k$ of the kth iteration step which has to be evaluated further. According to Eq. (C.5b) the force is given by

$$\overline{\mathbf{f}}_\Gamma^k \Delta t = \overline{\mathbf{f}}_\Gamma^{k-1} \Delta t + \mathbf{u}_\Gamma^{n+1} - \mathbf{u}^{k-1,n+1} \tag{C.8a}$$

$$= \overline{\mathbf{f}}_\Gamma^{k-1} \Delta t + \mathbf{u}_\Gamma^{n+1} - \mathbf{u}^{k-1,n} - \Delta t \left(\mathbf{rhs}(\mathbf{u}^{k-1,n}, t^n) + \overline{\mathbf{f}}_\Gamma^{k-1} \right) + \ldots$$
$$\ldots - \frac{\Delta t^2}{2} \left.\frac{\partial^2 \mathbf{u}^{k-1}}{\partial t^2}\right|_{t^n} + \mathcal{O}\left(\Delta t^3\right) \tag{C.8b}$$

$$= \mathbf{u}_\Gamma^{n+1} - \mathbf{u}^{k-1,n} - \Delta t\, \mathbf{rhs}(\mathbf{u}^{k-1,n}, t^n) - \frac{\Delta t^2}{2} \left.\frac{\partial^2 \mathbf{u}^{k-1}}{\partial t^2}\right|_{t^n} + \mathcal{O}\left(\Delta t^3\right) , \tag{C.8c}$$

where $\mathbf{u}^{k-1,n+1}$ is replaced by the Taylor series expansion (C.7a) with $k-1$. After inserting $\overline{\mathbf{f}}_\Gamma^k$ into Eq. (C.7b) it turns into

$$\mathbf{u}^{k,n+1} = \mathbf{u}_\Gamma^{n+1} + \mathbf{u}^{k,n} - \mathbf{u}^{k-1,n} + \Delta t \left(\mathbf{rhs}(\mathbf{u}^{k,n}, t^n) - \mathbf{rhs}(\mathbf{u}^{k-1,n}, t^n) \right) + \ldots$$
$$\ldots + \frac{\Delta t^2}{2} \left(\left.\frac{\partial^2 \mathbf{u}^k}{\partial t^2}\right|_{t^n} - \left.\frac{\partial^2 \mathbf{u}^{k-1}}{\partial t^2}\right|_{t^n} \right) + \mathcal{O}\left(\Delta t^3\right) . \tag{C.9}$$

As already mentioned above, the velocities at time t^n are unchanged during the iteration, i.e. $\mathbf{u}^{k,n} = \mathbf{u}^{k-1,n} = \mathbf{u}^n$, so that the second and third term of Eq. (C.9) vanish, i.e.

$$\mathbf{u}^{k,n+1} = \mathbf{u}_\Gamma^{n+1} + \frac{\Delta t^2}{2}\left(\left.\frac{\partial^2 \mathbf{u}^k}{\partial t^2}\right|_{t^n} - \left.\frac{\partial^2 \mathbf{u}^{k-1}}{\partial t^2}\right|_{t^n} \right) + \mathcal{O}\left(\Delta t^3\right) . \tag{C.10}$$

The derivation of the rate of convergence is not finished so far since the velocities $\mathbf{u}^k$ and $\mathbf{u}^{k-1}$ are influenced by $\overline{\mathbf{f}}_\Gamma^k$ and $\overline{\mathbf{f}}_\Gamma^{k-1}$, respectively, which are of order $\mathcal{O}\left(\Delta t^{-1}\right)$ concerning Eq. (C.5b). For that reason, the second term must be evaluated further. In general, the derivative of the kth iteration can be reformulated to

$$\frac{\partial^2 \mathbf{u}^k}{\partial t^2} = \frac{\partial}{\partial t}\left(\frac{\partial \mathbf{u}^k}{\partial t}\right) = \frac{\partial}{\partial t}\left(\mathbf{rhs}(\mathbf{u}^k, t) + \overline{\mathbf{f}}_\Gamma^k\right) = \frac{\partial\, \mathbf{rhs}(\mathbf{u}^k, t)}{\partial t} \tag{C.11a}$$

$$= \frac{\partial\, \mathbf{rhs}}{\partial t} + \frac{\partial\, \mathbf{rhs}}{\partial \mathbf{u}^k} \cdot \frac{\partial\, \mathbf{u}^k}{\partial t} = \frac{\partial\, \mathbf{rhs}}{\partial t} + \frac{\partial\, \mathbf{rhs}}{\partial \mathbf{u}^k} \cdot \left(\mathbf{rhs}(\mathbf{u}^k, t) + \overline{\mathbf{f}}_\Gamma^k\right) , \tag{C.11b}$$

so that the difference of second derivatives in Eq. (C.10) can be expressed as

$$\left.\frac{\partial^2 \mathbf{u}^k}{\partial t^2}\right|_{t^n} - \left.\frac{\partial^2 \mathbf{u}^{k-1}}{\partial t^2}\right|_{t^n} = \left.\frac{\partial\, \mathbf{rhs}}{\partial \mathbf{u}}\right|_{t^n} \cdot \left(\overline{\mathbf{f}}_\Gamma^k - \overline{\mathbf{f}}_\Gamma^{k-1}\right) , \tag{C.12}$$

and Eq. (C.10) turns into

$$\frac{\mathbf{u}_\Gamma^{n+1} - \mathbf{u}^{k,n+1}}{\Delta t} = -\frac{\Delta t}{2} \left.\frac{\partial\, \mathbf{rhs}}{\partial \mathbf{u}}\right|_{t^n} \cdot \left(\overline{\mathbf{f}}_\Gamma^k - \overline{\mathbf{f}}_\Gamma^{k-1}\right) + \mathcal{O}\left(\Delta t^2\right) . \tag{C.13}$$

Since the left-hand side coincides with definition (C.5b) of the direct forcing, Eq. (C.13) gives a very useful recursion formula for the force increment between two iterations

$$\left(\overline{\mathbf{f}}_\Gamma^{k+1} - \overline{\mathbf{f}}_\Gamma^k\right) = -\frac{\Delta t}{2} \left.\frac{\partial\, \mathbf{rhs}}{\partial \mathbf{u}}\right|_{t^n} \cdot \left(\overline{\mathbf{f}}_\Gamma^k - \overline{\mathbf{f}}_\Gamma^{k-1}\right) + \mathcal{O}\left(\Delta t^2\right) . \tag{C.14}$$

By applying Faà di Bruno's formula [204] on the higher derivatives it can be shown that the recursion also holds for the truncation term $\mathcal{O}\left(\Delta t^2\right)$, i.e.

$$\left(\overline{\mathbf{f}}_\Gamma^{k+1} - \overline{\mathbf{f}}_\Gamma^k\right) = \left\{ \mathcal{O}\left(\Delta t^2\right) - \frac{\Delta t}{2} \left.\frac{\partial\, \mathbf{rhs}}{\partial \mathbf{u}}\right|_{t^n} \right\} \cdot \left(\overline{\mathbf{f}}_\Gamma^k - \overline{\mathbf{f}}_\Gamma^{k-1}\right) . \tag{C.15}$$

Using definition (C.6), this recursion can be transferred to the numerical error of the kth iteration step, such that

$$\boldsymbol{\epsilon}^k = \left\{ \mathcal{O}\left(\Delta t^2\right) - \frac{\Delta t}{2} \left.\frac{\partial\, \mathbf{rhs}}{\partial \mathbf{u}}\right|_{t^n} \right\} \cdot \boldsymbol{\epsilon}^{k-1} . \tag{C.16}$$

Performing this recursion by a successive replacement of $\boldsymbol{\epsilon}^{k-1}$ until $\boldsymbol{\epsilon}^0$ is reached the error of the kth iteration is

$$\boldsymbol{\epsilon}^k = \left(-\frac{\Delta t}{2} \left.\frac{\partial\, \mathbf{rhs}}{\partial \mathbf{u}}\right|_{t^n} \right)^{(k)} \cdot \boldsymbol{\epsilon}^0 + \mathcal{O}\left(\Delta t^{(k+2)}\right) , \tag{C.17}$$

where (k) designates the kth power of the corresponding term on the right-hand side. According to Eq. (C.6), the remaining error is $\boldsymbol{\epsilon}^0 = -\Delta t \left(\overline{\mathbf{f}}_\Gamma^1 - \overline{\mathbf{f}}_\Gamma^0\right)$, where the force $\overline{\mathbf{f}}_\Gamma^0 = \mathbf{0}$ vanishes and $\overline{\mathbf{f}}_\Gamma^1$ can be expressed via Eq. (C.8c). Finally, the numerical error of the iterative direct forcing scheme with N_{iter} iteration steps is given by

$$\boldsymbol{\epsilon} = \left(-\frac{\Delta t}{2}\left.\frac{\partial \mathbf{rhs}}{\partial \mathbf{u}}\right|_{t^n}\right)^{N_{\text{iter}}} \cdot \left(\mathbf{u}^n - \mathbf{u}_\Gamma^{n+1}\right) + \mathcal{O}\left(\Delta t^{N_{\text{iter}}+1}\right) , \tag{C.18}$$

where for $\Delta t \to 0$ the first term dominates the error with $\boldsymbol{\epsilon} \propto \Delta t^{N_{\text{iter}}}$ and, correspondingly, the rate of convergence is $p = N_{\text{iter}}$. As a result, the non-iterative direct forcing with $N_{\text{iter}} = 1$ is a first order approximation of the constraint (C.1).
In the present work, this non-iterative version is preferred to keep the computational effort as small as possible. Of course, to achieve a second order direct forcing the solver must be executed twice within one time step, which doubles the overall computational time. Nevertheless, even for a first order approximation the resulting errors remain small for time step sizes Δt applied here (see Section 4.5).

D FSI algorithm in condensed form

This section provides an overview of the proposed semi-implicit direct forcing IBM for the coupling of an arbitrary number of Cosserat rods to the Navier-Stokes equations. All relevant equations are given for an individual Runge-Kutta sub-step r within the time interval $t \in [t^{r-1}, t^r]$. With the three-step Runge-Kutta scheme employed here, each time step Δt consists of three sub-steps, so that quantities at the new time level t^{n+1} are provided after the third sub-step. Quantities of the previous time level t^n are denoted by superscript 0, e.g. the velocity field $\mathbf{u}^0(\mathbf{x}_{ijk})$. The rth Runge-Kutta sub-step can be summarized as follows:

$$\frac{\tilde{\mathbf{u}} - \mathbf{u}^{r-1}}{\Delta t} = 2\alpha_r\, \nu_\mathrm{f}\, \nabla^2 \mathbf{u}^{\,r-1} - 2\alpha_r\, \nabla\big(p^{\,r-1}/\rho_\mathrm{f}\big) - \gamma_r\, \nabla\cdot(\mathbf{u}\otimes\mathbf{u})^{\,r-1} - \zeta_r\, \nabla\cdot(\mathbf{u}\otimes\mathbf{u})^{\,r-2} + \mathbf{f}_V \tag{D.1a}$$

$$\boldsymbol{\xi}_l^{r-1} = \mathbf{q}_e^{r-1} * \boldsymbol{\xi}_{0,l} * \overline{\mathbf{q}}_e^{r-1} \qquad \text{and} \qquad \mathbf{x}_l^{r-1} = \mathbf{c}_e^{r-1} + \boldsymbol{\xi}_l^{r-1} \tag{D.1b}$$

$$\tilde{\mathbf{u}}(\mathbf{x}_l^{r-1}) = \sum_{i=1}^{N_x}\sum_{j=1}^{N_y}\sum_{k=1}^{N_z} \tilde{\mathbf{u}}(\mathbf{x}_{ijk})\, \delta_h(\mathbf{x}_{ijk} - \mathbf{x}_l^{r-1})\, h^3 \tag{D.1c}$$

$$\ddot{\mathbf{c}}_{e+\frac{1}{2}} = \frac{1}{\rho_\mathrm{s} A}\left\{ \left(\mathbf{q} * \overset{\triangle}{\mathbf{f}}_0 * \overline{\mathbf{q}}\right)' + \overset{\triangledown}{\mathbf{f}}_\Gamma \right\}_{e+\frac{1}{2}} + \left(1 - \rho_\mathrm{f}/\rho_\mathrm{s}\right)\mathbf{g} \tag{D.1d}$$

$$\ddot{\mathbf{q}}_e = \frac{1}{2\rho_\mathrm{s}}\, \boldsymbol{\mathcal{M}}_e \cdot \Big\{ 4\rho_\mathrm{s}\, \dot{\mathbf{q}} * \boldsymbol{\mathcal{I}}_0 \cdot \big(\dot{\overline{\mathbf{q}}} * \mathbf{q}\big) + \mathbf{c}' * \mathbf{q} * \overset{\triangle}{\mathbf{f}}_0 + \big(\mathbf{q} * \overset{\triangle}{\mathbf{m}}_0\big)' + \mathbf{q}' * \overset{\triangle}{\mathbf{m}}_0 + \overset{\triangledown}{\mathbf{m}}_\Gamma * \mathbf{q} \Big\}_e - \|\dot{\mathbf{q}}_e\|^2 \mathbf{q}_e \tag{D.1e}$$

$$\mathbf{q}_e^r \leftarrow \mathbf{q}_e^r / \|\mathbf{q}_e^r\| \qquad \text{and} \qquad \dot{\mathbf{q}}_e^r \leftarrow \dot{\mathbf{q}}_e^r - (\mathbf{q}_e^r \cdot \dot{\mathbf{q}}_e^r)\, \mathbf{q}_e^r \tag{D.1f}$$

$$\mathbf{u}_\Gamma^r(\mathbf{x}_l^{r-1}) = \dot{\mathbf{c}}_e^r + (2\, \dot{\mathbf{q}}_e^r * \overline{\mathbf{q}}_e^r) \times \boldsymbol{\xi}_l^{r-1} \tag{D.1g}$$

$$\overline{\mathbf{f}}_\Gamma(\mathbf{x}_l^{r-1}) = \frac{\mathbf{u}_\Gamma^r(\mathbf{x}_l^{r-1}) - \tilde{\mathbf{u}}(\mathbf{x}_l^{r-1})}{2\alpha_r\, \Delta t} \tag{D.1h}$$

$$\overline{\mathbf{f}}_\Gamma(\mathbf{x}_{ijk}) = \sum_{\mathbf{x}_l \in \Gamma_e} \overline{\mathbf{f}}_\Gamma(\mathbf{x}_l^{r-1})\, \delta_h(\mathbf{x}_{ijk} - \mathbf{x}_l^{r-1})\, \Delta V_l \tag{D.1i}$$

$$\nabla^2 \mathbf{u}^* - \frac{\mathbf{u}^*}{\alpha_r \nu_\mathrm{f}\, \Delta t} = \nabla^2 \mathbf{u}^{r-1} - \frac{\tilde{\mathbf{u}} + 2\alpha_r\, \Delta t\, \overline{\mathbf{f}}_\Gamma}{\alpha_r \nu_\mathrm{f}\, \Delta t} \tag{D.1j}$$

$$\nabla^2 \phi^r = \nabla \cdot \mathbf{u}^* \tag{D.1k}$$

$$\mathbf{u}^r = \mathbf{u}^* - \nabla \phi^r \tag{D.1l}$$

$$\frac{p^{\,r}}{\rho_\mathrm{f}} = \frac{p^{\,r-1}}{\rho_\mathrm{f}} + \frac{\phi^r}{2\,\alpha_r\, \Delta t} - \frac{\nu_\mathrm{f}}{2}\, \nabla^2 \phi^r \tag{D.1m}$$

Further information are required for shorthanded terms contained in the Cosserat rod equations of motion (D.1d)-(D.1e) to provide the entire algorithm. Remaining definitions can be summarized as follows:

$$\left(\mathbf{q}{*}\overset{\wedge}{\mathbf{f}}_0{*}\overline{\mathbf{q}}\right)'_{e+\frac{1}{2}} = \left(\mathbf{q}_{e+1}{*}\overset{\wedge}{\mathbf{f}}_{0,e+1}{*}\overline{\mathbf{q}}_{e+1} - \mathbf{q}_e{*}\overset{\wedge}{\mathbf{f}}_{0,e}{*}\overline{\mathbf{q}}_e\right) / \Delta Z \tag{D.2a}$$

$$\overset{\vee}{\mathbf{f}}_{\Gamma,e+\frac{1}{2}} = (\overset{\vee}{\mathbf{f}}_{\Gamma,e} + \overset{\vee}{\mathbf{f}}_{\Gamma,e+1})/2 \tag{D.2b}$$

$$\dot{\mathbf{c}}_e = (\dot{\mathbf{c}}_{e+\frac{1}{2}} + \dot{\mathbf{c}}_{e-\frac{1}{2}})/2 \tag{D.2c}$$

$$\boldsymbol{\mathcal{M}}_e = \boldsymbol{\mathcal{Q}}(\mathbf{q}_e)\cdot\boldsymbol{\mathcal{I}}_0^{-1}\cdot\boldsymbol{\mathcal{Q}}^\top(\mathbf{q}_e) \qquad \text{with} \qquad \boldsymbol{\mathcal{Q}}(\mathbf{q}) = \begin{pmatrix} q_r & -\hat{q}^\top \\ \hat{q} & q_r\,\mathbb{I} + [\hat{q}]_\times \end{pmatrix} \tag{D.2d}$$

$$\mathbf{c}'_e = \left(\mathbf{c}_{e+\frac{1}{2}} - \mathbf{c}_{e-\frac{1}{2}}\right) / \Delta Z \tag{D.2e}$$

$$\left(\mathbf{q}{*}\overset{\wedge}{\mathbf{m}}_0\right)'_e + \mathbf{q}'_e{*}\overset{\wedge}{\mathbf{m}}_{0,e} = \left(\mathbf{q}_{e+1}{*}\overset{\wedge}{\mathbf{m}}_{0,e+\frac{1}{2}} - \mathbf{q}_{e-1}{*}\overset{\wedge}{\mathbf{m}}_{0,e-\frac{1}{2}}\right) / \Delta Z \tag{D.2f}$$

$$\overset{\wedge}{\mathbf{f}}_{0,e} = [\mathbf{C}_\gamma\cdot(\boldsymbol{\gamma}_0 - \boldsymbol{\gamma}_0|_{t=0}) + 2\,\mathbf{C}_{\dot\gamma}\cdot\dot{\boldsymbol{\gamma}}_0]_e \qquad \text{with} \quad \boldsymbol{\gamma}_{0,e} = \overline{\mathbf{q}}_e{*}\mathbf{c}'_e{*}\mathbf{q}_e \tag{D.2g}$$

$$\overset{\wedge}{\mathbf{m}}_{e+\frac{1}{2}} = \Big[\mathbf{C}_\kappa\cdot(\boldsymbol{\kappa}_0 - \boldsymbol{\kappa}_0|_{t=0}) + 2\,\mathbf{C}_{\dot\kappa}\cdot\dot{\boldsymbol{\kappa}}_0\Big]_{e+\frac{1}{2}} \quad \text{with} \quad \boldsymbol{\kappa}_{0,e+\frac{1}{2}} = \frac{2\sqrt{2}}{\Delta Z}\,\frac{\Im\left(\overline{\mathbf{q}}_e{*}\mathbf{q}_{e+1}\right)}{\sqrt{1+\Re\left(\overline{\mathbf{q}}_e{*}\mathbf{q}_{e+1}\right)}} \quad \text{(see [131])} \tag{D.2h}$$

$$\overset{\vee}{\mathbf{f}}_{\Gamma,e}\,\Delta Z = -\left[\frac{\mathbf{p}_\Gamma - \mathbf{p}_\Gamma^{r-1}}{t - t^{r-1}} + \frac{\mathbf{p}_\Gamma^{r-1} - \tilde{\mathbf{p}}}{2\alpha_r\,\Delta t}\right]_e \quad \text{with} \quad \begin{aligned} \mathbf{p}_{\Gamma,e} &= [m\,\dot{\mathbf{c}} + 2\dot{\mathbf{q}}{*}\overline{\mathbf{q}} \times \mathbf{q}{*}\mathbf{s}_0{*}\overline{\mathbf{q}}]_e \\ \tilde{\mathbf{p}}_e &= \sum_{\mathbf{x}_l\,\in\,\Gamma_e} \Delta m_l\,\tilde{\mathbf{u}}(\mathbf{x}_l^{r-1}) \end{aligned} \tag{D.2i}$$

$$\overset{\vee}{\mathbf{m}}_{\Gamma,e}\,\Delta Z = -\left[\frac{\mathbf{l}_\Gamma - \mathbf{l}_\Gamma^{r-1}}{t - t^{r-1}} + \frac{\mathbf{l}_\Gamma^{r-1} - \tilde{\mathbf{l}}}{2\alpha_r\,\Delta t}\right]_e \quad \text{with} \quad \begin{aligned} \mathbf{l}_{\Gamma,e} &= [\mathbf{q}{*}\mathbf{s}_0{*}\overline{\mathbf{q}} \times \dot{\mathbf{c}} + \mathbf{q}{*}\boldsymbol{\mathcal{J}}_0\cdot(2\overline{\mathbf{q}}{*}\dot{\mathbf{q}}){*}\overline{\mathbf{q}}]_e \\ \tilde{\mathbf{l}}_e &= \sum_{\mathbf{x}_l\,\in\,\Gamma_e} \Delta m_l\,\boldsymbol{\xi}_l^{r-1} \times \tilde{\mathbf{u}}(\mathbf{x}_l^{r-1}) \end{aligned} \tag{D.2j}$$

$$m_e = \sum_{\mathbf{x}_l\,\in\,\Gamma_e} \Delta m_l\,, \qquad \mathbf{s}_{0,e} = \sum_{\mathbf{x}_l\,\in\,\Gamma_e} \Delta m_l\,\boldsymbol{\xi}_{0,l}\,, \qquad \boldsymbol{\mathcal{J}}_{0,e} = 0 \oplus \sum_{\mathbf{x}_l\,\in\,\Gamma_e} \Delta m_l\,[\boldsymbol{\xi}_{0,l}]_\times^\top\cdot[\boldsymbol{\xi}_{0,l}]_\times \tag{D.2k}$$

Nomenclature

Abbreviations

ALE	arbitrary Lagrangian-Eulerian *method*
COP	cut orthogonal projection
CPU	central processing unit
DNS	direct numerical simulation
DOPRI5	explicit Runge-Kutta method of order 5 *(ODE-solver)* [93, 91]
FDM	finite difference method
FEM	finite element method
FFT	fast Fourier transform
FSI	fluid-structure interaction
GPU	graphics processing unit
HD	head-down *hairpin vortex*
HP	hairpin *vortex*
HS	high-speed *velocity streak*
HU	head-up *hairpin vortex*
Hypre	High Performance Preconditioners [132, 65]
IBM	immersed boundary method
KH	Kelvin-Helmholtz
LCP	linear complementary problem
LES	large eddy simulation
LS	low-speed *velocity streak*
MPI	Message Passing Interface *standard* [74, 166]
NSE	Navier-Stokes equations
ODE	ordinary differential equation
OHP	overhead projector
OpenMP	Open Multi-Processing *standard* [50, 181]
PET	polyethylene terephthalate
PETSc	Portable Extensible Toolkit for Scientific computations [13, 12, 14]
PGSM	projected Gauß-Seidel method
PRIME	phase-resolving simulation environment
PVC	polyvinyl chloride
RADAU5	implicit Runge-Kutta method of order 5 *(ODE-solver)* [92, 91]
RANS	Reynolds-averaged Navier-Stokes *equations*
SLERP	spherical linear interpolation

Roman symbols

A	cross sectional area	m^2
$\mathcal{A}$	averaging condition	–
A_c	contact area	m^2
a	frontal area of canopy volume	$1/\mathrm{m}$
a_{ij}	coefficient of the Runge-Kutta scheme used by RADAU5	1
$\mathcal{B}$	bounding operation	–
b_j	coefficient of the Runge-Kutta scheme used by RADAU5	1
$\mathbf{C},\ \mathbf{C}_\mathrm{lub}$	matrix connecting linear and angular momentum	1, m
$\mathcal{C}$	set of space-time coordinates $(\mathbf{x}_\mathrm{c}, t_\mathrm{c})$ fulfilling a condition	–
C^0	continuity of class C^0	–
Ca	Cauchy number	1
C_d	drag coefficient	1
CFL	Courant-Friedrichs-Lewy number (Courant number)	1
C_s	Smagorinsky constant	1
$\mathbf{C}_\varepsilon$	constitutive matrix w.r.t. strain vector $\boldsymbol{\varepsilon}$	N
$\mathbf{C}_{\dot{\varepsilon}}$	constitutive matrix w.r.t. strain rate vector $\dot{\boldsymbol{\varepsilon}}$	N s
$\mathbf{C}_\kappa$	constitutive matrix w.r.t. curvature vector $\boldsymbol{\kappa}$	Nm^2
$\mathbf{C}_{\dot{\kappa}}$	constitutive matrix w.r.t. curvature rate vector $\dot{\boldsymbol{\kappa}}$	$\mathrm{Nm}^2\,\mathrm{s}$
c	speed of sound	m/s
$\mathbf{c}$	position of center line ζ, $\mathbf{c} \in \Omega^\mathrm{s}$	m
c_b	structural viscosity w.r.t. bending	$\mathrm{Nm}^2\,\mathrm{s}$
c_e	structural viscosity w.r.t. axial extension/compression	N s
c_j	coefficient of the Runge-Kutta scheme used by RADAU5	1
c_s	structural viscosity w.r.t. shear	N s
c_t	structural viscosity w.r.t. torsion	$\mathrm{Nm}^2\,\mathrm{s}$
D	damping function, Van Driest damping function $D(y^+)$	1
D	diameter	m
$D_\mathrm{n},\ D_\mathrm{t}$	damping parameter in normal and tangential direction	kg/s
$\mathbf{d},\ d$	distance, displacement $\mathbf{d} = (d_x, d_y, d_z)^\top,\ d = \|\mathbf{d}\|$	m
$\mathrm{d}C$	infinitesimal line (contour) element	m
d_crit	critical distance	m
$\det(\mathbf{M})$	determinant of a square matrix $\mathbf{M} \in \mathbb{R}^{n\times n}$	–
$\mathrm{diag}(a,b,c)$	diagonal matrix with $d_{ij}=0$ for $i \neq j$ and $d_{11}=a$, $d_{22}=b$, $d_{33}=c$	–
$\mathrm{d}S$	infinitesimal surface element	m^2
d_sp	distance between two spheres	m
$\mathrm{d}V$	infinitesimal volume element	m^3
d_Λ	thickness of the fluid layer around Γ	m
d_Φ	width of the regularized delta function Φ	m
E	set of all structural rod elements	–
$\mathbf{E}$	Green-Lagrange strain tensor	$\mathrm{N/m}^2$
E_s	Young's modulus	$\mathrm{N/m}^2$

e	coefficient of restitution	1
$e,\ \tilde{e}$	index/label of a structural rod element	1
$\mathbf{e}_x$	unit vector in x-direction	1
F	applied external force	N
$\mathbf{F}$	deformation gradient tensor	1
F_d	drag force	N
F_l	lift force	N
f	frequency	Hz
$\mathbf{f},\ f$	force $\mathbf{f} = (f_x, f_y, f_z)^\top,\ f = \|\mathbf{f}\|$	N, $(\mathrm{m/s^2})$
$\overset{\triangledown}{\mathbf{f}}$	external (length-specific) force acting to the rod	N/m
$\overset{\triangle}{\mathbf{f}}$	internal force of the rod	N
$f_1,\ f_2,\ f_3$	dominant frequency peak f_1 and two subsequent harmonics f_2, f_3	Hz
f_c	contact force	N
$\overset{\triangledown}{\mathbf{f}}_\mathrm{c}$	collision force acting on the rod	N/m
$\mathbf{f}_\mathrm{dh},\ f_\mathrm{dh}$	downhill force, $f_\mathrm{dh} = \|\mathbf{f}_\mathrm{dh}\|$	N
f_ft	flow-through frequency	Hz
$\overset{\triangledown}{\mathbf{f}}_\mathrm{g}$	gravitational force acting to the rod	N/m
$\mathbf{f}_\mathrm{lub},\ f_\mathrm{lub}$	lubrication force, $f_\mathrm{lub} = \|\mathbf{f}_\mathrm{lub}\|$	N
f_n	natural frequency of the first bending mode	Hz
$\mathbf{f}_S$	surface-specific force, stress vector	$\mathrm{N/m^2}$
$\mathbf{f}_V$	mass-specific, volume force	$\mathrm{m/s^2}$
$\mathbf{f}_\Gamma$	coupling force (mass-specific, volumetric)	$\mathrm{m/s^2}$
$\overline{\mathbf{f}}_\Gamma$	average coupling force	$\mathrm{m/s^2}$
$\overset{\triangledown}{\mathbf{f}}_\Gamma$	coupling force (fluid force) acting to the rod	N/m
$\mathbf{g},\ g$	gravitational acceleration, $g = \|\mathbf{g}\|$	$\mathrm{m/s^2}$
G_s	shear modulus	$\mathrm{N/m^2}$
H	channel height	m
$\mathbb{H}$	multiplicative quaternion group	–
$H_\epsilon(x)$	unit step function with the smoothing parameter $0 < \epsilon \ll 1$ and $x \in \mathbb{R}$	1
h	grid step size, filter size (LES), $h = \sqrt[3]{\Delta x\, \Delta y\, \Delta z}$	m
h	thickness of the fluid film between two rods	m
$\overline{h}$	mean thickness of the fluid film between two rods	m
I	2nd moment of area	$\mathrm{m^4}$
$\mathbf{I}$	tensor of inertia	$\mathrm{kg\,m^2}$
$\mathbf{I}$	tensor of inertia of the cross sections (2nd moments of area)	$\mathrm{m^4}$
$\mathbb{I}$	identity matrix, $\mathbb{I} = \mathrm{diag}(1, 1, 1)$	1
$\boldsymbol{\mathcal{I}}_0$	quaternion matrix of inertia	$\mathrm{m^4}$
$\Im(\mathbf{q})$	imaginary part of a quaternion $\mathbf{q} \in \mathbb{H}$ with $\Im(\mathbf{q}) = \hat{q}$	–
$I_X,\ I_Y,\ I_Z$	2nd moment of area of the cross section Υ around $\mathbf{r}_X$, $\mathbf{r}_Y$, $\mathbf{r}_Z$	$\mathrm{m^4}$
i	spatial index, indexing in x-direction	1
$\mathbf{i}$	impulse wrench	N s, Nm s
$\hat{\mathbf{i}}$	virtual impulse wrench	N s, Nm s
$\mathbf{i}_\mathrm{v}$	impulse wrench to impose the velocity constraint	N s, Nm s

$\mathbf{i}_\mathrm{w}$	impulse wrench caused by the external loads	N s, Nm s
J	2nd polar moment of area (polar moment of inertia), $J = I_Z$	m^4
$\mathbf{J}$	Jacobian matrix	–
$\boldsymbol{\mathcal{J}}_0$	quaternionic tensor of inertia of the fluid layer	$\mathrm{kg\,m}^2$
j	spatial index, indexing in y-direction	1
$\mathbf{K}$	system matrix	–
$K(m)$	complete elliptical integral of the first kind, $m \in \mathbb{R}$	1
k	spatial index, indexing in z-direction	1
k_s	shear correction factor	1
k_t	torsion correction factor	1
L	length in general	m
L	rod length	m
L_x, L_y, L_z	expansion of rectangular domain in x-, y-, z-direction	m
L^*	reconfiguration height of the rod	m
$\widehat{L}^*$	complex Fourier spectrum of the reconfiguration height	m
$\langle L^* \rangle$	space-time averaged reconfiguration height	m
l	index/label of a Lagrangian marker point	1
$\mathbf{l}$	angular momentum vector	Nm s
$\tilde{\mathbf{l}}$	preliminary angular momentum vector	Nm s
M	applied external moment	Nm
$\mathbf{M}$	inertia matrix	kg, $\mathrm{kg\,m}^2$
$\mathbf{M}$	matrix in general	–
$\boldsymbol{\mathcal{M}}$	"inverse" quaternion matrix of inertia	$1/\mathrm{m}^4$
$\overset{\triangledown}{\mathbf{m}}$	external (length-specific) moment acting on the rod	N
$\overset{\vartriangle}{\mathbf{m}}$	internal moment of the rod	Nm
m	mass in general	kg
m	mass of the fluid layer around Γ	kg
$\mathbf{m}$	moment vector	Nm
m_add	added mass of fluid	kg
$\overset{\triangledown}{\mathbf{m}}_\mathrm{c}$	collision moment acting on the rod	N
m_s	structural mass	kg
$\overset{\triangledown}{\mathbf{m}}_\Gamma$	coupling moment (fluid moment) acting on the rod	N
N	natural number, $N \in \mathbb{N}$	1
N	total number of grid cells	1
$\mathbb{N}$	set of natural numbers	–
N_e	number of structural elements per rod	1
N_iter	number of iterations	1
N_s	total number of rod structures	1
N_x, N_y, N_z	number of grid cells in x-, y-, z-direction	1
$\mathbf{n}$	unit normal vector	1
$\mathbf{n}_\mathrm{cs}$	unit normal vector of a cross-section	1
$\mathcal{O}(\Delta x^n)$	Landau notation, nth order accuracy w.r.t. Δx	–
o	set of excluded elements	–

$\mathbf{P}$	1st Piola-Kirchhoff stress tensor	$\mathrm{N/m^2}$
$\mathcal{P}$	projection	–
p	fluid pressure field	$\mathrm{N/m^2}$
$\mathbf{p},\ p$	linear momentum vector, $p = \|\mathbf{p}\|$	$\mathrm{N\,s}$
$\tilde{\mathbf{p}}$	preliminary linear momentum vector	$\mathrm{N\,s}$
p_n	normal part of the linear momentum	$\mathrm{N\,s}$
p_t	tangential part of the linear momentum	$\mathrm{N\,s}$
$\mathbf{p}_\mathrm{v},\ p_\mathrm{v}$	linear momentum to impose the velocity constraint, $p_\mathrm{v} = \|\mathbf{p}_\mathrm{v}\|$	$\mathrm{N\,s}$
$\mathbf{p}_\mathrm{w},\ p_\mathrm{w}$	linear momentum caused by external loads, $p_\mathrm{w} = \|\mathbf{p}_\mathrm{w}\|$	$\mathrm{N\,s}$
$\boldsymbol{\mathcal{Q}}$	matrix representation $\boldsymbol{\mathcal{Q}}(\mathbf{q})$ of a quaternion $\mathbf{q} \in \mathbb{H}$	1
q	rate of convergence	1
$\mathbf{q}$	quaternion, $\mathbf{q} \in \mathbb{H}$	1
R	radius	m
$\mathbf{R}$	rotation matrix, $\mathbf{R} = [\mathbf{r}_X\, \mathbf{r}_Y\, \mathbf{r}_Z] \subset SO(3)$	1
$\mathbb{R}$	set of real numbers	–
Re_l	Reynolds number based on a reference length l, e.g. channel width H	1
Re_τ	Reynolds number based on the friction velocity u_τ	1
$\Re(\mathbf{q})$	real part of a quaternion $\Re(\mathbf{q}) = q_\mathrm{r}$ with $\mathbf{q} \in \mathbb{H}$	–
r	Runge-Kutta sub-step, $r = 1, 2, 3$	1
$\mathbf{r},\ r$	distance vector $\mathbf{r} = (r_x, r_y, r_z)^\top,\ r = \|\mathbf{r}\|$	m
$\mathbf{rhs}$	right-hand side	–
$\mathbf{rhs}_\Gamma$	right-hand side describing the unconstrained motion of Γ	m/s
$\mathbf{r}_X, \mathbf{r}_Y, \mathbf{r}_Z$	unit direction vector in X-, Y-, Z-direction	1
S	set of rod structures	–
$\mathbf{S}$	2nd Piola-Kirchhoff stress tensor	$\mathrm{N/m^2}$
$\mathbf{S}$	strain rate tensor and its norm $\|\mathbf{S}\|$	1/s
$\mathbb{S}^3$	set of unit quaternions $\mathbb{S}^3 \subset \mathbb{H}$	–
$SO(3)$	rotation group	–
S_Γ	surface area of the fluid-structure interface Γ	$\mathrm{m^2}$
s	coordinate of a local coordinate frame	1
s	index/label of a rod structure	1
s	scalar value in general	1
$\mathbf{s}_0$	static moment of the fluid layer around Γ	$\mathrm{kg\,m}$
$\mathrm{sn}(u; m)$	Jacobi elliptic function with $u, m \in \mathbb{R}$	1
T	rod thickness	m
T	time period, period of oscillation	s
t	time	s
$\mathbf{t}$	unit tangent vector	1
$t^{n+1},\ t^n$	new and previous discrete time level	s
t^*	dimensionless time	1
U	bulk velocity, mean velocity	m/s
$U_\tau,\ u_\tau$	friction velocity	m/s
$\mathbf{u}$	fluid velocity field $\mathbf{u}(\mathbf{x}, t)$, velocity vector $\mathbf{u} = (u, v, w)^\top$	m/s

$\mathbf{u}$	velocity component in x-direction, streamwise velocity	m/s
$\tilde{\mathbf{u}}$	preliminary velocity field	m/s
$\mathbf{u}_{ijk}$	spatially discrete velocity field	m/s
$\mathbf{u}_\Gamma$	velocity of the fluid-structure interface Γ	m/s
u^*	dimensionless velocity profile	1
$\mathbf{u}^*$	non-divergence free velocity field	m/s
$\mathbf{u}'$	velocity fluctuation field $\mathbf{u}' = (u', v', w')^\top$	m/s
$\langle u \rangle$	mean velocity profile	m/s
$\langle \mathbf{u} \rangle$	average velocity field	m/s
$\langle u \rangle_{\log}$	logarithmic velocity profile	m/s
$\mathbf{v}$	velocity component in y-direction, vertical velocity	m/s
$\mathbf{v},\ v$	linear velocity, $v = \|\mathbf{v}\|$	m/s
$\mathbf{v}_\mathrm{c}$	velocity vector at the contact point	m/s
$\mathbf{v}_\mathrm{n},\ v_\mathrm{n}$	normal relative velocity, $v_\mathrm{n} = \|\mathbf{v}_\mathrm{n}\|$	m/s
$\mathbf{v}_\mathrm{r},\ v_\mathrm{r}$	relative velocity, $v_\mathrm{r} = \|\mathbf{v}_\mathrm{r}\|$	m/s
$\mathbf{v}_\mathrm{t},\ v_\mathrm{t}$	tangential relative velocity, $v_\mathrm{t} = \|\mathbf{v}_\mathrm{t}\|$	m/s
$\mathbf{v}_\mathrm{tip}$	velocity of the rod tip	m/s
W	rod width	m
w	velocity component in z-direction, spanwise velocity	m/s
$\mathbf{w}$	wrench (screw theory)	N, Nm
$\mathbf{w}_\mathrm{c}$	collision wrench	N, Nm
$\mathbf{w}_\mathrm{lub}$	lubrication wrench	N, Nm
$\mathbf{X}$	material point of the reference configuration, $\mathbf{X} = (X, Y, Z)^\top \in \Omega_0^\mathrm{s}$	m
x	x-coordinate of the global Eulerian frame	m
x	component of $\mathbf{x}$ in x-direction	m
$\mathbf{x}$	material point in the current configuration, $\mathbf{x} = (x, y, z)^\top \in \Omega^\mathrm{s}$	m
$\mathbf{x}$	position vector in the global Eulerian frame	m
$\mathbf{x}$	spatially discrete array of the rods/blades, $\mathbf{x}(s; Z, t) = (\mathsf{x}, \mathsf{y}, \mathsf{z})^\top$	m
$\mathbf{x}_{ijk}$	Eulerian grid point with index i, j, k	m
$\mathbf{x}_l$	lth Lagrangian marker point	m
$\mathbf{x}'$	fluctuation of $\mathbf{x}$	m
y	y-coordinate of the global Eulerian frame	m
y	component of $\mathbf{x}$ in y-direction	m
y_0	roughness height of the canopy	m
y_1^+	normalized wall distance of the first grid point	1
y_m	displacement height of the canopy	m
$\mathbf{y}_\mathrm{tip},\ y_\mathrm{tip}$	vertical tip position of the rod, $y_\mathrm{tip} = \|\mathbf{y}_\mathrm{tip}\|$	m
y^*	dimensionless coordinate	1
Z	arc length of the rod	m
z	z-coordinate of the global Eulerian frame	m
z	component of $\mathbf{x}$ in z-direction	m
$\mathbf{z}$	state vector	–
$\mathbf{z}$	twist (screw theory)	m/s, Hz

Greek symbols

α_r	coefficient of the Runge-Kutta scheme	1
$\beta(r)$	shape function with the aspect ratio $r = W/L$	1
β	stretching factor	1
Γ	fluid-structure interface $\Gamma = \partial\Omega^{\mathrm{f}} \cap \partial\Omega^{\mathrm{s}}$	–
γ	part of the fluid-structure interface $\gamma \subset \Gamma$ cutting ω	–
γ_r	coefficient of the Runge-Kutta scheme	1
$\Delta\mathbf{i}$	corrective impulse wrench	N s, Nm s
ΔL	maximum contraction/elongation of the rod	m
ΔL^*	vertical tip displacement	m
Δl	longitudinal compression of the rod	m
Δm_l	Lagrange mass associated to a marker point l	kg
ΔS	rod spacing	m
ΔS_l	surface area attributed to a marker point l	m^2
Δt	time delay	s
Δt	time step size $\Delta t = t^{n+1} - t^n$	s
Δt_{c}	time period of a collision	s
$\Delta\mathbf{v}$	change of the relative velocity due to a collision	m/s
ΔV_l	Lagrange volume associated to a marker point l	m^3
Δx	grid step size in x-direction	m
Δx_l	grid step size of the Lagrangian marker points	m
Δy	grid step size in y-direction	m
ΔZ	length of a rod element, $\Delta Z = \int_{\zeta_{\mathrm{e}}} \mathrm{d}Z$	m
Δz	grid step size in z-direction	m
δ	channel half-width	m
δ	penalty depth, penetration depth	m
δ_h	three-dimensional delta function	1
δ_h^{1D}	one-dimensional delta function	1
δ_h	regularized delta function	1
δ_V	delta function connecting surface- and volume-specific quantities	1/m
$\boldsymbol{\epsilon}$, ϵ	relative error, $\epsilon = \|\boldsymbol{\epsilon}\|$	1
$\boldsymbol{\varepsilon}$, ε	strain vector, $\varepsilon = \|\boldsymbol{\varepsilon}\|$	1
$\dot{\boldsymbol{\varepsilon}}$	strain rate vector	1/s
ζ	center line of the rod, $\zeta \subset \Omega^{\mathrm{s}}$	–
ζ_r	coefficient of the Runge-Kutta scheme	1
κ	von Kármán constant	1
$\boldsymbol{\kappa}$, κ	curvature vector, $\kappa = \|\boldsymbol{\kappa}\|$	1/m
$\dot{\boldsymbol{\kappa}}$	curvature rate vector	Hz/m
Λ	infinitesimal fluid layer $\Lambda \subset \Omega^{\mathrm{f}}$ around Γ	–
λ	part of the fluid layer $\lambda \subset \Lambda$ in the cut volume ω	–
λ_2	scalar field for Lambda2 vortex criterion	$1/\mathrm{s}^2$
λ_{s}	Lamé constant	$\mathrm{N/m}^2$

μ_f	dynamic viscosity of the fluid	$\mathrm{N\,s/m^2}$
μ_k	coefficient of kinetic friction	1
μ_s	coefficient of static friction	1
$\boldsymbol{\mu}_\mathrm{sgs}$	subgrid-scale eddy viscosity	$\mathrm{N\,s/m^2}$
ν_s	Poisson's ratio	1
ν_f	kinematic viscosity of the fluid	$\mathrm{m^2/s}$
$\boldsymbol{\xi}$	cross-section vector	m
ρ_f	fluid density	$\mathrm{kg/m^3}$
ρ_s	structural density of the reference configuration Ω_0^s	$\mathrm{kg/m^3}$
ρ_{uu}	autocorrelation of the velocity fluctuation u'	1
$\boldsymbol{\sigma}$	hydrodynamic stress tensor	$\mathrm{N/m^2}$
$\boldsymbol{\sigma}_\mathrm{LES}$	hydrodynamic stress tensor (large eddy simulation)	$\mathrm{N/m^2}$
$\boldsymbol{\sigma}_\mathrm{s}$	Cauchy stress tensor	$\mathrm{N/m^2}$
$\boldsymbol{\tau}_\mathrm{sgs}$	subgrid-scale stress tensor	$\mathrm{N/m^2}$
τ_w	wall shear stress	$\mathrm{N/m^2}$
Υ	cross-sections of the rod $\Upsilon(Z) \subset \Omega^\mathrm{s}$	–
$\Phi_3,\ \Phi_4$	three-point (four-point) regularized delta function	1
ϕ	angle, inclination	rad
ϕ	pressure correction field	$\mathrm{m^2/s}$
$\boldsymbol{\varphi},\ \varphi$	arbitrary vector (scalar) field	–
$\boldsymbol{\chi}$	mapping $\mathbf{x} = \boldsymbol{\chi}(\mathbf{X}, t)$ between $\mathbf{x} \in \Omega^\mathrm{s}$ and $\mathbf{X} \in \Omega_0^\mathrm{s}$	–
Ω	entire physical domain $\Omega = \Omega^\mathrm{f} \cup \Omega^\mathrm{s}$	–
Ω^f	fluid domain $\Omega^\mathrm{f} \subset \Omega$	–
Ω^s	current configuration of the structure, structure domain $\Omega^\mathrm{s} \subset \Omega$	–
Ω_0^s	reference configuration of the structure at time $t = 0$	–
$\boldsymbol{\omega},\ \omega$	angular velocity, $\omega = \|\boldsymbol{\omega}\|$	Hz
ω	small finite volume $\omega \subset \Omega$ cut by $\gamma \subset \Gamma$	–
ω^+	"upper" subdomain of the cut volume ω	–
ω^-	"lower" subdomain of the cut volume ω	–

Subscripts

$(\cdot)_0$	related to reference configuration Ω_0^s
$(\cdot)_0$	initial condition
$(\cdot)_\mathrm{b}$	related to bending
$(\cdot)_\mathrm{c}$	related to collision/contact
$(\cdot)_\mathrm{c}$	related to conditional average
$(\cdot)_\mathrm{corr}$	corrected quantity
$(\cdot)_\mathrm{crit}$	critical value
$(\cdot)_\mathrm{e}$	related to axial extension
$(\cdot)_e$	related to structural element e
$(\cdot)_e$	index of element e

$(\cdot)_{e\pm\frac{1}{2}}$	half-index of element e
$(\cdot)_{\mathrm{f}}$	fluid quantity
$(\cdot)_{\mathrm{ft}}$	flow trough
$(\cdot)_h$	depending on grid step size h
$(\cdot)_i$	spatial index, indexing in x-direction
$(\cdot)_{ijk}$	spatially discrete quantity with index i, j, k
$(\cdot)_j$	spatial index, indexing in y-direction
$(\cdot)_k$	spatial index, indexing in z-direction
$(\cdot)_l$	related to a Lagrangian marker point l
$(\cdot)_{\mathrm{lin}}$	linear, linearized quantity
$(\cdot)_{\mathrm{lub}}$	lubrication
$(\cdot)_{\max}$	maximum value
$(\cdot)_{\min}$	minimum value
$(\cdot)_{\mathrm{n}}$	in normal direction
$(\cdot)_{\mathrm{r}}$	real part of quaternion
$(\cdot)_{\mathrm{ref}}$	reference value
$(\cdot)_{\mathrm{s}}$	related to shear
$(\cdot)_{\mathrm{s}}$	structure quantity
$(\cdot)_{\mathrm{sgs}}$	related to subgrid-scale model
$(\cdot)_{\mathrm{t}}$	related to torsion
$(\cdot)_{\mathrm{t}}$	in tangential direction
$(\cdot)_{\mathrm{th}}$	predefined threshold
$(\cdot)_{\mathrm{tip}}$	at tip position of the rod
$(\cdot)_{\mathrm{v}}$	related to velocity constraint
$(\cdot)_{\mathrm{w}}$	related to external loads
$(\cdot)_x$	related to x-direction
$(\cdot)_y$	related to y-direction
$(\cdot)_z$	related to z-direction
$(\cdot)_\Gamma$	related to fluid-structure interface Γ

Superscripts

$(\cdot)^0$	initial value of an iterative procedure
$(\cdot)^k$	kth iteration step
$(\cdot)^n$	temporal index, quantity at discrete time t^n
$(\cdot)^r$	temporal index, quantity at Runge-Kutta sub-step r
$(\cdot)'$	fluctuation of a quantity
$(\cdot)'$	spatial derivative w.r.t. arc length Z
$(\cdot)'$	state after collision
$(\cdot)^+$	normalized by friction velocity
$(\cdot)^+$	related to subdomain ω^+
$(\cdot)^-$	related to subdomain ω^-

Other Symbols

$A \cup B$	union of two sets A, B
$A \cap B$	intersection of two sets A, B
$A \subset B$	A is subset of B
$\mathbf{A} \oplus \mathbf{B}$	direct sum of two matrices $\mathbf{A}, \mathbf{B}$
$\mathbf{A} \cdot \mathbf{B}$	matrix-product of two matrices $\mathbf{A}, \mathbf{B}$
$\mathbf{A} \cdot \mathbf{b}$	matrix-vector multiplication of a matrix $\mathbf{A}$ and a vector $\mathbf{b}$
$\mathbf{a} \otimes \mathbf{b}$	tensor-product of two vectors $\mathbf{a}, \mathbf{b}$
$\mathbf{a} \times \mathbf{b}$	cross-product of two vectors (or quaternions) $\mathbf{a}, \mathbf{b}$
$\mathbf{a} \cdot \mathbf{b}$	dot-product of two vectors (or quaternions) $\mathbf{a}, \mathbf{b}$
$\mathbf{a} * \mathbf{b}$	multiplication of two quaternions $\mathbf{a}, \mathbf{b}$ (non-commutative)
$a \propto b$	proportionality between two quantities a, b
∇a	gradient of a scalar field a
$\nabla^2 a$	Laplacian of a scalar field a
$\nabla^2 \mathbf{a}$	Laplacian of a vector field $\mathbf{a}$
$\nabla \cdot \mathbf{a}$	divergence of a vector field $\mathbf{a}$
$\nabla \cdot \mathbf{A}$	divergence of a tensor field $\mathbf{A}$
∂A	boundary of a set A
$\lvert A \rvert$	cardinality of a set A
$\lVert \mathbf{a} \rVert$	Euclidean norm of a vector (or quaternion) $\mathbf{a}$
$[\,\mathbf{a}\,]_\times$	skew matrix of a vector $\mathbf{a}$
$\langle \mathbf{a} \rangle$	average of a quantity $\mathbf{a}$
$\langle \mathbf{a} \rangle_{\mathrm{c}}$	conditional average of $\mathbf{a}$
$\langle \mathbf{a} \rangle_{\mathrm{E}}$	ensemble average of $\mathbf{a}$
$\lvert a \rvert$	absolute value of a scalar a
$\widehat{a}$	Fourier spectrum of a scalar function a
$\hat{a}$	imaginary part of a quaternion $\mathbf{a}$, i.e. $\Im(\mathbf{a}) = \hat{a}$
$\tilde{a}$	selected value of a field quantity a
$\overline{a}$	mean value of a scalar function a
$\overline{\mathbf{a}}$	conjugate of a quaternion $\mathbf{a}$
$\dot{\mathbf{a}}$	first time derivative of $\mathbf{a}$
$\ddot{\mathbf{a}}$	second time derivative of $\mathbf{a}$
$\mathbf{a}'$	spatial derivative of $\mathbf{a}$ w.r.t. arc length Z

Bibliography

[1] H. Abe, H. Kawamura, and Y. Matsuo. Direct Numerical Simulation of a Fully Developed Turbulent Channel Flow With Respect to the Reynolds Number Dependence. *Journal of Fluids Engineering*, 123(2):382–393, 2001.

[2] M. Acarlar and C. Smith. A study of hairpin vortices in a laminar boundary layer. Part 1. Hairpin vortices generated by a hemisphere protuberance. *Journal of Fluid Mechanics*, 175:1–41, 1987.

[3] J. Ackerman and A. Okubo. Reduced mixing in a marine macrophyte canopy. *Functional Ecology*, 7(3):305–309, 1993.

[4] R. Adrian. Hairpin vortex organization in wall turbulence. *Physics of Fluids*, 19(4):041301, 2007.

[5] S. Aland, S. Schwarz, J. Fröhlich, and A. Voigt. Modeling and numerical approximations for bubbles in liquid metal. *European Physical Journal - Special Topics*, 220:185–194, 2013.

[6] A. Ambroziak. The Design and Implementation of hypre, a Library of Parallel High Performance Preconditioners. In W. Pietraszkiewicz and J. Górski, editors, *Shell Structures: Theory and Applications*, pages 369–372. CRC Press/Balkema, 2014.

[7] S. Antman, J. Marsden, and L. Sirovich, editors. *Nonlinear Problems of Elasticity*, volume 107. Springer, 2004.

[8] M. Ardekani, P. Costa, W. Breugem, and L. Brandt. Numerical study of the sedimentation of spheroidal particles. *International Journal of Multiphase Flow*, 87:16–34, 2016.

[9] F. Auricchio, P. Carotenuto, and A. Reali. On the geometrically exact beam model: A consistent, effective and simple derivation from three-dimensional finite-elasticity. *International Journal of Solids and Structures*, 45:4766–4781, 2008.

[10] F. Baaijens. A fictitious domain/mortar element method for fluid-structure interaction. *International Journal for Numerical Methods in Fluids*, 35(7):743–761, 2001.

[11] B. Bailey and R. Stoll. The creation and evolution of coherent structures in plant canopy flows and their role inăturbulent transport. *Journal of Fluid Mechanics*, 789:425Ű460, 2016.

[12] S. Balay, S. Abhyankar, M. Adams, J. Brown, P. Brune, K. Buschelman, L. Dalcin, V. Eijkhout, W. Gropp, D. Kaushik, M. Knepley, D. May, L. McInnes, K. Rupp, P. Sanan, B. Smith, S. Zampini, H. Zhang, and H. Zhang. PETSc users manual. Technical Report ANL-95/11 - Revision 3.8, Argonne National Laboratory, 2017. [online; accessed 12-October-2017].

[13] S. Balay, S. Abhyankar, M. Adams, J. Brown, P. Brune, K. Buschelman, L. Dalcin, V. Eijkhout, W. Gropp, D. Kaushik, M. Knepley, D. May, L. McInnes, K. Rupp, B. Smith, S. Zampini, H. Zhang, and H. Zhang. PETSc Web page. `http://www.mcs.anl.gov/petsc`, 2017. [online; accessed 12-October-2017].

[14] S. Balay, W. Gropp, L. McInnes, and B. Smith. Efficient Management of Parallelism in Object Oriented Numerical Software Libraries. In E. Arge, A. Bruaset, and H. Langtangen, editors, *Modern Software Tools in Scientific Computing*, pages 163–202. Birkhäuser Press, 1997.

[15] M. Bao and H. Yang. Squeeze film air damping in MEMS. *Sensors and Actuators*, A 136:3–7, 2007.

[16] D. Baraff. Coping with friction for non-penetrating rigid body simulation. In *Computer Graphics and Interactive Techniques*, pages 31–41, 1991.

[17] D. Baraff. Non-penetrating Rigid Body Simulation. In *Eurographics '93 State of the Art Reports*, pages 1–23, 1993.

[18] D. Baraff. Fast contact force computation for nonpenetrating rigid bodies. In *Computer Graphics and Interactive Techniques*, pages 23–34, 1994.

[19] H. Barrios-Pina, H. Ramírez-León, C. Rodríguez-Cuevas, and C. Couder-Castaneda. Multilayer Numerical Modeling of Flows through Vegetation Using a Mixing-Length Turbulence Model. *Water*, 6(7):2084–2103, 2014.

[20] K.-J. Bathe and S. Bolourchi. Large displacement analysis of three-dimensional beam structures. *International Journal for Numerical Methods in Engineering*, 14(7):961–986, 1979.

[21] O. Bauchau and J. Craig. *Euler-Bernoulli beam theory*, pages 173–221. Springer, 2009.

[22] R. Baudille and M. Biancolini. A general approach for studying the motion of a cantilever beam interacting with a 2D fluid flow. *Interaction and Multiscale Mechanics*, 1(4):449–465, 2008.

[23] A. Beléndez, C. Pascual, D. Méndez, T. Beléndez, and C. Neipp. Exact solution for the nonlinear pendulum. *Revista Brasileira de Ensino de Física*, 29:645–648, 2007.

[24] J. Bender and A. Schmitt. Constraint-based collision and contact handling using impulses. In *19th International Conference on Computer Animation and Social Agents*, pages 3–11, 2006.

[25] M. Bergou, M. Wardetzky, S. Robinson, B. Audoly, and E. Grinspun. Discrete Elastic Rods. In *ACM Transactions on Graphics*, volume 27, pages 63:1–63:12, 2008.

[26] M. Berins. *SPI Plastics Engineering Handbook of the Society of the Plastics Industry, Inc.* Springer, 2000.

[27] F. Bertails. Linear Time Super-Helices. *Computer Graphics Forum*, 28:417–426, 2009.

[28] F. Bertails, B. Audoly, M.-P. Cani, B. Querleux, F. Leroy, and J.-L. Lévêque. Super-Helices for Predicting the Dynamics of Natural Hair. In *ACM Transactions on Graphics*, pages 1180–1187, 2006.

[29] P. Betsch, A. Menzel, and E. Stein. On the parametrization of finite rotations in computational mechanics: A classification of concepts with application to smooth shells. *Computer Methods in Applied Mechanics and Engineering*, 155(3):273–305, 1998.

[30] R. Beyer and R. LeVeque. Analysis of a One-Dimensional Model for the Immersed Boundary Method. *SIAM Journal on Numerical Analysis*, 29(2):332–364, 1992.

[31] A. Bhalla, R. Bale, B. Griffith, and N. Patankar. A unified mathematical framework and an adaptive numerical method for fluid-structure interaction with rigid, deforming, and elastic bodies. *Journal of Computational Physics*, 250:446–476, 2013.

[32] R. Bhardwaj and R. Mittal. Benchmarking a Coupled Immersed-Boundary-Finite-Element Solver for Large-Scale Flow-Induced Deformation. *AIAA Journal*, 50(7):1638–1642, 2012.

[33] C. L. Bouteiller and J. Venditti. Sediment transport and shear stress partitioning in a vegetated flow. *Water Resources Research*, 51(4):2901–2922, 2015.

[34] K. Brenan, S. Campbell, and L. Petzold, editors. *Numerical Solution of Initial-Value Problems in Differential-Algebraic Equations*, volume 2. Society for Industrial and Applied Mathematics, 1996.

[35] W.-P. Breugem. A second-order accurate immersed boundary method for fully resolved simulations of particle-laden flows. *Journal of Computational Physics*, 231:4469–4498, 2012.

[36] R. Bridson, R. Fedkiw, and J. Anderson. Robust treatment of collisions, contact and friction for cloth animation. In *29th Annual Conference on Computer Graphics and Interactive Techniques*, pages 594–603, 2002.

[37] D. Brown, R. Cortez, and M. Minion. Accurate Projection Methods for the Incompressible Navier-Stokes Equations. *Journal of Computational Physics*, 168(2):464–499, 2001.

[38] J. Brydson. *Plastics Materials*. Butterworth-Heinemann, 1999.

[39] H.-J. Bungartz, M. Schäfer, and (Eds.). *Fluid-Structure Interaction - Modelling, Simulation, Optimisation*. Springer, 2006.

[40] A. Cardona and M. Geradin. A beam finite element non-linear theory with finite rotations. *International Journal for Numerical Methods in Engineering*, 26(11):2403–2438, 1988.

[41] F. Carollo, V. Ferro, and D. Termini. Flow Resistance Law in Channels with Flexible Submerged Vegetation. *Journal of Hydraulic Engineering*, 131(7):554–564, 2005.

[42] B. Choe, M. Choi, and H.-S. Ko. Simulating complex hair with robust collision handling. In *ACM SIGGRAPH/Eurographics Symposium on Computer Animation*, pages 153–160, 2005.

[43] A. Chorin. Numerical Solution of the Navier-Stokes Equations. *Mathematics of Computation*, 22(104):754–762, 1968.

[44] M. Clerici. *Finite-Elemente-Modellierung und Simulation von geometrisch exakten Timoshenko-Balken*. PhD thesis, ETH Zürich, 2001.

[45] E. Cosserat and F. Cosserat. *Théorie des corps dé formables*. Librairie Scientifique A. Hermann et Fils (Translation: Theory of deformable bodies, NASA TT F-11 561, 1968), 1909.

[46] R. Costanza, R. d'Arge, R. de Groot, S. Farber, M. Grasso, B. Hannon, K. Limburg, S. Naeem, R. O'Neill, J. Paruelo, R. Raskin, P. Sutton, and M. van den Belt. The value of the world's ecosystem services and natural capital. *Nature*, 387:253–260, 1997.

[47] G.-H. Cottet and E. Maitre. A semi-implicit level set method for multiphase flows and fluid-structure interaction problems. *Journal of Computational Physics*, 314:80–92, 2016.

[48] M. Crisfield. A consistent co-rotational formulation for non-linear, three-dimensional, beam-elements. *Computer Methods in Applied Mechanics and Engineering*, 81(2):131–150, 1990.

[49] L. Crivelli and C. Felippa. A three-dimensional non-linear Timoshenko beam based on the core-congruential formulation. *International Journal for Numerical Methods in Engineering*, 36(21):3647–3673, 1993.

[50] L. Dagum and R. Menon. OpenMP: an industry standard API for shared-memory programming. *Computational Science & Engineering*, 5(1):46–55, 1998.

[51] F. Daviaud, J. Hegseth, and P. Bergé. Subcritical transition to turbulence in plane Couette flow. *Physical Review Letters*, 69(17):2511–2514, 1992.

[52] E. de Langre. Methodological advances in predicting flow-induced dynamics of plants using mechanical-engineering theory. *Journal of Experimental Biology*, 215(6):914–921, 2012.

[53] M. de Tullio and G. Pascazio. A moving-least-squares immersed boundary method for simulating the fluid-structure interaction of elastic bodies with arbitrary thickness. *Journal of Computational Physics*, 325:201–225, 2016.

[54] D. Dennis. Coherent structures in wall-bounded turbulence. *Anais da Academia Brasileira de Ciências*, 87:1161–1193, 2015.

[55] M. Detert. *Hydrodynamic processes at the water-sediment interface of streambeds*. PhD thesis, Universität Karlsruhe - Institut für Hydromechanik, 2008.

[56] W. Dettmer and D. Perić. A computational framework for fluid-structure interaction: Finite element formulation and applications. *Computer Methods in Applied Mechanics and Engineering*, 195(41):5754–5779, 2006.

[57] D. Dichmann and J. Maddocks. An impetus-striction simulation of the dynamics of an elastica. *Journal of Nonlinear Science*, 6(3):271–292, 1996.

[58] J. Dijkstra and R. Uittenbogaard. Modeling the interaction between flow and highly flexible aquatic vegetation. *Water Resources Research*, 46(12):W12547, 2010.

[59] R. Dong. *Effective mass and damping of submerged structures*. Lawrence Livermore Laboratory, UCRL-52342, 1978.

[60] E. V. Driest. On Turbulent Flow Near a Wall. *Journal of the Aeronautical Sciences*, 23(11):1007–1011, 1956.

[61] E. Drumwright. A Fast and Stable Penalty Method for Rigid Body Simulation. *IEEE Transactions on Visualization and Computer Graphics*, 14:231–240, 2008.

[62] S. Dupont, F. Gosselin, C. Py, E. de Langre, P. Hemon, and Y. Brunet. Modelling waving crops using large-eddy simulation: comparison with experiments and a linear stability analysis. *Journal of Fluid Mechanics*, 652:5–44, 2010.

[63] C. Duriez, F. Dubois, A. Kheddar, and C. Andriot. Realistic haptic rendering of interacting deformable objects in virtual environments. In *IEEE Transactions on Visualization and Computer Graphics*, pages 36–47, 2006.

[64] E. Fadlun, R. Verzicco, P. Orlandi, and J. Mohd-Yusof. Combined Immersed-Boundary Finite-Difference Methods for Three-Dimensional Complex Flow Simulations. *Journal of Computational Physics*, 161:35–60, 2000.

[65] R. Falgout, J. Jones, and U. Yang. The Design and Implementation of hypre, a Library of Parallel High Performance Preconditioners. In A. Bruaset and A. Tveito, editors, *Numerical Solution of Partial Differential Equations on Parallel Computers*, pages 267–294. Springer, 2006.

[66] F. Farassat. Introduction to generalized functions with applications in aerodynamics and aeroacoustics. *NASA Technical Paper 3428 (Hampton, Virginia: NASA Langley Research Center)*, 1996.

[67] J. Favier, A. Revell, and A. Pinelli. A Lattice Boltzmann-Immersed Boundary method to simulate the fluid interaction with moving and slender flexible objects. *Journal of Computational Physics*, 261:145–161, 2014.

[68] M. Fernández, J.-F. Gerbeau, and C. Grandmont. A projection algorithm for fluid-structure interaction problems with strong added-mass effect. *Comptes Rendus Mathematique*, 342:279–284, 2006.

[69] H. Fernando. *Handbook of Environmental Fluid Dynamics, Volume One: Overview and Fundamentals*. CRC Press, 2012.

[70] J. Ferziger and M. Perić. *Computational Methods for Fluid Dynamics*. Springer, 2002.

[71] J. Finnigan. Turbulence in Plant Canopies. *Annual Review of Fluid Mechanics*, 32(1):519–571, 2000.

[72] J. Finnigan, R. Shaw, and E. Patton. Turbulence structure above a vegetation canopy. *Journal of Fluid Mechanics*, 637:387–424, 2009.

[73] C. Förster, W. Wall, and E. Ramm. Artificial added mass instabilities in sequential staggered coupling of nonlinear structures and incompressible viscous flows. *Computer Methods in Applied Mechanics and Engineering*, 196(7):1278–1293, 2007.

[74] M. P. Forum. MPI: A Message-Passing Interface Standard. Technical report, University of Tennessee, 1994.

[75] Fraunhofer Institute for Industrial Mathematics ITWM. FIDYST - Fiber Dynamics Simulation Tool. `https://www.itwm.fraunhofer.de/en/departments/tv/products-and-services/fidyst-fiber-dynamics-simulation-tool.html`, 2018. [online; accessed 19-April-2018].

[76] J. Freund and A. Karakoç. Shear and torsion correction factors of Timoshenko beam model for generic cross sections. *Research on Engineering Structures and Materials*, 2:19–27, 2016.

[77] J. Fröhlich. *Large Eddy Simulation turbulenter Strömungen*. B.G. Teubner, 2006.

[78] J. Gac. A large eddy based lattice-Boltzmann simulation of velocity distribution in an open channel flow with rigid and flexible vegetation. *Acta Geophysica*, 62(1):180–198, 2014.

[79] GESTIS Substance Database of IFA. `http://www.dguv.de/ifa/gestis/gestis-stoffdatenbank/index-2.jsp`, 2018. [online; accessed 15-January-2018].

[80] B. Geurts and J. Fröhlich. A framework for predicting accuracy limitations in large-eddy simulation. *Physics of Fluids*, 14(6):L41–L44, 2002.

[81] M. Ghisalberti and H. Nepf. Mixing layers and coherent structures in vegetated aquatic flows. *Journal of Geophysical Research: Oceans*, 107(C2):277–301, 2002.

[82] M. Ghisalberti and H. Nepf. Mass Transport in Vegetated Shear Flows. *Environmental Fluid Mechanics*, 5(6):527–551, 2005.

[83] M. Ghisalberti and H. Nepf. The structure of the shear layer in flows over rigid and flexible canopies. *Environmental Fluid Mechanics*, 6(3):277–301, 2006.

[84] T. Giang and C. O. G. Bradshaw. Complementarity Based Multiple Point Collision Resolution. In *20th Annual Conference on Computer Graphics and Interactive Techniques*, SIGGRAPH '93, pages 313–320, 2003.

[85] A. Gilmanov and F. Sotiropoulos. A hybrid Cartesian/immersed boundary method for simulating flows with 3D, geometrically complex, moving bodies. *Journal of Computational Physics*, 207(2):457–492, 2005.

[86] R. Glowinski, T. Pan, T. Hesla, D. Joseph, and J. Périaux. A Fictitious Domain Approach to the Direct Numerical Simulation of Incompressible Viscous Flow past Moving Rigid Bodies: Application to Particulate Flow. *Journal of Computational Physics*, 169(2):363–426, 2001.

[87] R. Glowinski, T.-W. Pan, and J. Périaux. A Lagrange multiplier/fictitious domain method for the numerical simulation of incompressible viscous flow around moving rigid bodies: (I) case where the rigid body motions are known a priori. *Comptes Rendus de l'Académie des Sciences - Series I - Mathematics*, 324(3):361–369, 1997.

[88] P. Gresho and R. Sani. On pressure boundary conditions for the incompressible Navier-Stokes equations. *International Journal for Numerical Methods in Fluids*, 7(10):1111–1145, 1987.

[89] B. Griffith and S. Lim. Simulating an Elastic Ring with Bend and Twist by an Adaptive Generalized Immersed Boundary Method. *Communications in Computational Physics*, 12(2):433–461, 2012.

[90] E. Guendelman, R. Bridson, and R. Fedkiw. Nonconvex Rigid Bodies with Stacking. *ACM Transactions on Graphics*, 22(3):871–878, 2003.

[91] E. Hairer. Fortran and Matlab Codes. `https://www.unige.ch/~hairer/software.html`, 2017. [online; accessed 6-November-2017].

[92] E. Hairer and G. Wanner. *Solving Ordinary Differential Equations II*. Springer, 1996.

[93] E. Hairer and G. Wanner. Stiff differential equations solved by Radau methods. *Journal of Computational and Applied Mathematics*, 111(1):93–111, 1999.

[94] F. Ham, F. Lien, and A. Strong. A Fully Conservative Second-Order Finite Difference Scheme for Incompressible Flow on Nonuniform Grids. *Journal of Computational Physics*, 177(1):117–133, 2002.

[95] S. Han, H. Benaroya, and T. Wei. Dynamics of transversely vibrating beams using four engineering theories. *Journal of Sound and Vibration*, 225(5):935–988, 1999.

[96] C. Harper. *Modern Plastics Handbook*. McGraw Hill Professional, 2000.

[97] S. Hartmann, A. Meister, M. Schäfer, S. Turek, and (Eds.). *International Workshop on Fluid-Structure Interaction. Theory, Numerics and Applications*. Kassel University Press, 2008.

[98] B. Heidelberger, M. Teschner, R. Keiser, and M. Müller. Consistent penetration depth estimation for deformable collision response. In *Vision, Modeling and Visualization*, pages 339–346, 2004.

[99] H. Hesse and R. Palacios. Consistent structural linearisation in flexible-body dynamics with large rigid-body motion. *Computers & Structures*, 110:1–14, 2012.

[100] C. Hirt and B. Nichols. Volume of fluid (VOF) method for the dynamics of free boundaries. *Journal of Computational Physics*, 39(1):201–225, 1981.

[101] K. Hsiao, J. Lin, and W. Lin. A consistent co-rotational finite element formulation for geometrically nonlinear dynamic analysis of 3-D beams. *Computer Methods in Applied Mechanics and Engineering*, 169(1):1–18, 1999.

[102] W.-X. Huang, S. Shin, and H. Sung. Simulation of flexible filaments in a uniform flow by the immersed boundary method. *Journal of Computational Physics*, 226(2):2206–2228, 2007.

[103] B. Hübner, E. Walhorn, and D. Dinkler. A monolithic approach to fluid-structure interaction using space-time finite elements. *Computer Methods in Applied Mechanics and Engineering*, 193(23):2087–2104, 2004.

[104] A. Ibrahimbegovic. On the choice of finite rotation parameters. *Computer Methods in Applied Mechanics and Engineering*, 149(1):49–71, 1997.

[105] A. Ibrahimbegovic and M. Mikdad. Finite rotations in dynamics of beams and implicit time-stepping schemes. *International Journal for Numerical Methods in Engineering*, 41(5):781–814, 1998.

[106] J. Järvelä. Effect of submerged flexible vegetation on flow structure and resistance. *Journal of Hydrology*, 307(1):233–241, 2005.

[107] G. Jelenić and M. Crisfield. Geometrically exact 3D beam theory: implementation of a strain-invariant finite element for statics and dynamics. *Computer Methods in Applied Mechanics and Engineering*, 171(1):141–171, 1999.

[108] J. Jeong and F. Hussain. On the identification of a vortex. *Journal of Fluid Mechanics*, 285:69–94, 1995.

[109] E. Jeppesen, M. Søndergaard, M. Søndergaard, and K. Christoffersen. *The Structuring Role of Submerged Macrophytes in Lakes*. Springer, 1998.

[110] P. Jung, S. Leyendecker, J. Linn, and M. Ortiz. A discrete mechanics approach to the Cosserat rod theory–Part 1: static equilibria. *International Journal for Numerical Methods in Engineering*, 85(1):31–60, 2011.

[111] J. Kaimal and J. Finnigan. *Atmospheric boundary layer flows: their structure and measurement*. Oxford University Press, 1994.

[112] T. Kajishima and K. Taira. *Computational Fluid Dynamics: Incompressible Turbulent Flows*. Springer, 2016.

[113] D. Kamensky, M.-C. Hsu, D. Schillinger, J. Evans, A. Aggarwal, Y. Bazilevs, M. Sacks, and T. Hughes. An immersogeometric variational framework for fluid-structure interaction: Application to bioprosthetic heart valves. *Computer Methods in Applied Mechanics and Engineering*, 284:1005–1053, 2015.

[114] M. Kanda, R. Moriwaki, and F. Kasamatsu. Large-Eddy Simulation of Turbulent Organized Structures within and above Explicitly Resolved Cube Arrays. *Boundary-Layer Meteorology*, 112(2):343–368, 2004.

[115] T. Kane, R. Ryan, and A. Banerjee. Dynamics of a Beam Attached to a Moving Base. In *AAS/AIAA Astrodynamics Specialist Conference*, 1985.

[116] T. Kane, R. Ryan, and A. Banerjee. Dynamics of a cantilever beam attached to a moving base. *Journal of Guidance, Control, and Dynamics*, 10(2):139–151, 1987.

[117] H. Kawamura. Kawamura Lab - DNS Database of Wall Turbulence and Heat Transfer. `http://www.rs.tus.ac.jp/~t2lab/db/index.html`, 2008. [online; accessed 20-October-2017].

[118] T. Kempe. *A numerical method for interface-resolving simulations of particle-laden flows with collisions*. PhD thesis, Technische Universität Dresden, 2011.

[119] T. Kempe and J. Fröhlich. An improved immersed boundary method with direct forcing for the simulation of particle laden flows. *Journal of Computational Physics*, 231:3663–3684, 2012.

[120] T. Kempe and J. Fröhlich. Collision modelling for the interface-resolved simulation of spherical particles in viscous fluids. *Journal of Fluid Mechanics*, 709:445–489, 2012.

[121] A. Kidanemariam and M. Uhlmann. Formation of sediment patterns in channel flow: minimal unstable systems and their temporalăevolution. *Journal of Fluid Mechanics*, 818:716–743, 2017.

[122] J. Kim, D. Kim, and H. Choi. An Immersed-Boundary Finite-Volume Method for Simulations of Flow in Complex Geometries. *Journal of Computational Physics*, 171:132–150, 2001.

[123] J. Kim and P. Moin. Application of a fractional-step method to incompressible Navier-Stokes equations. *Journal of Computational Physics*, 59(2):308–323, 1985.

[124] J. Kim, P. Moin, and R. Moser. Turbulence statistics in fully developed channel flow at low Reynolds number. *Journal of fluid mechanics*, 177:133–166, 1987.

[125] W. Kim, I. Lee, and H. Choi. A weak-coupling immersed boundary method for fluid-structure interaction with low density ratio of solid to fluid. *Journal of Computational Physics*, 359:296–311, 2018.

[126] Y. Kim and C. Peskin. A penalty immersed boundary method for a rigid body in fluid. *Physics of Fluids*, 28(3):033603, 2016.

[127] K. Kondoh and S. Atluri. Large-deformation, elasto-plastic analysis of frames under nonconservative loading, using explicitly derived tangent stiffnesses based on assumed stresses. *Computational Mechanics*, 2:1–25, 1987.

[128] F. Koschnick. *Geometrische Locking-Effekte bei Finiten Elementen und ein allgemeines Konzept zu ihrer Vermeidung*. PhD thesis, Technische Universität München, 2004.

[129] J. Kuipers. *Quaternions and rotation sequences: a primer with applications to orbits, aerospace and virtual reality*. Princeton University, Princeton, NJ, 1999.

[130] U. Lacis, N. Brosse, F. Ingremeau, A. Mazzino, F. Lundell, H. Kellay, and S. Bagheri. Passive appendages generate drift through symmetry breaking. *Nature Communications*, 5:5310, 2014.

[131] H. Lang, J. Linn, and M. Arnold. Multibody dynamics simulation of geometrically exact Cosserat rods. *Multibody System Dynamics*, 25(3):285–312, 2011.

[132] Lawrence Livermore National Laboratory. Hypre Web page. `https://computation.llnl.gov/projects/hypre-scalable-linear-solvers-multigrid-methods/software`, 2017. [online; accessed 17-October-2017].

[133] A. Layton. An efficient numerical method for the two-fluid Stokes equations with a moving immersed boundary. *Computer Methods in Applied Mechanics and Engineering*, 197:2147–2155, 2008.

[134] D. Le, J. White, J. Peraire, K. Lim, and B. Khoo. An implicit immersed boundary method for three-dimensional fluid-membrane interactions. *Journal of Computational Physics*, 228(22):8427–8445, 2009.

[135] I. Lee and H. Choi. A discrete-forcing immersed boundary method for the fluid-structure interaction of an elastic slender body. *Journal of Computational Physics*, 280:529–546, 2015.

[136] J. Lenoir, P. Meseure, L. Grisoni, and C. Chaillou. Surgical thread simulation. In *Modelling & Simulation for Computer-aided Medicine and Surgery*, volume 12, pages 102–107, 2002.

[137] A. Leung and C. Wong. Symmetry Reduction of Structures for Large Rotations. *Advances in Structural Engineering*, 3(1):81–102, 2000.

[138] R. LeVeque and Z. Li. The Immersed Interface Method for Elliptic Equations with Discontinuous Coefficients and Singular Sources. *SIAM Journal on Numerical Analysis*, 31(4):1019–1044, 1994.

[139] R. Levien. The elastica: a mathematical history. Technical report, EECS Department, University of California, Berkeley, 2008.

[140] J. Li. A geometrically exact curved beam theory and its finite element formulation/implementation. Master's thesis, Virginia Polytechnic Institute and State University, 2000.

[141] Z. Li. A co-rotational formulation for 3D beam element using vectorial rotational variables. *Computational Mechanics*, 39(3):309–322, 2007.

[142] Z. Li and K. Ito. *The Immersed Interface Method: Numerical Solutions of PDEs Involving Interfaces and Irregular Domains*. Society for Industrial and Applied Mathematics, 2006.

[143] Z. Li and M.-C. Lai. The Immersed Interface Method for the Navier-Stokes Equations with Singular Forces. *Journal of Computational Physics*, 171(2):822–842, 2001.

[144] J. Linn. Private communication, 2014.

[145] Y. Liu and Y. Mori. Properties of Discrete Delta Functions and Local Convergence of the Immersed Boundary Method. *SIAM Journal on Numerical Analysis*, 50(6):2986–3015, 2012.

[146] S. Lo. Geometrically nonlinear formulation of 3D finite strain beam element with large rotations. *Computers & Structures*, 44(1):147–157, 1992.

[147] A. Love. *A treatise on the mathematical theory of elasticity*. Dover Publications, 1944.

[148] E. D. Lozzo. *Geometrically exact three-dimensional beam theory: modeling and FEM implementation for statics and dynamics analysis*. PhD thesis, Università degli Studi di Pavia, 2010.

[149] S. Lu and J. Chen. Effects of Rigid Vegetation on the Turbulence Characteristics in Sediment-Laden Flows. *Journal of Applied Mathematics and Physics*, 2(12):1091, 2014.

[150] M. Luhar and H. Nepf. Flow-induced reconfiguration of buoyant and flexible aquatic vegetation. *Limnology and Oceanography*, 56(6):2003–2017, 2011.

[151] H. Luo, H. Dai, P. F. de Sousa, and B. Yin. On the numerical oscillation of the direct-forcing immersed-boundary method for moving boundaries. *Computers & Fluids*, 56:61–76, 2012.

[152] T. Marjoribanks. *High resolution modelling of flexible submerged vegetation in rivers*. PhD thesis, Durham University, 2013.

[153] T. Marjoribanks, R. Hardy, S. Lane, and D. Parsons. High-resolution numerical modelling of flow-vegetation interactions. *Journal of Hydraulic Research*, 52(6):775–793, 2014.

[154] B. Markert, editor. *Weak or Strong: On Coupled Problems In Continuum Mechanics*, volume 1. Universität Stuttgart Inst. f. Mechanik (Bauwesen), 2010.

[155] F. Mathey, J. Fröhlich, and W. Rodi. LES of Heat Transfer in Turbulent Flow over a Wall-Mounted Matrix of Cubes. In P. Voke, N. Sandham, and L. Kleiser, editors, *Direct and Large-Eddy Simulation III: Proceedings of the Isaac Newton Institute Symposium/ERCOFTAC Workshop held in Cambridge, U.K., 12–14 May 1999*, pages 51–62. Springer, 1999.

[156] H. Matthies, R. Niekamp, and J. Steindorf. Algorithms for strong coupling procedures. *Computer Methods in Applied Mechanics and Engineering*, 195(17):2028–2049, 2006.

[157] C. Meier. *Geometrically Exact Finite Element Formulations for Slender Beams and Their Contact Interaction*. PhD thesis, Technische Universität München, 2016.

[158] M. Meyers and K. Chawla. *Mechanical Behavior of Materials*. Prentice Hall, 1999.

[159] S. Miller, R. Campbell, C. Elsworth, J. Pitt, and D. Boger. An Overset Grid Method for Fluid-Structure Interaction. *World Journal of Mechanics*, 4:217–237, 2014.

[160] B. Mirtich. *Impulse-based Dynamic Simulation of Rigid Body Systems*. PhD thesis, University of California at Berkeley, 1996.

[161] B. Mirtich and J. Canny. Impulse-based Simulation of Rigid Bodies. In *Symposium on Interactive 3D Graphics*, I3D '95, page 181, 1995.

[162] R. Mittal and G. Iaccarino. Immersed boundary methods. *Annual Review of Fluid Mechanics*, 37(1):239–261, 2005.

[163] J. Mohd-Yusof. Combined immersed boundary/B-Spline method for simulations of flows in complex geometries. *Center for Turbulence Research. Annual Research Briefs. NASA Ames/Stanford University*, pages 317–327, 1997.

[164] D. Mokbel, H. Abels, and S. Aland. A Phase-Field Model for Fluid-Structure-Interaction. *ArXiv e-prints*, 2018.

[165] R. Moser, J. Kim, and N. Mansour. Direct numerical simulation of turbulent channel flow up to $Re_\tau = 590$. *Physics of Fluids*, 11(4):943–945, 1999.

[166] MPI Forum. `http://mpi-forum.org/`, 2017. [online; accessed 12-October-2017].

[167] T. U. N. Kouwen. Flexible roughness in open channels. *Journal of the Hydraulics Division*, 99:713–728, 1973.

[168] H. Nepf. Drag, turbulence, and diffusion in flow through emergent vegetation. *Water Resources Research*, 35(2):479–489, 1999.

[169] H. Nepf. Flow and transport in regions with aquatic vegetation. *Annual Review of Fluid Mechanics*, 44:123–142, 2012.

[170] H. Nepf. Hydrodynamics of vegetated channels. *Journal of Hydraulic Research*, 50(3):262–279, 2012.

[171] H. Nepf and E. Vivoni. Flow structure in depth-limited, vegetated flow. *Journal of Geophysical Research: Oceans*, 105:28547–28557, 2000.

[172] H. M. Nepf and M. Ghisalberti. Flow and transport in channels with submerged vegetation. *Acta Geophysica*, 56:753–777, 2008.

[173] I. Nezu and M. Sanjou. Turburence structure and coherent motion in vegetated canopy open-channel flows. *Journal of Hydro-environment Research*, 2(2):62–90, 2008.

[174] V. Nikora, S. Cameron, I. Albayrak, O. Miler, N. Nikora, F. Siniscalchi, M. Stewart, and M. O'Hare. Flow-biota interactions in aquatic systems: Scales, mechanisms, and challenges. In W. Rodi and M. Uhlmann, editors, *Environmental Fluid Mechanics*, IAHR monograph, pages 217–235. CRC Press, 2012.

[175] T. Okamoto and I. Nezu. Turbulence structure and "Monami" phenomena in flexible vegetated open-channel flows. *Journal of Hydraulic Research*, 47(6):798–810, 2009.

[176] T. Okamoto and I. Nezu. Flow resistance law in open-channel flows with rigid and flexible vegetation. In *Proceedings of the International Conference on Fluvial Hydraulics*, volume 1, pages 261–268. Bundesanstalt für Wasserbau, 2010.

[177] T. Okamoto and I. Nezu. Large eddy simulation of 3-D flow structure and mass transport in open-channel flows with submerged vegetations. *Journal of Hydro-environment Research*, 4:185–197, 2010.

[178] T. Okamoto, I. Nezu, and M. Sanjou. Flow-vegetation interactions: length-scale of the "monami" phenomenon. *Journal of Hydraulic Research*, 54(3):251–262, 2016.

[179] A. Okubo and S. Levin. *Diffusion and Ecological Problems: Modern Perspectives*. Springer, 2001.

[180] L. Onural. Impulse functions over curves and surfaces and their applications to diffraction. *Journal of Mathematical Analysis and Applications*, 322:18–27, 2006.

[181] OpenMP - Enabling HPC since 1997. `http://www.openmp.org/`, 2017. [online; accessed 12-October-2017].

[182] A. Pankonien and Z. Ounaies. Piezoelectric Artificial Kelp for Energy Harvesting. In *ASME 2010 Conference on Smart Materials, Adaptive Structures and Intelligent Systems*, volume 2, pages 223–232, 2010.

[183] H. Patel, S. Das, J. Kuipers, J. Padding, and E. Peters. A coupled Volume of Fluid and Immersed Boundary Method for simulating 3D multiphase flows with contact line dynamics in complex geometries. *Chemical Engineering Science*, 166:28–41, 2017.

[184] E. Patton and J. Finnigan. Canopy Turbulence. In *H.J.S. Fernando (Ed.), Handbook of Environmental Fluid Dynamics, Volume One: Overview and Fundamentals*, pages 311–328. CRC Press, 2013.

[185] C. Peskin. Numerical analysis of blood flow in the heart. *Journal of Computational Physics*, 25:220–252, 1977.

[186] C. Peskin. The immersed boundary method. *Acta Numerica*, 11:479–517, 2002.

[187] C. Peskin and B. Printz. Improved volume conservation in the computation of flows with immersed elastic boundaries. *Journal of Computational Physics*, 105:33–46, 1993.

[188] J. Phillips, A. Ladd, and L. Kavraki. Surgical thread simulation. In *International Conference on Robotics and Automation*, pages 841–846, 2002.

[189] D. Poggi, A. Porporato, L. Ridolfi, J. Albertson, and G. Katul. The Effect of Vegetation Density on Canopy Sub-Layer Turbulence. *Boundary-Layer Meteorology*, 111(3):565–587, 2004.

[190] D. Prieve. The Lubrication Approximation. `https://www.andrew.cmu.edu/course/06-703/Lubrication.pdf`, 2001. [online; accessed 6-August-2015].

[191] A. Prosperetti and G. Tryggvason. *Computational Methods for Multiphase Flow*. Cambridge University Press, 2009.

[192] S. Puijalon, T. Bouma, C. Christophe, J. van Groenendael, N. Anten, E. Martel, and G. Bornette. Plant resistance to mechanical stress: evidence of an avoidance-tolerance trade-off. *New Phytologist*, 191(4):1141–1149, 2011.

[193] S. Puijalon, J.-P. Léna, N. Rivière, J.-Y. Champagne, J.-C. Rostan, and G. Bornette. Phenotypic plasticity in response to mechanical stress: hydrodynamic performance and fitness of four aquatic plant species. *New Phytologist*, 177(4):907–917, 2008.

[194] M. Rai and P. Moin. Direct simulations of turbulent flow using finite-difference schemes. *Journal of Computational Physics*, 96(1):15–53, 1991.

[195] S. Rao, editor. *Vibration of Continuous Systems*, volume 1. John Wiley & Sons, Inc., 2007.

[196] M. Rashidifar. *Nonlinear Vibrations of Cantilever Beams and Plates*. Anchor Academic Publishing, 2016.

[197] M. Raupach, J. Finnigan, and Y. Brunei. Coherent eddies and turbulence in vegetation canopies: The mixing-layer analogy. *Boundary-Layer Meteorology*, 78(3):351–382, 1996.

[198] S. Ray, T. Kempe, and J. Fröhlich. Efficient modelling of particle collisions using a non-linear viscoelastic contact force. *International Journal of Multiphase Flow*, 76:101–110, 2015.

[199] E. Reissner. On finite deformations of space-curved beams. *Zeitschrift für angewandte Mathematik und Physik ZAMP*, 32(6):734–744, 1981.

[200] J. Rhim and S. Lee. A vectorial approach to computational modelling of beams undergoing finite rotations. *International Journal for Numerical Methods in Engineering*, 41(3):527–540, 1998.

[201] T. Richter. A Fully Eulerian formulation for fluid-structure-interaction problems. *Journal of Computational Physics*, 233:227–240, 2013.

[202] M. Ritto-Corrêa and D. Camotim. On the differentiation of the Rodrigues formula and its significance for the vector-like parameterization of Reissner-Simo beam theory. *International Journal for Numerical Methods in Engineering*, 55(9):1005–1032, 2002.

[203] A. Roma, C. Peskin, and M. Berger. An Adaptive Version of the Immersed Boundary Method. *Journal of Computational Physics*, 153(2):509–534, 1999.

[204] S. Roman. The Formula of Faa di Bruno. *The American Mathematical Monthly*, 87:805–809, 1980.

[205] J. Rominger and H. Nepf. Effects of blade flexural rigidity on drag force and mass transfer rates in model blades. *Limnology and Oceanography*, 59(6):2028–2041, 2014.

[206] J. Sandhu, K. Stevens, and G. Davies. A 3-D, co-rotational, curved and twisted beam element. *Computers & Structures*, 35(1):69–79, 1990.

[207] M. Sanjou. Turbulence Diffusion Mechanism in Submerged Vegetation Flows. In D. Bucur, editor, *River Basin Management*, chapter 11, pages 225–247. InTech, 2016.

[208] Y. Sankin and N. Yuganova. Longitudinal vibrations of elastic rods of stepwise-variable cross-section colliding with a rigid obstacle. *Journal of Applied Mathematics and Mechanics*, 65(3):427–433, 2001.

[209] C. Santarelli and J. Fröhlich. Direct Numerical Simulations of spherical bubbles in vertical turbulent channel flow. *International Journal of Multiphase Flow*, 75:174–193, 2015.

[210] M. Schulze, S. Dietz, B. Burgermeister, A. Tuganov, H. Lang, J. Linn, and M. Arnold. Integration of Nonlinear Models of Flexible Body Deformation in Multibody System Dynamics. *Journal of Computational and Nonlinear Dynamics*, 9(1):011012, 2013.

[211] S. Schwarz, T. Kempe, and J. Fröhlich. An immersed boundary method for the simulation of bubbles with varying shape. *Journal of Computational Physics*, 315:124–149, 2016.

[212] R. Shaw and U. Schumann. Large-eddy simulation of turbulent flow above and within a forest. *Boundary-Layer Meteorology*, 61(1):47–64, 1992.

[213] K. Shoemake. Animating rotation with quaternion curves. In *ACM SIGGRAPH*, pages 245–254, 1985.

[214] A. Shvidchenko and G. Pender. Macroturbulent structure of open-channel flow over gravel beds. *Water Resources Research*, 37(3):709–719, 2001.

[215] J. Simo. A finite strain beam formulation. The three-dimensional dynamic problem. Part I. *Computer Methods in Applied Mechanics and Engineering*, 49:55–70, 1985.

[216] J. Simo, N. Tarnow, and M. Doblare. Non-linear dynamics of three-dimensional rods: Exact energy and momentum conserving algorithms. *International Journal for Numerical Methods in Engineering*, 38(9):1431–1473, 1995.

[217] J. Simo and L. Vu-Quoc. On the Dynamics of Flexible Beams Under Large Overall Motion – The Plane Case: Part II. *Journal of Applied Mechanics*, 53:855–863, 1986.

[218] J. Simo and L. Vu-Quoc. On the dynamics in space of rods undergoing large motions - A geometrically exact approach. *Computer Methods in Applied Mechanics and Engineering*, 66(2):125–161, 1988.

[219] R. Singh, M. Bandi, A. Mahadevan, and S. Mandre. Linear stability analysis for monami in a submerged seagrass bed. *Journal of Fluid Mechanics*, 786:R1, 2016.

[220] F. Siniscalchi, V. Nikora, and J. Aberle. Plant patch hydrodynamics in streams: Mean flow, turbulence, and drag forces. *Water Resources Research*, 48(1):W01513, 2012.

[221] J. Smagorinsky. General circulation experiments with the primitive equations. *Monthly Weather Review*, 91:99–164, 1963.

[222] F. Sotiropoulos and X. Yang. Immersed boundary methods for simulating fluid-structure interaction. *Progress in Aerospace Sciences*, 65:1–21, 2014.

[223] J. Spillmann. *CoRDE: Cosserat Rod Elements for the Animation of Interacting Elastic Rods*. PhD thesis, Albert-Ludwigs-Universität Freiburg, 2008.

[224] J. Spillmann, M. Becker, and M. Teschner. Non-iterative Computation of Contact Forces for Deformable Objects. *Journal of WSCG*, 15(1-3):33–40, 2007.

[225] J. Spillmann and M. Teschner. CoRdE: Cosserat rod elements for the dynamic simulation of one-dimensional elastic objects. In *ACM SIGGRAPH/Eurographics Symposium on Computer Animation*, pages 63–72, 2007.

[226] J. Steindorf. *Partitionierte Verfahren für Probleme der Fluid-Struktur Wechselwirkung*. PhD thesis, Technische Universität Braunschweig - Fachbereich für Mathematik und Informatik, 2002.

[227] T. Stoesser, S. J. Kim, and P. Diplas. Turbulent Flow through Idealized Emergent Vegetation. *Journal of Hydraulic Engineering*, 136(12):1003–1017, 2010.

[228] T. Stumpp, J. Spillmann, M. Becker, and M. Teschner. A Geometric Deformation Model for Stable Cloth Simulation. In *Workshop on Virtual Reality Interaction and Physical Simulation*, pages 39–46, 2008.

[229] K. Sugiyama, S. Ii, S. Takeuchi, S. Takagi, and Y. Matsumoto. A full Eulerian finite difference approach for solving fluid-structure coupling problems. *Journal of Computational Physics*, 230(3):596–627, 2011.

[230] T. Sukhodolova. *Studies of Turbulent Flow in Vegetated River Reaches with Implications for Transport and Mixing Processes*. PhD thesis, Humboldt-Universität zu Berlin, 2008.

[231] D. Sundararajan. *The Discrete Fourier Transform: Theory, Algorithms and Applications*. World Scientific, 2001.

[232] M. Sussman, P. Smereka, and S. Osher. A Level Set Approach for Computing Solutions to Incompressible Two-Phase Flow. *Journal of Computational Physics*, 114(1):146–159, 1994.

[233] I. Sutherland and G. Hodgman. Reentrant Polygon Clipping. *Communications of the ACM*, 17(1):32–42, 1974.

[234] M. Tang, D. Manocha, M. Otaduy, and R. Tong. Continuous Penalty Forces. *ACM Transactions on Graphics*, 31(4):107:1–107:9, 2012.

[235] S. Tardu. Characteristics of single and multiple bursting events in the inner layer. Part 2. Level-crossing events. *Experiments in Fluids*, 33(5):640–652, 2002.

[236] G. Taubin. 3D Rotations. *IEEE Computer Graphics and Applications*, 31(6):84–89, 2011.

[237] The Engineering ToolBox. `http://www.engineeringtoolbox.com`, 2018. [online; accessed 15-January-2018].

[238] B. Thomaszewski, M. Wacker, and W. Straßer. A consistent bending model for cloth simulation with corotational subdivision finite elements. In *ACM SIGGRAPH/Eurographics Symposium on Computer Animation*, pages 107–116, 2006.

[239] F.-B. Tian, H. Dai, H. Luo, J. Doyle, and B. Rousseau. Fluid-structure interaction involving large deformations: 3D simulations and applications to biological systems. *Journal of Computational Physics*, 258:451–469, 2014.

[240] S. Timoshenko. LXVI. On the correction for shear of the differential equation for transverse vibrations of prismatic bars. *The London, Edinburgh, and Dublin Philosophical Magazine and Journal of Science*, 41(245):744–746, 1921.

[241] S. Timoshenko. *History of Strength of Materials*. Dover Publications, 1983.

[242] W. Titow. *PVC Technology*. Elsevier Applied Science Publishers, 1984.

[243] R. Tonge, F. Benevolenski, and A. Voroshilov. Mass Splitting for Jitter-free Parallel Rigid Body Simulation. *ACM Transactions on Graphics*, 31(4):105:1–105:8, 2012.

[244] E. Tozzi. *Hydrodynamics, Rheology and Conduction in Suspensions of Arbitrary Shaped Fibers*. PhD thesis, University of Wisconsin-Madison, 2008.

[245] C. Truesdell and W. Noll. *The Non-Linear Field Theories of Mechanics*. Springer, third edition edition, 2003.

[246] S. Tschisgale, T. Kempe, and J. Fröhlich. A non-iterative immersed boundary method for spherical particles of arbitrary density ratio. *Journal of Computational Physics*, 339:432–452, 2017.

[247] S. Tschisgale, T. Kempe, and J. Fröhlich. A general implicit direct forcing immersed boundary method for rigid particles. *Computers & Fluids*, 170:285–298, 2018.

[248] S. Turek and J. Hron. Proposal for Numerical Benchmarking of Fluid-Structure Interaction between an Elastic Object and Laminar Incompressible Flow. In H.-J. Bungartz and M. Schäfer, editors, *Fluid-Structure Interaction: Modelling, Simulation, Optimisation*, chapter 1, pages 371–385. Springer, 2006.

[249] S. Turek, J. Hron, M. Razzaq, H. Wobker, and M. Schäfer. Numerical Benchmarking of Fluid-Structure Interaction: A Comparison of Different Discretization and Solution Approaches. In H.-J. Bungartz, M. Mehl, and M. Schäfer, editors, *Fluid Structure Interaction II: Modelling, Simulation, Optimization*, chapter 1, pages 413–424. Springer, 2010.

[250] M. Uhlmann. Simulation of particulate flows on multi-processor machines with distributed memory. Technical Report 1039, Centre for Energy, Environment and Technology, 2003.

[251] M. Uhlmann. An immersed boundary method with direct forcing for the simulation of particulate flows. *Journal of Computational Physics*, 209(2):448–476, 2005.

[252] G. van den Bergen, editor. *Collision Detection in Interactive 3D Environments*. Morgan Kaufmann publishers, 2004.

[253] R. van Loon, P. Anderson, F. van de Vosse, and S. Sherwin. Comparison of various fluid-structure interaction methods for deformable bodies. *Computers & Structures*, 85(11):833–843, 2007.

[254] D. Velasco, A. Bateman, and V. Medina. A new integrated, hydro-mechanical model applied to flexible vegetation in riverbeds. *Journal of Hydraulic Research*, 46(5):579–597, 2008.

[255] A. Verkaik, M. Hulsen, A. Bogaerds, and F. van de Vosse. An overlapping domain technique coupling spectral and finite elements for fluid-structure interaction. *Computers & Fluids*, 123:235–245, 2015.

[256] R. Vetter, F. Wittel, N. Stoop, and H. Herrmann. Finite element simulation of dense wire packings. *European Journal of Mechanics - A/Solids*, 37:160–171, 2013.

[257] S. Vogel. *Life in Moving Fluids: The Physical Biology of Flow*. Princeton University Press, 1994.

[258] B. Vowinckel, T. Kempe, and J. Fröhlich. Fluid-particle interaction in turbulent open channel flow with fully-resolved mobile beds. *Advances in Water Resources*, 72:32–44, 2014.

[259] L. Vu-Quoc and J. Simo. Dynamics of Earth-Orbiting Flexible Satellites with Multibody Components. *Journal of Guidance, Control, and Dynamics*, 10(6):549–558, 1987.

[260] W. Wall. *Fluid-Struktur-Interaktion mit stabilisierten Finiten Elementen*. PhD thesis, Universität Stuttgart - Institut für Baustatik, 2002.

[261] W. Wall and E. Ramm. *Fluid Structure Interaction Based Upon a Stabilized (ALE) Finite Element Method*. Sonderforschungsbereich Mehrfeldprobleme in der Kontinuumsmechanik. Stuttgart SFB 404, 1998.

[262] H. Weiß. *Zur Dynamik geometrisch nichtlinearer Balken*. PhD thesis, Technische Universität Chemnitz, 1999.

[263] J. Wiens and J. Stockie. An efficient parallel immersed boundary algorithm using a pseudo-compressible fluid solver. *Journal of Computational Physics*, 281:917–941, 2015.

[264] J. Wiens and J. Stockie. Simulating flexible fiber suspensions using a scalable immersed boundary algorithm. *Computer Methods in Applied Mechanics and Engineering*, 290:1–18, 2015.

[265] C. Wilson, T. Stoesser, P. Bates, and A. B. Pinzen. Open Channel Flow through Different Forms of Submerged Flexible Vegetation. *Journal of Hydraulic Engineering*, 129(11):847–853, 2003.

[266] G. Xia and C.-L. Lin. An unstructured finite volume approach for structural dynamics in response to fluid motions. *Computers & Structures*, 86(7):684–701, 2008.

[267] J. Yang, S. Preidikman, and E. Balaras. A strongly coupled, embedded-boundary method for fluid-structure interactions of elastically mounted rigid bodies. *Journal of Fluids and Structures*, 24(2):167–182, 2008.

[268] X. Yang, X. Zhang, Z. Li, and G.-W. He. A smoothing technique for discrete delta functions with application to immersed boundary method in moving boundary simulations. *Journal of Computational Physics*, 228(20):7821–7836, 2009.

[269] Z. Yu. A DLM/FD method for fluid/flexible-body interactions. *Journal of Computational Physics*, 207(1):1–27, 2005.

[270] B. Yusuf, O. Karim, and S. Osman. Numerical solution for open channel flow with submerged flexible vegetation. *International Journal of Engineering and Technology*, 6(1):39–50, 2009.

[271] L. Zhang, A. Gerstenberger, X. Wang, and W. Liu. Immersed finite element method. *Computer Methods in Applied Mechanics and Engineering*, 193(21):2051–2067, 2004.

[272] L. Zhu and C. Peskin. Simulation of a Flapping Flexible Filament in a Flowing Soap Film by the Immersed Boundary Method. *Journal of Computational Physics*, 179(2):452–468, 2002.

[273] X. Zhu, G. He, and X. Zhang. An Improved Direct-Forcing Immersed Boundary Method for Fluid-Structure Interaction Simulations. *Journal of Fluids Engineering*, 136(4):040903, 2014.

[274] D. Zupan and M. Saje. Finite-element formulation of geometrically exact three-dimensional beam theories based on interpolation of strain measures. *Computer Methods in Applied Mechanics and Engineering*, 192(49):5209–5248, 2003.

[275] E. Zupan, M. Saje, and D. Zupan. Dynamics of spatial beams in quaternion description based on the Newmark integration scheme. *Computational Mechanics*, 51(1):47–64, 2013.

[276] An ocean underwater reef with sun light through water surface. `http://www.stock.adobe.com`, 2018. [license acquired on 24-April-2018].

Publications

Journals

S. Tschisgale, L. Thiry, J. Fröhlich. *A constraint-based collision model for Cosserat rods*. Archive of Applied Mechanics, Vol. 89(2), pp. 167–193, 2019.

S. Tschisgale, T. Kempe, J. Fröhlich. *A general implicit direct forcing immersed boundary method for rigid particles*. Computers & Fluids, Vol. 170, pp. 285–298, 2018.

S. Tschisgale, T. Kempe, J. Fröhlich. *A non-iterative immersed boundary method for spherical particles of arbitrary density ratio*. Journal of Computational Physics, Vol. 339, pp. 432–452, 2017.

Conferences

S. Tschisgale*, R. Meller, J. Fröhlich. *Simulation of the turbulent flow over an array of flexible blades*. 10th International Symposium on Turbulence and Shear Flow Phenomena (TSFP), Chicago, USA, 2017.

S. Tschisgale*, T. Kempe, J. Fröhlich. *A novel non-iterative immersed boundary method for rigid particles of arbitrary density ratio*. 3rd International Conference on Numerical Methods in Multiphase Flows (ICNMMF), Tokyo, Japan, 2017.

R. Meller*, **S. Tschisgale**, J. Fröhlich. *Numerical study on the fluid-structure interaction in a model aquatic canopy flow*. Proceedings in Applied Mathematics and Mechanics, Vol. 17(1), pp. 523–524, 2017.

S. Tschisgale*, T. Kempe, J. Fröhlich. *A new approach to define a non-iterative immersed boundary method for spherical particles of arbitrary density ratio*. 9th International Conference on Multiphase Flow (ICMF), Firenze, Italy, 2016.

S. Tschisgale*, J. Fröhlich. *Simulation of a long slender structure in turbulent flow*. Proceedings in Applied Mathematics and Mechanics, Vol. 14(1), pp. 499–500, 2014.

∗ presenting author

This thesis presents a numerical method for the simulation of fluid-structure interaction (FSI) problems on high-performance computers. The proposed method is specifically tailored to interactions between Newtonian fluids and a large number of slender viscoelastic structures, the latter being modeled as Cosserat rods. From a numerical point of view, such kind of FSI requires special techniques to reach numerical stability. When using a partitioned fluid-structure coupling approach this is usually achieved by an iterative procedure, which drastically increases the computational effort. In the present work, an alternative coupling approach is developed based on an immersed boundary method (IBM). It is unconditionally stable and exempt from any global iteration between the fluid part and the structure part.

The proposed FSI solver is employed to simulate the flow over a dense layer of vegetation elements, usually designated as canopy flow. The abstracted canopy model used in the simulation consists of 800 strip-shaped blades, which is the largest canopy-resolving simulation of this type done so far. To gain a deeper understanding of the physics of aquatic canopy flows the simulation data obtained are analyzed, e.g., concerning the existence and shape of coherent structures.

TUDpress

ISBN 978-3-95908-195-5